NASA Contractor Report 3902

Investigations Into the Triggered Lightning Response of the F106B Thunderstorm Research Aircraft

Terence H. Rudolph, Rodney A. Perala,
Paul M. McKenna, and Steven L. Parker

CONTRACT NAS1-16984
JUNE 1985

NASA Contractor Report 3902

Investigations Into the Triggered Lightning Response of the F106B Thunderstorm Research Aircraft

Terence H. Rudolph, Rodney A. Perala,
Paul M. McKenna, and Steven L. Parker
Electro Magnetic Applications, Inc.
Denver, Colorado

Prepared for
Langley Research Center
under Contract NAS1-16984

National Aeronautics
and Space Administration

Scientific and Technical
Information Branch

1985

N88-29258#

TABLE OF CONTENTS

LIST OF FIGURES

LIST OF FIGURES (Sheet 2)

LIST OF FIGURES (Sheet 3)

LIST OF FIGURES (Sheet 4)

LIST OF FIGURES (Sheet 5)

LIST OF TABLES

LIST OF SYMBOLS

B	- magnetic induction
B-dot $\equiv \dot{B}$	- time derivative of magnetic induction
c	- speed of light
D	- electric displacement
D-dot $\equiv \dot{D}$	- time derivative of electric displacement
E	- electric field
E_b	- electric field magnitude necessary for air breakdown
E_r	- radial electric field
F	- flux
F^{coarse}	- general coarse grid field
f^{fine}	- general fine grid field
g	- avalanche rate
H	- magnetic intensity
H_e	- energy diffusion coefficient
I	- electric current
I-dot $\equiv \dot{I}$	- time derivative of electric current
$\tilde{I}$	- frequency domain representation of electric current
k	- Boltzmann's constant
k_e	- particle diffusion coefficient
$k_{excitation}$	- generic term representing excitation of molecular vibrational states.
m_α	- mass of species α
n_α	- particle density of species α
p_α	- partial pressure of species α
Q	- ambient ionization rate in the atmosphere
Q_o	- net charge on the F-106B aircraft
q_α	- charge on a particle of species α
$\tilde{R}$	- frequency domain representation of an aircraft response
r_{trig}	- distance at which natural lightning can trigger a strike to the F106B aircraft
T	- transfer function
T_α	- temperature of species α

LIST OF SYMBOLS CONT'D

u_α	- mobility of species α
$\vec{v}_\alpha$	- velocity of species α
x_α	- expansion factor in α direction
α_e	- attachment rate
β	- electron-ion recombination rate
γ	- ion-ion recombination
ε_o	- permittivity of free space
ε_α	- energy density of species α
ε_α^o	- ambient energy density of species α
ε_{ion}	- energy necessary to ionize a heavy particle
ε_Q	- energy gained from ambient ionization processes
λ	- charge per unit length
υ_c	- collision frequency

CHAPTER 1

INTRODUCTION

For several years the NASA Langley Research Center has been flying an instrumented F106B aircraft into thunderstorms collecting information on direct lightning strikes. The ultimate goal of the effort is to be able to characterize the lightning environment so that the effect of direct lightning strikes to arbitrary aircraft can be predicted. The F106B carries instruments to measure such quantities as electric and magnetic fields on the aircraft, current flowing on the pitot boom, and ambient temperature. The electromagnetic measurements are made as a function of time with a resolution of 10 nanoseconds. This is sufficient to resolve the evolution of a lightning channel as it forms, usually near the extremities of the aircraft. The task of the analyst is to use the electromagnetic responses measured on the F106B to determine the characteristics of the lightning which caused the response.

This report concentrates on the 1982 direct strike data [1]. The analytic thrust is the investigation of triggered lightning on the F106B, because recent studies [2] have shown this to be quite likely. The major analytical tool is the computer code T3DFD, a three dimensional finite difference model which solves Maxwell's equations in the time domain. The physics of the air is taken into account with a three species air chemistry model which provides a nonlinear air conductivity to Maxwell's equations.

A block model of the F106B, which is how the airplane appears to the finite difference code, is shown in Figure 1.1. The locations of the B-dot and D-dot electromagnetic sensors are indicated in the figure. The grid resolution of the finite difference model is one meter in the direction along the fuselage and one-half meter in the other two dimensions. This requires a time step of one nanosecond, which is the temporal resolution of the model. The specifics of the finite difference model have been covered in some detail in previous reports [3,4], and will therefore be omitted here.

As stated earlier, the body of this report is concerned with the interpretation and analysis of the 1982 direct strike lightning data in light

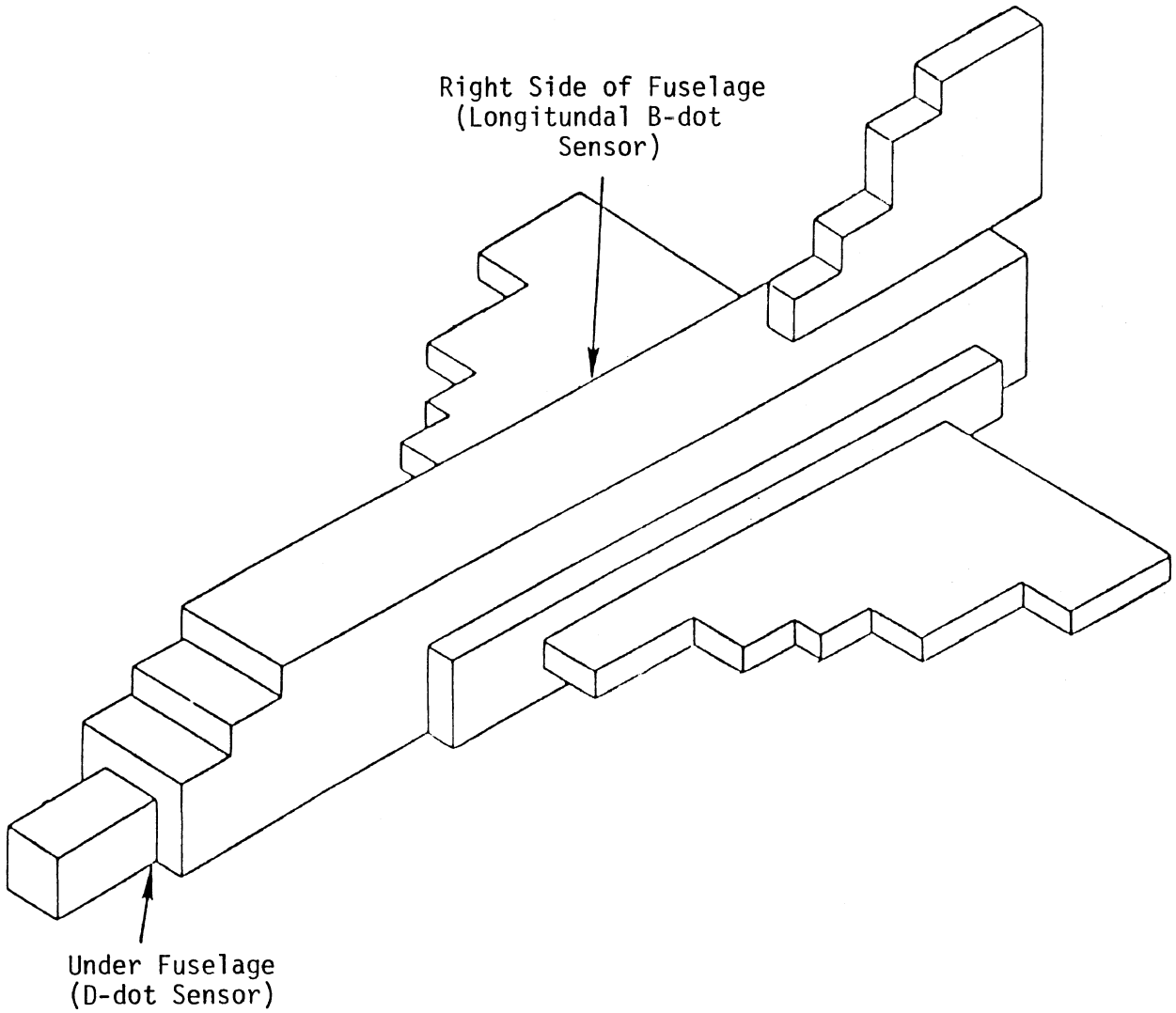

Figure 1.1 Block Model of F106B Showing Sensor Locations

of the possibility that much or all of it may be from triggered lightning. Chapter 2 is concerned with data classification in the time domain, searching for trends that could indicate similar physical processes. Chapter 3 analyzes the data in the frequency domain, with emphasis on aircraft resonances which should be present. Chapter 4 deals in a general fashion with the triggered lightning environment, and its relation to the direct strike program. Chapter 5 discusses the modeling of triggered lightning on the F106B and presents results from the computer code T3DFD. Chapter 6 presents a new enhanced nonlinear model which includes fluid equations for particle momentum and energy densities. This model, because of its size, is currently only two dimensional and is still under development. Chapter 7 is concerned with the details surrounding subgrid implementation. This allows one to model a given region in a finite difference code with greater spatial resolution than is present in the rest of the problem space. Chapter 8 details the calculation of transfer functions for the F106B in three different current injection configurations. Chapter 9 presents a summary and conclusions.

CHAPTER 2

DATA CLASSIFICATION

In an effort to identify trends in the measured data from 1982, the D-dot and B-dot records have been classified into categories according to waveshape. The classifications are by necessity somewhat subjective, and it is certainly possible that some waveforms belong in a different category. The categories are intended to highlight waveforms with similar characteristics, which may indicate similar physical phenomena. Descriptions of the eight D-dot categories and six B-dot categories are given below, with the number of waveforms in each category in parentheses.

D-Dot

1. Slow positive, then negative, bipolar pulse. (35)
2. Double bipolar pulses separated by $\sim$200-400 ns, initially >0, with $\int \dot{D}\, dt \approx 0$. (11)
3. Single negative pulse with little structure. (15)
4. Bipolar pulses, first negative, then positive (3)
5. Fast bipolar pulses, initially positive. (21)
6. Initial large fast pulse with much structure and having a late time tail, mainly unipolar. (24)
7. Simple unstructured positive pulse. (6)
8. Miscellaneous. (8)

B-Dot

1. Initially positive pulse with much late time structure. (7)
2. Slow positive and negative half cycles, usually small. (1)
3. Initially positive single cycle followed by low amplitude structure. (15)
4. Unstructured single positive cycle. (5)
5. Single negative slow pulse. (3)
6. Fast double pulses, separated by 200-500 ns, initially positive. (19)

The waveforms themselves along with their Fourier transforms are presented in Appendix A. The format of the majority of the figures there is to overlay three of the time domain waveforms in a given category in the

upper left corner of the page. The legend giving the flight number and characteristics of the strike (attach point, temperature, flight altitude) is coded according to the line type of the waveform (dashed, dotted, or solid). The other three positions on the page are the Fourier transform of the time domain waveforms coded as in the time domain plot. The exceptions to this format occur if there are not three time domain waveforms to overlay, as in Category 8 of the D-dot records (Miscellaneous). The format of the first exception is transparent. For Category 8 of the D-dots, no overlays were made because the waveforms were judged to be unique. Hence the two plots on the left hand side of the page are time domain waveforms with the corresponding Fourier transforms on the right of the page.

Not all of the 1982 data records are included in this cassification. Records having very small amplitude ($\sim$two or three digitization increments) and records with saturated sensors were omitted. Although the saturated records probably could have been included in the time domain classification, it was impossible to get accurate Fourier transforms of them.

Finding a correspondence between the classification categories and particular physical phenomena is difficult. There appears to be no obvious correlation between temperature and category or flight altitude and category. The correlation between attach point and category may be slightly better, although the attach point for the majority of strikes is unknown. It is very possible that D-dot records from Categories 2 and 5 and B-dot records from Categories 3 and 6 are caused by lightning triggered at the nose of the aircraft. (See Chapter 5 for representative waveforms). These categories probably represent the same type of phenomena, except that in the categories with double pulses, a similar event happens twice (e.g. air breakdown at nose and later at tail). The hypothesis that triggered lightning causes these pulses is supported by the simultaneous D-dot and B-dot records. The models for natural and nearby lightning do not reproduce the relative amplitude and timing of D-dot and B-dot responses seen in the measured records, while the model for triggered lightning does. Although it is not possible to exclude natural and nearby lightning as responsible for the measured records without examining in detail all possible cases, the evidence so far tends to lend credence to the triggered lightning hypothesis.

The other categories have not been identified with physical events as yet, although if triggered lightning is responsible, it could be triggered at points other than the nose of the aircraft. Triggering at locations other than the nose will be investigated in the near future and may give insight into the physical events which produce many of the D-dot and B-dot categories.

CHAPTER 3

STATISTICAL ANALYSIS OF FOURIER TRANSFORMED DATA

3.1 Fourier Transform Analysis of Measured Data

From the time domain data measured on the F106B it is difficult to recognize the presence of aircraft resonances. This can be much more easily done if the data is transformed into the frequency domain. This has been accomplished for most of the measured data, and a statistical study performed on the results.

The data transformed was that from the D-dot forward, B-dot longitudinal, I (current on nose boom), and I-dot (time derivative of current on nose boom) sensors. The only records from these sensors which were not transformed were records with very small amplitude ($\sim$ few digitization steps), obviously saturated records, and records having data dropouts. The magnitude of the transform of all the B-dot and D-dot records are presented in Appendix A, along with their associated time domain waveforms.

I and I-dot records are not included in Appendix A because their numbers were not sufficient to warrant a classification as was done with the D-dot and B-dot records.

The statistical analysis of the Fourier transforms proceeded as follows. For each transform magnitude a search was done to find the maxima and minima of the transform as a function of frequency. A database was constructed which included the frequency location of all the maxima and minima as a function of type of record (D-dot, B-dot, I, I-dot). The database also included the absolute value of the transform at the maxima and minima. Because the absolute value of a transform at any point is not a particularly useful parameter in searching for resonances, another parameter was developed which measured the relative importance of a given maximum or minimum in a frequency spectrum. If one calls the maxima and minima of a spectrum the "resonances", this parameter will be called the "relative amplitude" of the resonances. For the definition of the relative amplitude consider Figure 3.1. In that figure is shown a typical piece of a Fourier transform, with frequency on the horizontal axis and the magnitude of the transform

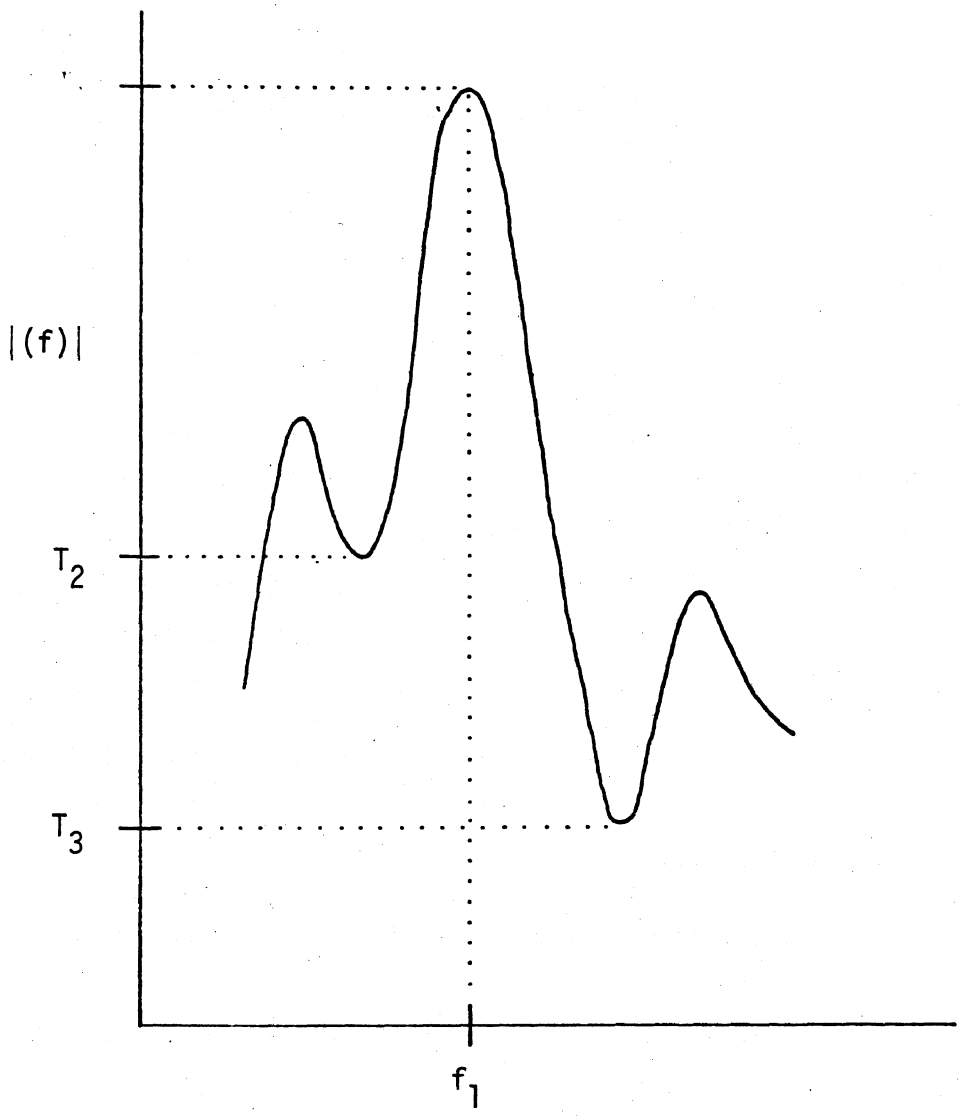

Figure 3.1 Definition of Amplitude

on the vertical axis. The relative amplitude of the peak at frequency f_1 is defined to be the average of the height of the peak above the two minima on either side.

Relative amplitude of peak at f_1 is given by:

$$\text{Relative amplitude} = 1/2\ (T_1 - T_2 + T_1 - T_3). \tag{3.1}$$

Similarily the relative amplitude of a minimum is defined to be its average depth below the two peaks on either side of it. Using these definitions the relative amplitude parameter is always a positive number and gives a measure of the prominence of a resonance in a given spectrum.

Having defined the relative amplitude parameter, it was then incorporated into the database and used as a filter in searching for aircraft resonances. This was done by producing histograms showing number of resonances in a given frequency bandwidth as a function of frequency, type of record, type of resonance (maximum or minimum), and relative amplitude. As mentioned the relative amplitude was used as a filter. First all resonances of a given type were included in a histogram. Next only those with relative amplitudes greater than 2.5 dB were included. The relative amplitude filter was raised in this way until only a statistically insignificant number of resonances could meet the criteria. Using this method it was hoped that as the relative amplitude filter was increased, physical aircraft resonances would rise out of the noise in the spectrum. The resulting histograms are presented in Figures 3.2 to 3.39. I-dot sensor results are not presented, because the small number of I-dot records was statistically insignificant. The histograms have a bandwidth of 500 kHz, so that each bar represents the number of resonances falling in a 500 kHz window centered on the frequency label below it. For example, the bar labelled 15 MHz actually contains all the resonances falling between 14.75 MHz and 15.25 MHz.

Interpretation of the histogram figures is relatively easy. As one moves from small relative amplitude filter to larger relative amplitude filter, the total number of resonances goes down. This occurs as the small resonances produced by numerical and measurement noise are eliminated. Therefore the signal to noise ratio of the remaining data is improved. Using the D-dot maximum histograms as an example, one starts with a relatively flat

(text continued on page 48)

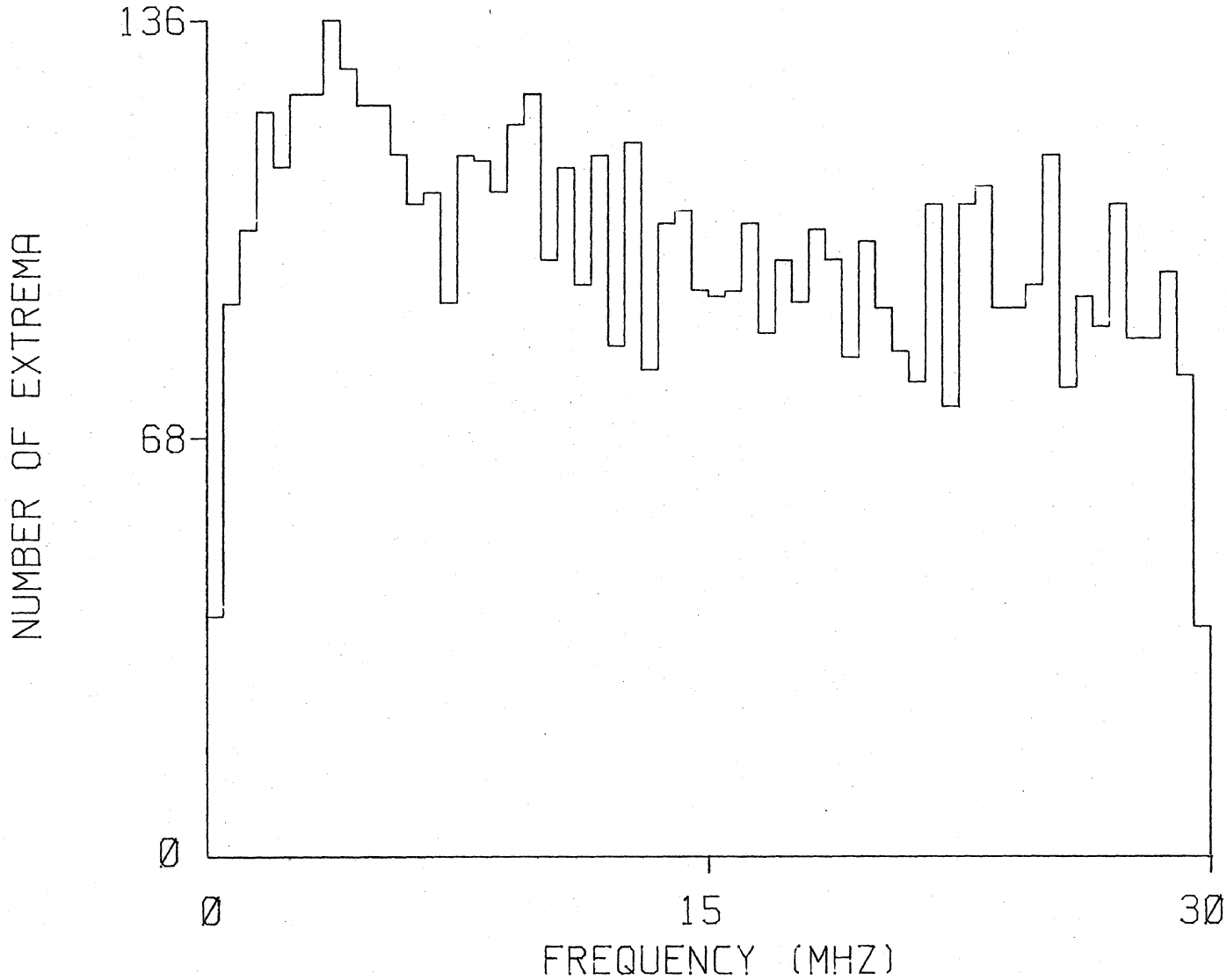

FIGURE 3.2 D-DOT MINIMA, AMPLITUDE FILTER= Ø DB.

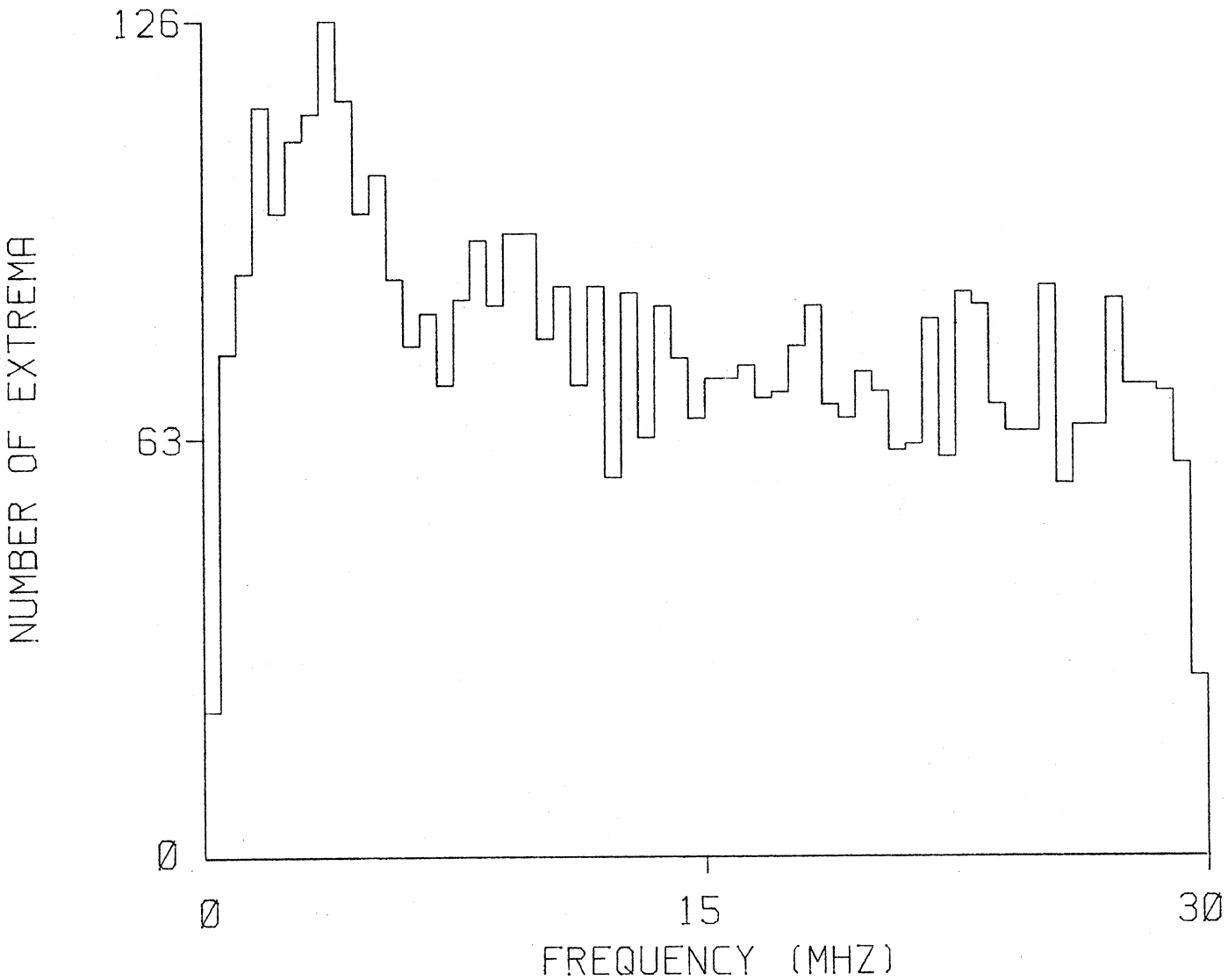

FIGURE 3.3 D-DOT MINIMA, AMPLITUDE FILTER= 2.5 DB.

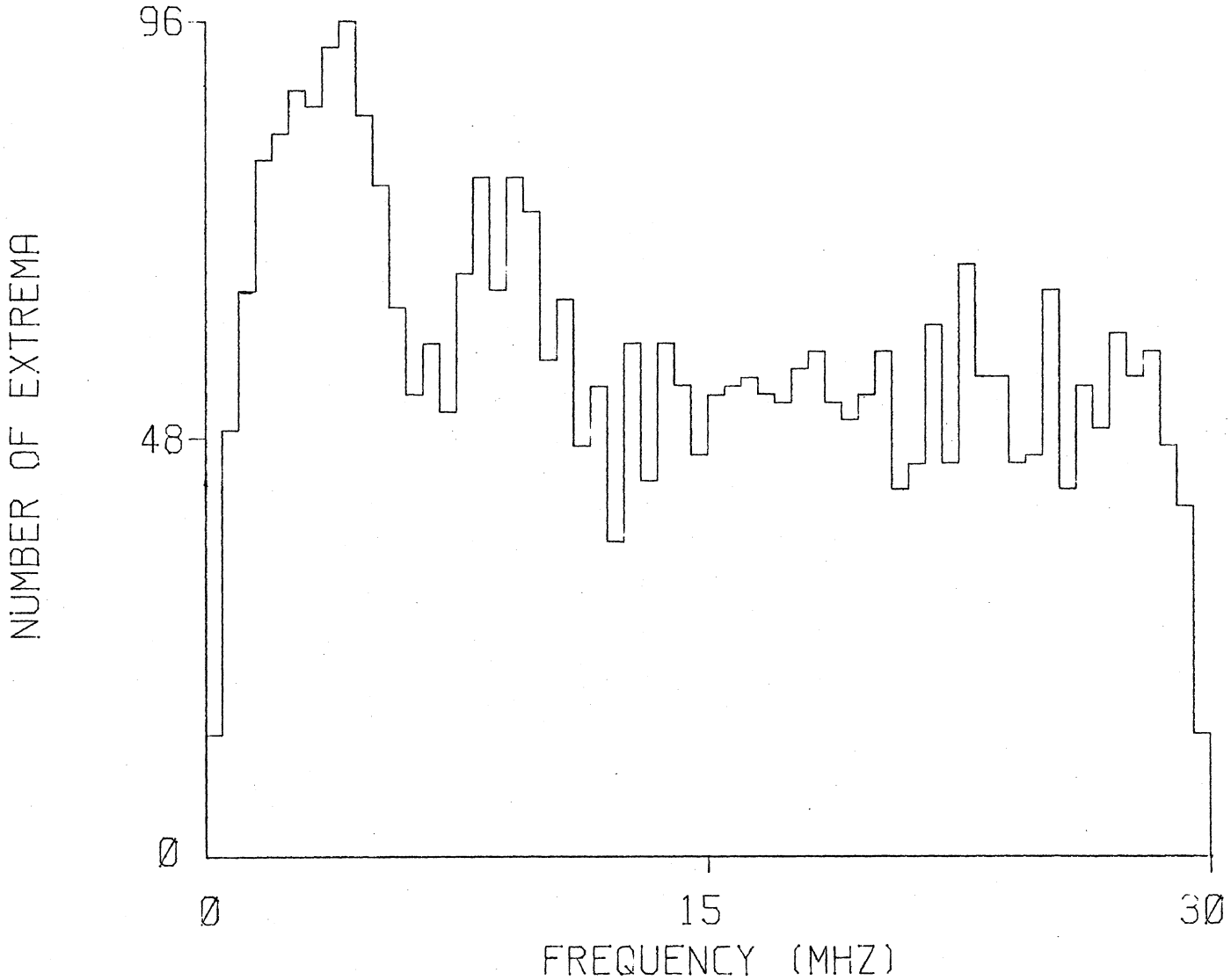

FIGURE 3.4 D-DOT MINIMA, AMPLITUDE FILTER= 5 DB.

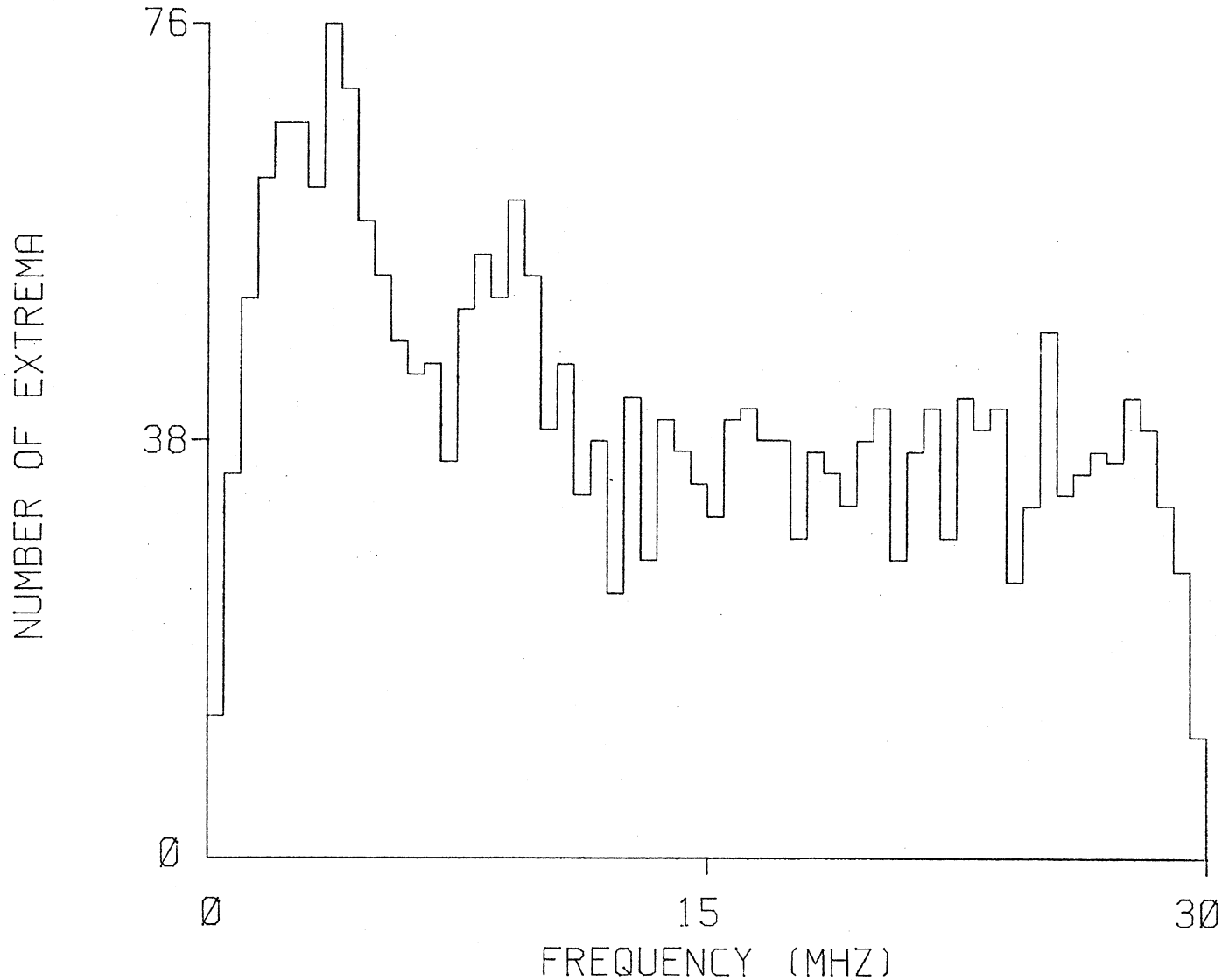

FIGURE 3.5 D-DOT MINIMA, AMPLITUDE FILTER= 7.5 DB.

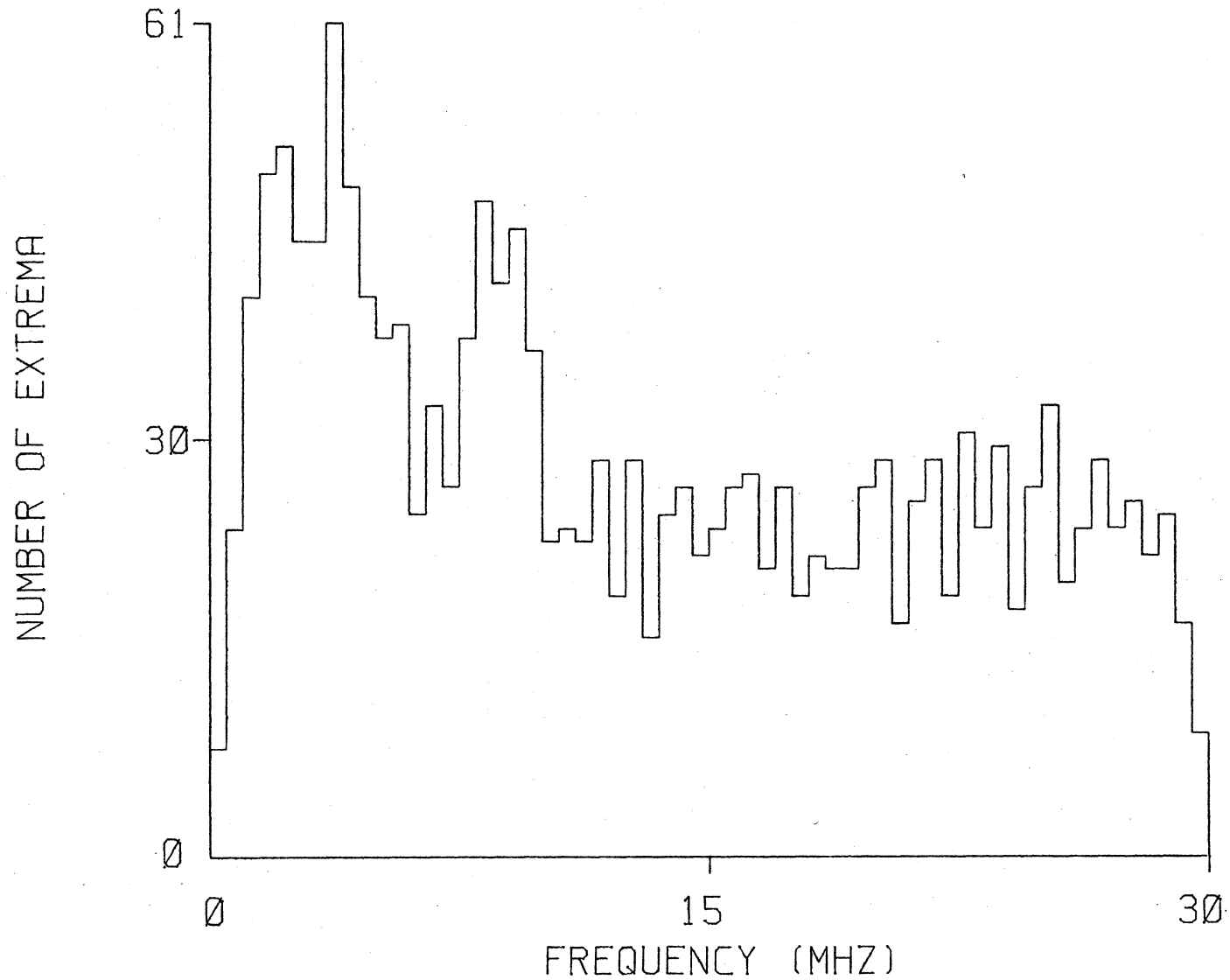

FIGURE 3.6 D-DOT MINIMA, AMPLITUDE FILTER= 10.0 DB.

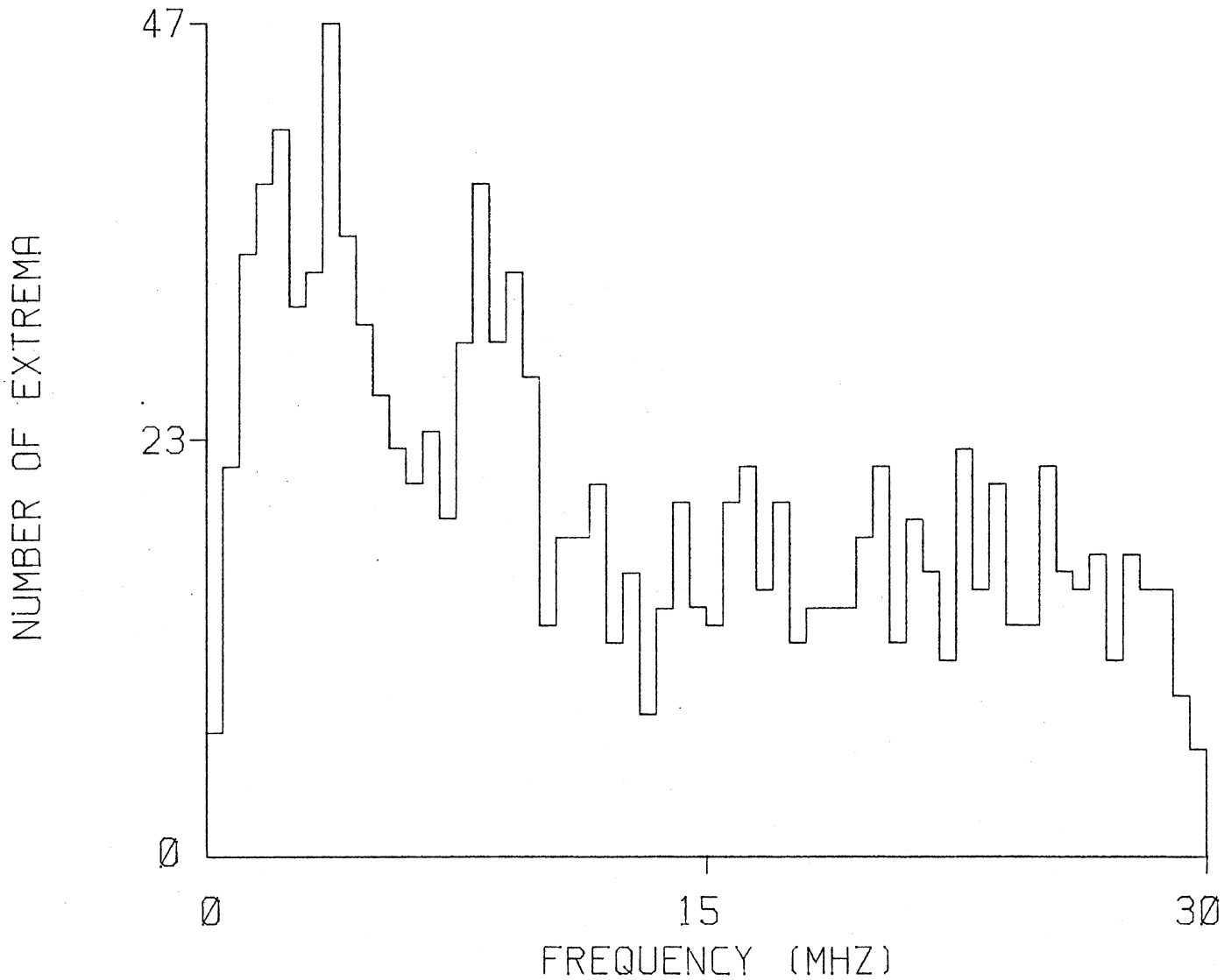

FIGURE 3.7 D-DOT MINIMA, AMPLITUDE FILTER= 12.5 DB.

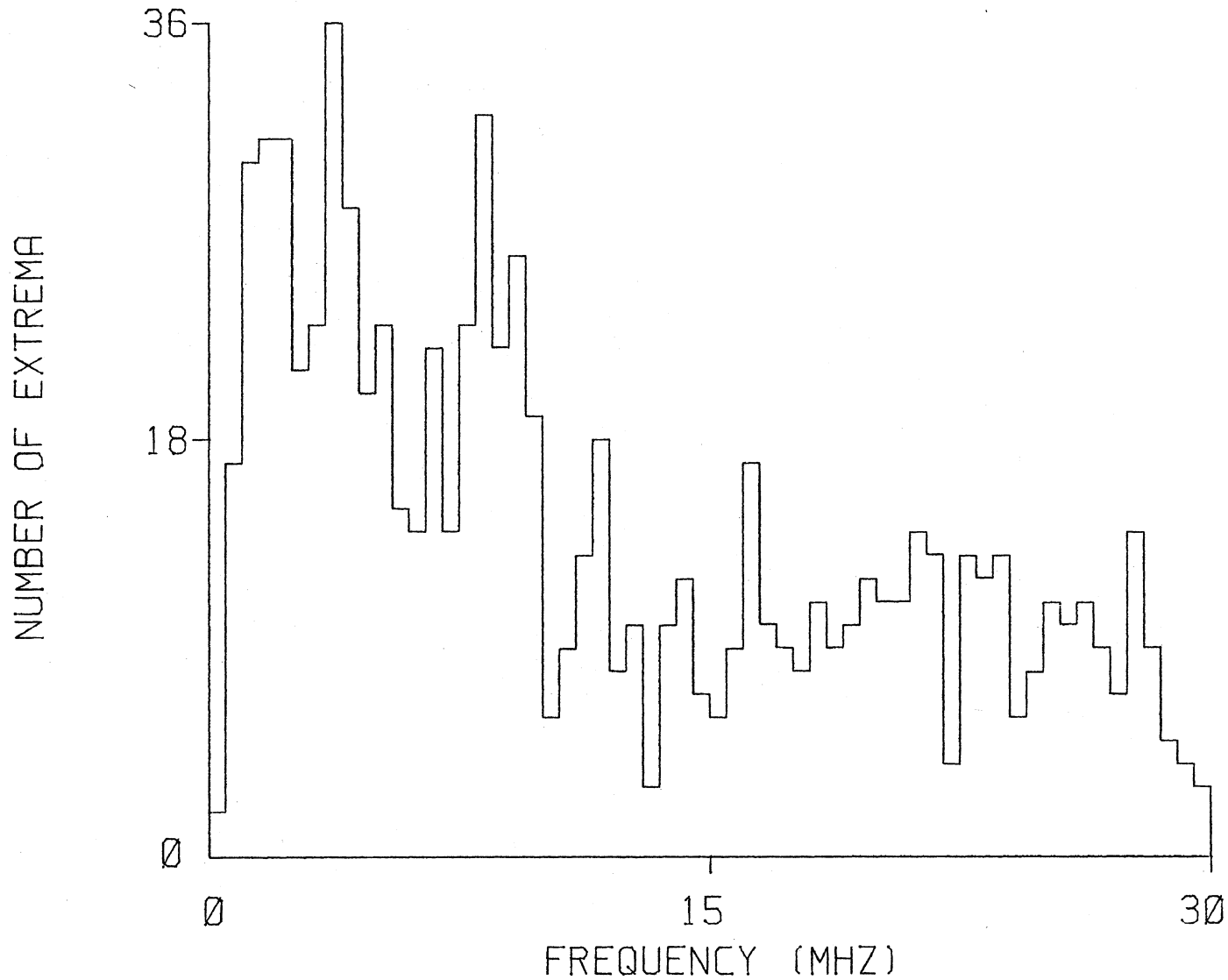

FIGURE 3.8 D-DOT MINIMA, AMPLITUDE FILTER= 15.Ø DB.

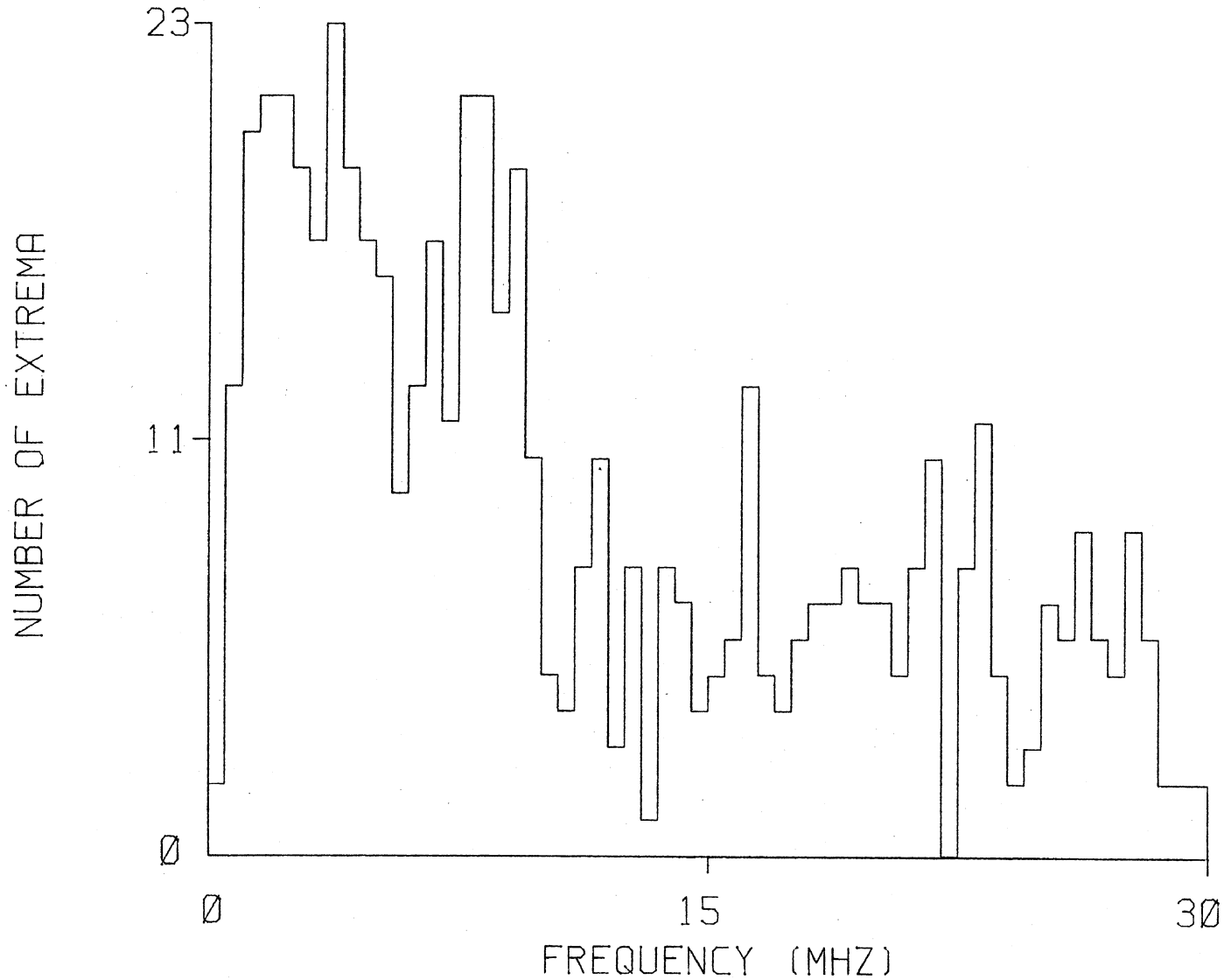

FIGURE 3.9 D-DOT MINIMA, AMPLITUDE FILTER= 17.5 DB.

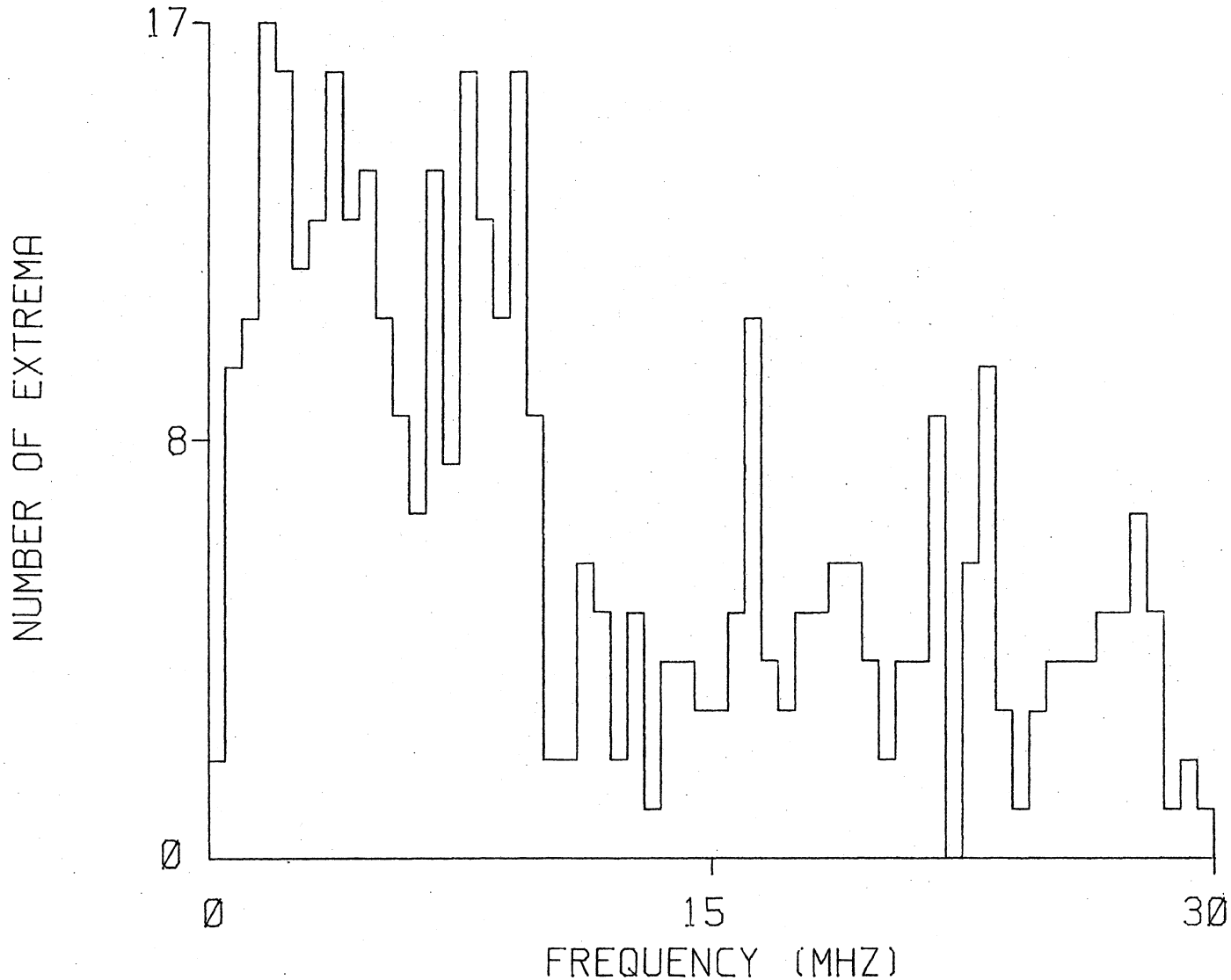

FIGURE 3.10 D-DOT MINIMA, AMPLITUDE FILTER= 20.0 DB.

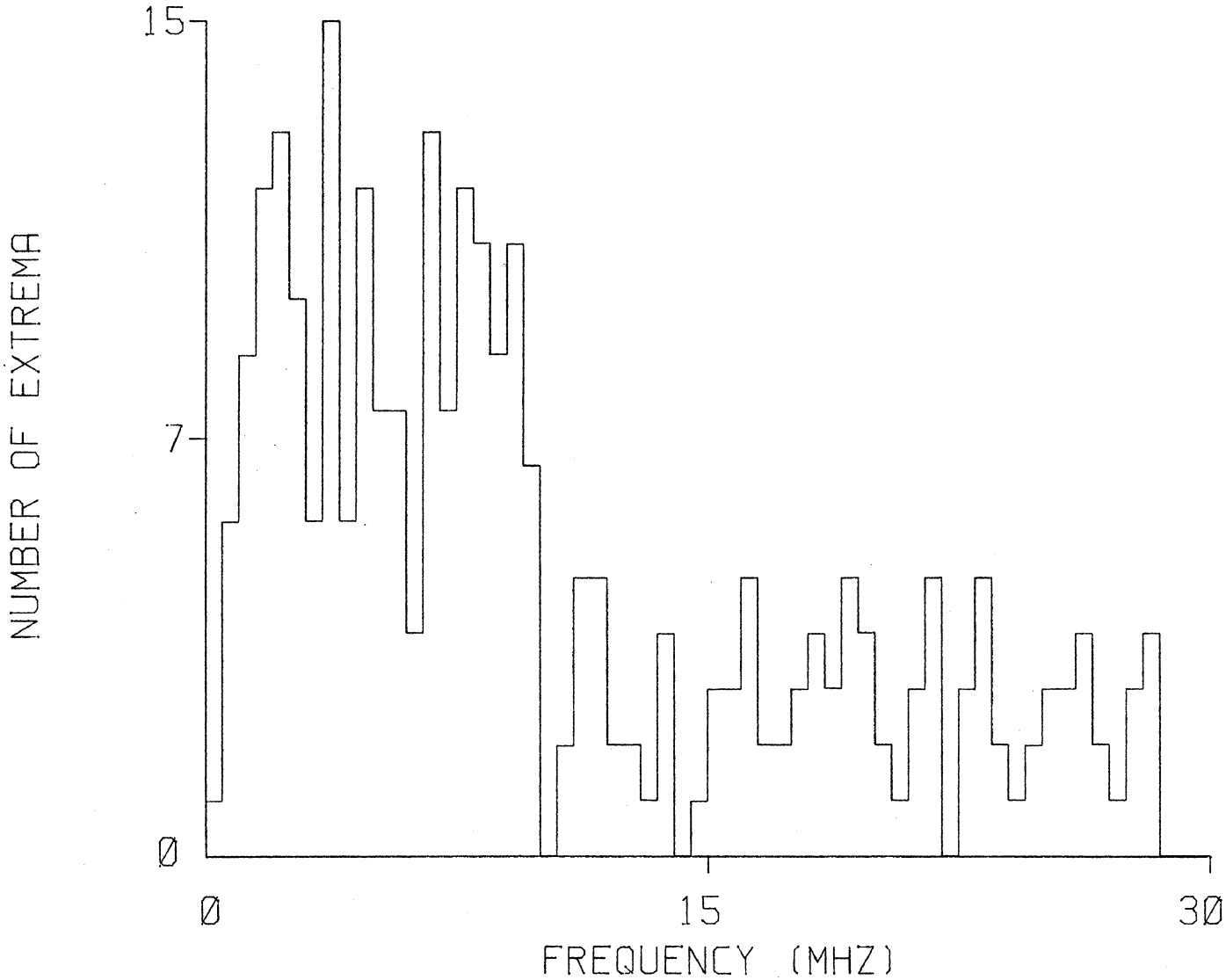

FIGURE 3.11 D-DOT MINIMA, AMPLITUDE FILTER= 22.5 DB.

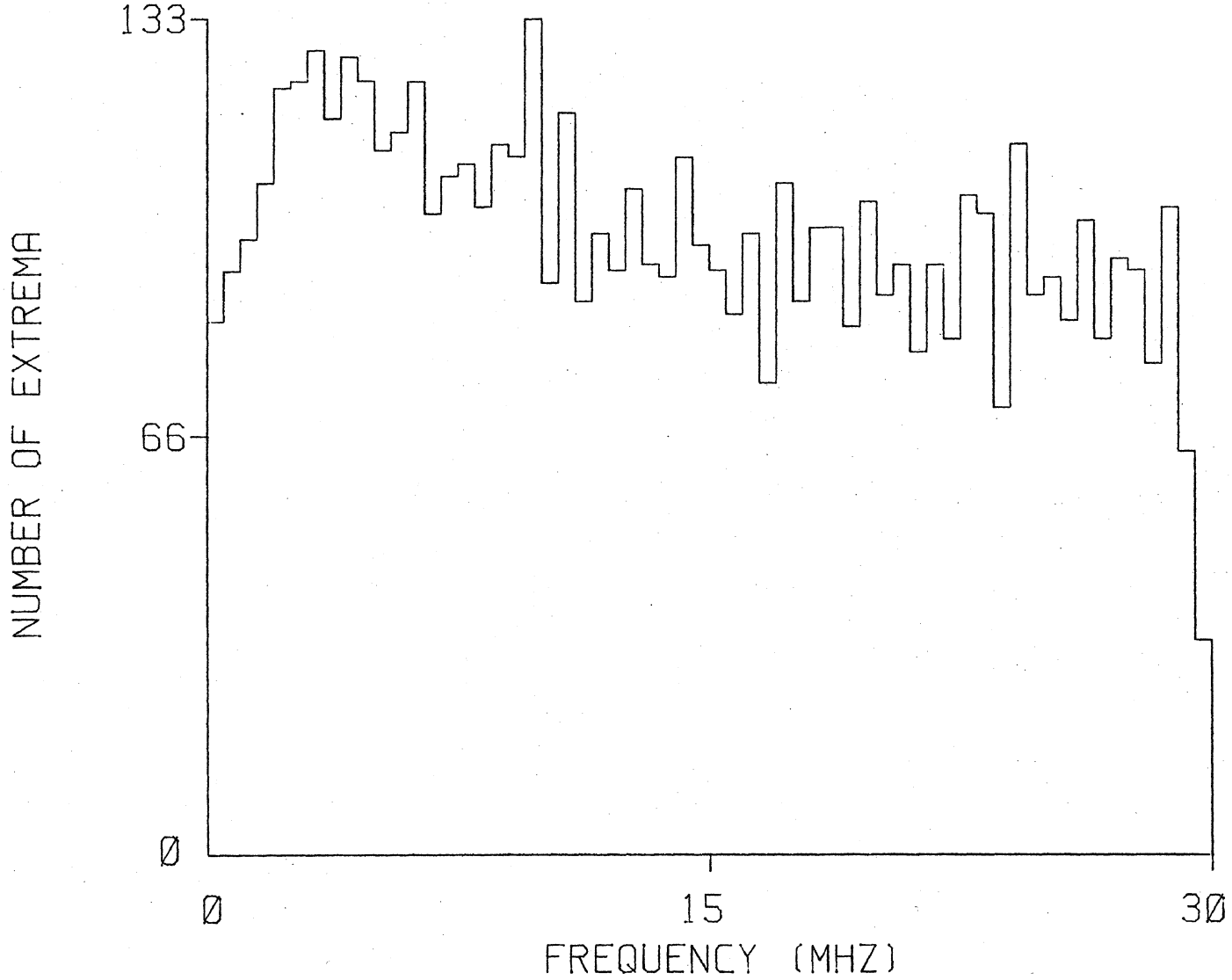

FIGURE 3.12 D-DOT MAXIMA, AMPLITUDE FILTER= .0 DB.

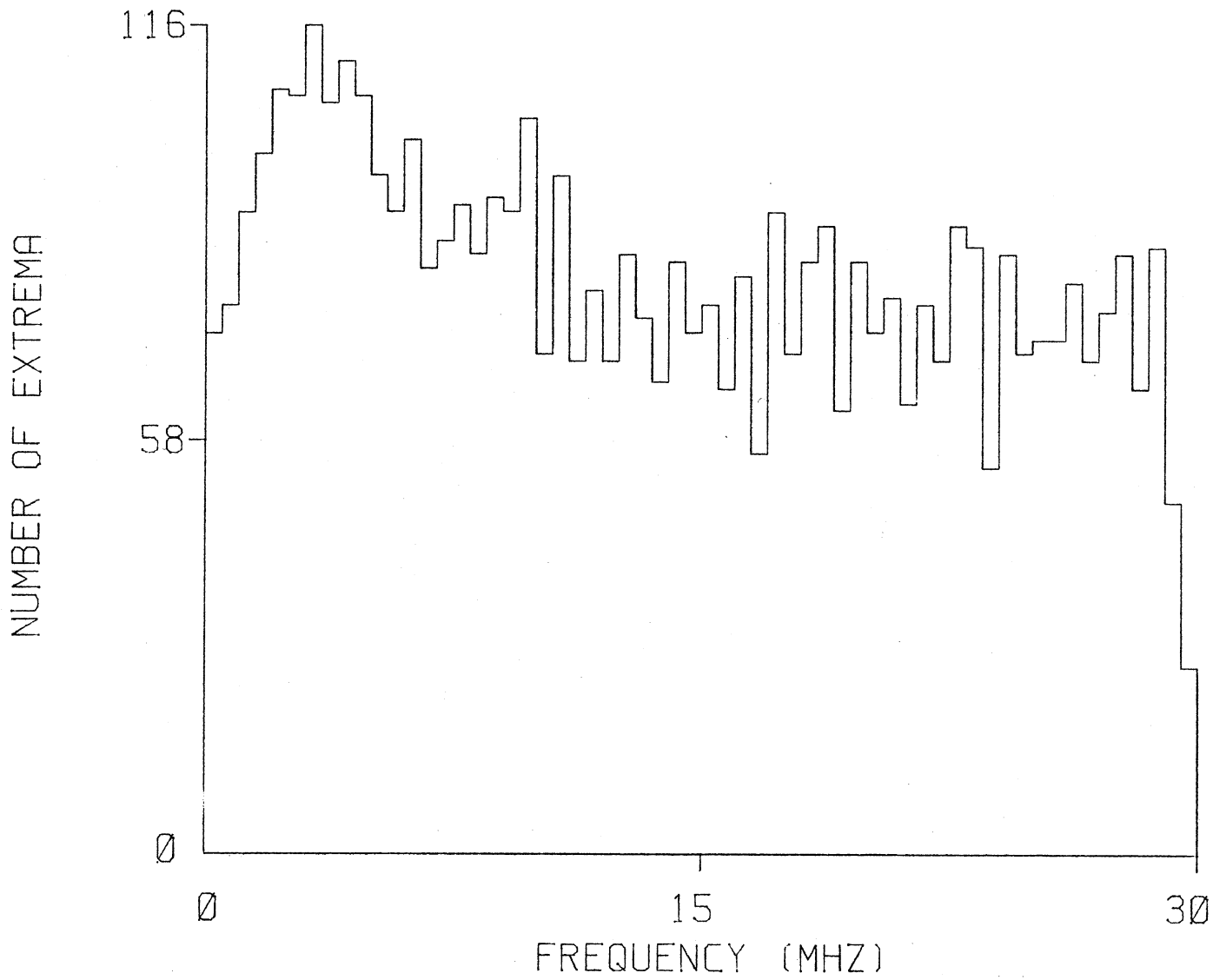

FIGURE 3.13 D-DOT MAXIMA, AMPLITUDE FILTER= 2.5 DB.

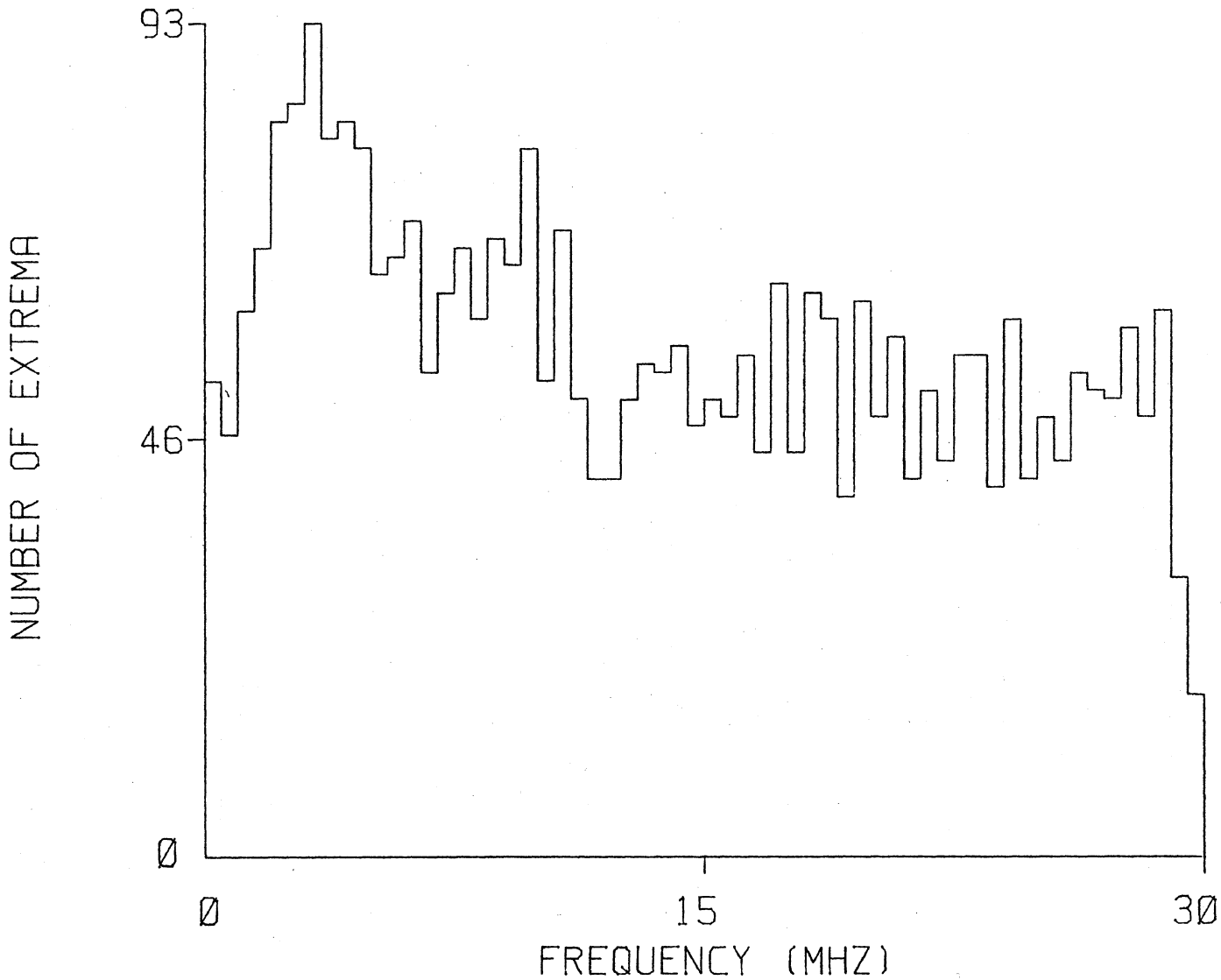

FIGURE 3.14 D-DOT MAXIMA, AMPLITUDE FILTER= 5.Ø DB.

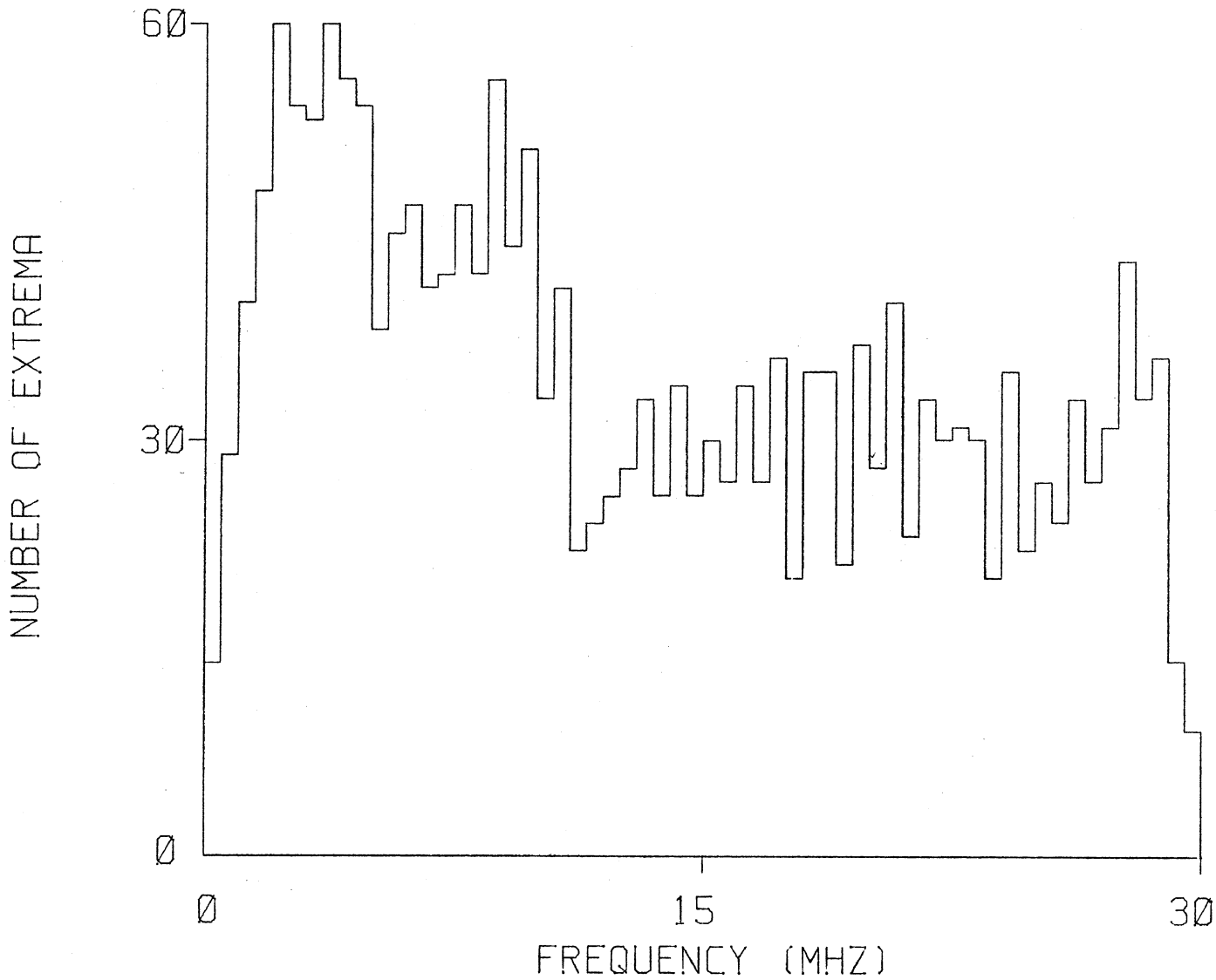

FIGURE 3.15 D-DOT MAXIMA, AMPLITUDE FILTER= 7.5 DB.

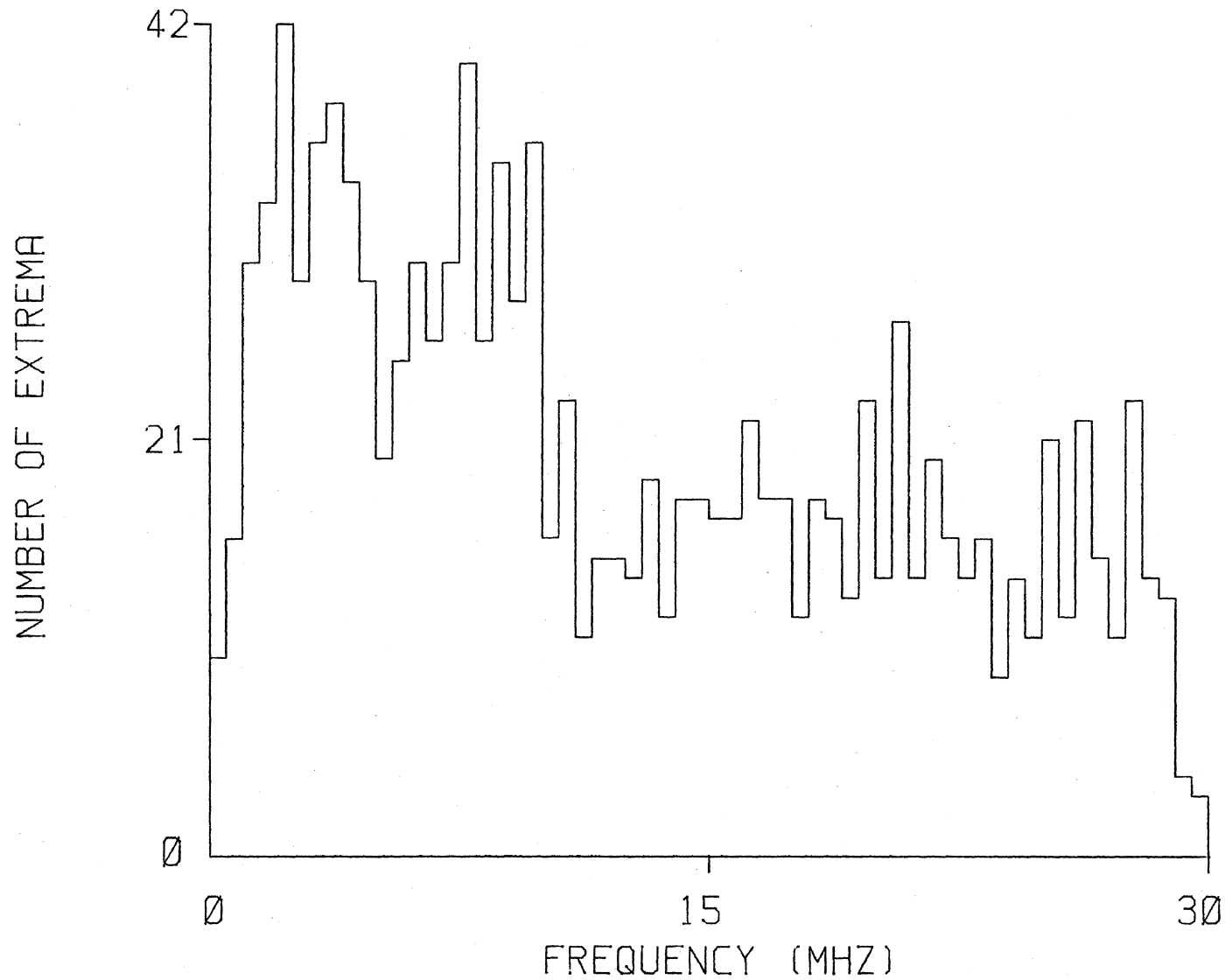

FIGURE 3.16 D-DOT MAXIMA, AMPLITUDE FILTER= 10.0 DB.

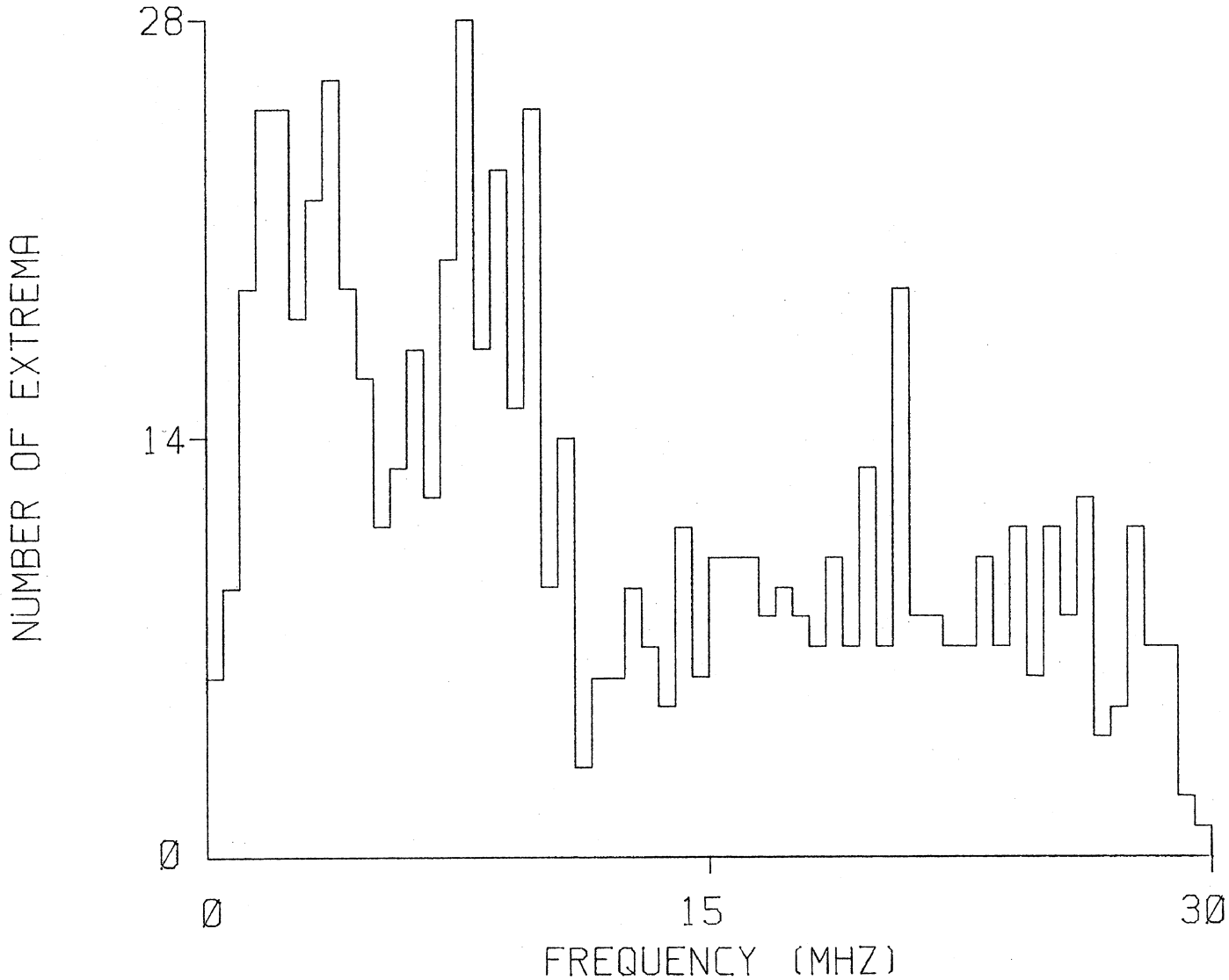

FIGURE 3.17 D-DOT MAXIMA, AMPLITUDE FILTER= 12.5 DB.

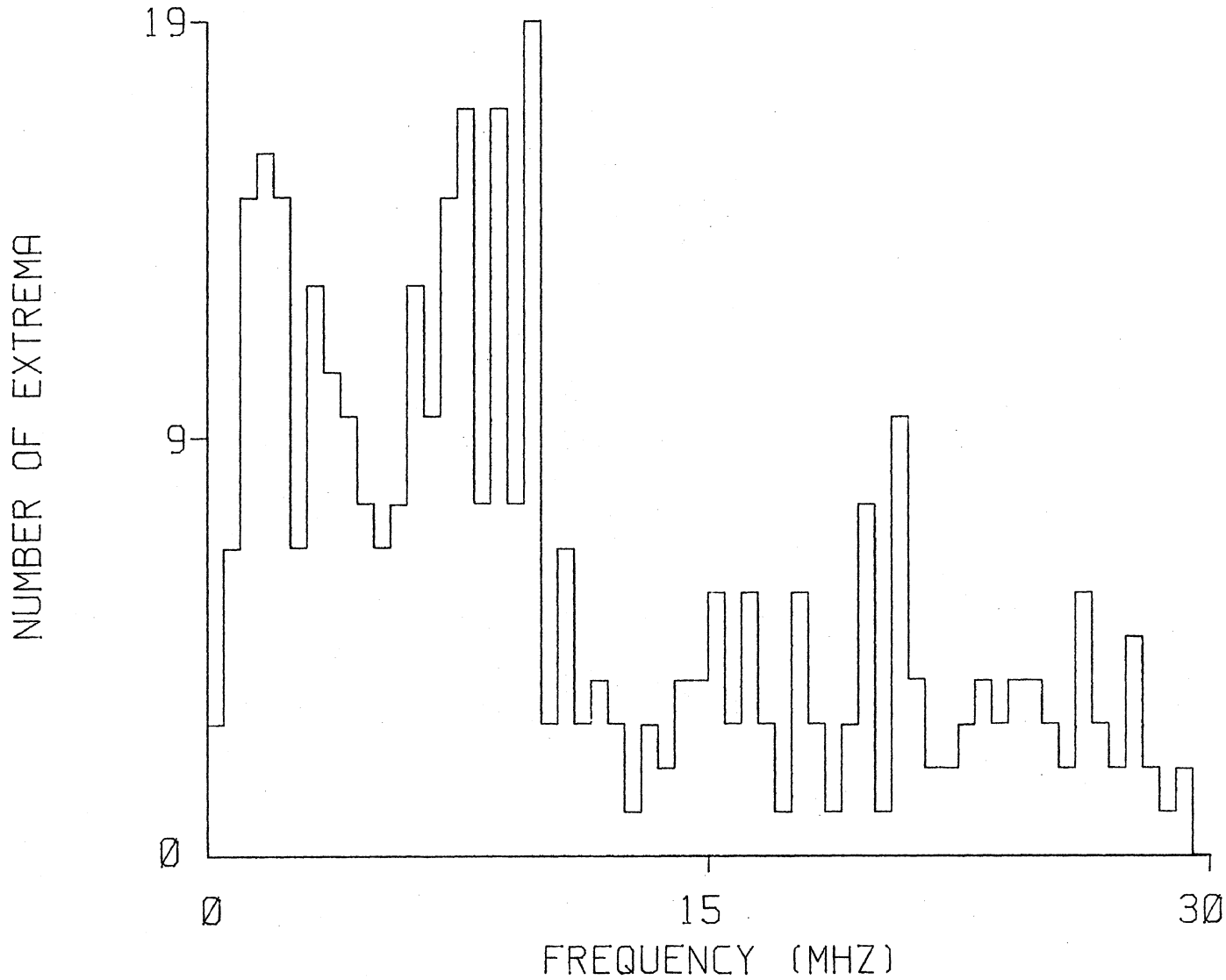

FIGURE 3.18 D-DOT MAXIMA, AMPLITUDE FILTER= 15.Ø DB.

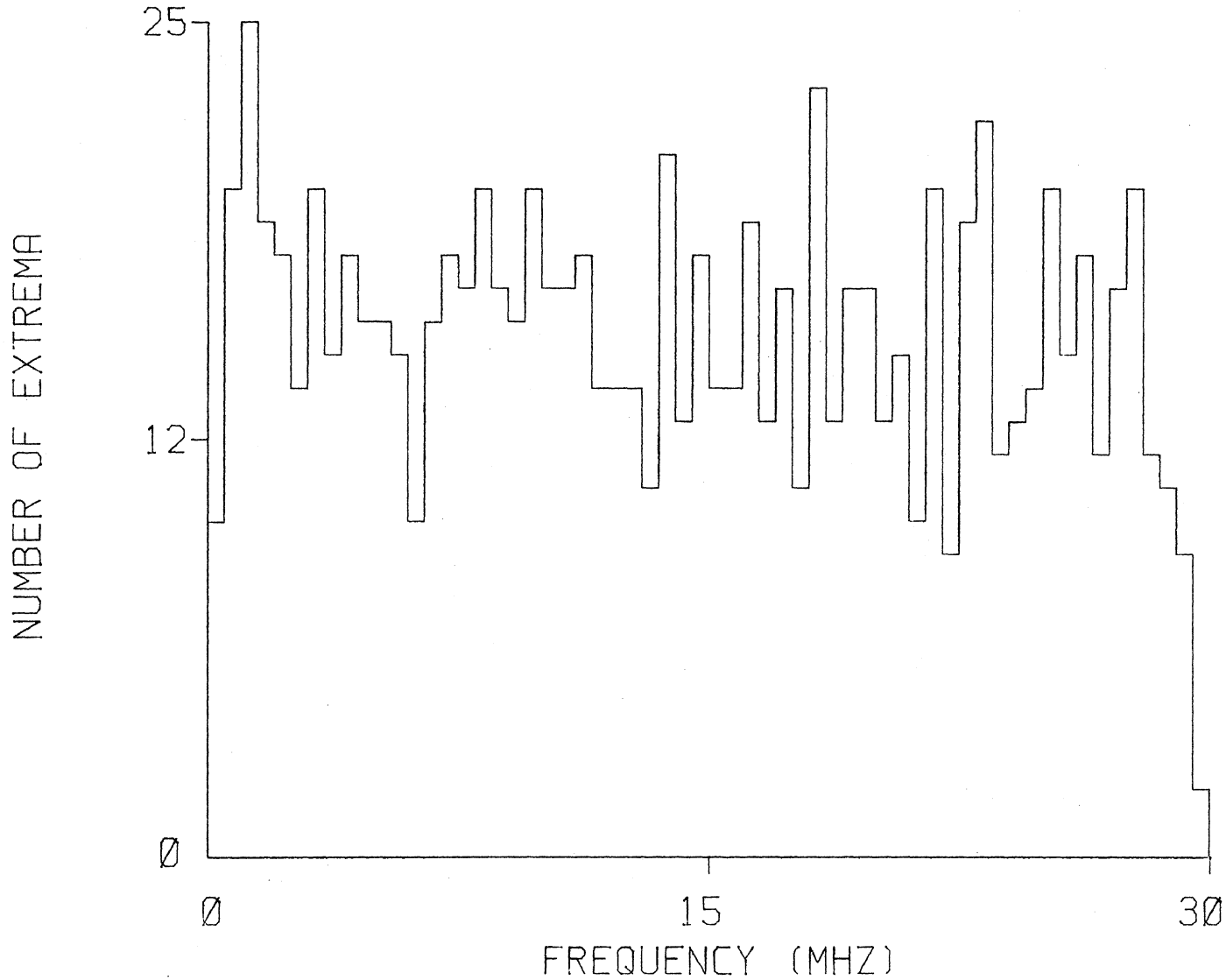

FIGURE 3.19 B-DOT MINIMA, AMPLITUDE FILTER= .Ø DB.

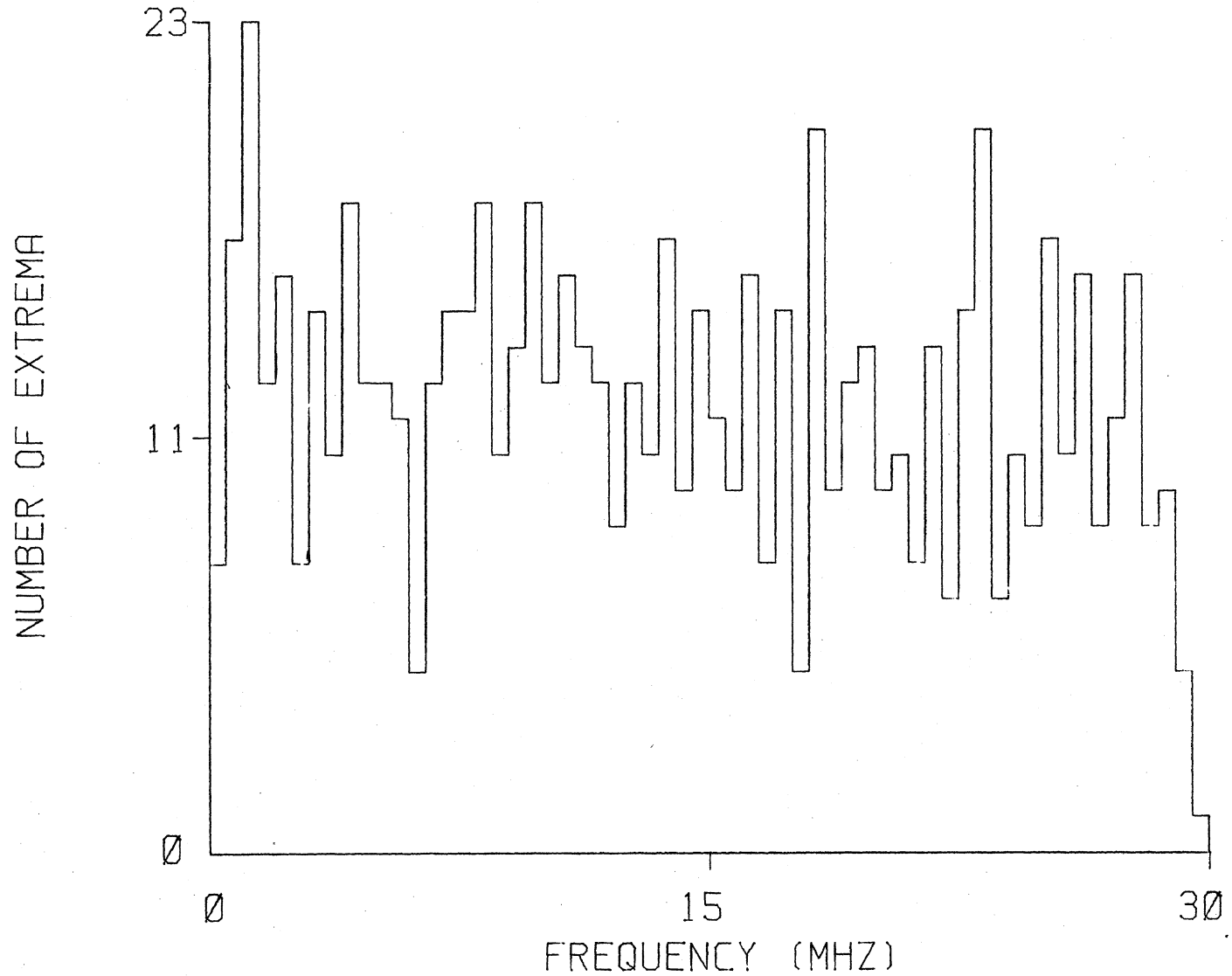

FIGURE 3.2Ø B-DOT MINIMA, AMPLITUDE FILTER= 2.5 DB.

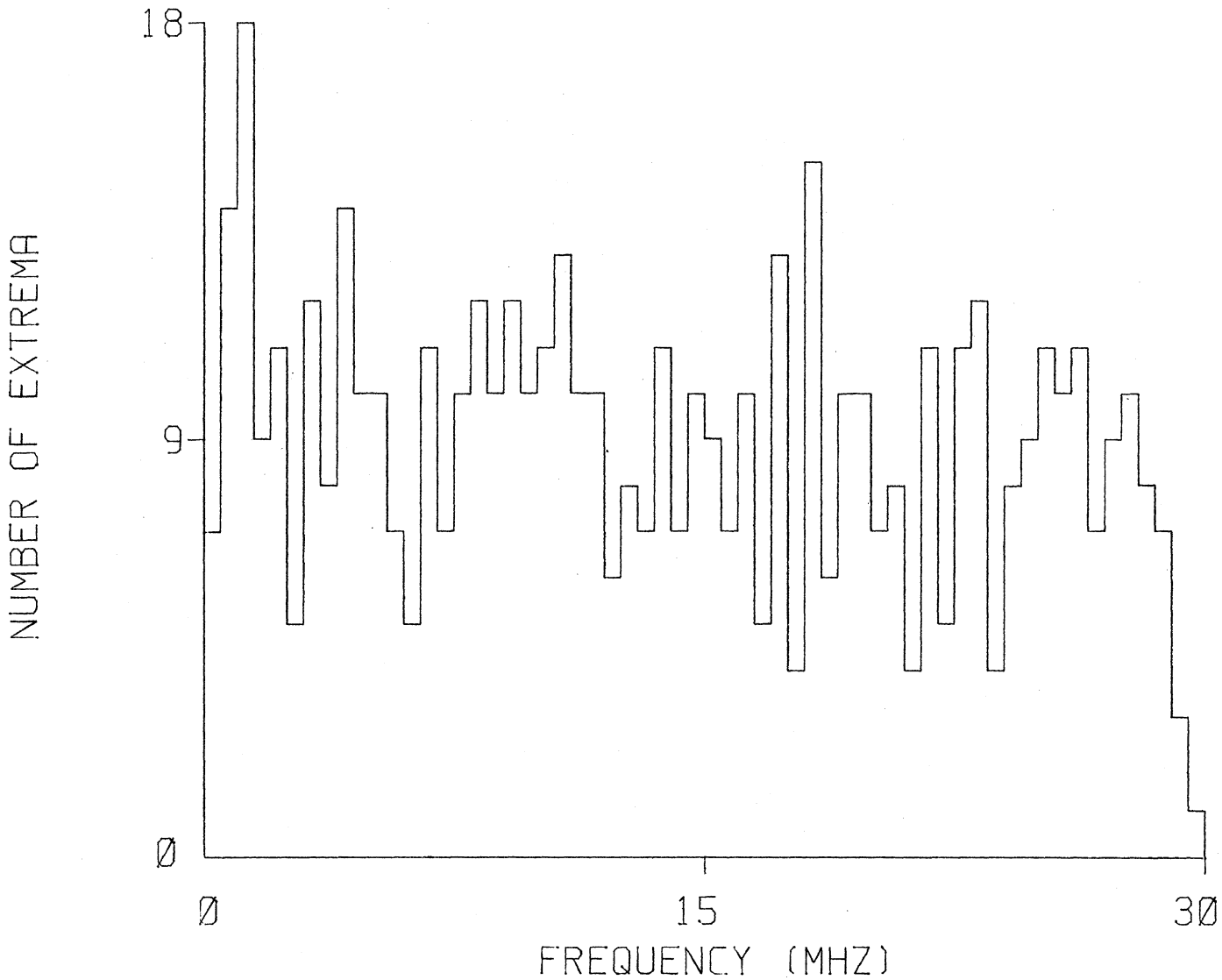

FIGURE 3.21 B-DOT MINIMA, AMPLITUDE FILTER= 5.Ø DB

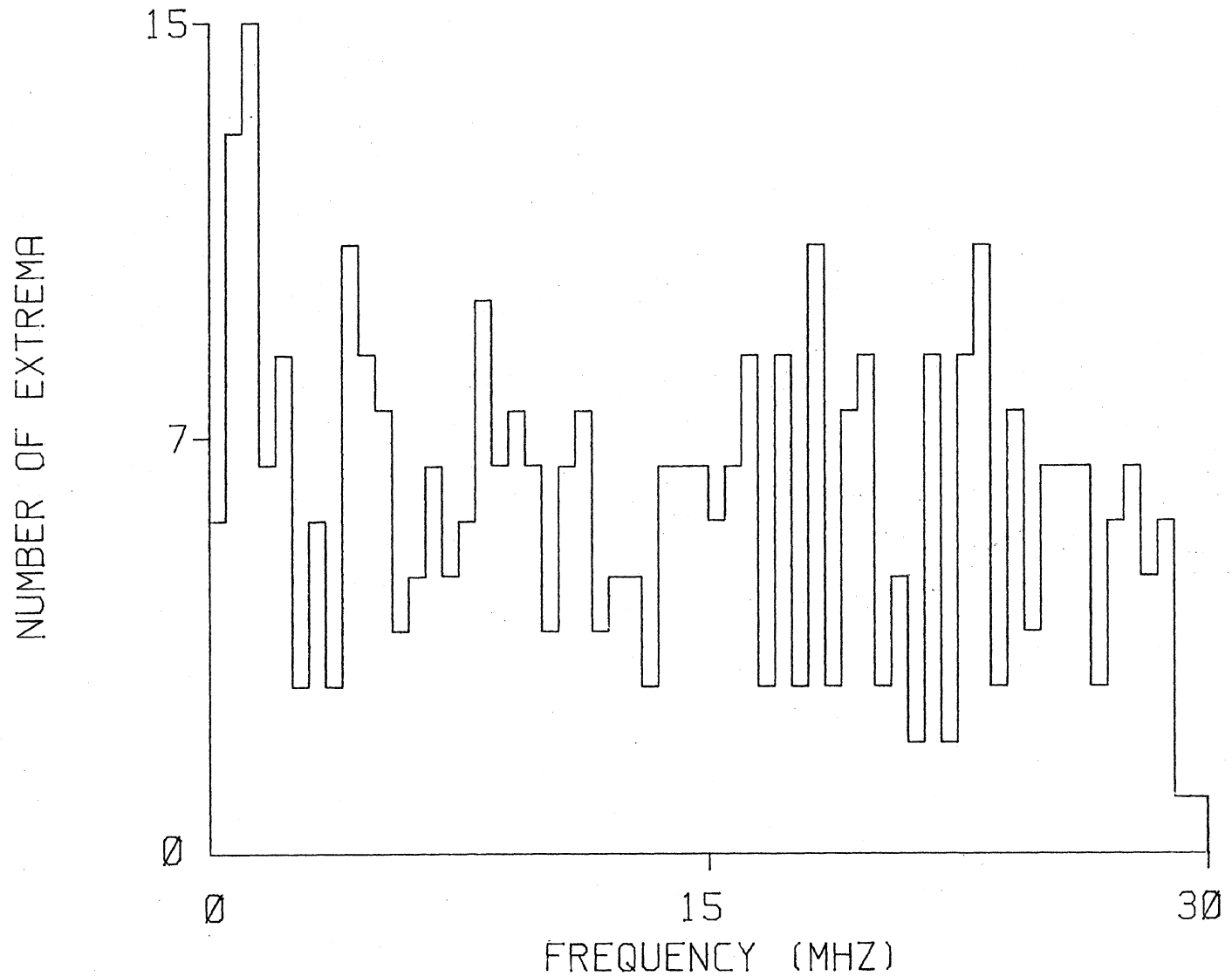

FIGURE 3.22 B-DOT MINIMA, AMPLITUDE FILTER= 7.5 DB.

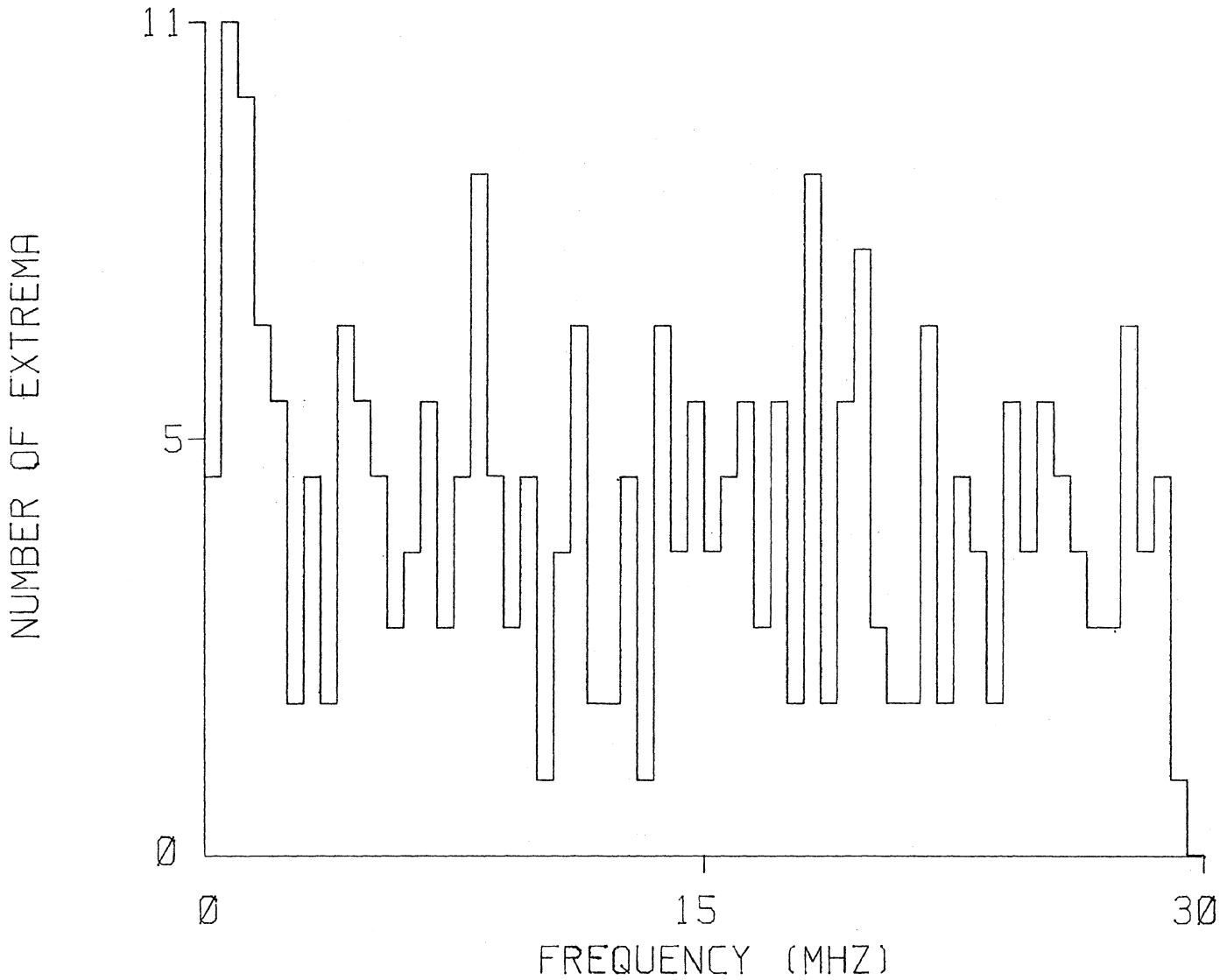

FIGURE 3.23 B-DOT MINIMA, AMPLITUDE FILTER= 1Ø.Ø DB.

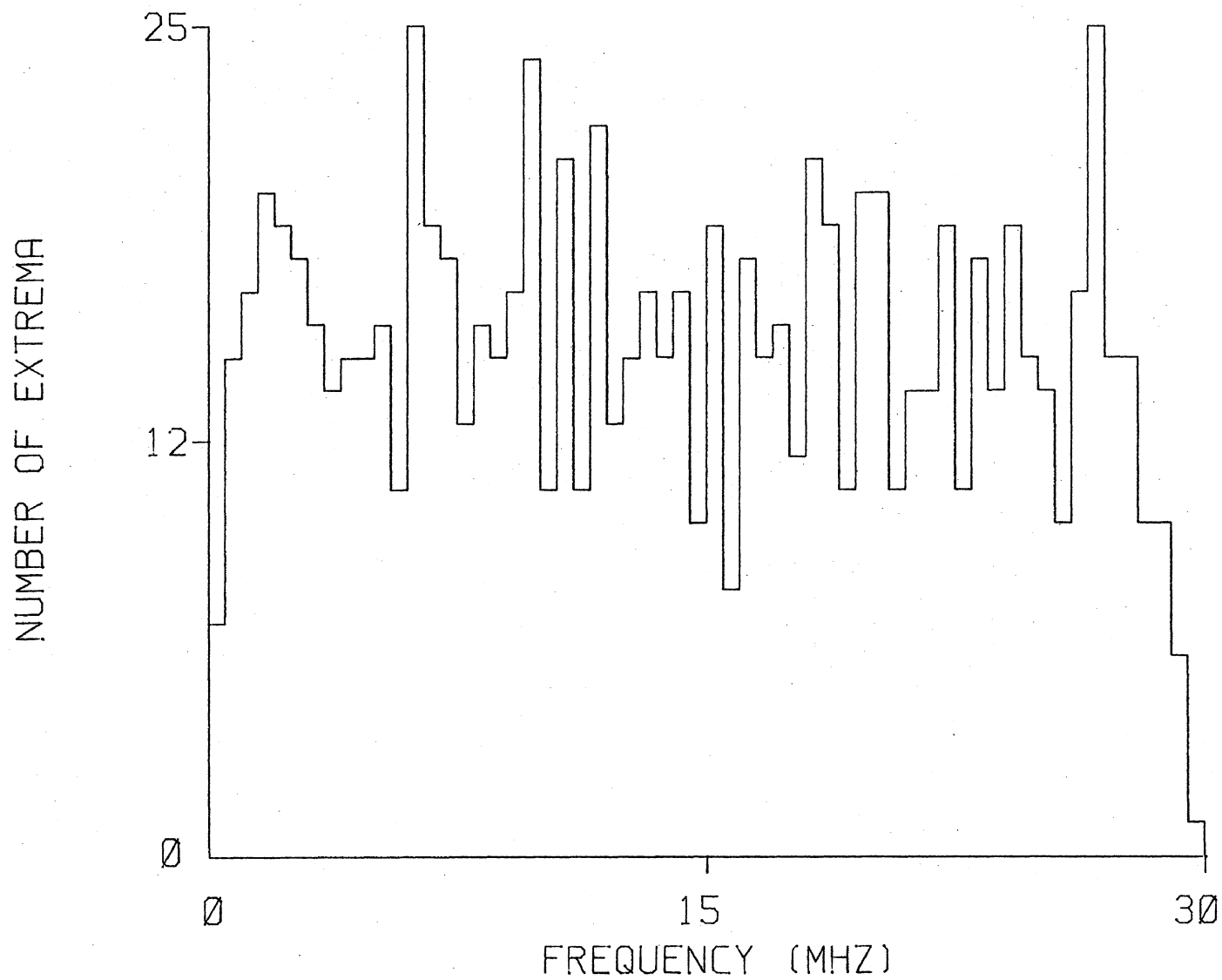

FIGURE 3.24 B-DOT MAXIMA, AMPLITUDE FILTER= .Ø DB.

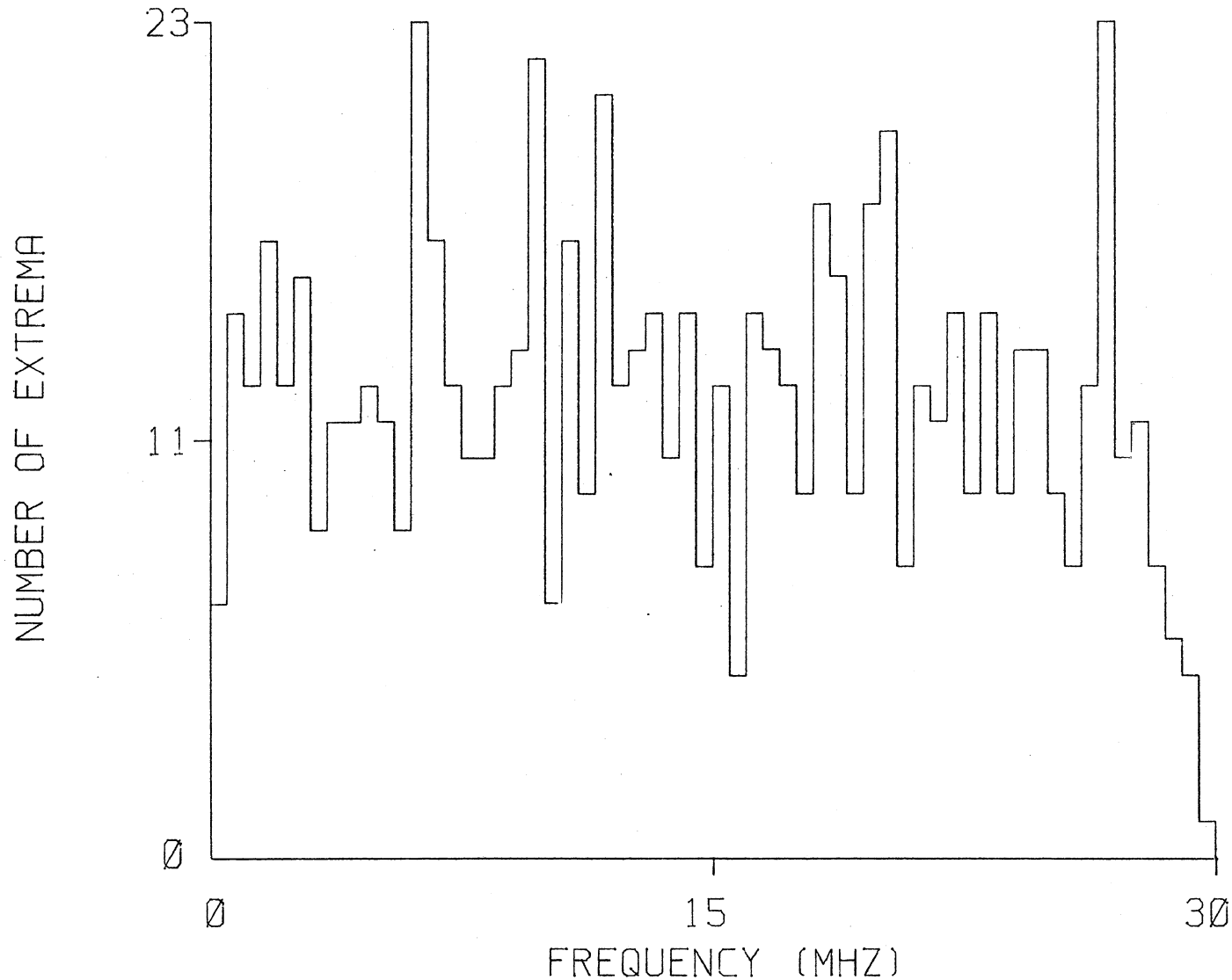

FIGURE 3.25 B-DOT MAXIMA, AMPLITUDE FILTER= 2.5 DB.

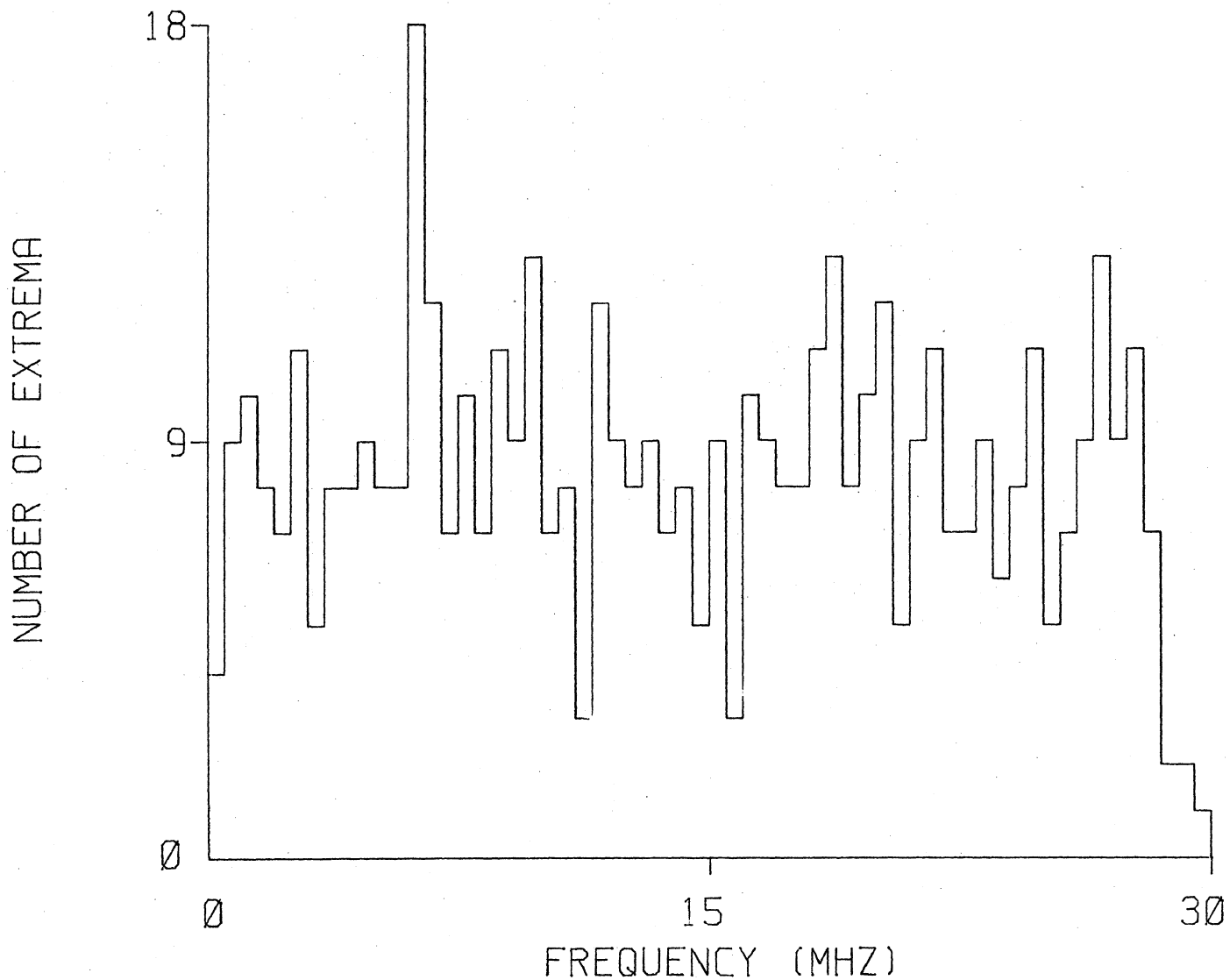

FIGURE 3.26 B-DOT MAXIMA, AMPLITUDE FILTER= 5.0 DB.

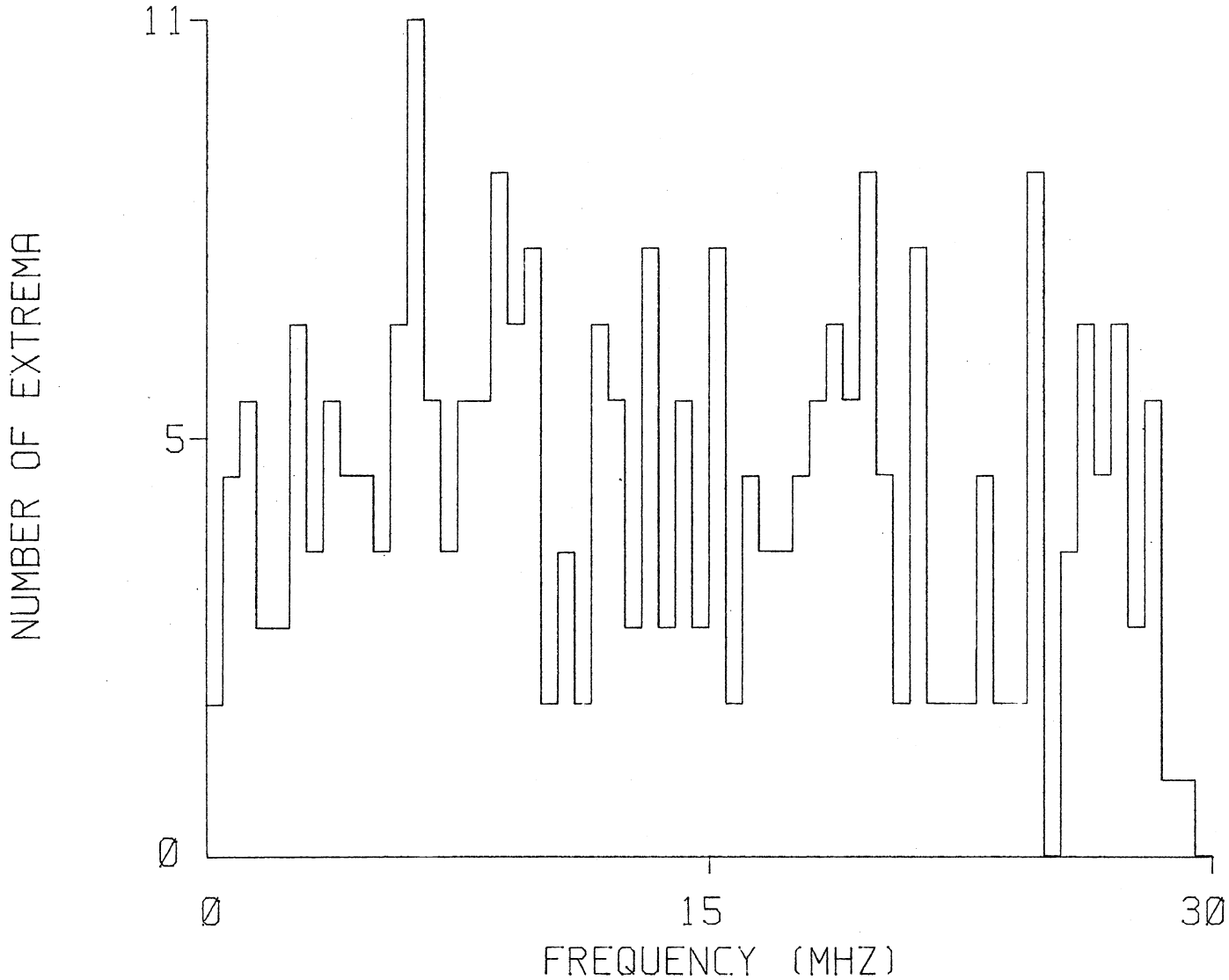

FIGURE 3.27 B-DOT MAXIMA, AMPLITUDE FILTER= 7.5 DB.

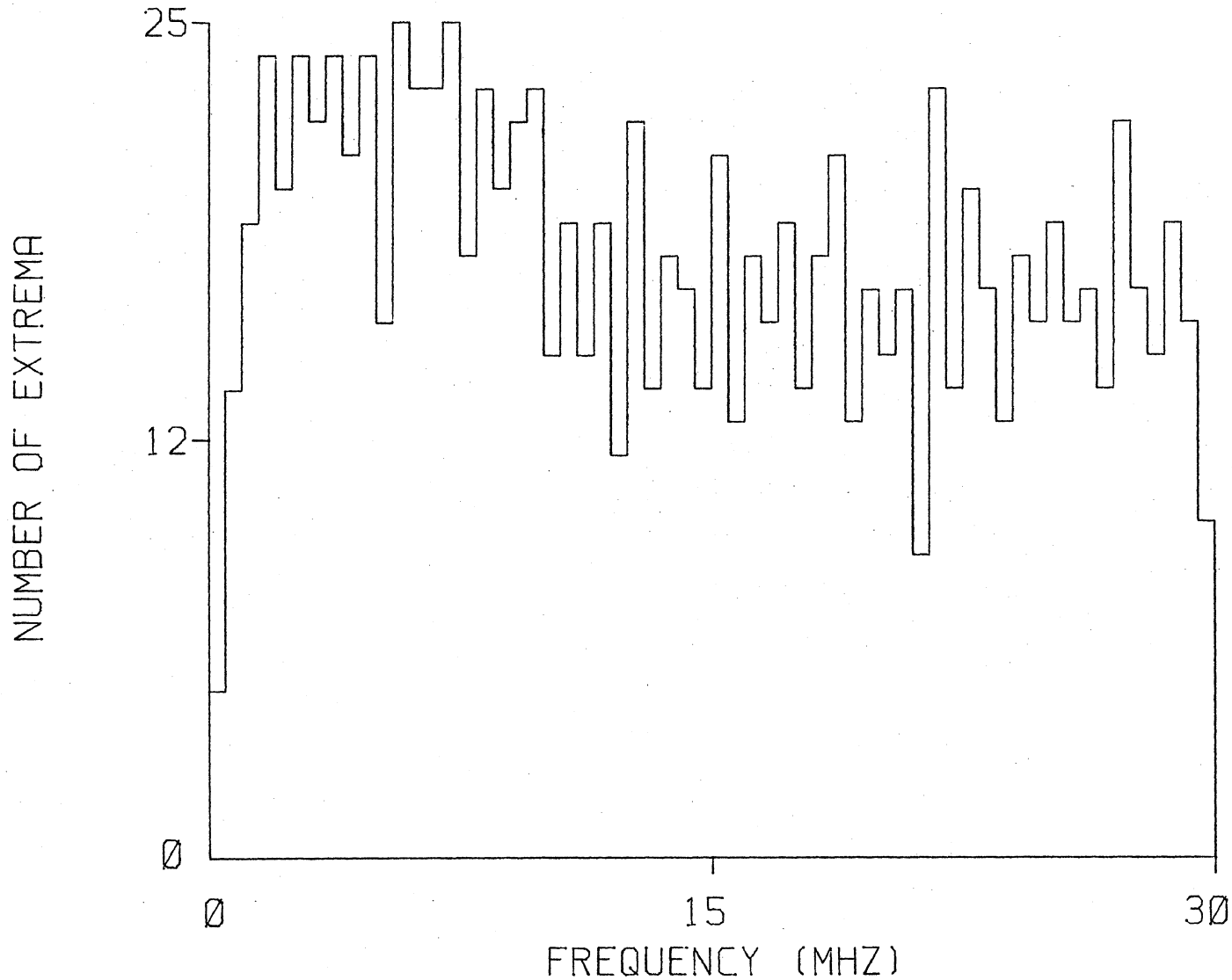

FIGURE 3.28 I-DOT MINIMA, AMPLITUDE FILTER= Ø DB.

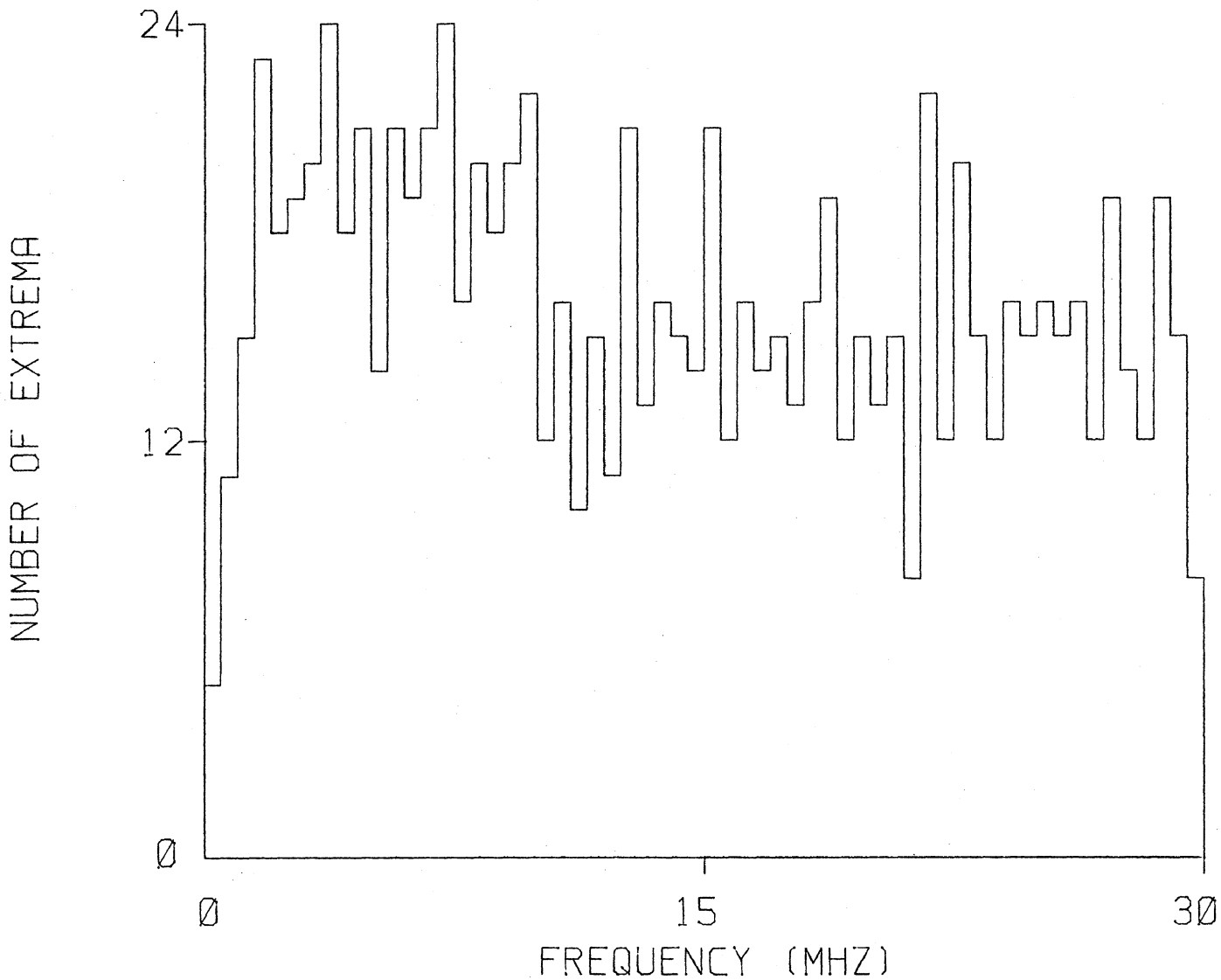

FIGURE 3.29 I-DOT MINIMA, AMPLITUDE FILTER= 2.5 DB.

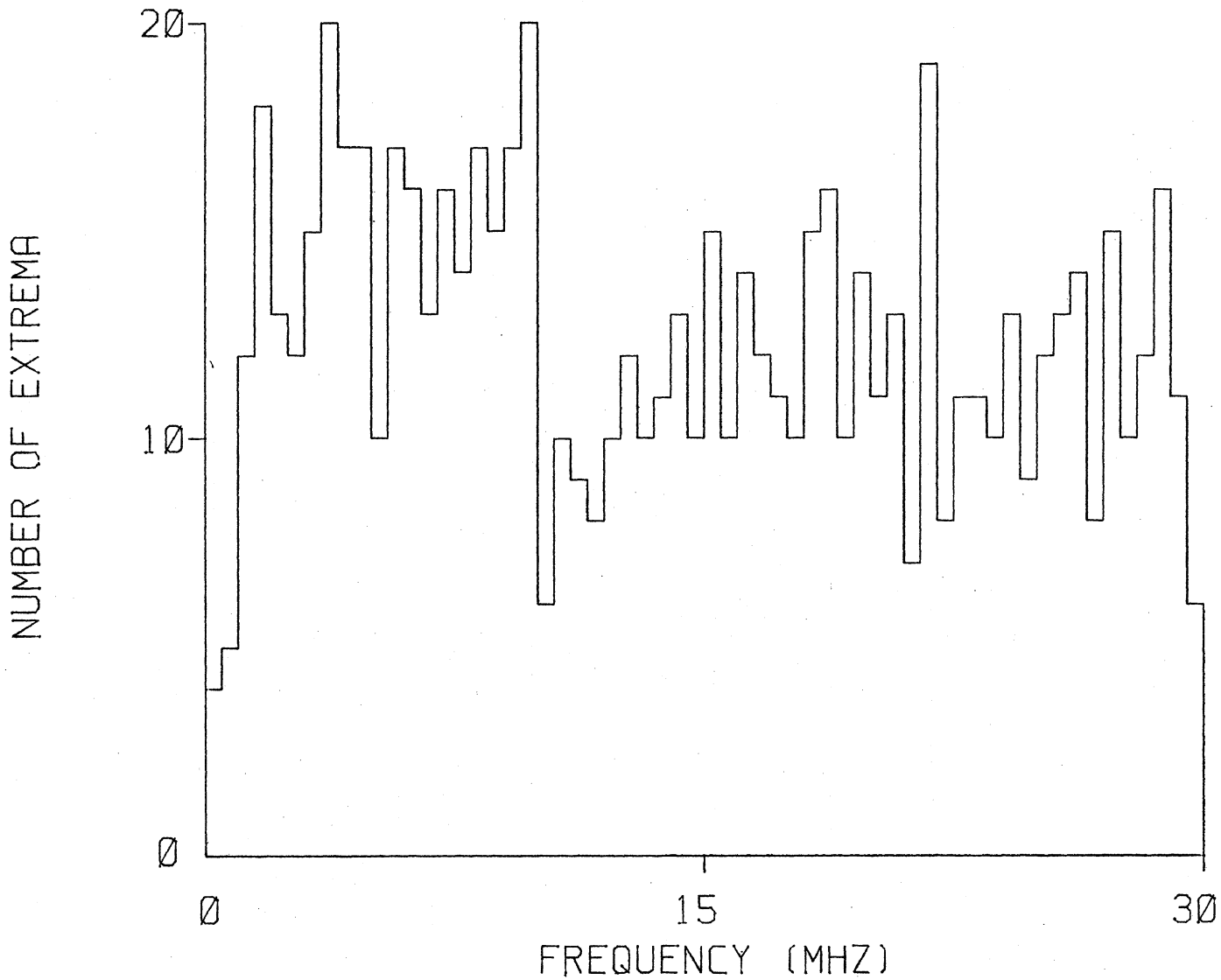

FIGURE 3.30 I-DOT MINIMA, AMPLITUDE FILTER= 5.0 DB.

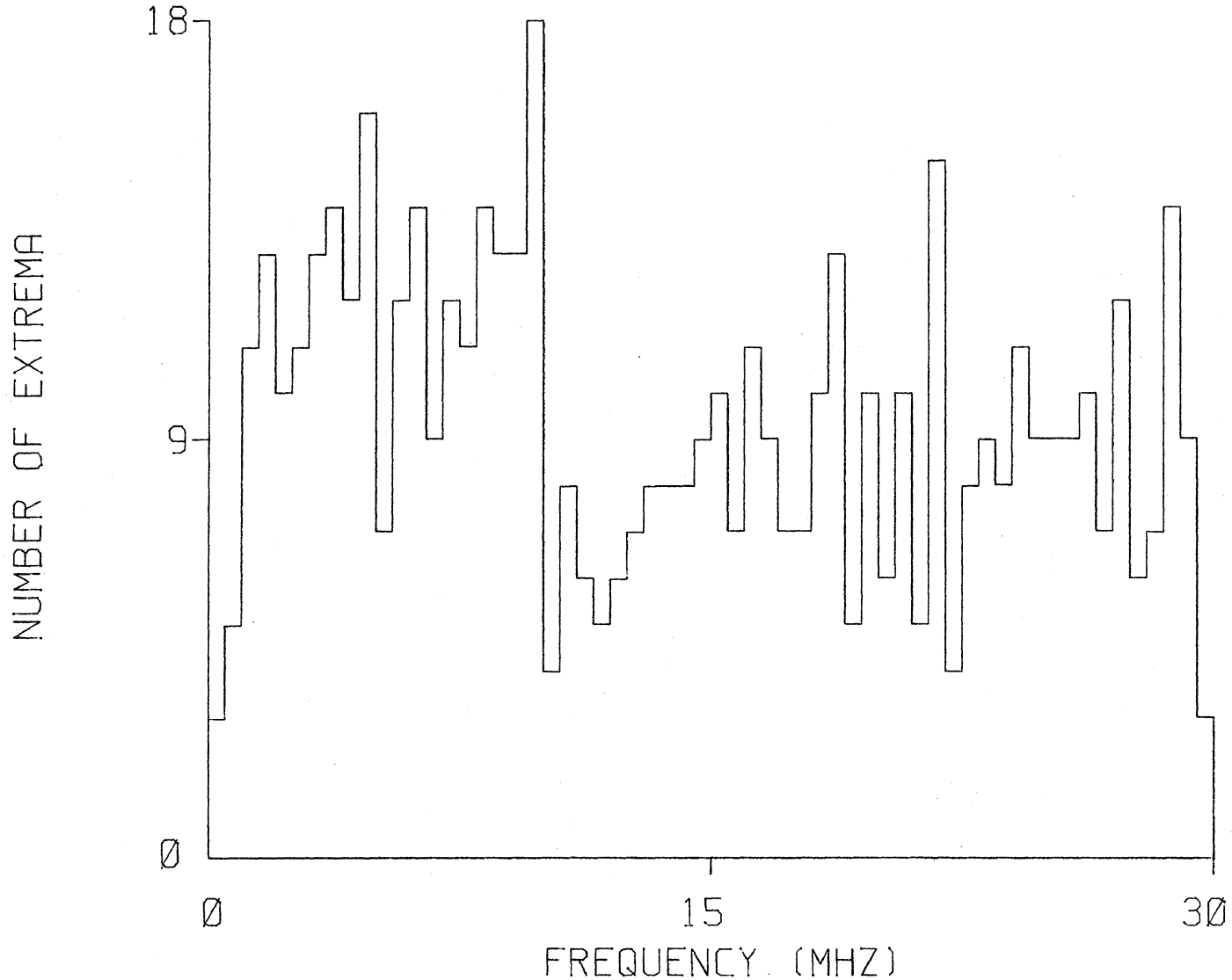

FIGURE 3.31 I-DOT MINIMA, AMPLITUDE FILTER= 7.5 DB.

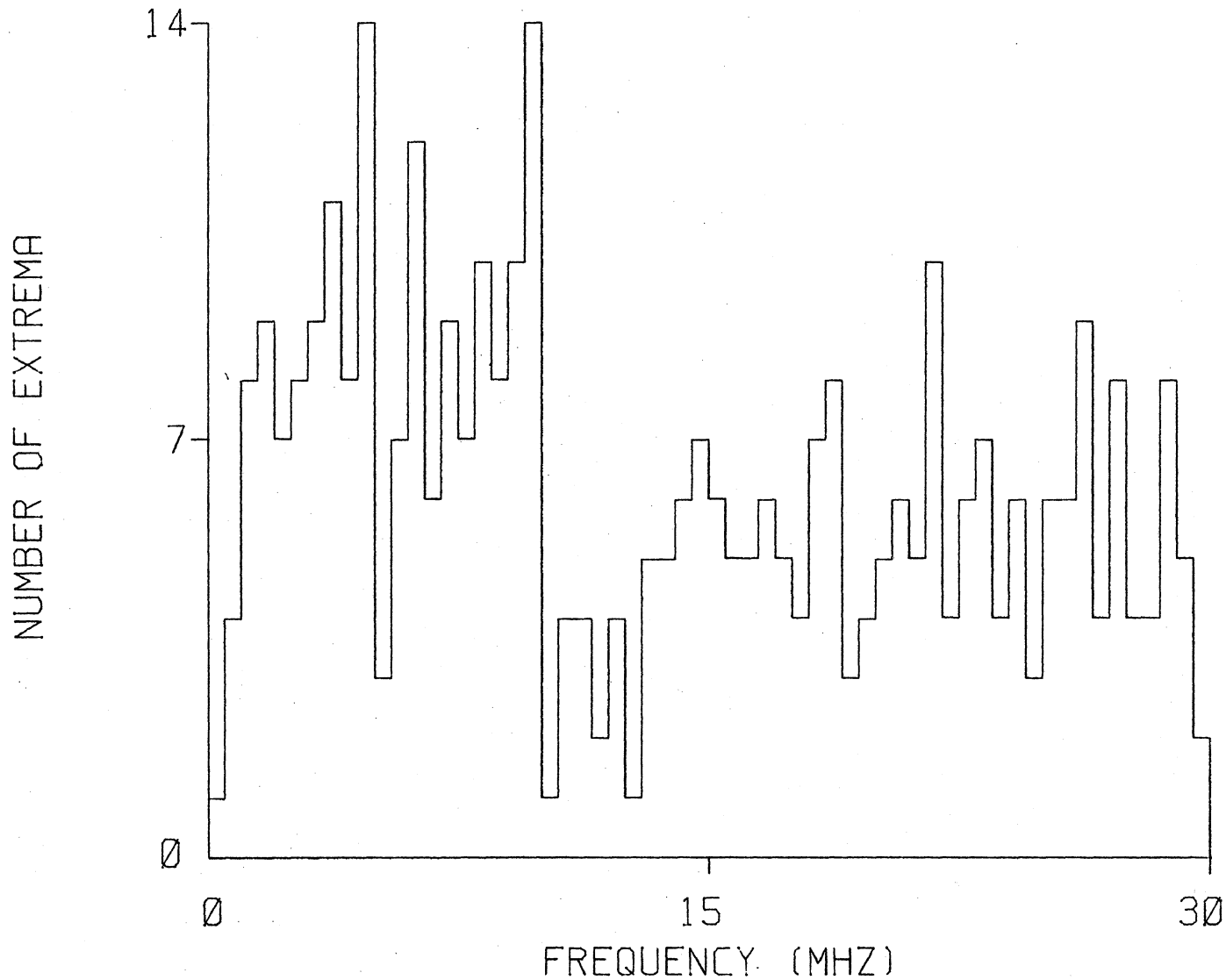

FIGURE 3.32 I-DOT MINIMA, AMPLITUDE FILTER= 10.0 DB.

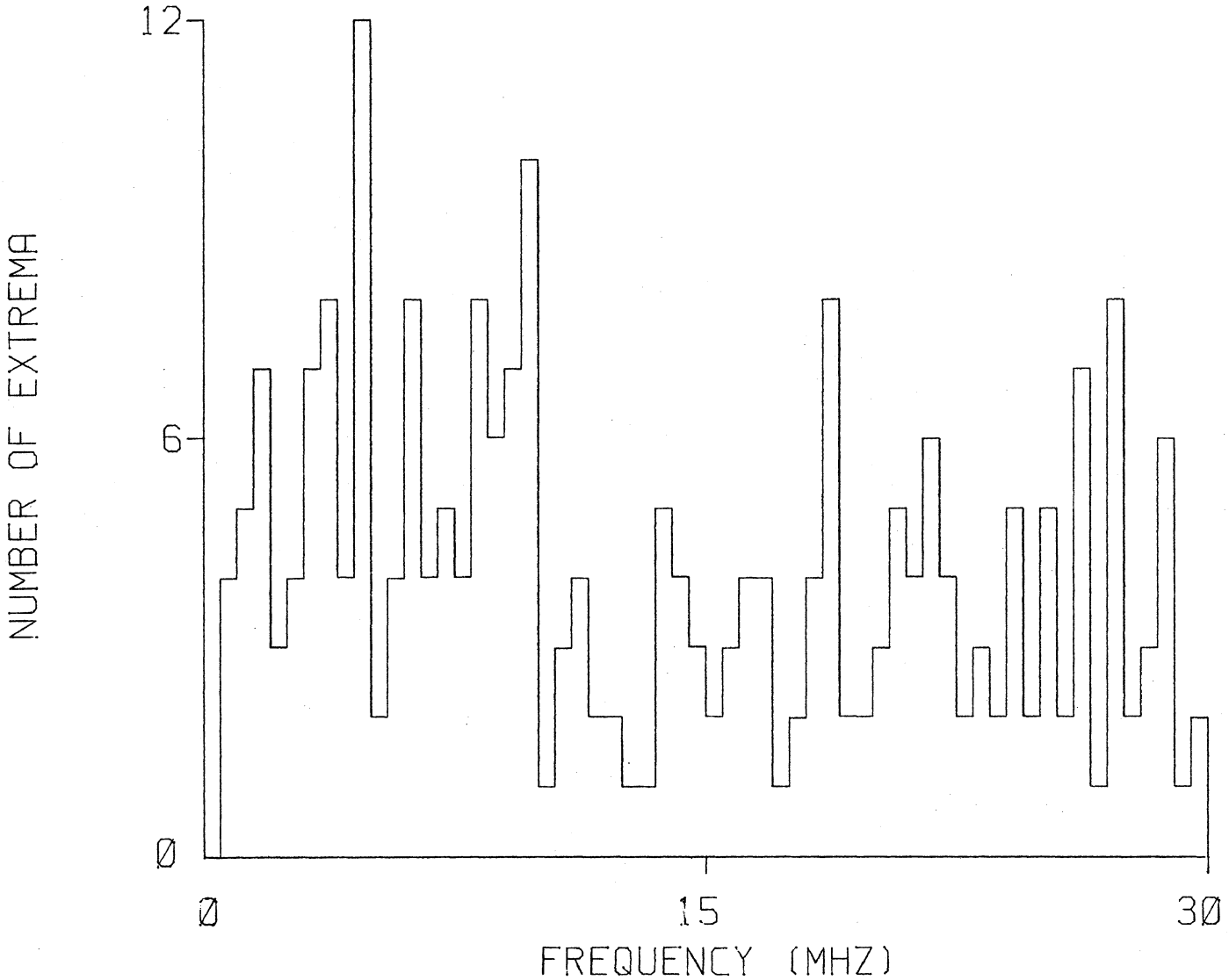

FIGURE 3.33 I-DOT MINIMA, AMPLITUDE FILTER= 12.5 DB.

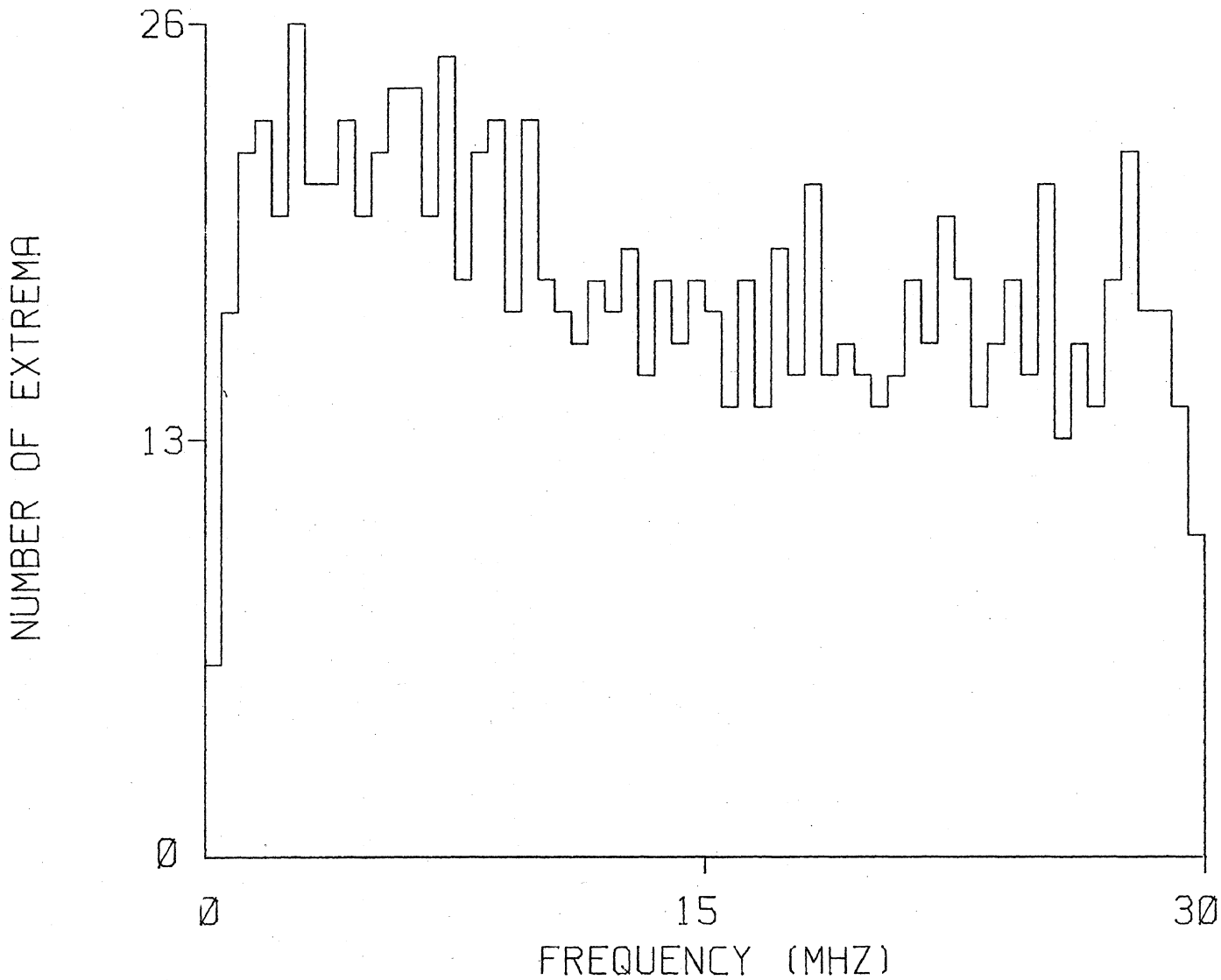

FIGURE 3.34 I-DOT MAXIMA, AMPLITUDE FILTER= .Ø DB.

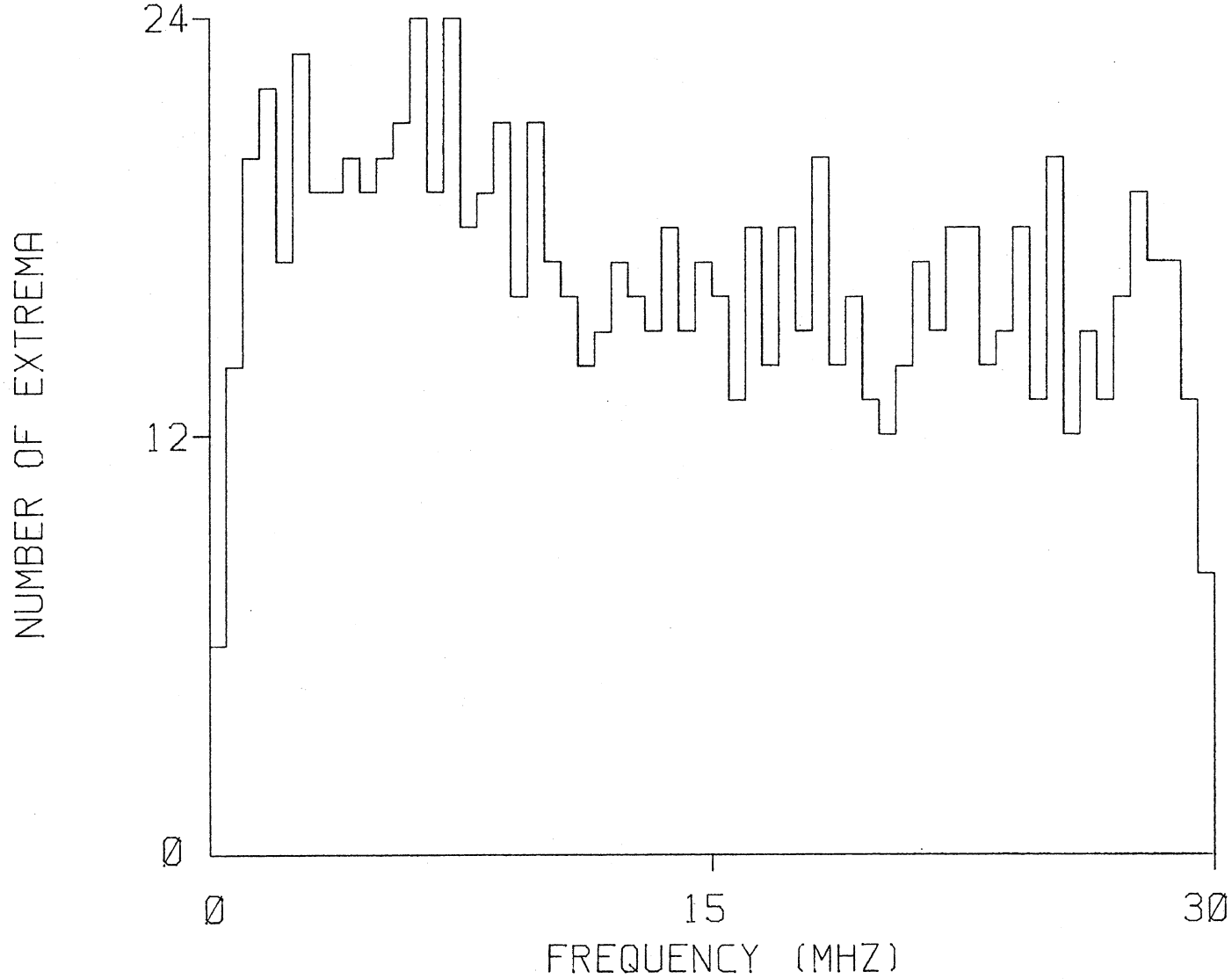

FIGURE 3.35 I-DOT MAXIMA, AMPLITUDE FILTER= 2.5 DB.

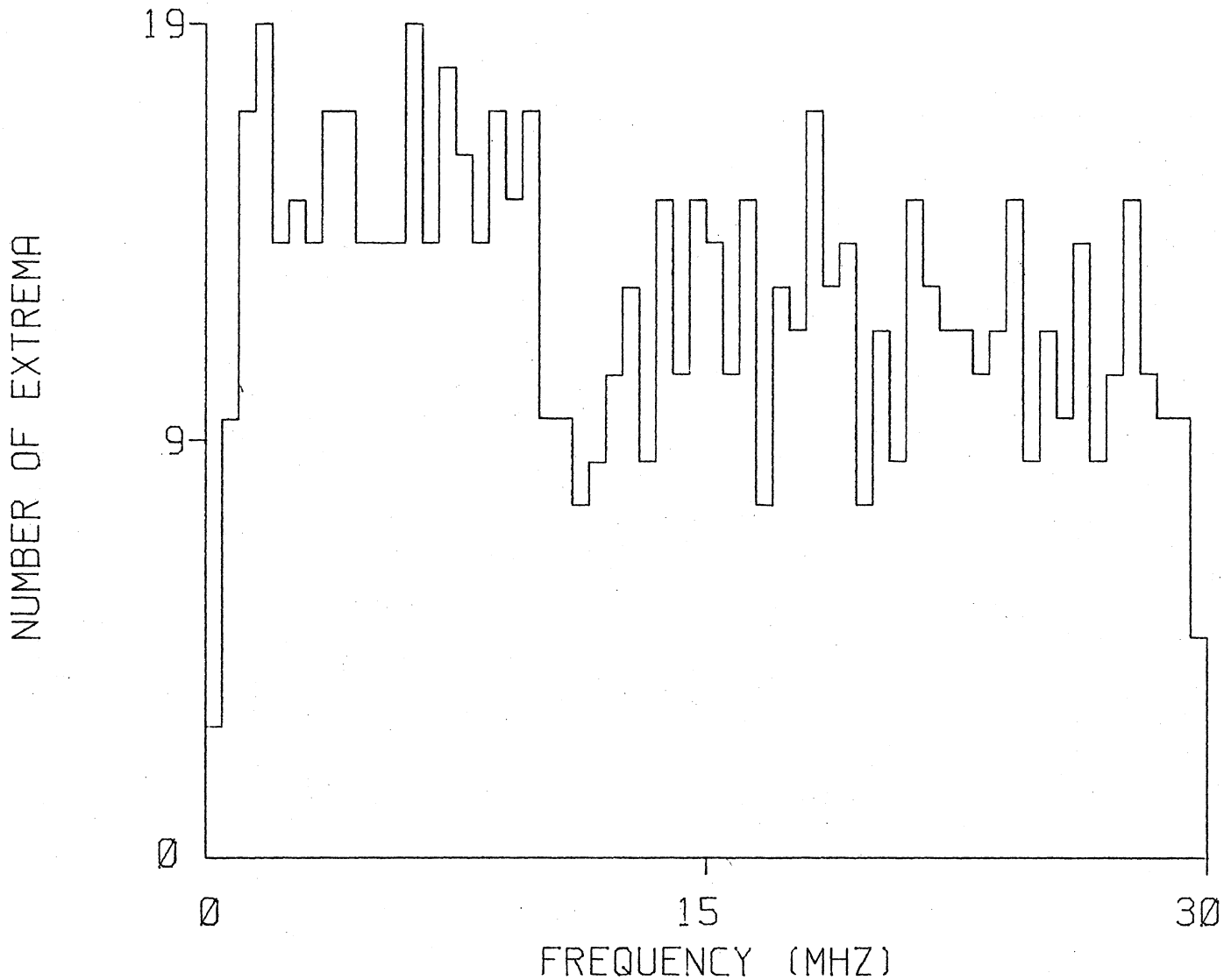

FIGURE 3.36 I-DOT MAXIMA, AMPLITUDE FILTER= 5.Ø DB.

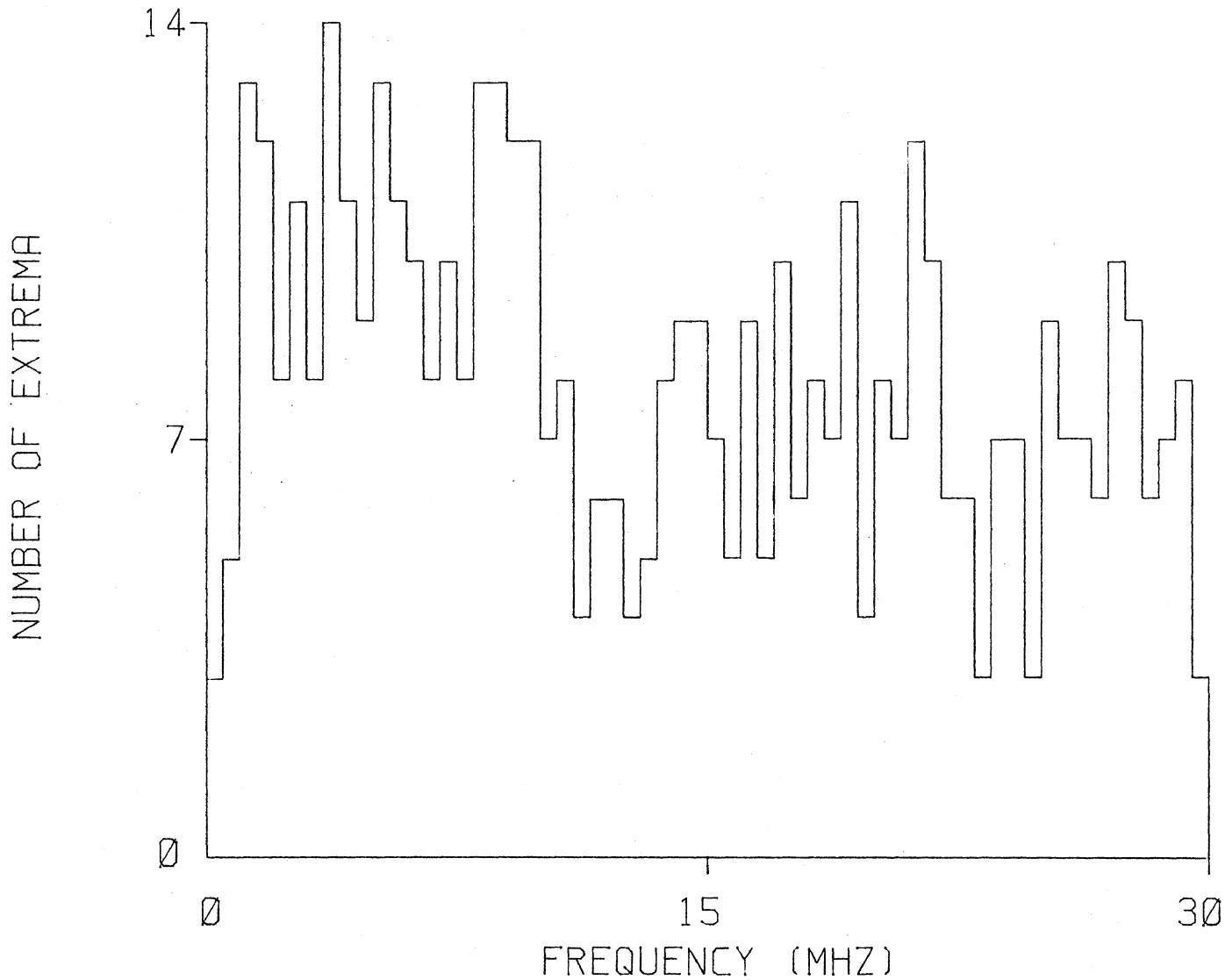

FIGURE 3.37 I-DOT MAXIMA, AMPLITUDE FILTER= 7.5 DB.

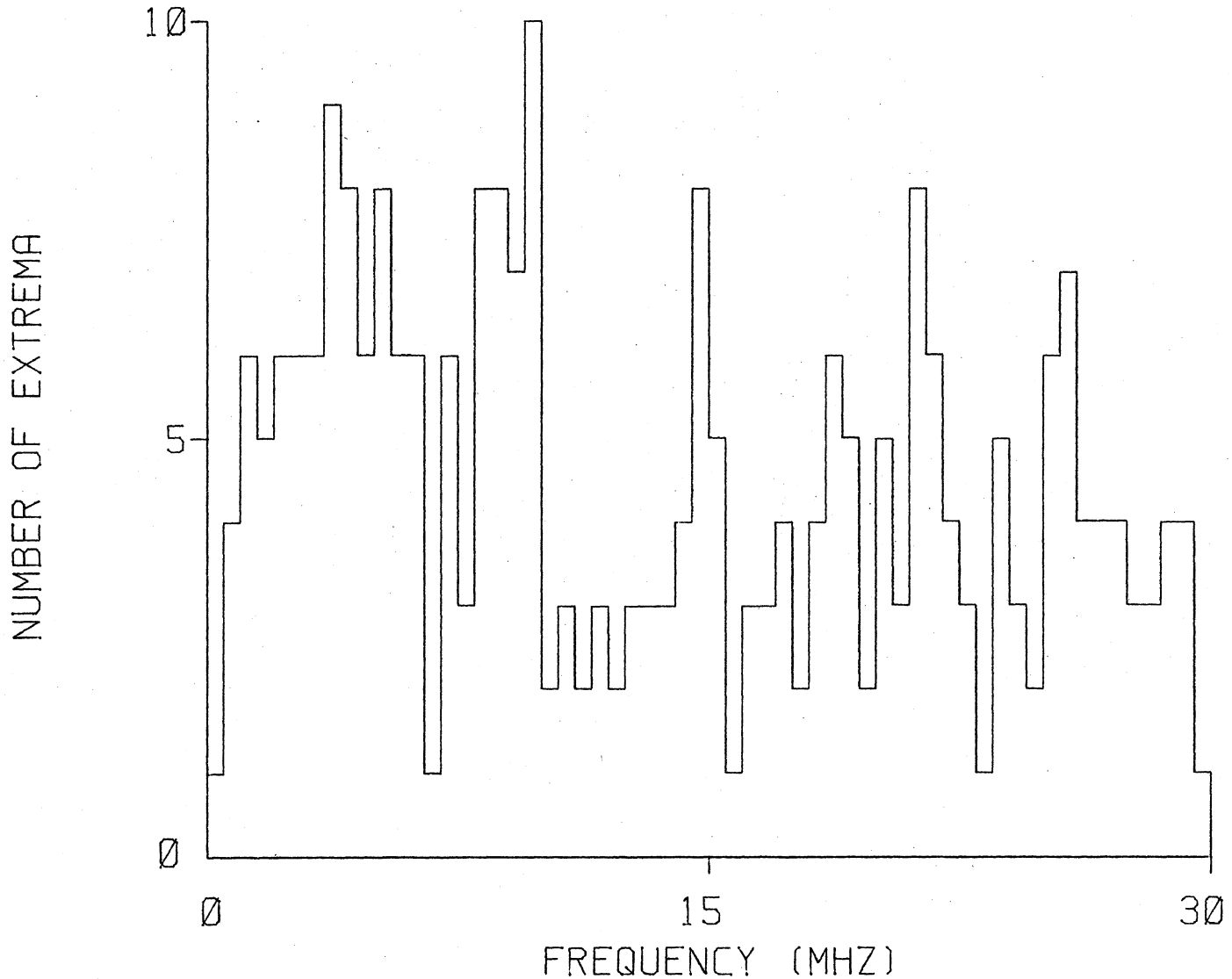

FIGURE 3.38 I-DOT MAXIMA, AMPLITUDE FILTER= 10.0 DB.

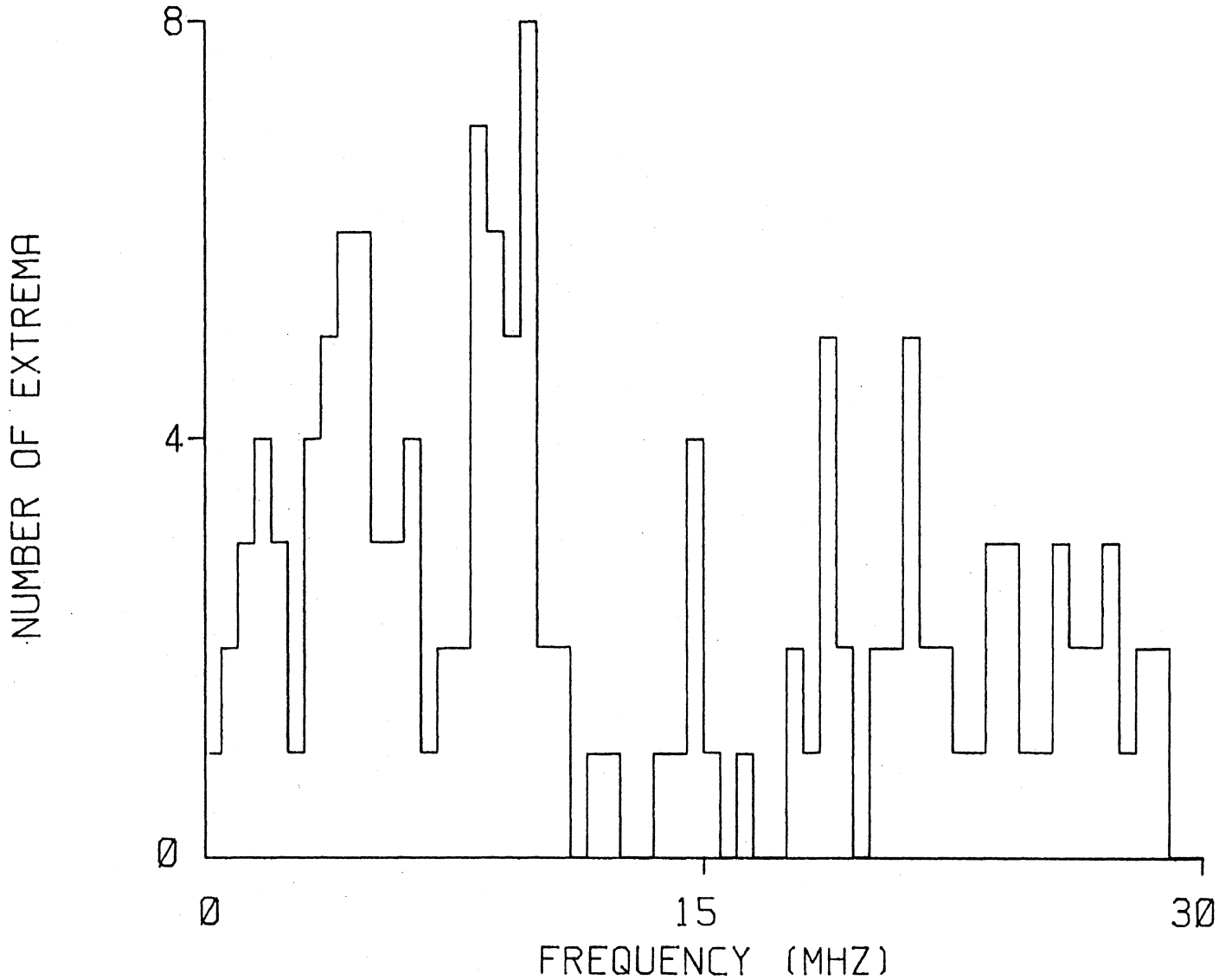

FIGURE 3.39 I-DOT MAXIMA, AMPLITUDE FILTER= 12.5 DB.

graph for a zero dB filter. By the time one reaches the 10 dB filter graph, several frequencies have begun to assume prominence. There is a low frequency bulge below 5 MHz, another between 7 and 10 MHz, and indications of resonant behavior in the ranges around 17 MHz, 21 MHz, and 27 MHz. At even larger relative amplitude filters the 7 to 10 MHz and 21 MHz resonances become dominant. It may be noted that the period of the 7 MHz oscillation ($\sim$ 140 ns) corresponds to the round trip travel time of a signal from the nose of the aircraft to the tail and back.

The B-dot histograms are less amenable to simple explanations, possibly because of the location of the sensor. At the largest relative amplitude filter values, there does appear to be some activity near 7 MHz, but it does not rise above the background as prominently as in the D-dot histograms. This may be because the D-dot sensor, located forward on the fuselage, is affected most strongly by fuselage resonances. Although the B-dot sensor can also be affected by these, it will also respond to modes which include the wings, and then may be expected to contain frequencies other than the basic fuselage resonance.

If this is the case, one would expect the current histograms to exhibit similar behavior to the D-dot's. This is indeed the case, as one sees the 7 to 10 MHz resonance rising above the background for the largest filter values. Also the resonance near 21 MHz is prominent again in the current data.

This method of analyzing the Fourier transformed in-flight data has shown that aircraft resonances do indeed exist in the data, and that they are predominantly fuselage resonances. This is consistent with a source at the nose of the aircraft, which is, of course, where many of the strikes are known to have attached.

CHAPTER 4

TRIGGERED LIGHTNING CONCEPTS

4.1 Introduction

Triggered lightning is so-called because it occurs only in the presence of a conducting object which is able to enhance the local electric field enough to cause air breakdown. Although any conducting object will produce some field enhancement, the largest enhancements will occur for objects having sharp points or edges, particularly if those points and edges are oriented in the direction of the ambient field. An aircraft in flight such as the F106B has many sharp points (e.g. nose) and sharp edges (e.g. wings, tail) around which the fields will be enhanced if the aircraft is immersed in a static electric field. These locally (within a half meter or so from the aircraft) enhanced fields are likely to be a factor of ten or more larger than the ambient field. Hence it is considerably more likely that initial air breakdown and formation of a lightning channel will occur in the presence of the F106B than in its absence.

Since the possibility exists of triggered lightning occurring during the F106B flights, several questions must be addressed. First, what is the relative likelihood of a given strike being triggered or natural lightning? Here natural refers to the event in which the F106B accidentally happens to be in the path of a lightning stroke which would exist without the aircraft. Second, if one assumes that triggered lightning is important, what can be said about its variation with flight parameters such as altitude and flight heading? A related issue concerns how one could modify the flight profile to increase strikes, especially at low altitudes. Third, the inflight data must be evaluated with the possibility that much of the data is from triggered strikes. Finally, the triggered lightning hypothesis must be applied to the overall goals of the program. That is, how can triggered lightning data gleaned from the F106B be used to determine the effects of lightning, triggered or natural, on other aircraft.

4.2 Relative Likelihood of Triggered and Natural Lightning

To determine the relative importance of triggered versus natural lightning, it is helpful to investigate the circumstances under which both

occur. The requirements are simply stated for triggered lightning. The static electric field which the aircraft sees must be large enough and oriented properly so that the locally enhanced fields at the extremes of the aircraft exceed the local air breakdown value. The ambient field must also be large enough to form and propagate a channel, once a breakdown region has been established. A net charge on the aircraft can either suppress or enhance the breakdown, and this may significantly change the requirements for the occurrence of triggered lightning. Also a net charge can change the location of initial air breakdown by altering the local field distribution around the aircraft. Finally, one may conclude that triggered lightning will occur if the proper conditions are satisfied. Essentially what this means is that the local field somewhere on the aircraft must exceed the breakdown values of approximately 1.5×10^6 V/m at 20,000 ft and 3×10^6 V/m at sea level. It should also be noted at this point that triggered lightning will occur at the lowest possible field level. Hence all the strikes should be similar in amplitude depending on where on the aircraft the initial breakdown occurs.

The conditions under which natural lightning will interact with an aircraft are much less certain. The element of chance is far more important, because the aircraft must at least be "near" a normal lightning channel in order for attachment to occur. The term "near" requires some definition. The aircraft must be close enough to perturb the electric field distribution of the channel, to alter the normal channel path and cause it to pass through the aircraft. A general rule of thumb for the perturbing effects of a conducting object is that they extend the maximum dimension of the object in all directions. That is, an aircraft can perturb the fields in a volume about three aircraft lengths in diameter. The region of strong perturbation is much smaller than that. For example. the local field around the pitot boom of the F106B can be quite large, but its extent is very small, reaching only a meter or two from the boom. Beyond that the field is essentially the ambient field slightly enhanced by the presence of the aircraft as a whole. Therefore the large locally enhanced fields around the extremes of an aircraft are likely to have little effect on natural lightning channels. This means that natural lightning strikes to the nose (and other sharp points and edges) are only slightly more probable than strikes to other parts of the aircraft. Then in conclusion one can say that natural lightning strikes to the F106B will occur

only if the channel happens to intersect a small volume around the aircraft. In addition the statistics of attachment may not be strongly biased toward edges, (i.e. nose, tail, wing tips), but may be more evenly distributed around the aircraft.

A third type of strike to the aircraft may be possible, which will be called a "hybrid" strike. In this case, a natural leader channel would be positioned somewhere near the aircraft, but not near enough for the aircraft's field distortion to alter the channel's course. The lightning leader leaves behind it in the channel a certain charge per unit length, which produces to lowest order a static field around the channel. This static field, at the location of the aircraft, may be large enough to cause a triggered streamer from the aircraft. The streamer would then certainly propagate to the natural channel, becoming a branch of the natural stroke. It is unclear whether a strike of this kind would be more characteristic of a natural strike or a triggered strike.

A simple calculation can be done to get some idea of how near a natural stroke must be to the aircraft to cause a hybrid strike. For simplicity one may assume that the natural channel is vertical and has a uniform charge density per unit length. Because only order of magnitude numbers are desired, it will also be assumed that the situation is quasi-steady state. That is, changes in the field distribution around the channel occur slowly and the static solution is approximately correct. The electric field around a line charge of charge per unit length λ, which is effectively infinitely long, is radially directed and given by:

$$E_r = \frac{\lambda}{2\pi\varepsilon_0 r} . \tag{4.1}$$

Choosing an enhancement factor for the aircraft of about 10, which is typical around the nose of the aircraft, one finds that triggering will occur at a distance,

$$r_{trig} = \frac{\lambda}{2\pi\varepsilon_0 (E_b/10)} , \tag{4.2}$$

where E_b represents the air breakdown field. A typical value for λ, calculated for a channel lowering 5 coulombs of total charge over a 3 kilometer distance, is 1.667×10^{-3} coul/m. E_b varies with altitude, at sea level being about 3×10^6 V/m and at 20,000 feet about 1.5×10^6 V/m. Substituting

these numbers into (4.2) gives triggering distances of approximately 100 meters at sea level and twice that at 20,000 feet altitude. This is a significantly greater distance than the distance at which the presence of the aircraft can directly alter the course of a natural lightning channel. Hence this hybrid strike is much more probable than a natural strike. It may even be that the natural strike as defined here does not exist in that all strikes involving a natural lightning channel occur according to the hybrid scenario. If this is the case then natural strike attachment locations will be strongly biased toward sharp points and edges, as these are the locations from which hybrid streamers will emerge.

It is possible that the hybrid process could account for some of the variability in the measured data. The reasoning behind this is the following. The normal triggered lightning model which has the aircraft flying into a slowly increasing ambient electric field requires that the triggering occur at the smallest possible field level. This must result in aircraft responses which are very similar in amplitude and structure, because the only really significant adjustable parameters are the orientation of the field with respect to the aircraft and the net charge on the aircraft. However, in the hybrid model the natural channel can appear at any distance from the aircraft in a relatively short time, so triggering may occur at field levels which are significantly above the minimum level. This may result in aircraft responses which have a much wider variety, both in amplitude and structure.

Given the conditions under which natural and triggered lightning strikes occur, it appears far more likely that most strikes to the F106B are triggered. Triggered lightning is <u>certain</u> to occur under the proper conditions, while natural lightning is probabalistic even under ideal conditions.

4.3 Triggered Lightning Environment

To investigate the triggered lightning environment a typical thunderstorm will be used [5]. The static electrical characteristics of

this thunderstorm are a +40 Coulomb charge centered at 10 km above ground, a -40 Coulomb charge centered at 5 km, and a +10 Coulomb charge centered at 2 km, as shown in Figure 4.1. The model of Figure 4.1 will be simplified slightly by assuming the charges can be considered to be point charges, and that they are located in a vertical line. For this simplification the static electric field can be calculated as a function of space. The calculation assumes that the earth is a perfect ground plane, so it can be

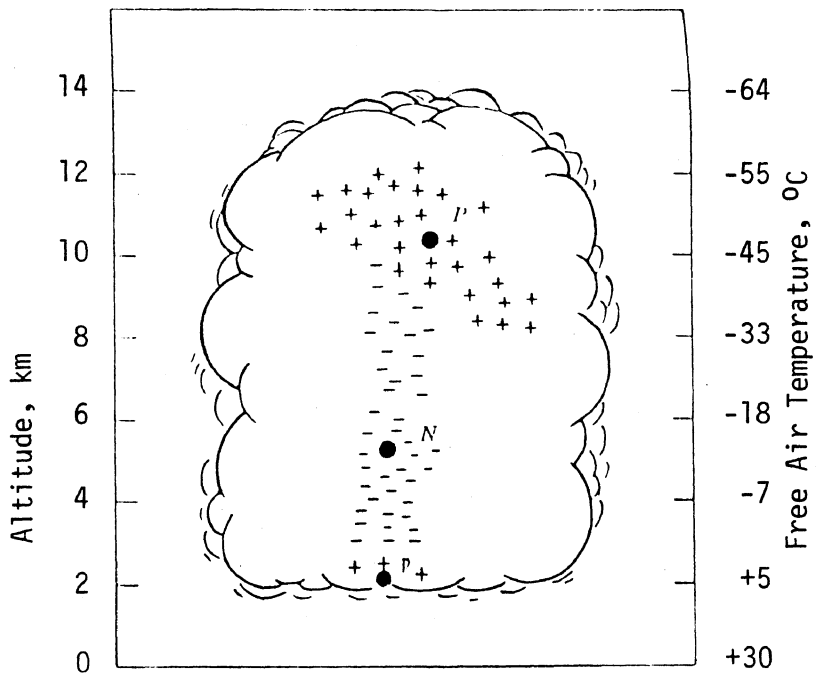

Figure 4.1 Typical Thunderstorm Charge Distribution [5].
P = + 40 coul., N = - 40 coul., p = + 10 coul.

replaced by image charges. The results of the calculation are shown in Figures 4.2a - 4.2c. These figures show contours of constant field as a function of space. The vertical scale is altitude and the horizontal scale is radial distance from the (assumed) vertical line of charges. Figure 4.2a shows contours of the radial component of the field, Figure 4.2b the verti-

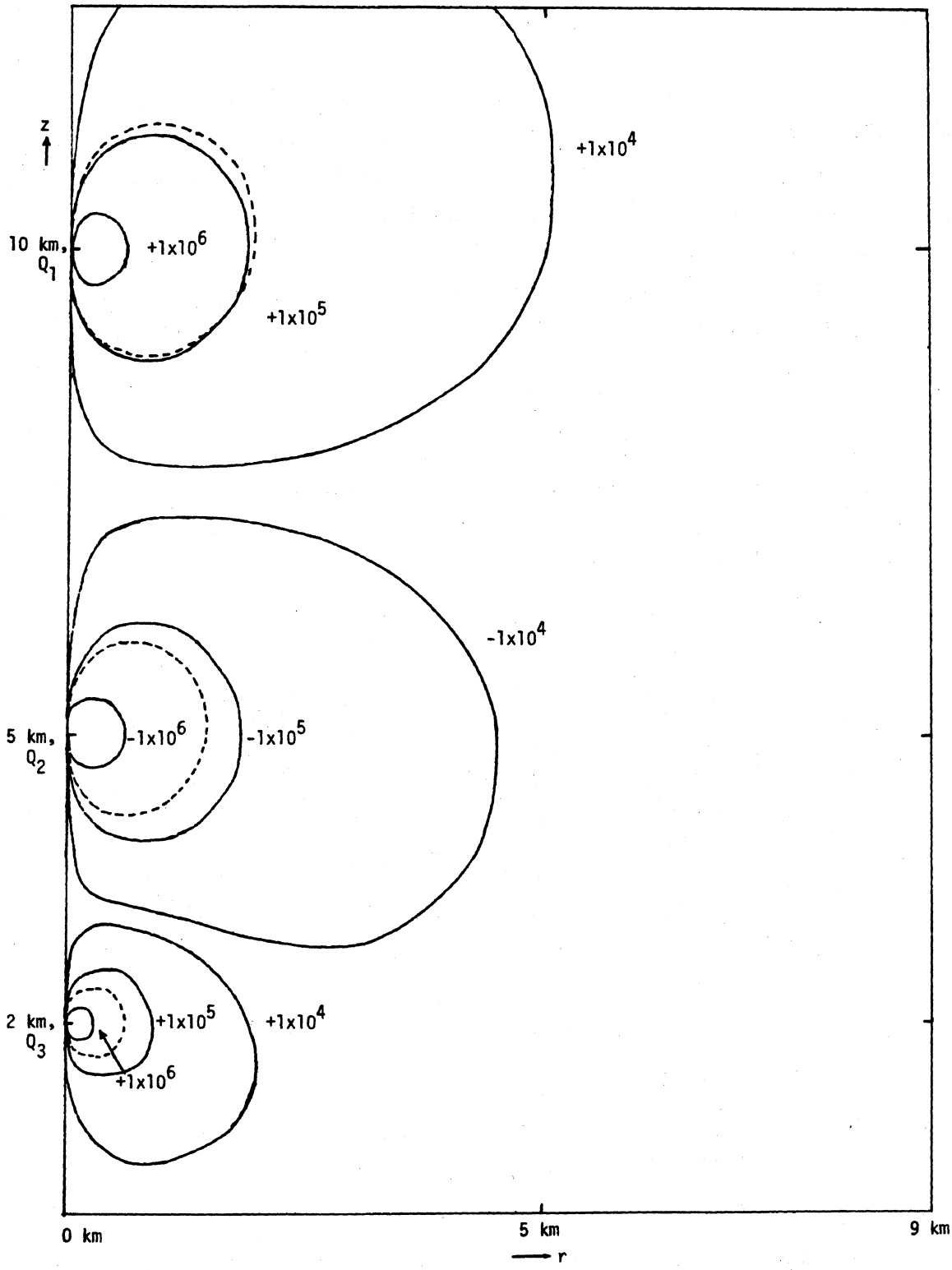

Figure 4.2a Contours Showing Variation of the Radial Horizontal Electric Field Around a Typical Thunderstorm Charge Distribution. Contour Labels Indicate Electric Field Strength. The Dashed Lines Indicate the Location of the Minimum Field Necessary to Trigger Lightning on the F106B.

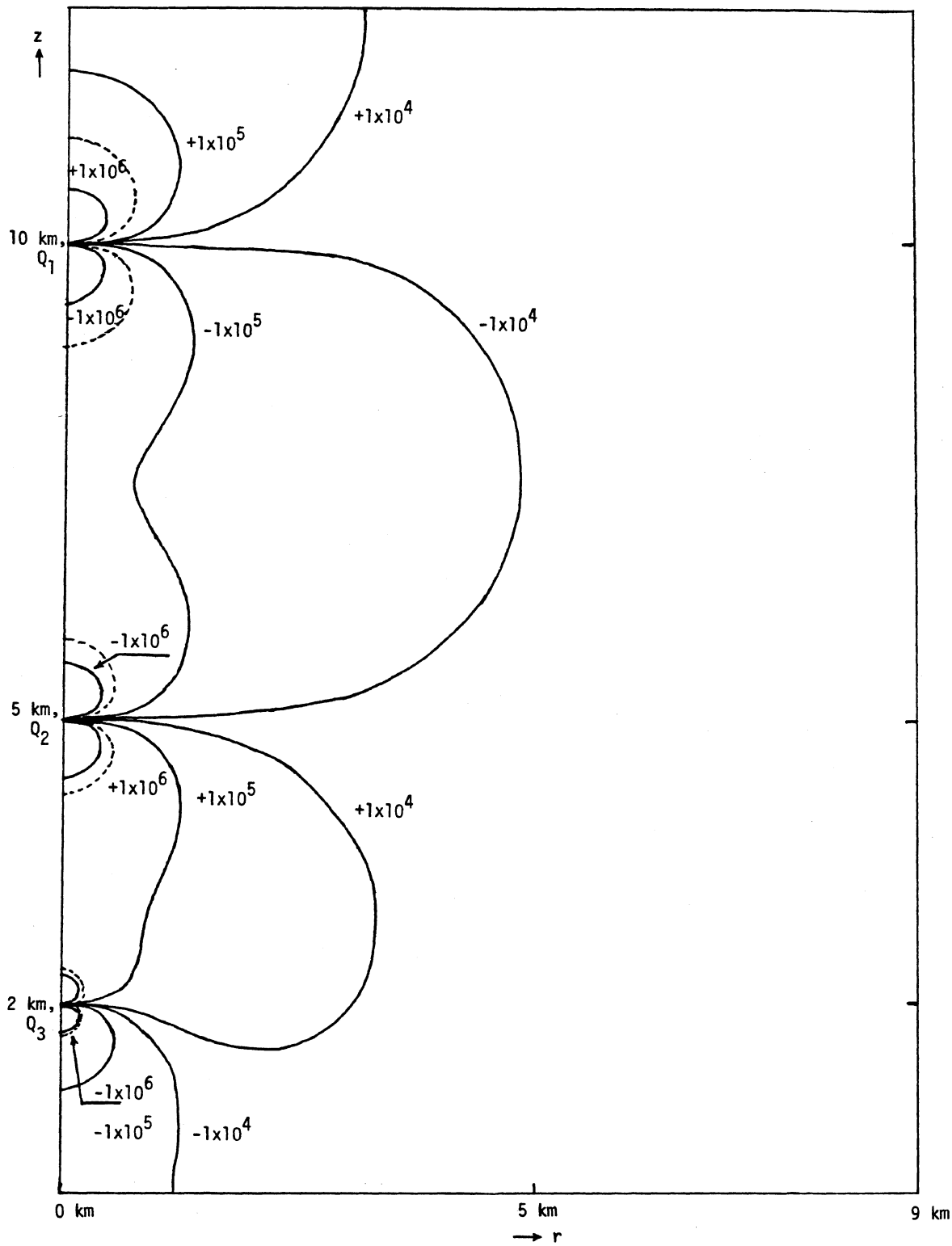

Figure 4.2b Contours Showing Variation of the Vertical Electric Field Around a Typical Thunderstorm Charge Distribution. Contour Labels Indicate Electric Field Strength. The Dashed Lines Indicate the Location of the Minimum Field Necessary to Trigger Lightning on the F106B

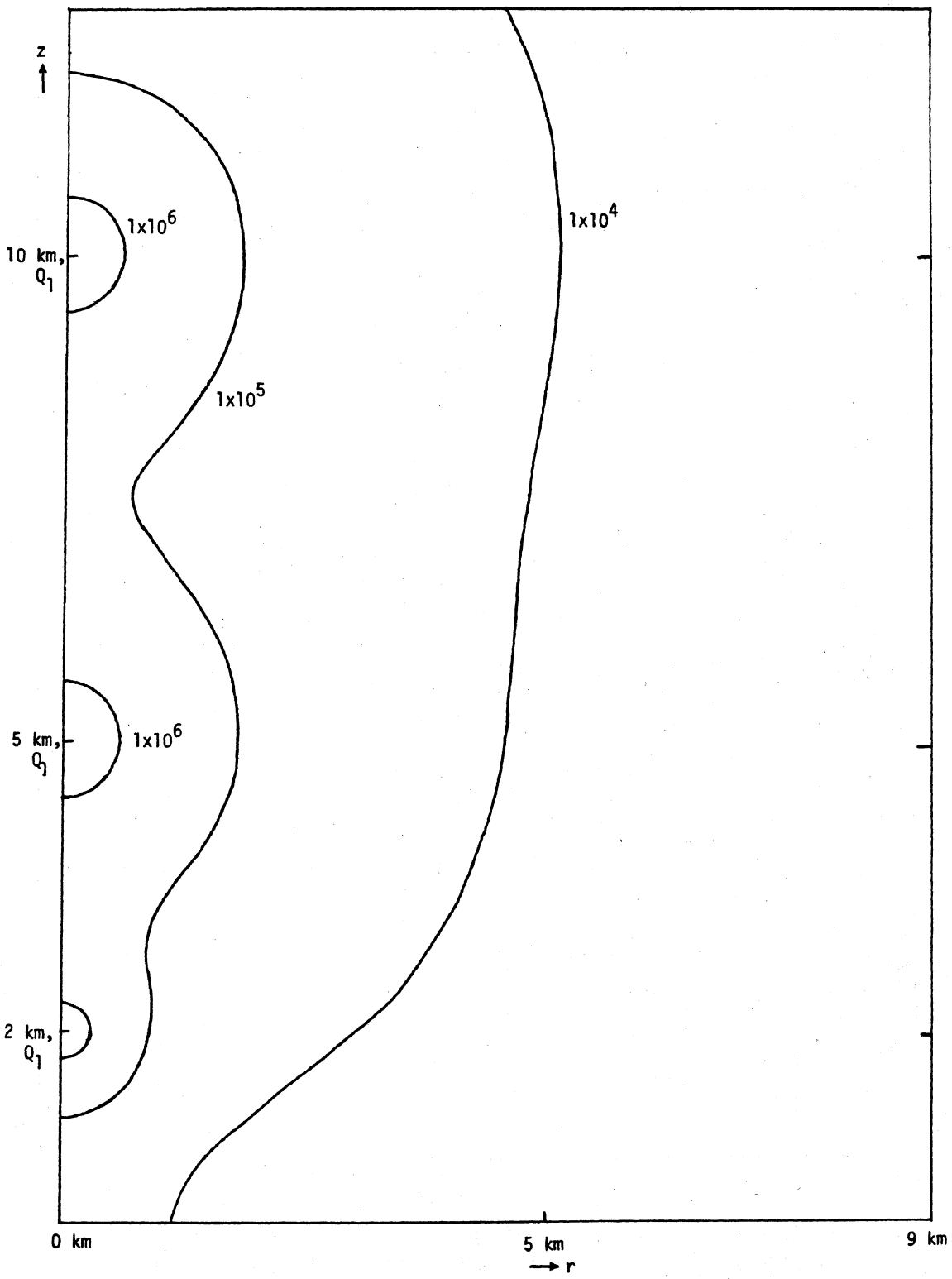

Figure 4.2c Contours Showing Variation of the Total Electric Field Around a Typical Thunderstorm Charge Distribution. Contour Labels Indicate Electric Field Strength

cal component of the field, and Figure 4.2c the total field magnitude. It should be remembered that the contours shown on the figures were calculated assuming point charges, so the fields shown are really upper limits on the actual field. If one of the contours is inside an extended charge cloud, the actual field is likely to be somewhat smaller at that point than the contour indicates.

Figure 4.2a is the most interesting for the purposes of investigating triggered lightning on the F106B. Assuming the aircraft is always in essentially level flight, the horizontal field is the one which will be most enhanced. Linear calculations done on the F106B show that fields along the axis of the aircraft fuselage are enhanced by about a factor of ten at the nose. Wing - wing ambient fields are enhanced by about a factor of seven at each wing tip. Vertical ambient fields are enhanced by about a factor of three at the tip of the vertical stabilizer. Hence for level flight vertical ambient fields are much less important than radial fields, unless the ambient vertical field is several times larger than the radial field.

Another factor that must be considered is that the minimum air breakdown field is larger at lower altitudes because of the increased air density there. Hence a field which causes triggered lightning at a high altitude ($\sim$ 10 km) may not do so at lower altitudes because of the greater air density. The dashed lines in Figures 4.2a and 4.2b illustrate this effect. They are the locus of points in space at which an electric field of breakdown strength can be reached on the aircraft with proper orientation. They also indicate the regions inside which triggered lightning can occur for the F106B in level flight. Note that the volumes are much larger at high altitude, extending to almost two kilometers from the charge center for the radial field case. At the very low altitudes ($\sim$ 2 km) the trigger region is only a few hundred meters across. In fact because the charges are really extended and not point sources, it is possible that at these low altitudes no triggering region exists at all.

This very simple model illustrates the environment for triggered lightning in the vicinity of a typical thunderstorm. Many complicating factors have been left out. In a real thunderstorm the charge centers are not points

but exist in extended regions. They also may be clumped into several smaller charge centers, around which locally high electric fields may exist. Secondly, in most thunderstorms there is a shear in the vertical direction, so that the charge centers are not in a vertical line. This destroys the cylindrical symmetry. Third, other thunderclouds in the vicinity will alter the field distribution around any given cloud. Finally, the effect of a net charge on an aircraft has been omitted. Therefore, the preceding discussion should be regarded as a guide only to the generally expected behavior of triggered lightning and not to any specific thunderstorm situation.

4.4 Triggered Lightning and the Measured Data

In interpreting F106B direct strike data, it is of some interest to investigate in a simple way the expected response of the aircraft. That is, given that triggered lightning occurs, what will the measured D-dot and B-dot records show, and can one expect any significant difference from records produced by natural lightning ?

To begin, consider the situation in Figure 4.3. This would corresp to the F106B flying directly toward a positive charge center. The aircraft i polarized oppositely to the ambient field, resulting in a field at the D-dot sensor point which points toward the fuselage. Presumably this field has grown slowly over several seconds, as the aircraft flies into a slowly increasing ambient field. This slow growth is far below the trigger level for the derivative sensors on the aircraft. For this geometry the largest enhanc field is at the nose of the aircraft, and eventually the enhanced field ther will become large enough to cause corona. At that time electrons will flow off the nose causing the field at the D-dot sensor location to become less negative. This will happen very quickly, and will probably trigger the on board instrumentation. As the air breaks down at the front of the F106B, the field will increase at the aft end, possibly causing another breakdown there That event is dependent on the characteristics of the breakdown at the nose. The corona at the nose effectively increases the length of the F106B and therefore enhances the local field at the rear of the aircraft. Therefore a large corona at the nose will be more likely to cause a breakdown behind

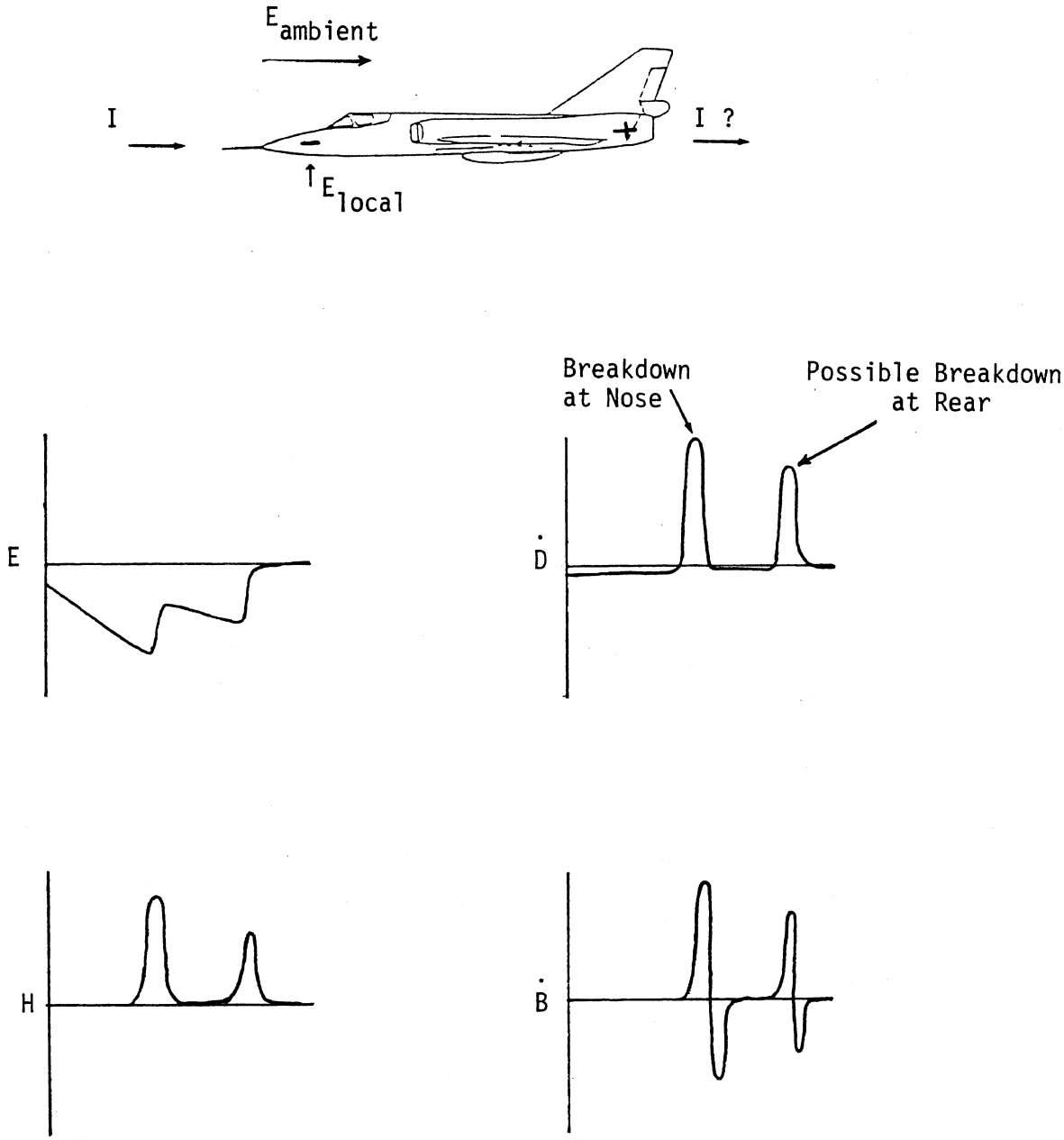

Figure 4.3 Simplified Drawing of the Expected Behavior of Triggered Lightning on the F106B for Ambient Electric Field Oriented Nose to Tail

the plane also. It should also be mentioned that the hot plume of exhaust behind the aircraft may also increase the probability of an air breakdown there. This has yet to be investigated in detail.

Figure 4.3 also shows the expected behavior of the fields and their time derivatives at the D-dot and B-dot sensor positions. The plots are simplified to the extent of ignoring any behavior caused by the resonances of the aircraft. Actual records could be expected to look like those in Figure 4.3 only with respect to general features. The pulses seeen there could be separated by several hundred nanoseconds or longer, depending on the growth of the corona at the nose. It is significant that both single pulses and double pulses as shown in Figure 4.3 are seen in the measured data. (Consider D-dot categories 2 and 5 and B-dot categories 3 and 6 of Appendix A).

An example from the measured data that may illustrate this behavior is shown in Figure 4.4. Presented there are the D-dot and B-dot records from Flight 82-041 run 20. There are two D-dot and B-dot events for that record separated by about 170 microseconds, which behave in a similar manner to the simplified waveforms shown in Figure 4.3. This is good evidence that the events depicted in Figure 4.3 are actually occurring during the flights of the F106B.

Figure 4.5 shows the D-dot and B-dot records from another event (82-041, run 6) in which some different process is occurring. Here, the records happen about 700 microseconds apart, and their general behavior is different than that of Figure 4.3. This type of measured data, in which two or more D-dot and B-dot events exist on a single data record, could be quite helpful in characterizing the lightning phenomena occurring on a given flight. For example, two D-dot events on a single record could indicate breakdown at two different locations on the aircraft. The relative amplitude of the two events can provide information as to the location of these breakdowns. From that information, in turn, can be inferred possible ambient field strength, orientation, and aircraft charge.

The case in which the ambient field is reversed in direction is shown in Figure 4.6. This would occur if the aircraft were flying away from a positive charge center or toward a negative charge center. If one

(text continued on page 64)

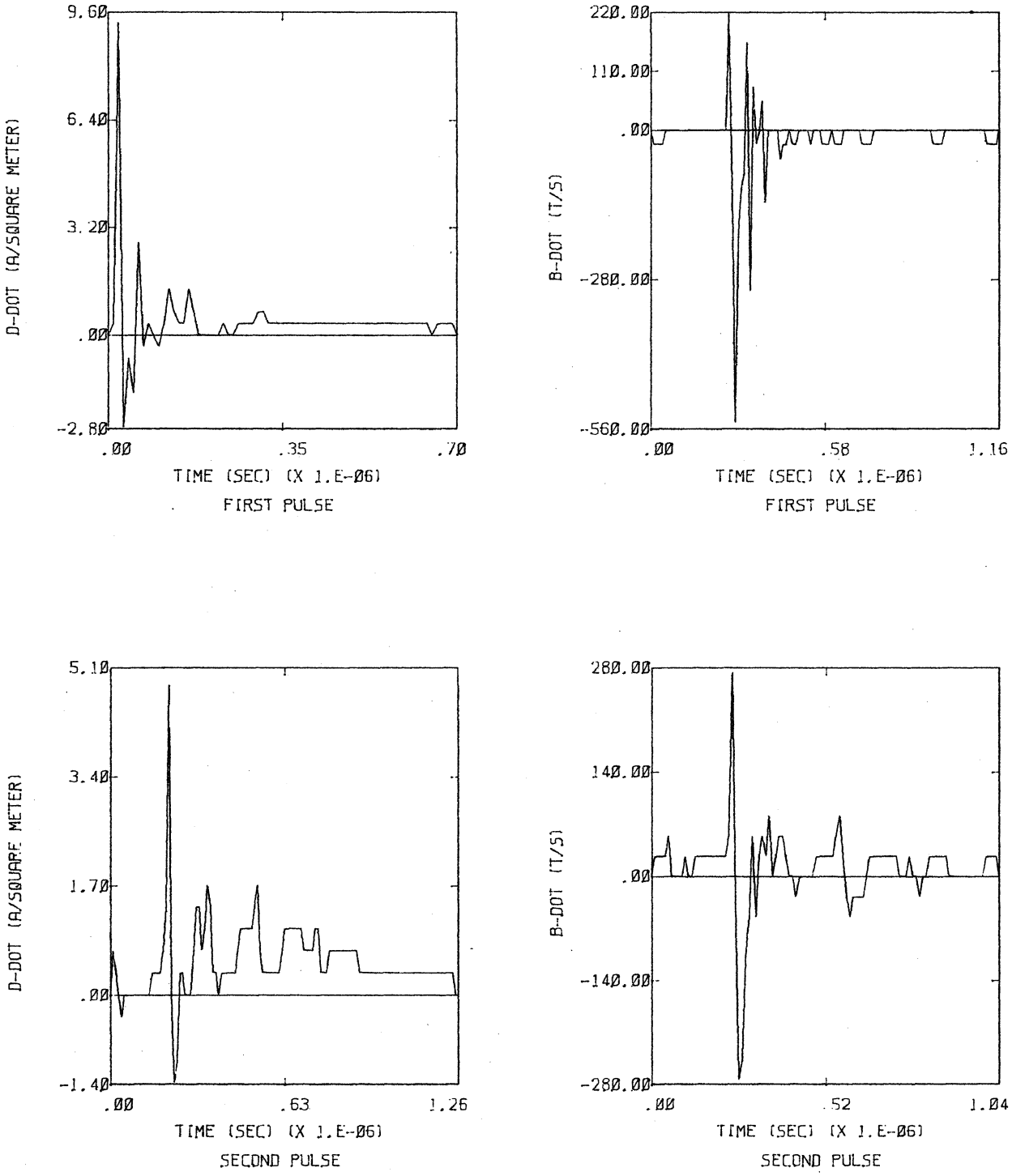

FIGURE 4.4 EXAMPLE FROM THE MEASURED DATA (FLIGHT 82-041, RUN 20) EXHIBITING THE SAME TYPE OF BEHAVIOR AS SCHEMATICALLY DEPICTED IN FIGURE 4.3. TIME DIFFERENCE BETWEEN THE TWO PULSES IS ABOUT 170 MICROSECONDS.

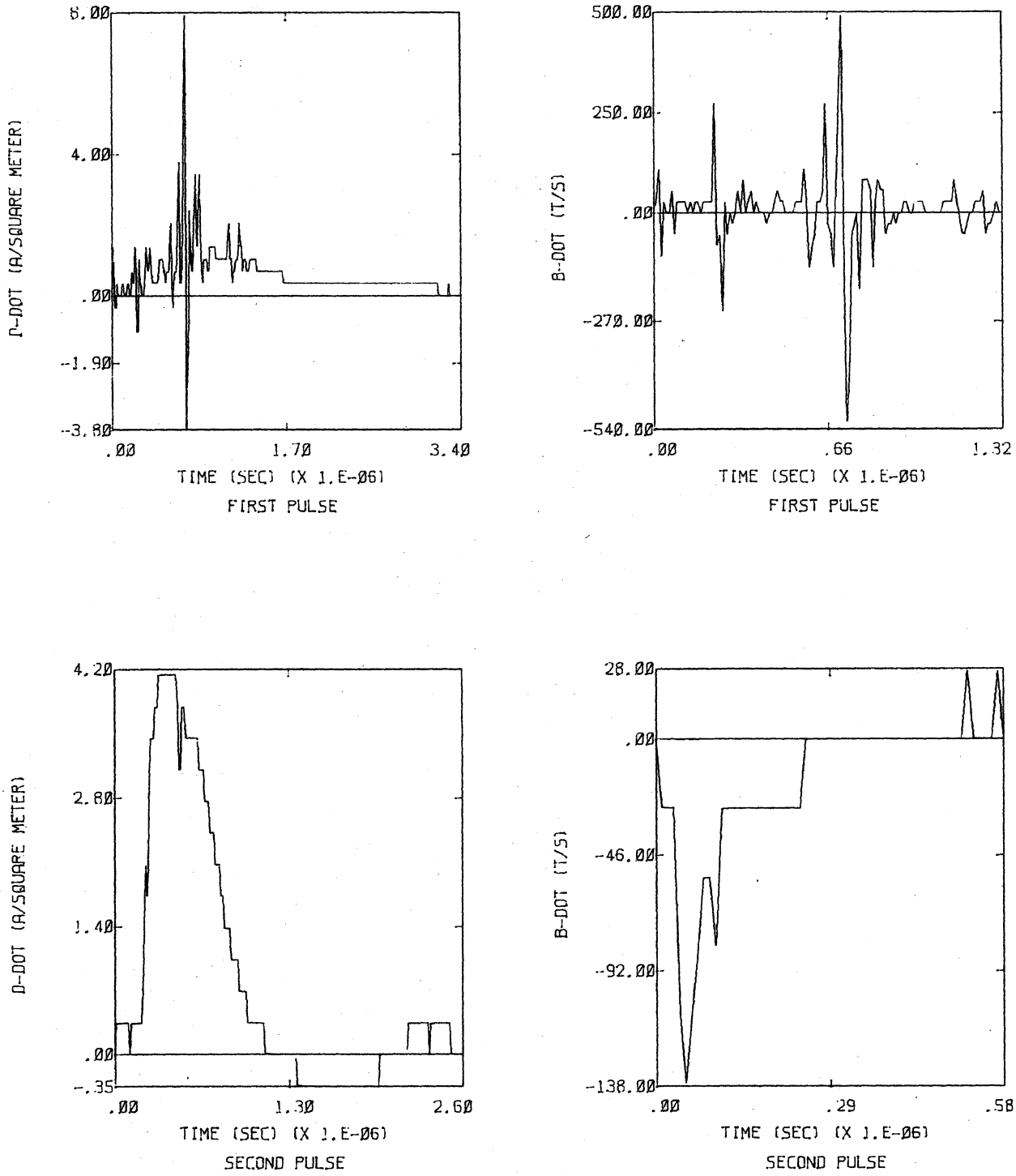

FIGURE 4.5 EXAMPLE FROM THE MEASURED DATA (FLIGHT 82-041, RUN 6) EXHIBITING BEHAVIOR DIFFERENT FROM ANY OF THE SIMPLE MODELS DISCUSSED IN THIS CHAPTER. TIME DIFFERENCE BETWEEN THE PULSES IS ABOUT 700 MICROSECONDS.

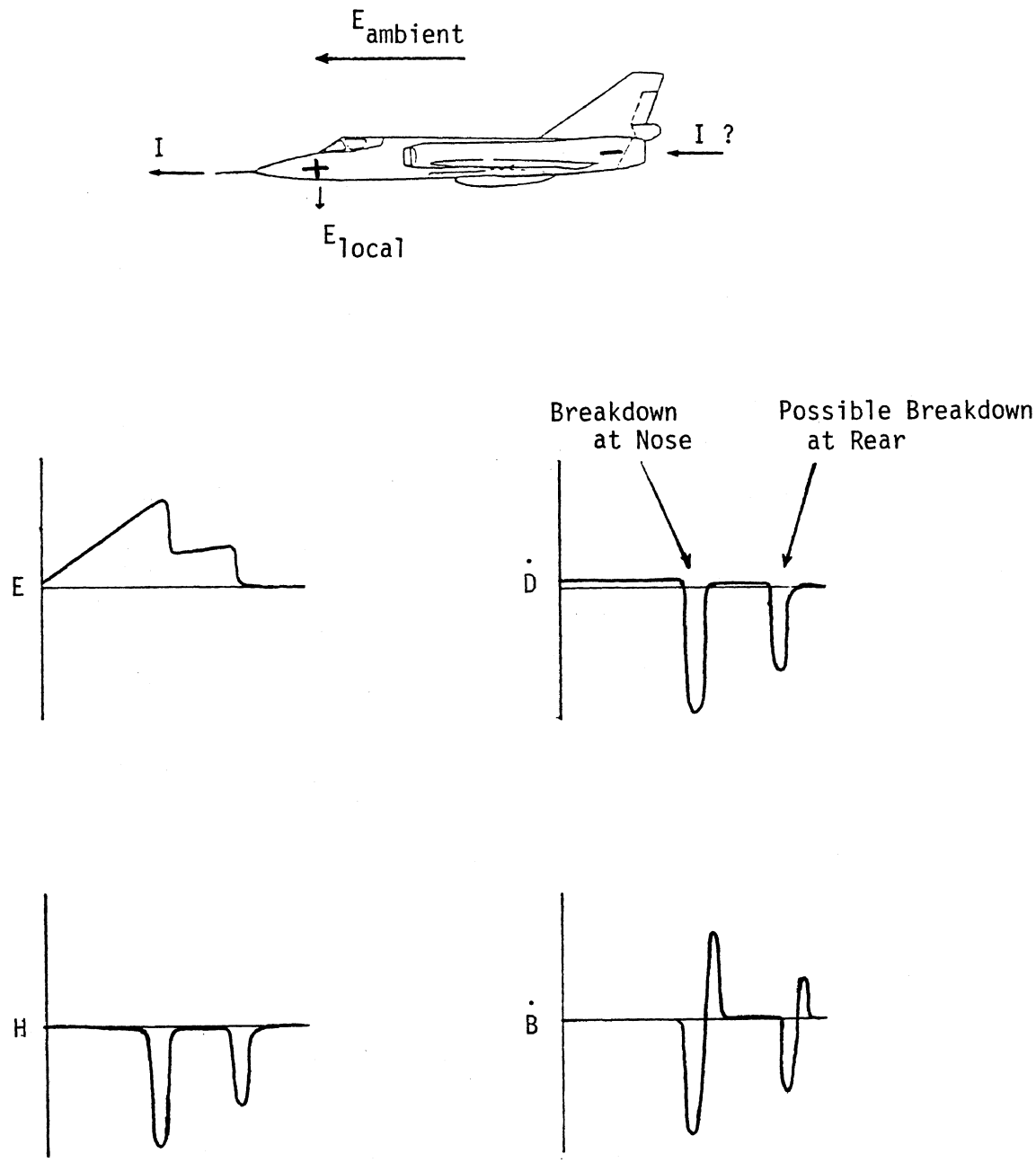

Figure 4.6 Simplified Drawing of the Expected Behavior of Triggered Lightning on the F106B for Ambient Electric Field Oriented Tail to Nose

assumes once again that the initial breakdown is at the nose and a possible second breakdown occurs at the aft end, the expected field behavior is shown in the figure. It looks very similar to the waveforms of Figure 4.3, simply reversed in polarity. The actual situation is somewhat different between the two cases however. In the case of Figure 4.3 a negative corona forms around the nose, since the front of the aircraft is negatively charged In Figure 4.6 a positive corona forms there. It is well known that a negativ corona requires a higher electric field to form than a positive corona, so the details of the two cases can be expected to differ somewhat. Intuitively it would seem reasonable that the smaller field required to initiate a positive corona would result in a slower and smaller measured D-dot response as the corona expands outward from the aircraft. The negative corona would result in a faster breakdown when the required higher field is finally reached. This would appear to be characteristic of the measured data, in that initially positive D-dot records (near the F106B nose) tend to be large and have more high frequency content than initially negative records.

This type of simple analysis has been done for the geometry having electric field oriented along the fuselage, three possibilities of charge on the aircraft, and two breakdown locations. The three charge cases are $+Q_0$, $-Q_0$ and zero charge, where Q_0 has a magnitude such that it can significantly alter breakdown characteristics and locations. That is, Q_0 cannot cause air breakdown by itself, but it can change the magnitude of the electri field which results in breakdown. The two possible breakdown locations are the nose and tail. Rather than presenting a picture of each case separately, the results of the analysis are presented in Table 4.1. For each case is indicated the direction of the electric field, the charge on the aircraft, the point of breakdown, the initial excursion of the D-dot and B-dot sensors, and the initial sign of the current at the breakdown point. The sign convention for the current was chosen so that a positive sign indicates current flowing off the aircraft.

It is interesting to note that the majority of the measured records which include simultaneous D-dot and B-dot data show both being positive for the initial excursion. This occurs only three times in Table 4.1, and one of those three cases is unlikely. The two remaining cases both have a front

Table 4.1 Parameterization Indicating Initial Sensor Signs for Differing Choices of Electric Field Orientation, Charge on Aircraft, and Air Breakdown Location (B-F - back to front, F-B = front to back, N = nose, T = tail).

E	Q	Breakdown Location	D-dot	B-dot	I_{Nose}	I_{Tail}
B-F	0	N	-	-	+	
B-F	0	T	+	-		-
B-F	$+Q_o$	N	-	-	+	
B-F	$+Q_o$	T(unlikely)	+	-		-
B-F	$-Q_o$	N(unlikely)	-	-	+	
B-F	$-Q_o$	T	+	-		-
F-B	0	N	+	+	-	
F-B	0	T	-	+		+
F-B	$+Q_o$	N(unlikely)	+	+	-	
F-B	$+Q_o$	T	-	+		+
F-B	$-Q_o$	N	+	+	-	
F-B	$-Q_o$	T(unlikely)	-	+		+

to back electric field, and breakdown at the nose of the aircraft. The net charges for these cases are zero and a negative charge. This is consistent with the expected negative charging of the aircraft from collisions with ice particles.

Cases in which the ambient field is not oriented along the fuselage are far more difficult to analyze simply, because then aircraft resonances are much more important for the D-dot and B-dot responses. That is, it isn't clear what D-dot behavior will result from a wing to wing triggered lightning event. For that case the shape of the aircraft must be considered in detail.

To examine possible differences between triggered and natural lightning responses of the F106B, consider Figure 4.7. That figure shows the approach of a negative leader toward the nose of the plane. The aircraft polarizes as in Figure 4.6 and the D-dot and B-dot responses as attachment occurs are also much the same as in that figure. Physically the only major difference between the triggered and natural lightning cases is the non-

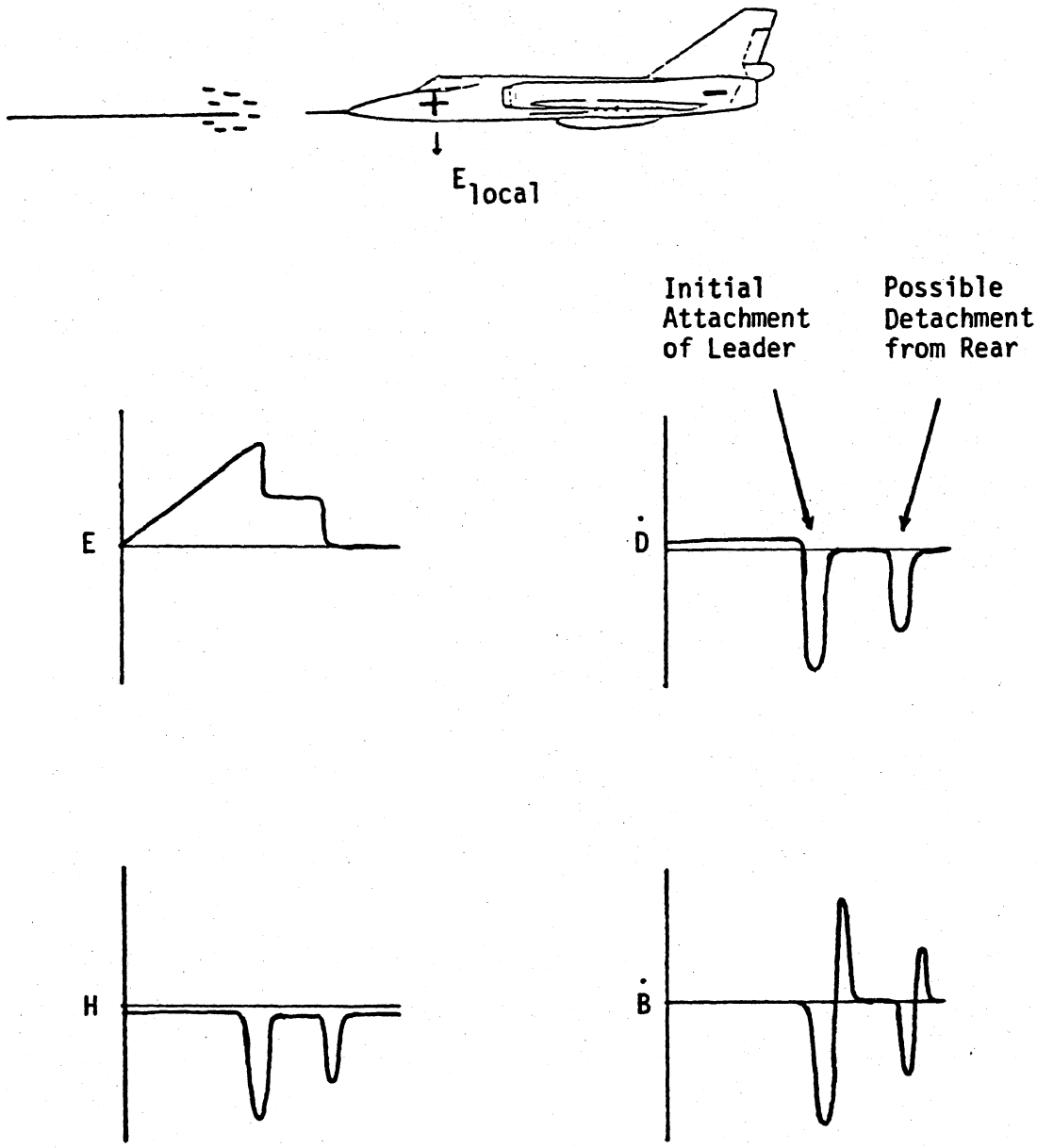

Figure 4.7 Simplified Drawing of the Expected Behavior of the Fields on the F106B During the Approach and Attachment of a Natural Leader Channel

uniformity of the electric field around the tip of the leader. This would change the polarization of the aircraft before attachment somewhat, but the responses of the D-dot and B-dot sensors at attachment and detachment should not be greatly altered. Therefore, it seems unlikely that the two D-dot and B-dot records alone can distinguish between triggered and natural lightning.

4.5 Effects of Triggered Lightning on Other Aircraft

Because the NASA thunderstorm research program is eventually aimed at determining the effect of lightning on other aircraft than the F106B, it is of interest to examine whether the study of lightning triggered by the F106B accomplishes that objective. Is triggered lightning, specifically that triggered by the F106B, of interest to other aircraft ? The answer to this is that it is of interest, in that most lightning strikes to aircraft may be triggered. Although natural lightning strikes surely do occur, they are probably far less frequent, though possibly more severe, than triggered lightning. They will occur more frequently at low altitude than triggered strikes, because an aircraft at low altitude is unfavorably oriented to produce large local electric fields in the presence of a typical thunderstorm. Therefore at low altitudes a given strike has a greater probability of being due to natural lightning, but one must also expect the probability of <u>any</u> strike occurring to be lower.

Then given that the majority of strikes to aircraft could be from triggered lightning, certainly one must investigate its effects. The difficulty is that triggering by a given aircraft is strongly dependent on the shape of that aircraft. For example, the F106B with its aerodynamic shape and sharply pointed nose is far more likely to trigger a lightning strike than is an aircraft of similar size designed for slower speeds. Also aircraft such as commercial jets and military transports, though not having sharp points, can trigger lightning simply by virtue of their large size. Hence each aircraft must be considered individually with regard to its shape to determine its potential for triggered lightning.

In addition, typical flight altitude must be considered, since the breakdown field is a function of height. At high altitudes two effects combine to increase the probability of triggered lightning. Because the air density is less the breakdown field is less, so the enhancement of the ambient field required to achieve breakdown is smaller. Secondly, fields at high altitude tend to be oriented more horizontally, and as such can be enhanced significantly by an aircraft in level flight, something which does not happen for the predominantly vertical fields at lower altitude.

The advantage of triggered lightning over natural lightning is that it can be predicted to some extent. Enhancement factors for the field around a given aircraft can be easily calculated, and using these one can predict with a fair amount of certainty whether triggered lightning will occur in a given ambient field. This opens the possibility that it can be mitigated either by avoidance of the conditions that cause it, or by protecting the aircraft from its deleterious effects.

There are other conditions not covered in the simple considerations of this chapter which can affect a triggered lightning event. One of these is the net charge on the aircraft. The net charge will always enhance the effect of an ambient field at some locations on the aircraft and suppress it at other locations. Hence, depending on the sign of the charge and the direction of the ambient field, a net charge may either suppress or enhance a triggered lightning event. It can also move the location of the initial breakdown from one place to another.

Another factor that has not been considered is the effect of particles in the air around the aircraft. These could be rain, cloud droplets, hail, graupel, or ice crystals. For most of the F106B data, ice crystals are most likely, because of the flight altitude and low air temperatures. These particles, depending on conductivity, can locally enhance electric fields around themselves, and this could further support a triggered lightning event. This may be particularly important for the case of ice crystals, where irregular shapes are likely to be found. The effect of these particles will be investigated in future work.

A third factor which has not been considered is the effect of air pressure variations around the F106B while in flight. Because air breakdown is strongly dependent on the local pressure, these pressure variations may be expected to significantly affect the location of initial air breakdown. These locations should show a strong preference toward low pressure regions. Also, because the pressure around the aircraft is a function of air speed, the presence or absence of triggered strikes is expected to be a function of flight speed.

CHAPTER 5

TRIGGERED LIGHTNING MODELING

In order to model triggered lightning it is necessary to place the F106B in a static electric field with an arbitrary orientation, and to allow for an arbitrary net charge on the aircraft. Physically what happens is that the F106B flies into a slowly increasing field and picks up a net charge over a period of seconds or minutes. This slow buildup means that at any given time the field and charge distributed on the aircraft are static. Because the triggered lightning model [4] operates with one nanosecond time steps, the slow buildup cannot be modeled. Therefore it is necessary to use the static solution as an initial condition. The way in which this initial condition is found is described below.

The modeling procedure is as follows: Four linear codes are run initially. In three of these codes the ambient electric field is oriented along one of the coordinate axes, either along the fuselage, wing to wing, or vertically. Huygens' surfaces [6] are used to produce the field, which is brought from zero to one volt per meter in a time of four hundred nanoseconds. The long risetime of the field is needed to minimize the excitation of aircraft resonances. The code is then run to one microsecond at a constant one volt per meter ambient field level in order to assure that aircraft resonances have died away and a static solution is obtained. At the one microsecond point all the fields in the problem space are stored so that the electrostatic solution at that time may be used as initial conditions for the nonlinear corona model.

The fourth code to be run introduces a known current which flows between the F106B and the boundary of the problem space. This produces a net charge which is then allowed to flow around the aircraft until equilibrium has been reached. At this time all the fields in the problem space are again stored to provide initial conditons for the nonlinear model. This is then the linear static solution for a known net charge on the aircraft.

Because these four codes are linear the superposition principle applies, and any ambient field and net charge combination can be constructed from the results. Therefore, by combining the linear results properly, initial conditions for arbitrary orientation and amplitude of electric field and arbitrary charge on the F106B can be obtained for the nonlinear code. For example, consider the case of an ambient field of magnitude E_0 oriented at a 45^0 angle between the left wing and the tail section of the F106B, with no vertical component. For simplicity assume there is no net charge on the aircraft. The 45^0 angle means that there are equal components of the field along the fuselage and in the wing-wing direction of magnitude $.707\ E_0$. The static solution for this case is constructed from two solutions:

1) solution with electric field along the fuselage;

2) solution with electric field oriented from right to left wing.

If one designates the first solution by S_1 and the second by S_2, then the solution to the particular case being considered may be written, $S = .707E_0S_1 + .707E_0S_2$. The solutions are first scaled from the 1 V/m normalized field to the desired magnitude, and then added together to get the solution to the more general case. In a similar manner, the static solution for any ambient field and net charge can be constructed from the four basic solutions.

Finally, using these linearly derived initial conditions, the nonlinear code is run for a microsecond, which is normally long enough to observe air breakdown at one or more points on the aircraft.

There is a point that should be made here about the correspondence between actual triggered lightning and the model. Before triggering, the assumption is made that the aircraft is flying through a slowly increasing ambient electric field, so that the field distribution can be regarded as static at all times. A slowly increasing field is one that changes very little in a typical air breakdown time scale ($\sim$ few microseconds). This being the case, it is clear that the aircraft will form corona and probably trigger lightning at the lowest ambient field for which this is possible. That is,

given that the field is slowly changing, air breakdown will occur at some point on the aircraft as soon as the field at that point has reached minimum intensity for breakdown. No field on the plane can be above that minimum intensity, at least not before breakdown has occurred. After breakdown at some point has occurred, the field distribution may vary quite rapidly, allowing some fields to rise above minimum breakdown intensity. At any rate, the fact that it is always a minimum intensity field which initially causes air breakdown means that corona formation will occur quite slowly, possibly taking several microseconds to develop. Slow corona formation implies that triggered lightning D-dot and B-dot amplitudes measured on the F106B should be quite small when compared to those caused by the strike of a fully formed leader at some attach point.

The relevance of this discussion to the nonlinear modeling is as follows. The nonlinear model uses as an initial condition what is essentially the linear solution to the problem of the aircraft in a static ambient field with an arbitrary charge on the aircraft surface. Because the solution is linear, fields can exist in the problem space which are above air breakdown intensity. This is not possible physically, because any field above breakdown level would of necessity have caused air breakdown at some earlier time while the ambient field was increasing. Hence the proper initial condition for the nonlinear model is a static field distribution in which the largest field is of air breakdown intensity. However, this is difficult to accomplish exactly, and it is often the case that at some point in the problem space the local field is larger than the minimum breakdown field. At that point corona will grow much faster than it would in reality, giving rise to predicted D-dot and B-dot responses that are much higher than are measured. The trick the analyst must perform is to reduce the ambient field until the largest field on the aircraft is at or near minimum breakdown intensity. For that case only can the predicted and measured responses be expected to agree. In the predicte waveforms to be presented later in this chapter, some amplitudes are far above any responses which were measured. That is because the ambient field chosen for those cases was too large, resulting in an unrealistic corona growth.

Linear enhancement factors for selected points on the block model of the F106B are shown in Figures 5.1 - 5.4. In Figures 5.1 to 5.3 the numbers are the electric field intensity in the direction of the arrow for an ambient field intensity of one volt per meter in the direction indicated on the figure. In Figure 5.4 the numbers are the electric field intensity in the direction of the arrow for a one microcoulomb charge on the aircraft. These numbers allow a rough estimation of how large the ambient field and charge need to be in order for an air breakdown field to exist at some point on the aircraft. Note that the largest field enhancement for the ambient field cases (Figures 5.2 - 5.3) is at the nose of the aircraft, as expected.

In Figures 5.5 to 5.16 are presented the results of the triggered lightning runs which have been completed. They consist of D-dot, B-dot, and current waveforms as a function of time. The current waveform is the current flowing onto or off the aircraft at a location near the expected air breakdown point. For example, if the expected breakdown point is at the nose of the F106B, the current is that flowing on the fuselage just behind the nose. The environmental conditions for each run (e.g. orientation of field, charge on F106B, relative air density, humidity) are indicated in the legend of each figure.

Several points should be made about the triggered lightning results. First, note that the largest ambient field runs produced predicted D-dot and B-dot responses which are much larger than any measured responses. The reason for this was discussed earlier in this chapter. Second, notice that when the ambient field level is reduced, the responses are slower and smaller in amplitude. This too is expected since the corona forms more slowly for the lower field levels. Although it is not apparent from the figures, the responses also occurred later in time for the lower ambient field levels. Also, note that the predicted response amplitudes approach the measured amplitudes as the ambient field is reduced. Finally, one should be aware that the predicted ambient field levels for triggering are certainly somewhat high. The block model of the F106B produces local fields near the sharp edges and points of the aircraft which are lower than would be found around the real aircraft

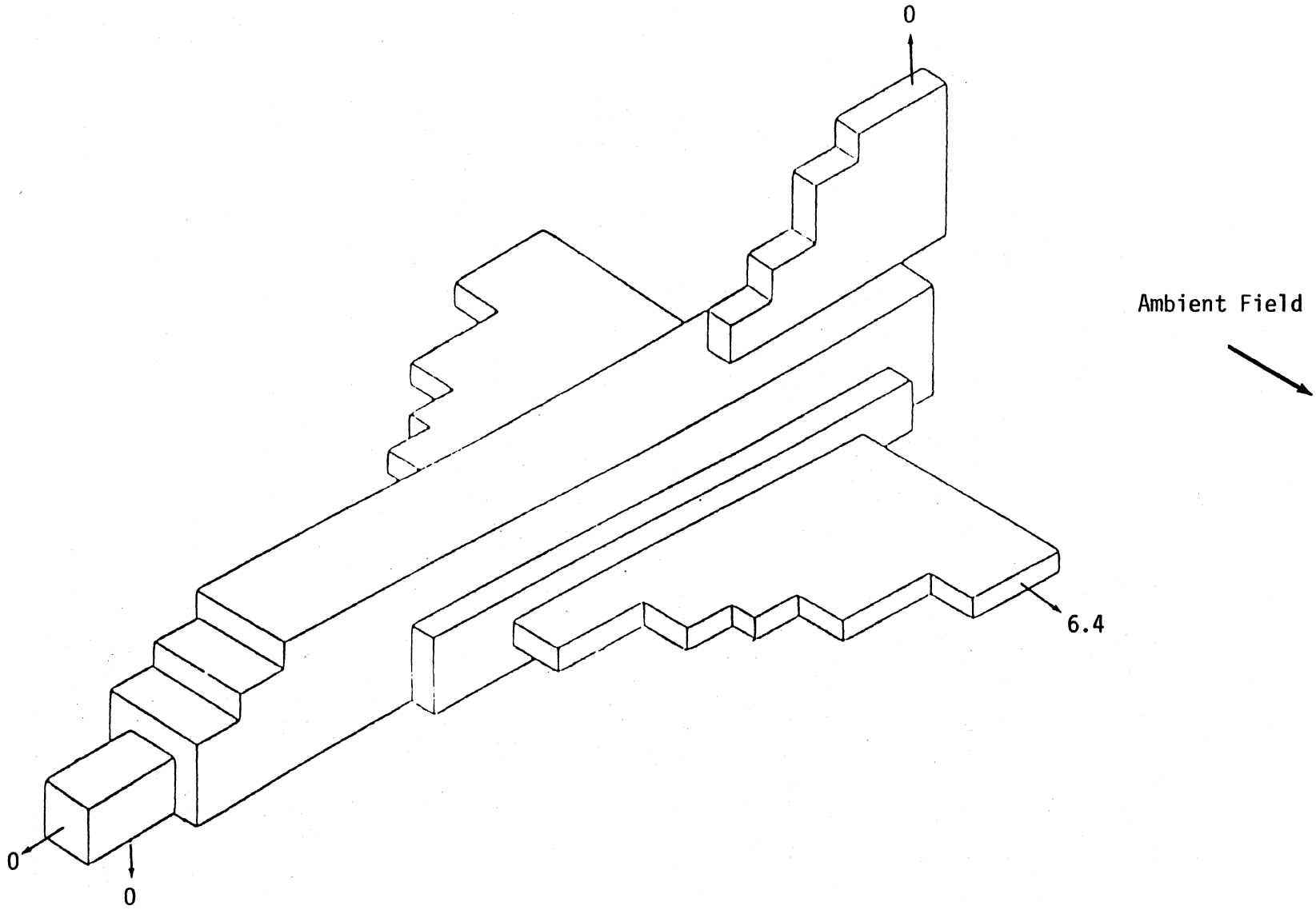

Figure 5.1 Enhanced Electric Fields for 1 V/m Wing-Wing Oriented Electric Field

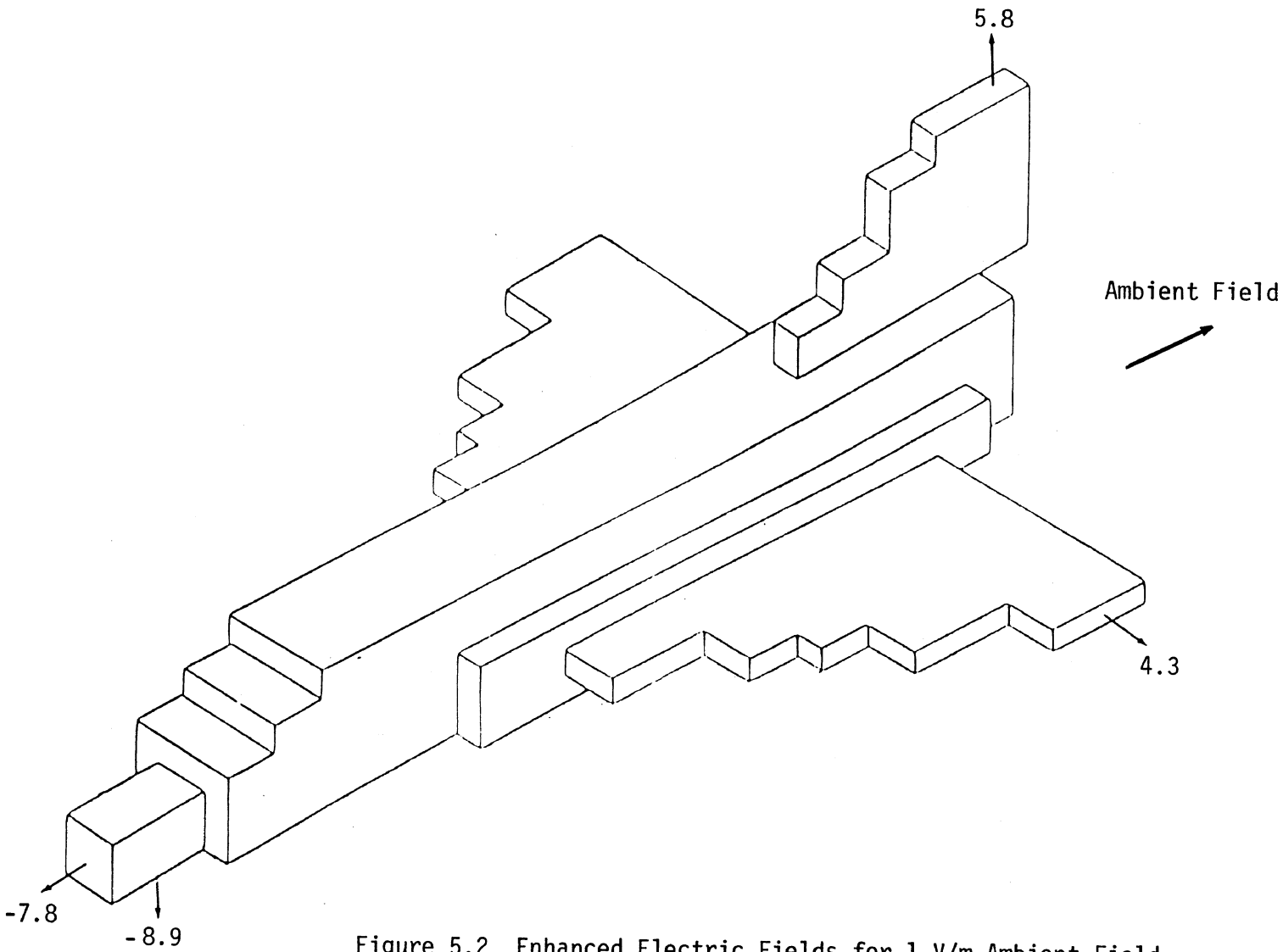

Figure 5.2 Enhanced Electric Fields for 1 V/m Ambient Field Oriented Along the Fuselage

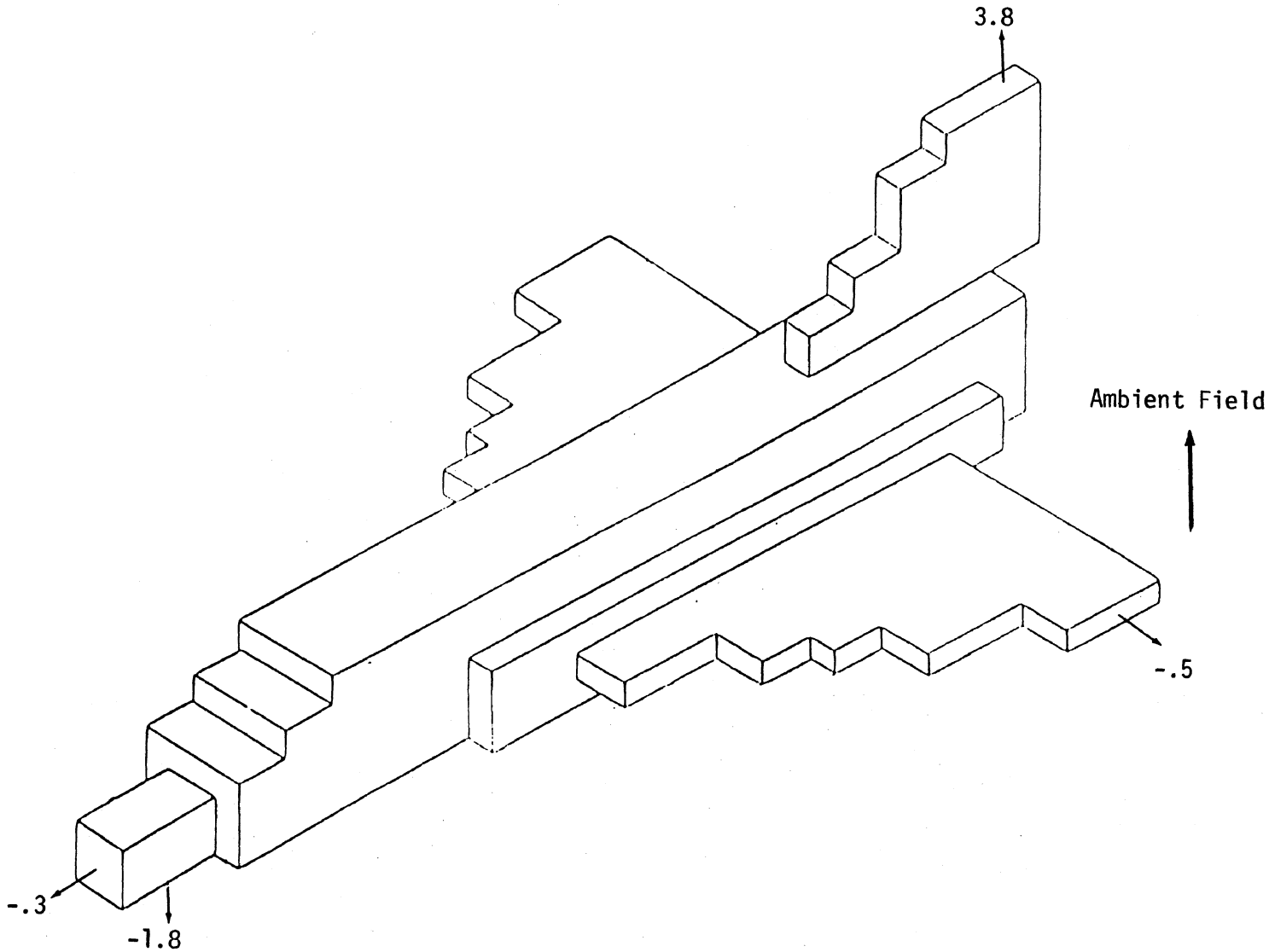

Figure 5.3 Enhanced Electric Fields for 1 V/m Ambient Field Oriented Vertically

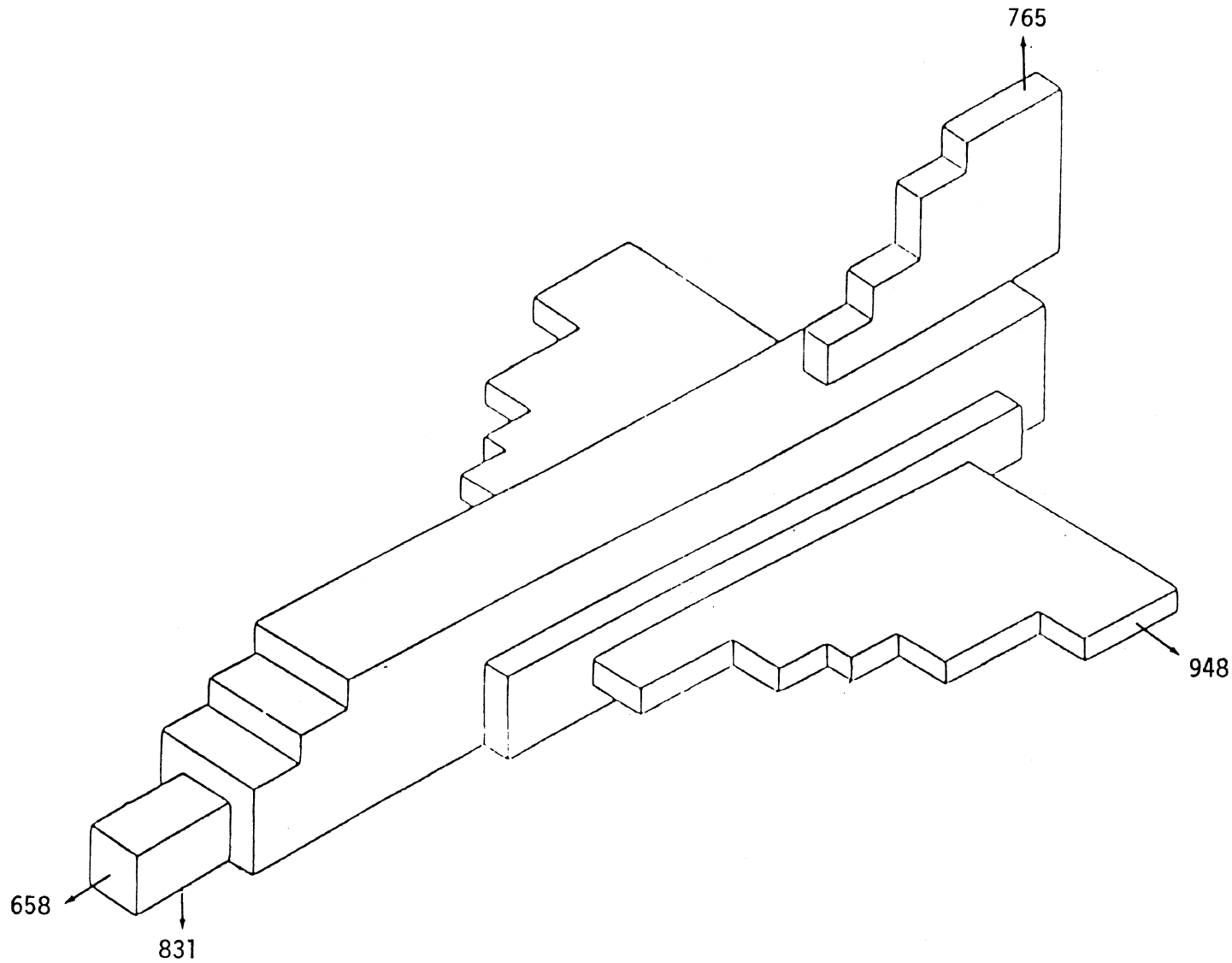

Figure 5.4 Electric Fields (V/m) for 1 μC Positive Charge on the Aircraft

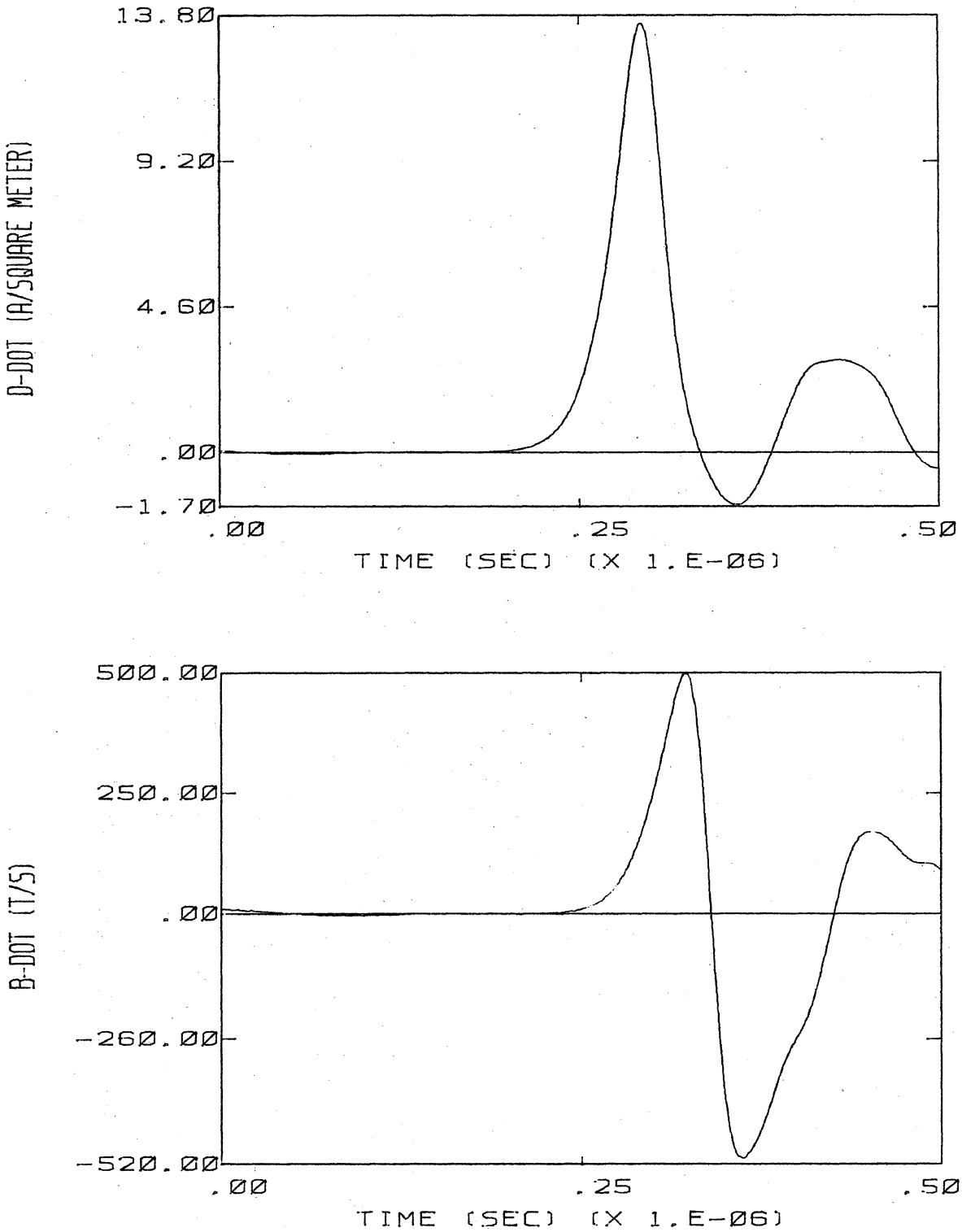

FIGURE 5.5 PREDICTED D-DOT AND B-DOT RESPONSES FOR THE CASE OF ELECTRIC FIELD OF MAGNITUDE 1.9E5 V/M ORIENTED NOSE TO TAIL, NO CHARGE ON THE AIRCRAFT, RELATIVE AIR DENSITY OF .5, AND 6% WATER VAPOR CONTENT

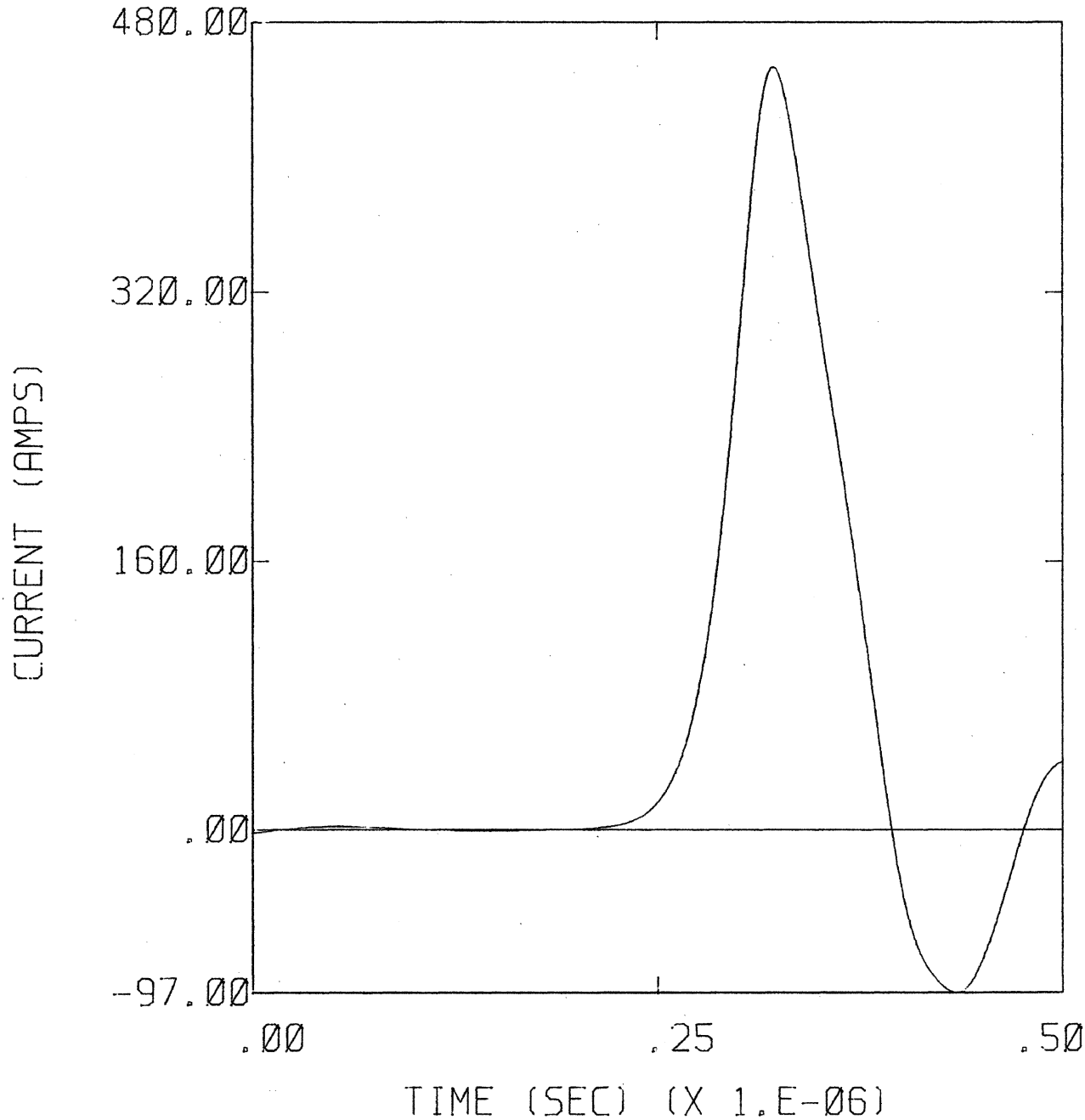

FIGURE 5.6 PREDICTED CURRENT FLOWING ON NOSE FOR THE CASE OF ELECTRIC FIELD OF MAGNITUDE 1.9E5 V/M ORIENTED NOSE TO TAIL, NO CHARGE ON THE AIRCRAFT, RELATIVE AIR DENSITY OF .5, AND 6% WATER VAPOR CONTENT

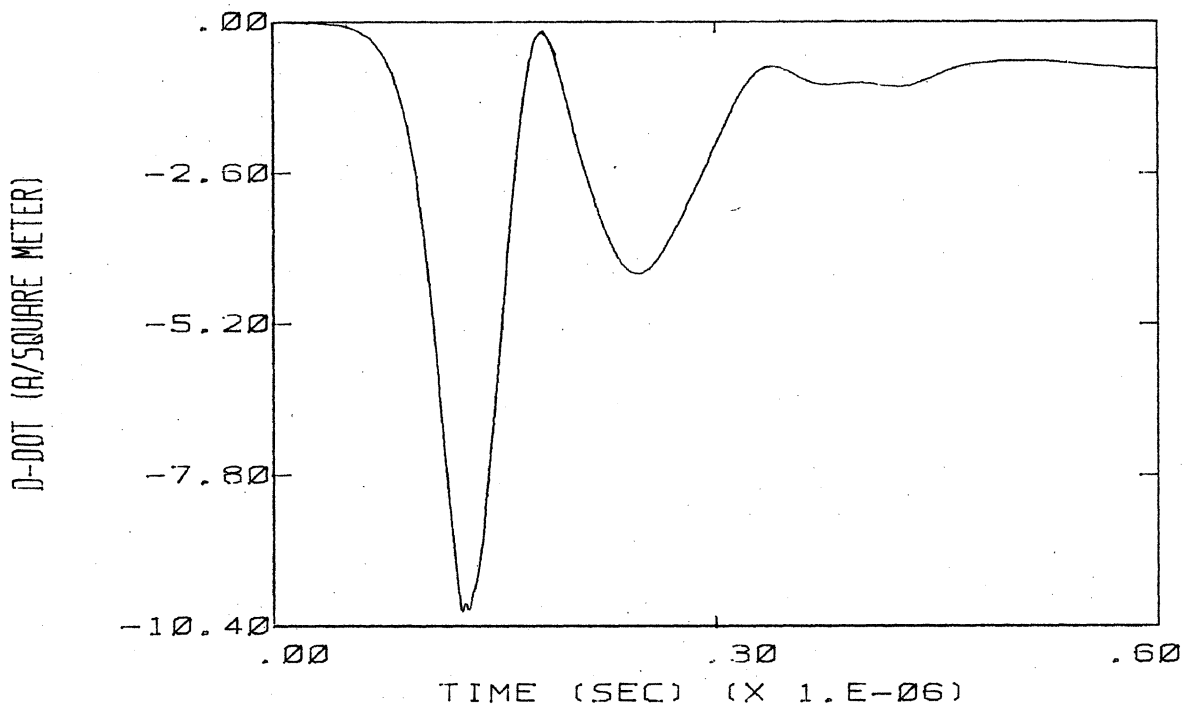

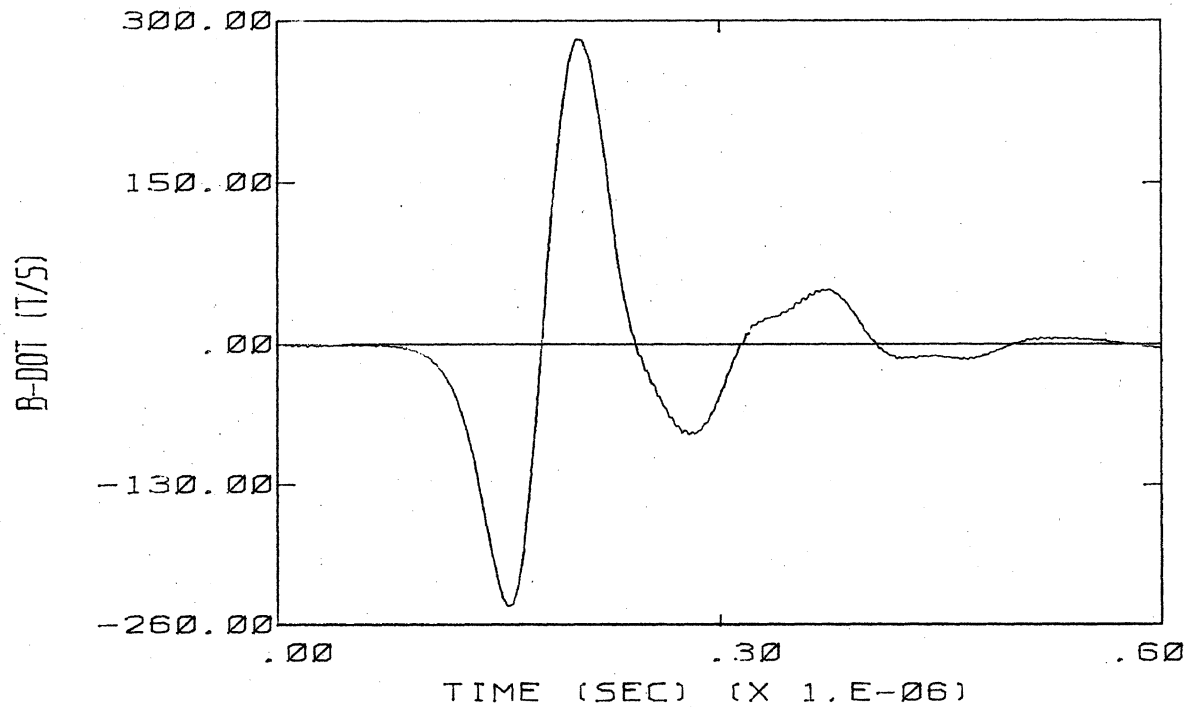

FIGURE 5.7 PREDICTED D-DOT AND B-DOT RESPONSES FOR THE CASE OF ELECTRIC FIELD OF MAGNITUDE 1.9E5 V/M ORIENTED TAIL TO NOSE, NO CHARGE ON THE AIRCRAFT, RELATIVE AIR DENSITY OF .5, AND 6% WATER VAPOR CONTENT

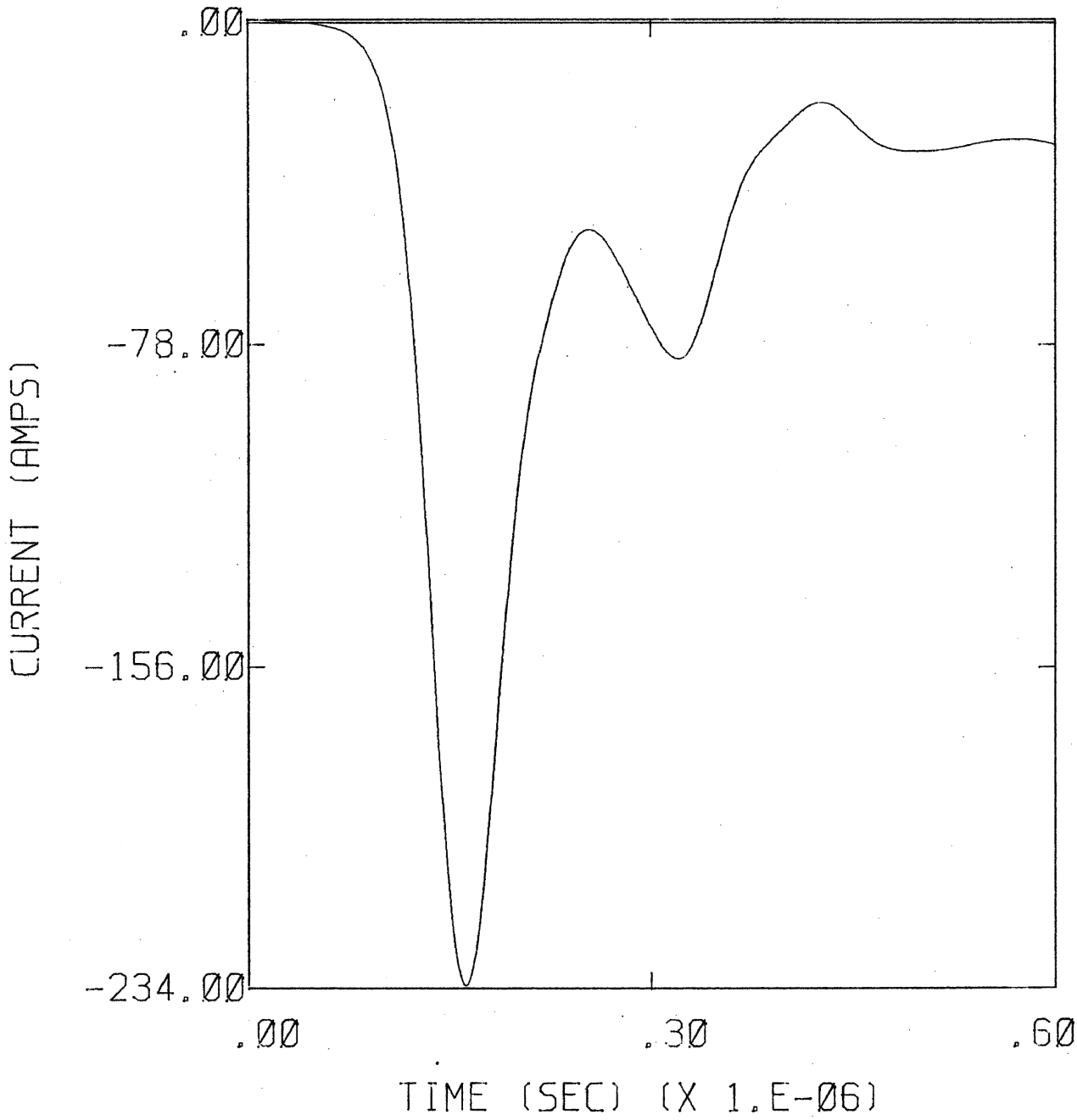

FIGURE 5.8 PREDICTED CURRENT FLOWING ON NOSE FOR THE CASE OF ELECTRIC FIELD OF MAGNITUDE 1.9E5 V/M ORIENTED TAIL TO NOSE, NO CHARGE ON THE AIRCRAFT, RELATIVE AIR DENSITY OF .5, AND 6% WATER VAPOR CONTENT

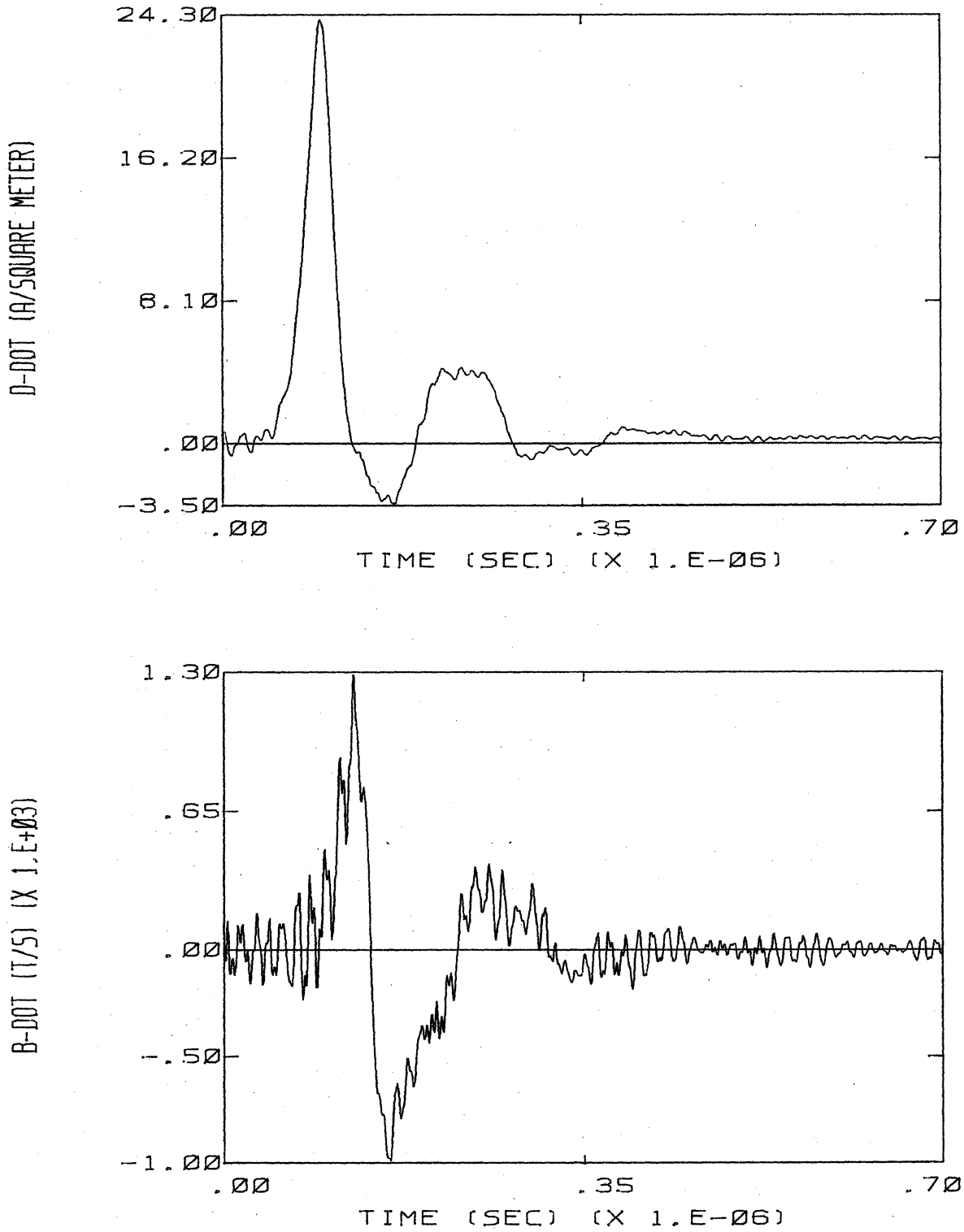

FIGURE 5.9 PREDICTED D-DOT AND B-DOT RESPONSES FOR THE CASE OF ELECTRIC FIELD OF MAGNITUDE 1.9E5 V/M ORIENTED NOSE TO TAIL, 100 MICROCOULOMBS OF NEGATIVE CHARGE ON THE AIRCRAFT, RELATIVE AIR DENSITY .5, AND 6% WATER VAPOR CONTENT

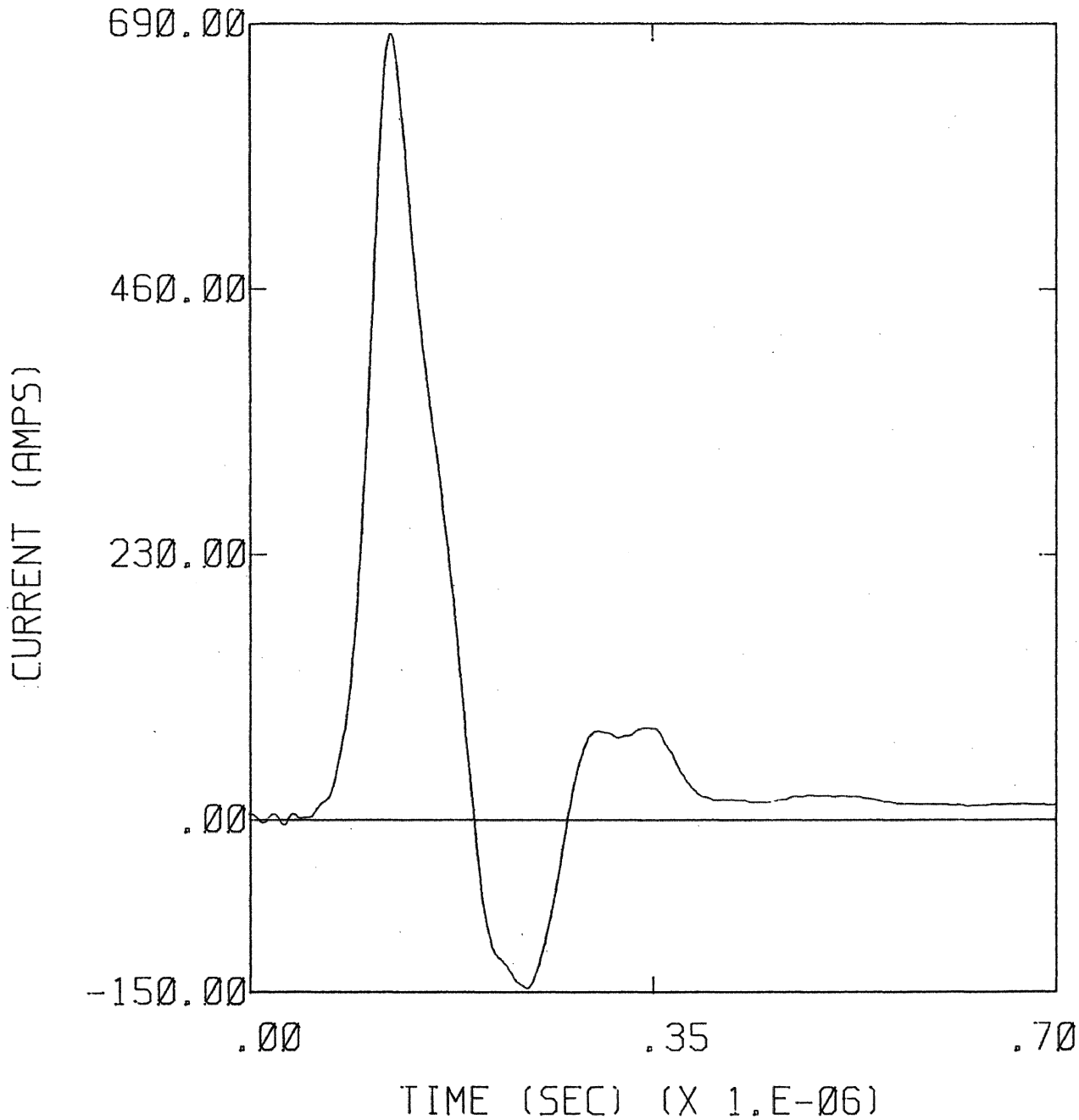

FIGURE 5.10 PREDICTED CURRENT FLOWING ON NOSE FOR THE CASE OF ELECTRIC FIELD OF MAGNITUDE 1.9E5 V/M ORIENTED NOSE TO TAIL, 100 MICROCOULOMBS OF NEGATIVE CHARGE ON THE AIRCRAFT, RELATIVE AIR DENSITY OF .5, AND 6% WATER VAPOR CONTENT

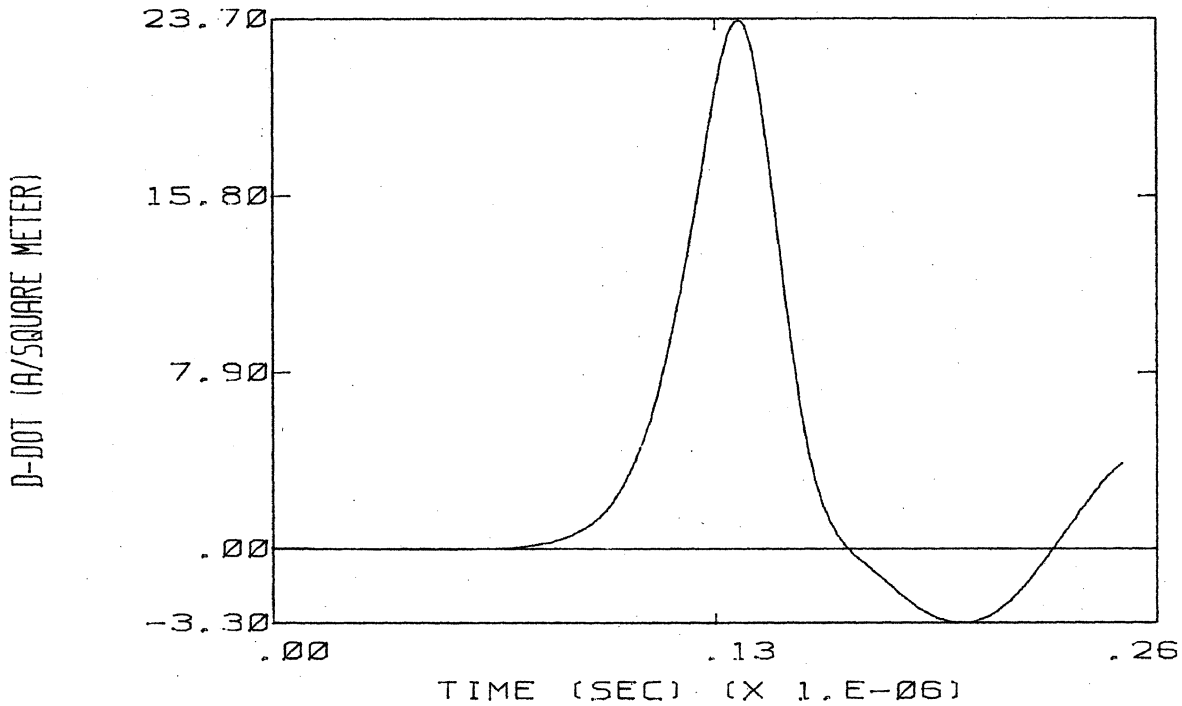

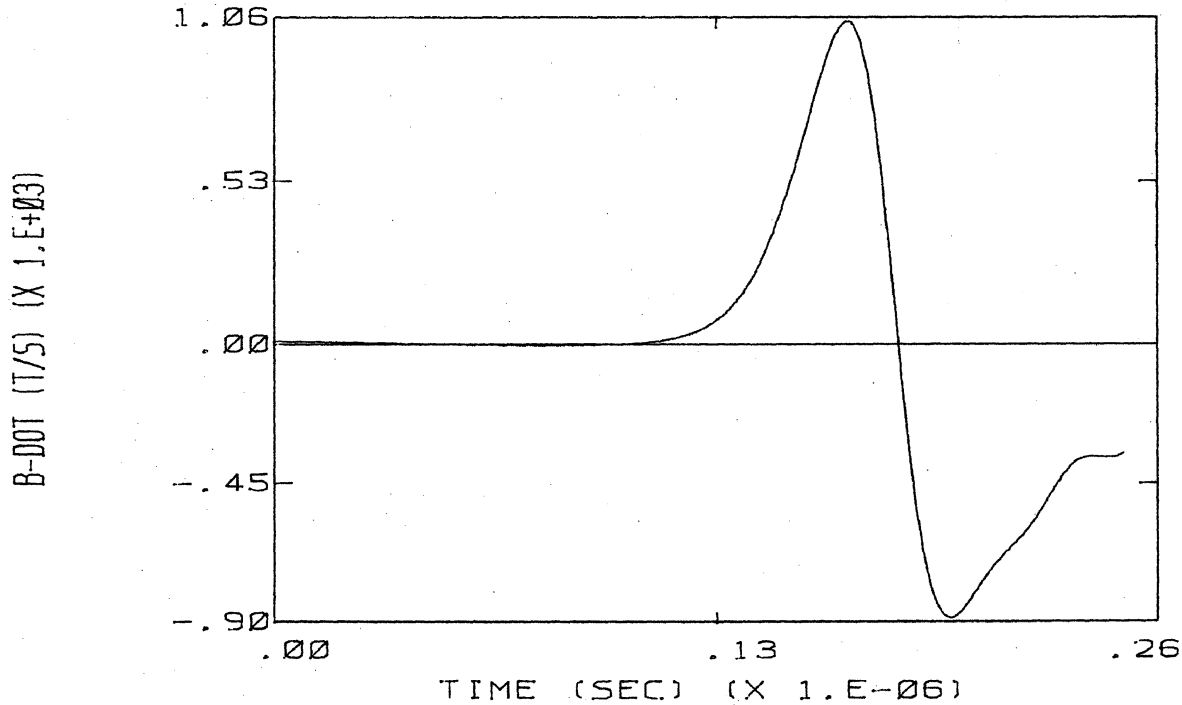

FIGURE 5.11 PREDICTED D-DOT AND B-DOT RESPONSES FOR THE CASE OF ELECTRIC FIELD OF MAGNITUDE 2.E5 V/M ORIENTED NOSE TO TAIL, NO CHARGE ON THE AIRCRAFT, RELATIVE AIR DENSITY OF .5, AND 6% WATER VAPOR CONTENT

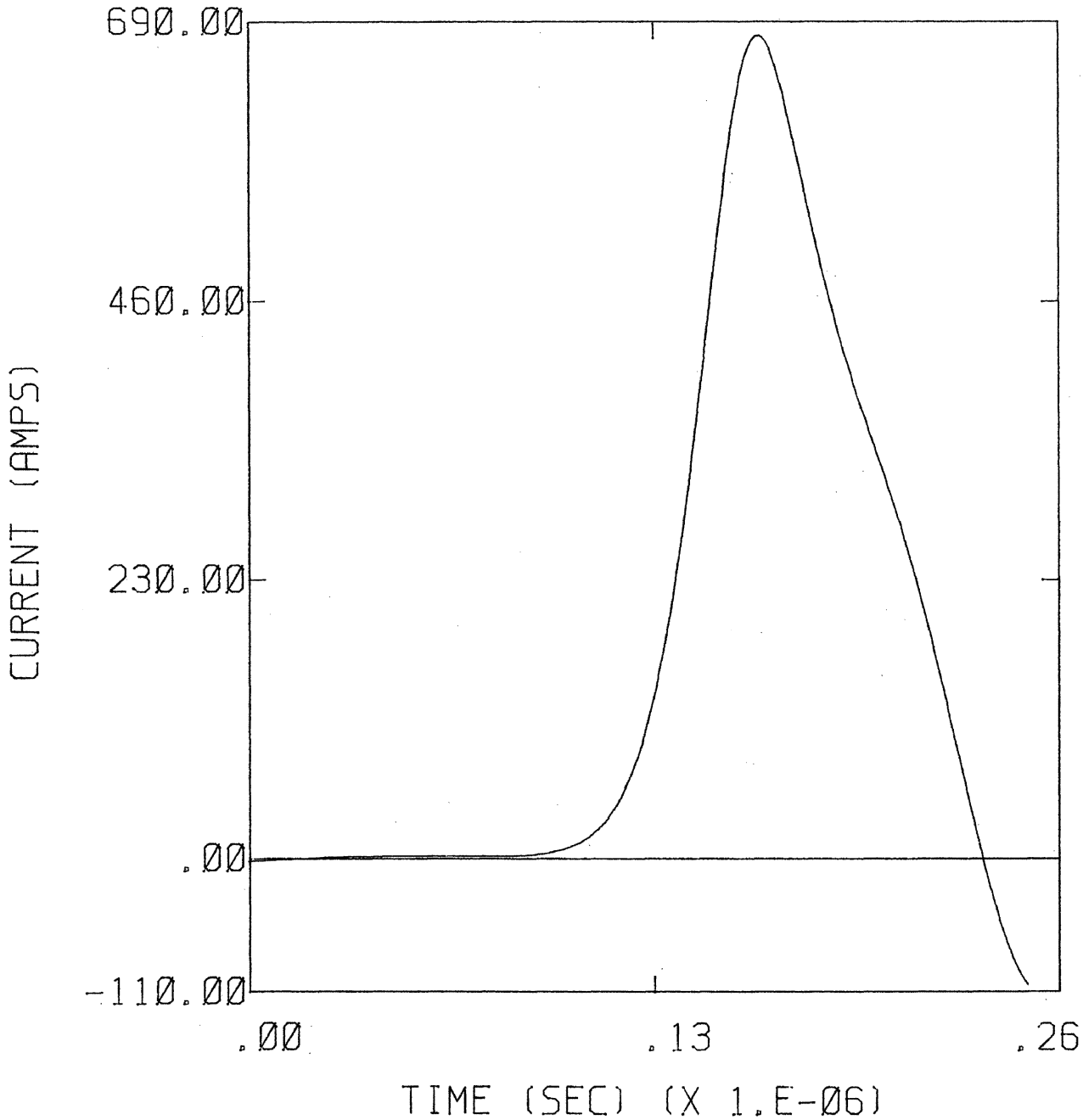

FIGURE 5.12 PREDICTED CURRENT FLOWING ON NOSE FOR THE CASE OF ELECTRIC FIELD OF MAGNITUDE 2.E5 V/M ORIENTED NOSE TO TAIL, NO CHARGE ON THE AIRCRAFT, RELATIVE AIR DENSITY OF .5, AND 6% WATER VAPOR CONTENT

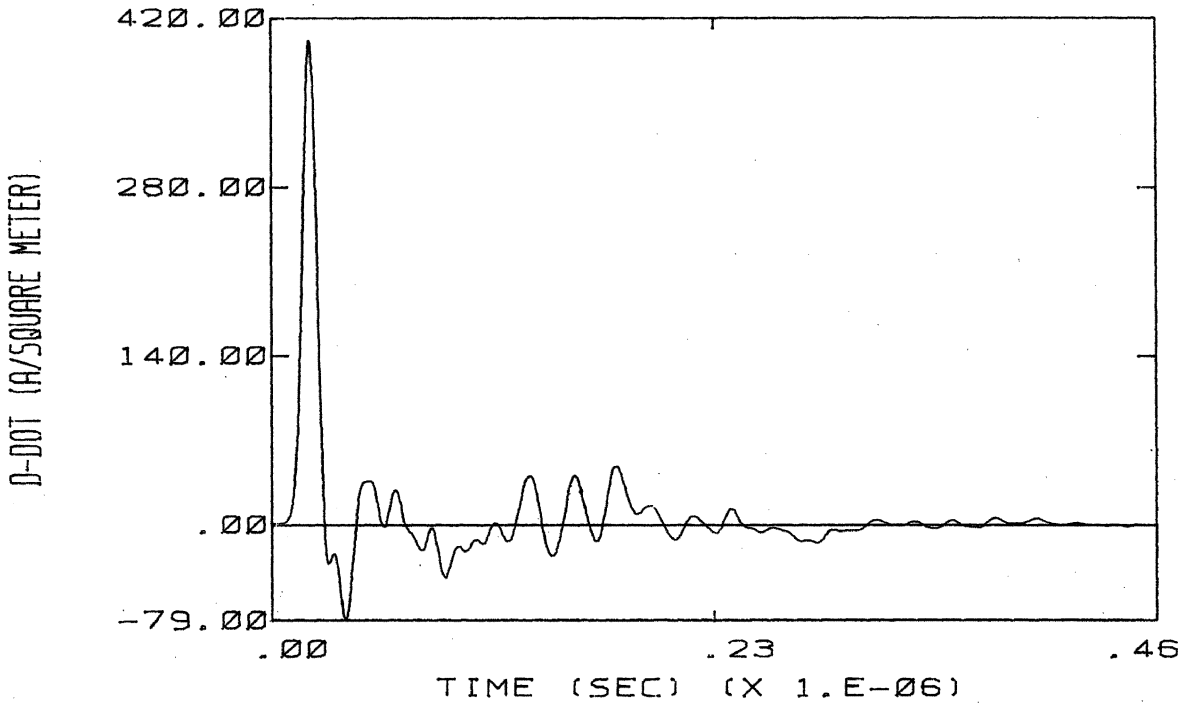

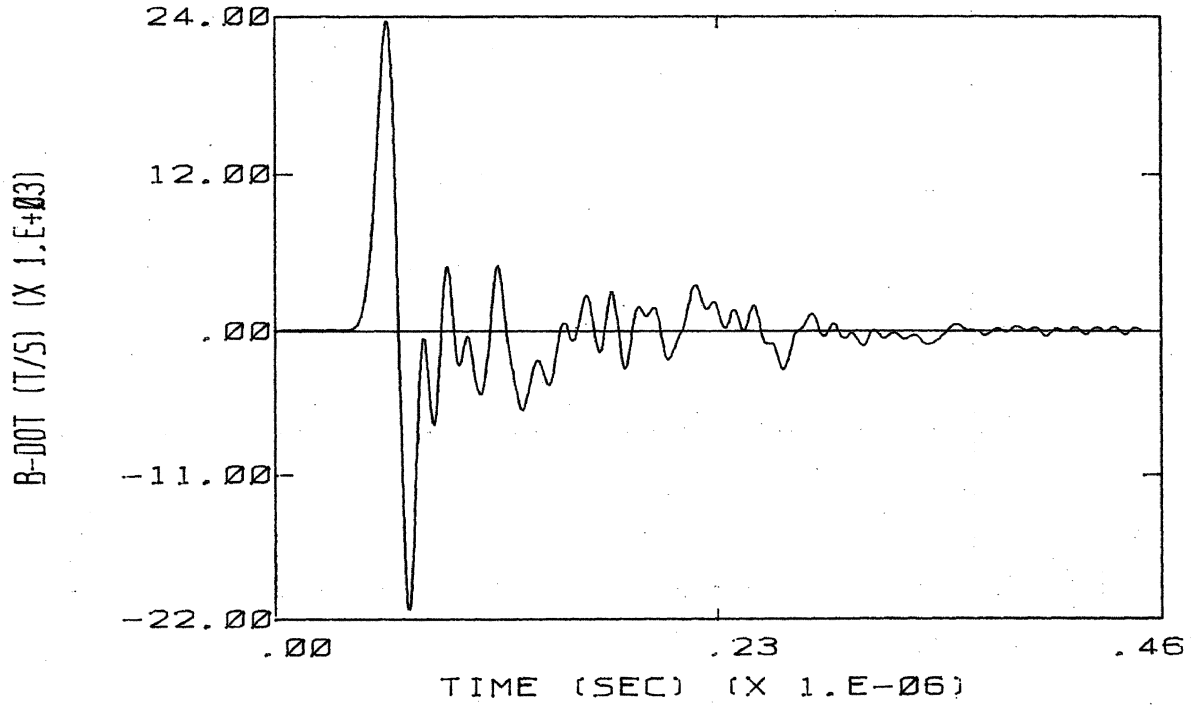

FIGURE 5.13 PREDICTED D-DOT AND B-DOT RESPONSES FOR THE CASE OF ELECTRIC FIELD OF MAGNITUDE 3.E5 V/M ORIENTED NOSE TO TAIL, NO CHARGE ON THE AIRCRAFT, RELATIVE AIR DENSITY OF .5, AND 6% WATER VAPOR CONTENT

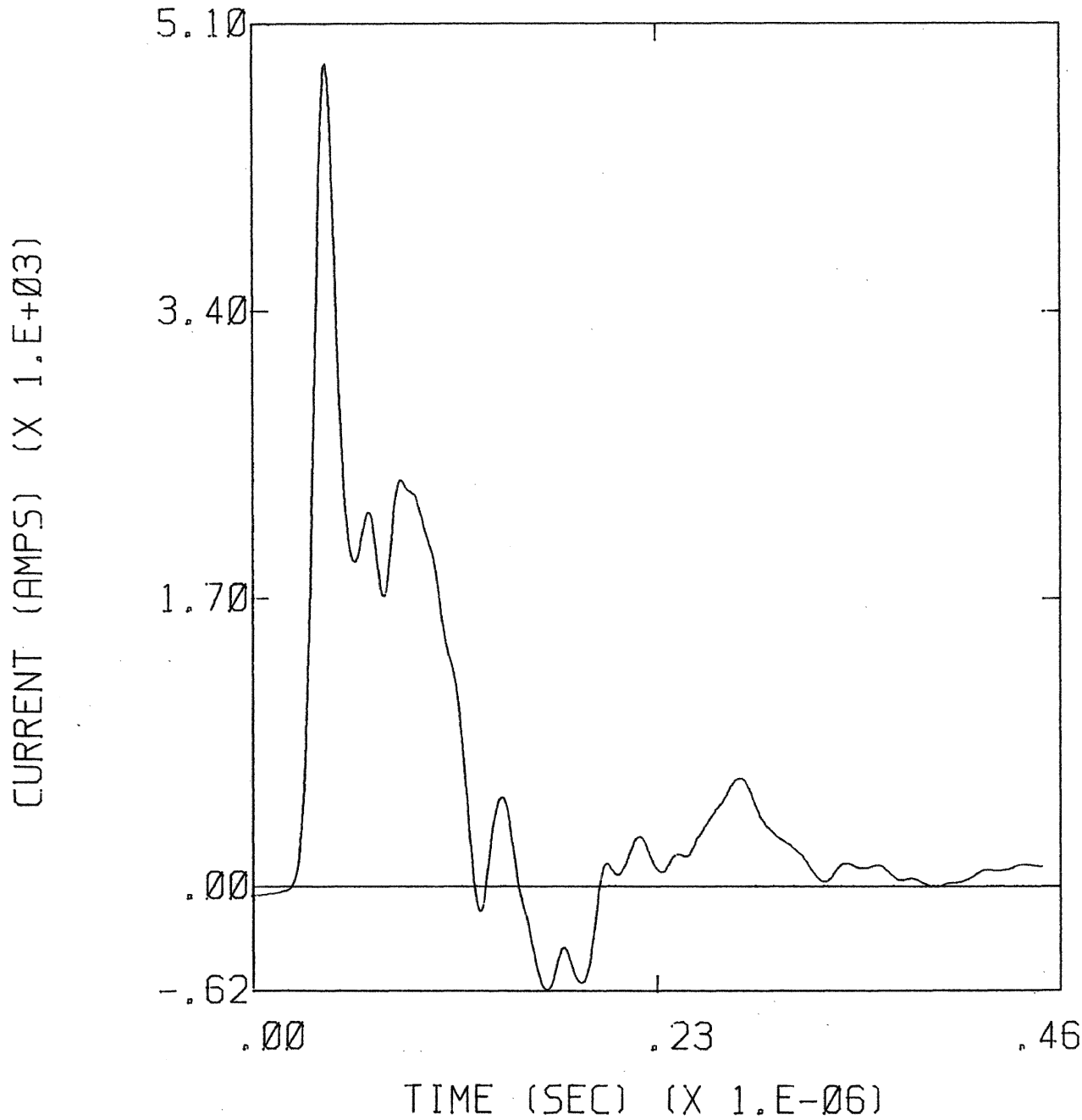

FIGURE 5.14 PREDICTED CURRENT FLOWING ON NOSE FOR THE CASE OF ELECTRIC FIELD OF MAGNITUDE 3.E5 V/M ORIENTED NOSE TO TAIL, NO CHARGE ON THE AIRCRAFT, RELATIVE AIR DENSITY OF .5, AND 6% WATER VAPOR CONTENT

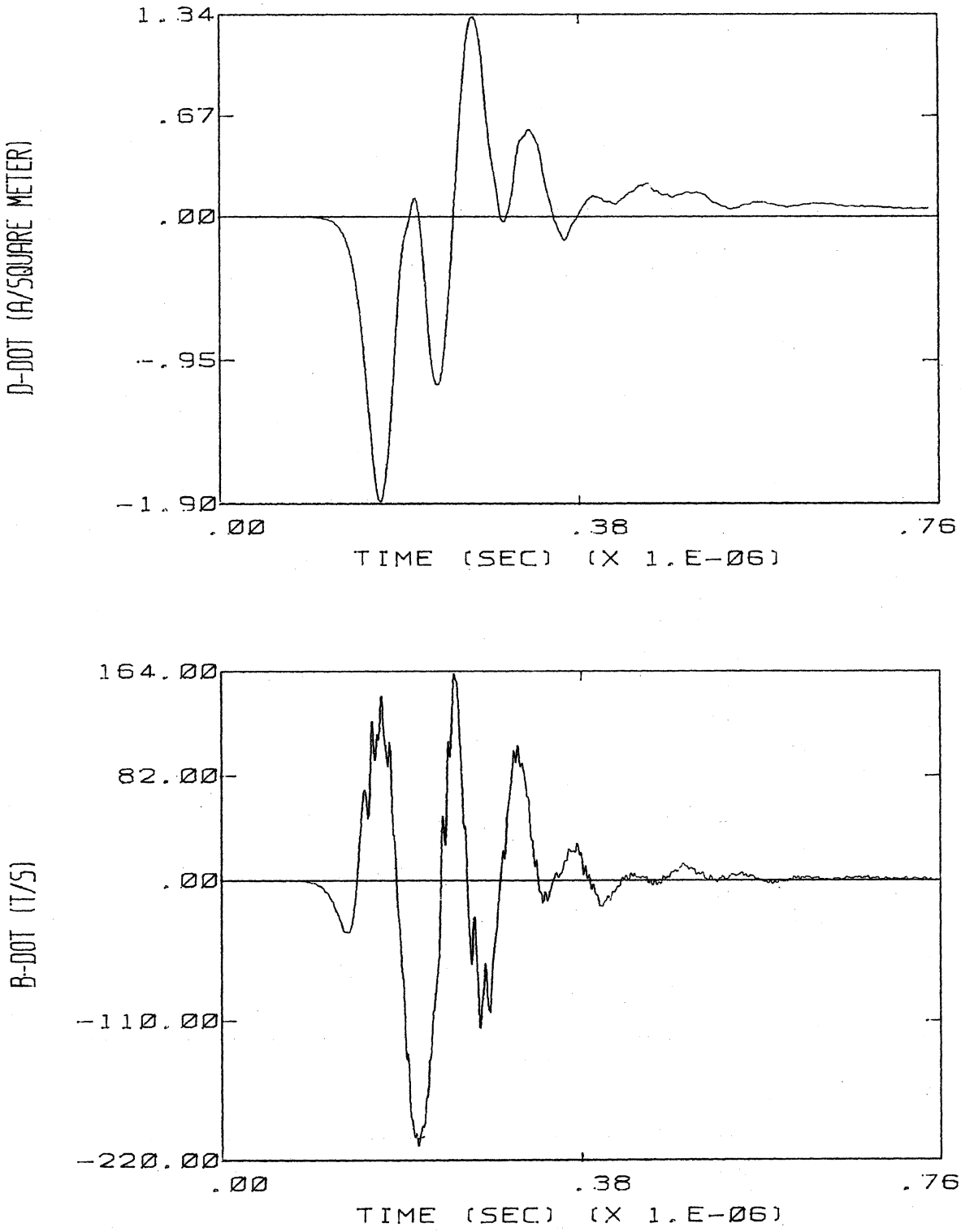

FIGURE 5.15 PREDICTED D-DOT AND B-DOT RESPONSES FOR THE CASE OF ELECTRIC FIELD OF MAGNITUDE 3.E5 V/M ORIENTED RIGHT WING TO LEFT WING, NO CHARGE ON THE AIRCRAFT, RELATIVE AIR DENSITY OF .5, AND 6% WATER VAPOR CONTENT

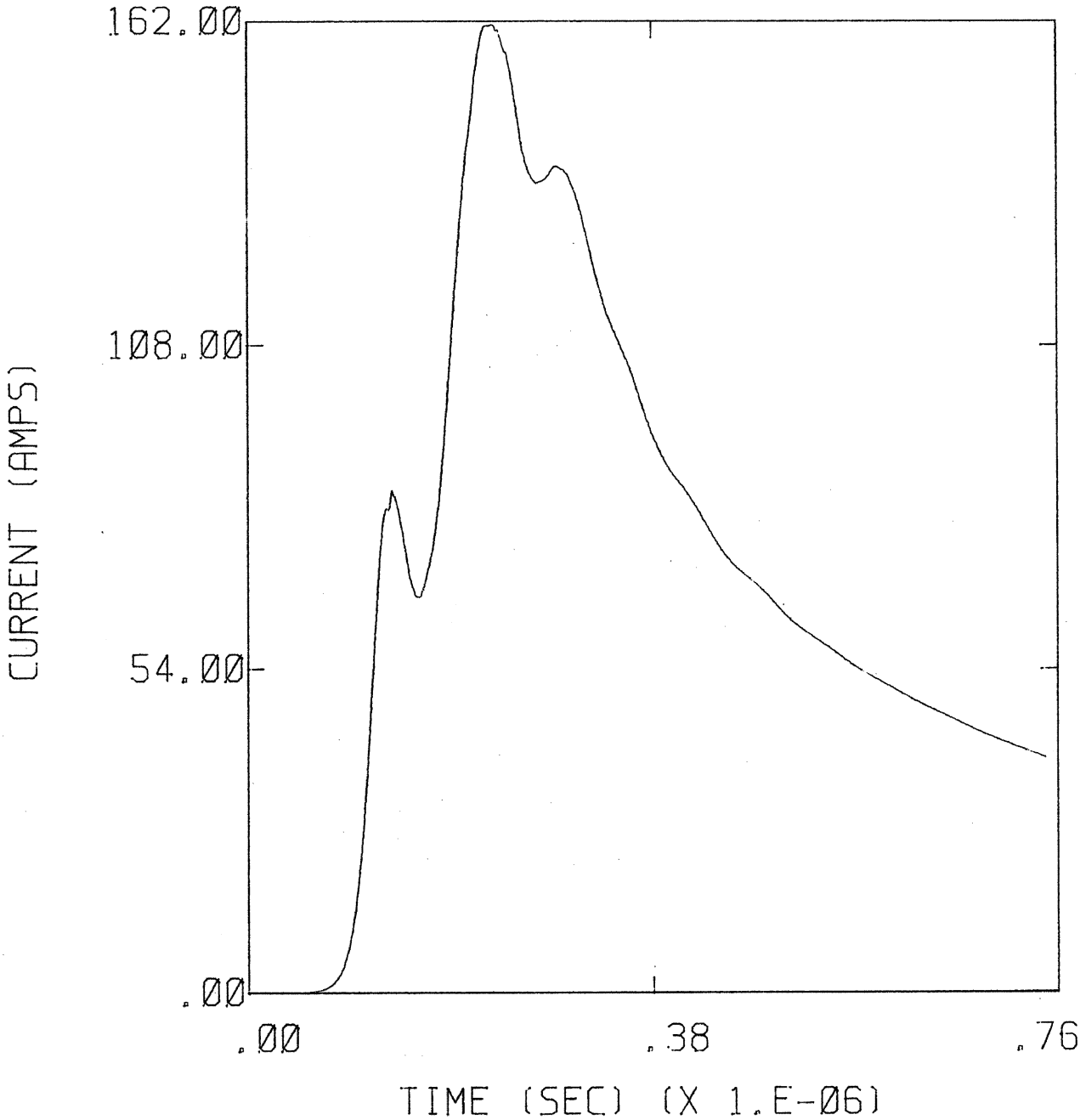

FIGURE 5.16 PREDICTED CURRENT FLOWING ONTO RIGHT WING FOR THE CASE OF ELECTRIC FIELD OF MAGNITUDE 3.E5 V/M ORIENTED RIGHT WING TO LEFT WING, NO CHARGE ON THE AIRCRAFT, RELATIVE AIR DENSITY OF .5, AND 6% WATER VAPOR CONTENT

for the same ambient field level. Hence the ambient field needed to trigger lightning from, for example, the nose of the aircraft may be as much as a factor of two or three lower than that seen in Figures 5.5 to 5.16. This problem will be investigated in more detail when the subgrid (Chapter 7) is incorporated into the nonlinear model.

Figures 5.17 and 5.18 show two of the predicted nonlinear responses from the same run overlaid on a pair of simultaneous D-dot and B-dot records. It is worth mentioning that the nonlinear triggered lightning model is the only model which has been able to even approximately match both the D-dot and B-dot records in amplitude and waveshape. With linear models it has been possible to match one or the other of the measured records exactly, but never both in the same run. This gives credence both to the hypothesis that triggered lightning is responsible for the majority of the measured F106B responses, and to the nonlinear corona model as a vehicle for analyzing the phenomena.

The reader may note that all the currents calculated by the nonlinear model are small, usually less than a kiloamp at peak. This is not only a function of the triggering condition (e.g. electric fields near breakdown intensity), but is also a function of the model. Because the current model cannot follow the formation of a lightning channel, the currents are restricted to levels appropriate to times before channel formation. It is hoped that the more complete model described in the next chapter will correct this shortcoming.

In addition to the triggered lightning calculations for the F106B, one run has been done to investigate the triggered lightning response of the C130 aircraft. Although the C130 is larger than the F106B, it is considerably less streamlined, and therefore has fewer sharp points. Because of this the ambient field needed to trigger on the C130 is larger by almost a factor of two over that on the F106B. Figures 5.19 and 5.20 show the D-dot, B-dot and current responses on the C130 for the case of ambient electric field oriented along the fuselage. Figures 5.21 and 5.22 show the corresponding frequency

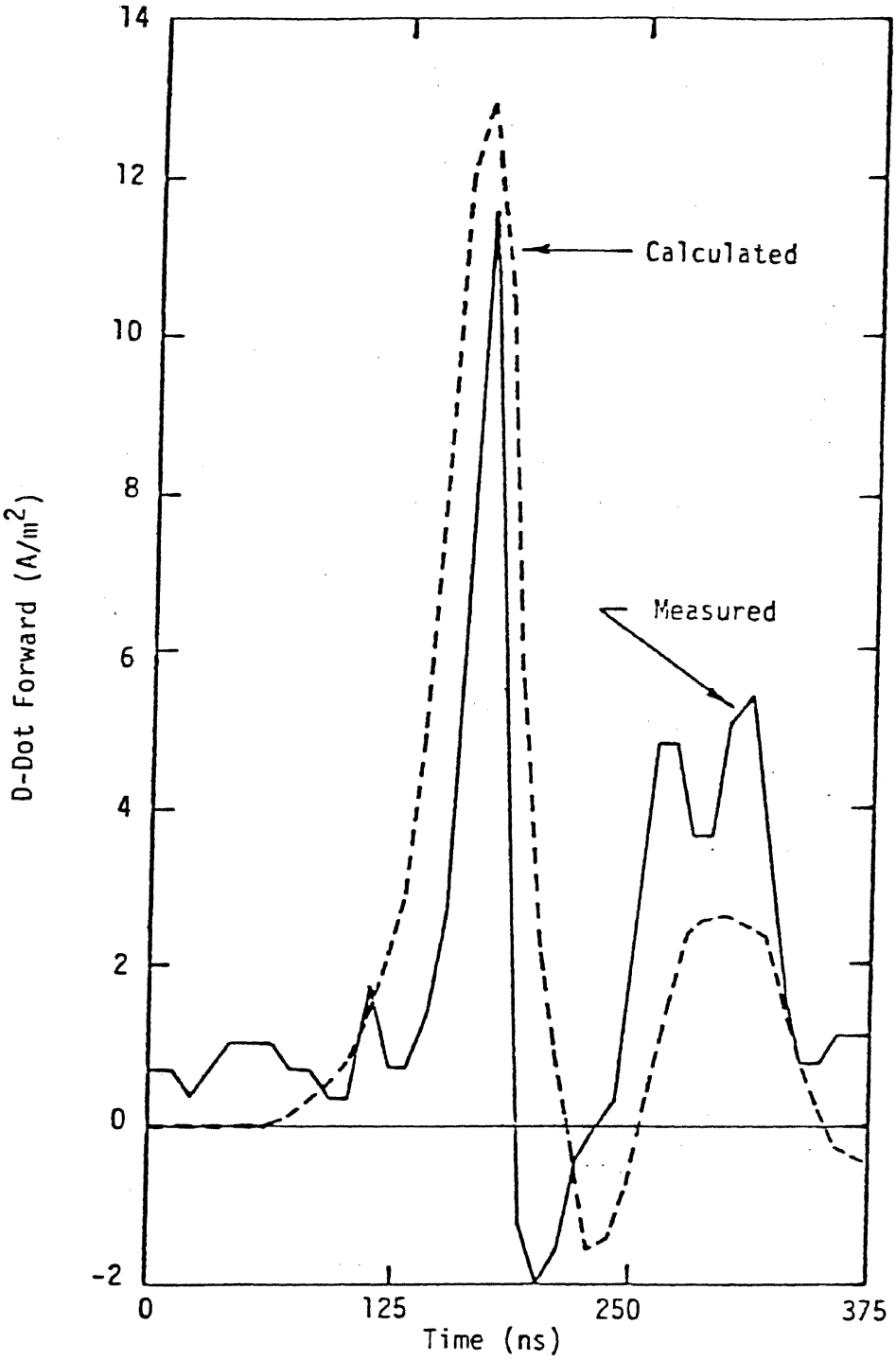

Figure 5.17 Calculated Non-Linear D-Dot Overlaid on Measured D-Dot from Flight 82-042 (Ambient Field 1.9 x 10^5 V/m, Oriented Nose to Tail)

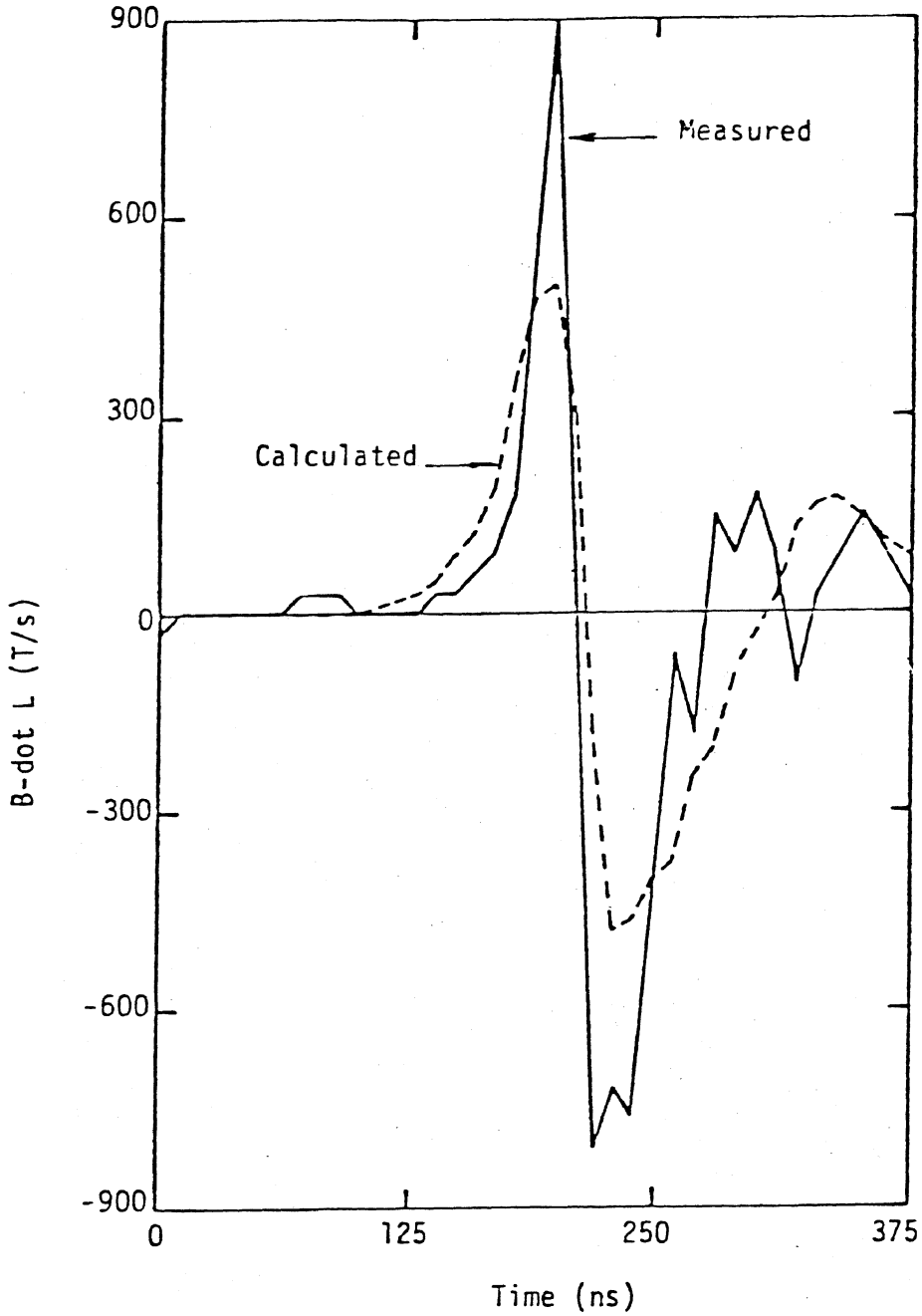

Figure 5.18 Calculated B-Dot Overlaid on Measured B-Dot from Flight 82-042 (Ambient Field 1.9 x 10^5 V/m, Oriented Nose to Tail)

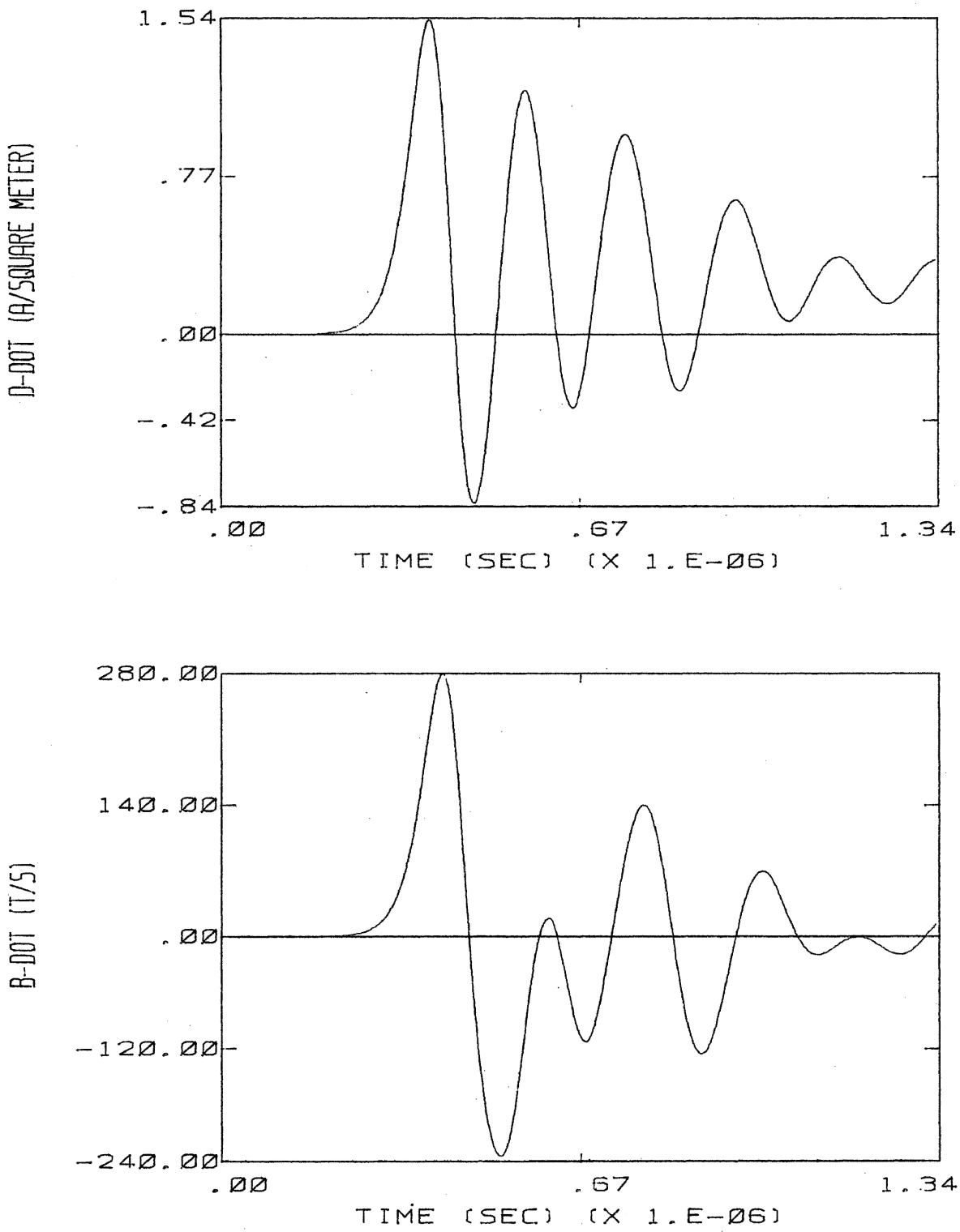

FIGURE 5.19 PREDICTED D-DOT AND B-DOT RESPONSES ON THE C130 AIRCRAFT FOR THE CASE OF ELECTRIC FIELD OF MAGNITUDE 3.E5 V/M ORIENTED NOSE TO TAIL, NO CHARGE ON THE AIRCRAFT, RELATIVE AIR DENSITY OF .5, AND 6% WATER VAPOR CONTENT

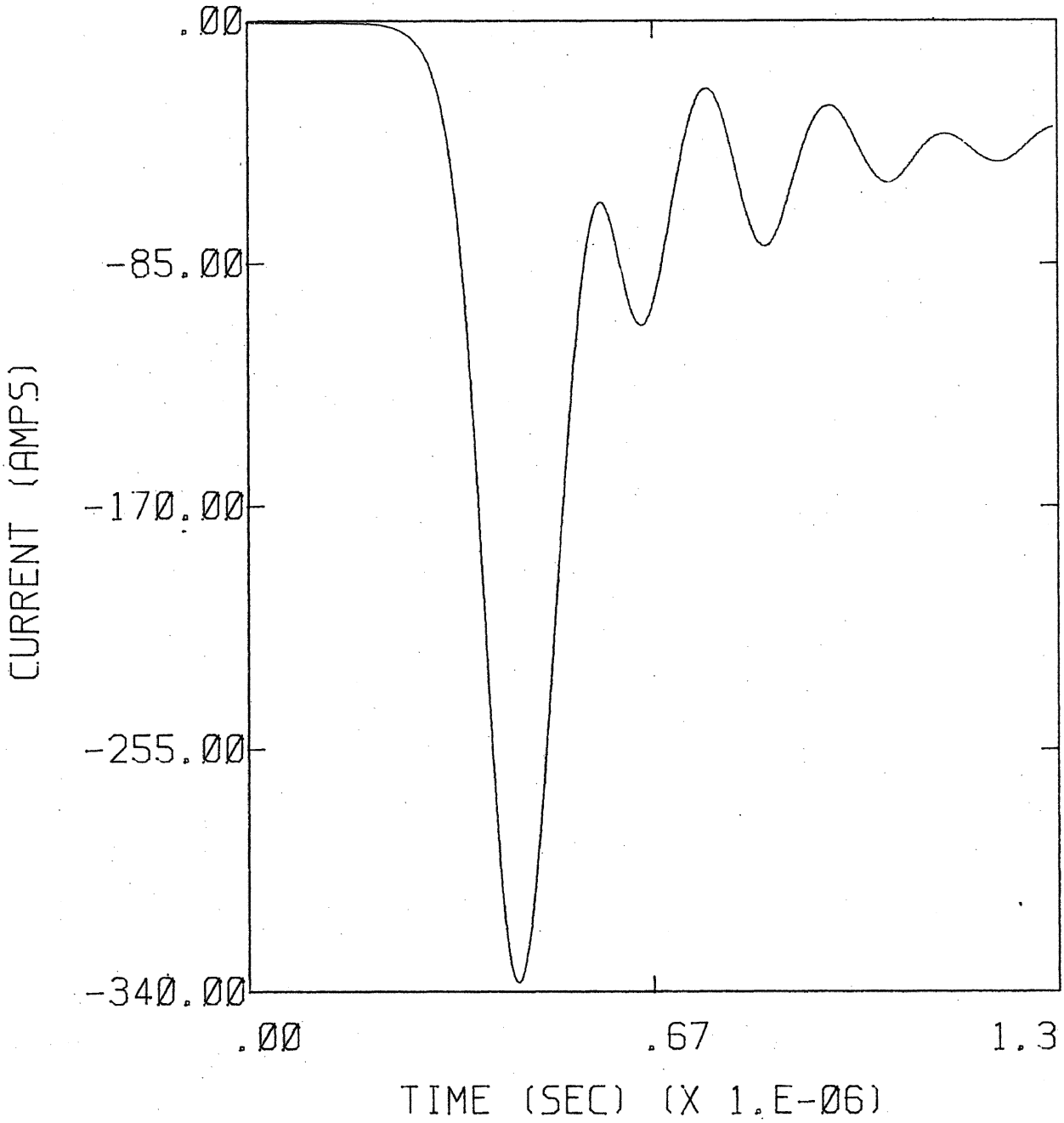

FIGURE 5.20 PREDICTED CURRENT FLOWING ON NOSE ON THE C130 AIRCRAFT FOR THE CASE OF ELECTRIC FIELD OF MAGNITUDE 3.E5 V/M ORIENTED NOSE TO TAIL, NO CHARGE ON THE AIRCRAFT, RELATIVE AIR DENSITY OF .5, AND 6% WATER VAPOR CONTENT

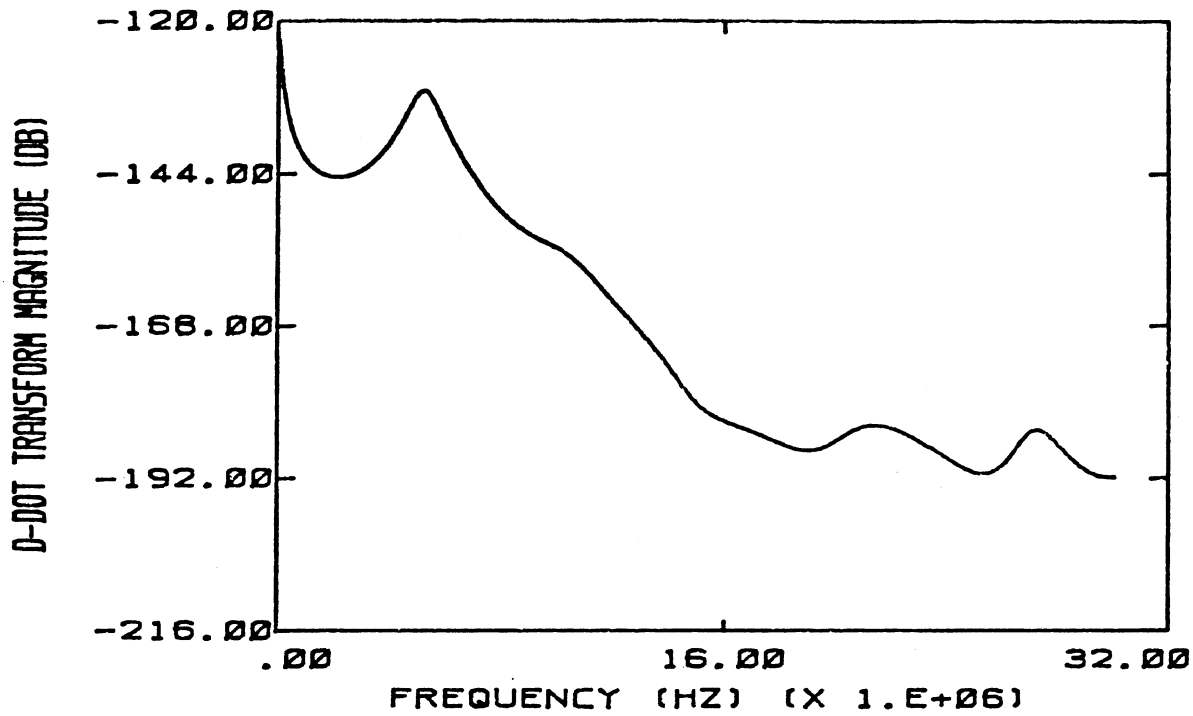

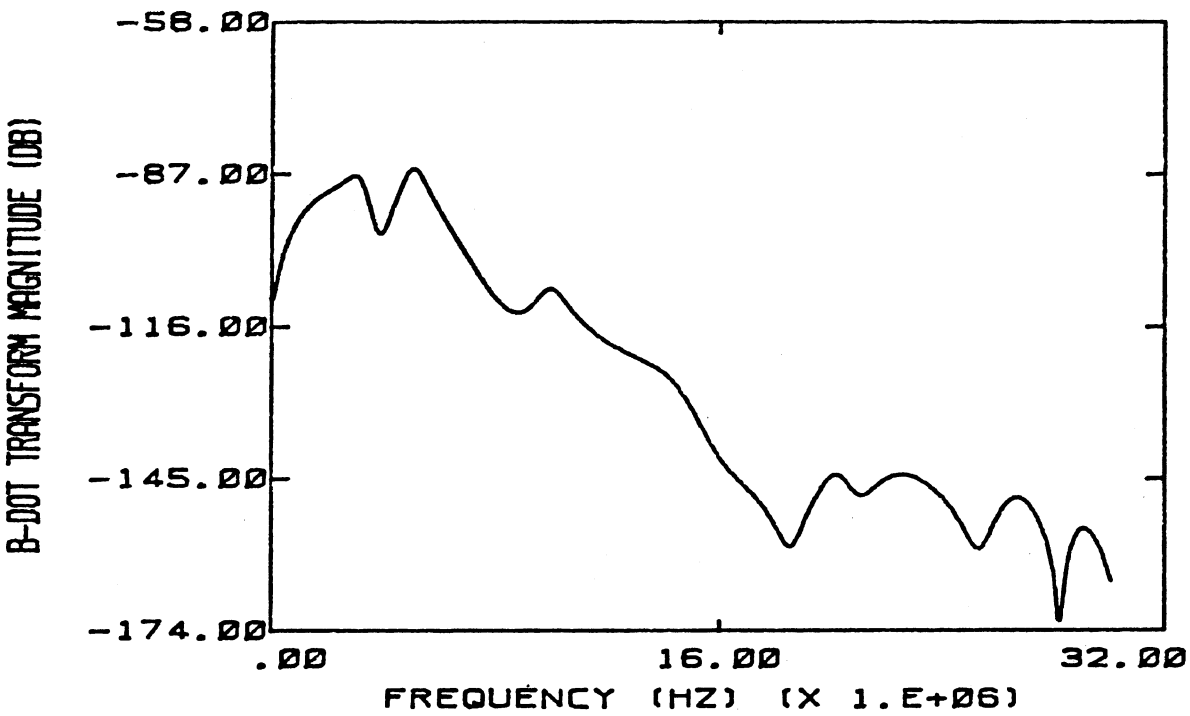

FIGURE 5.21 FOURIER TRANSFORM MAGNITUDES FOR THE D-DOT AND B-DOT RESPONSES SHOWN IN FIGURE 5.19

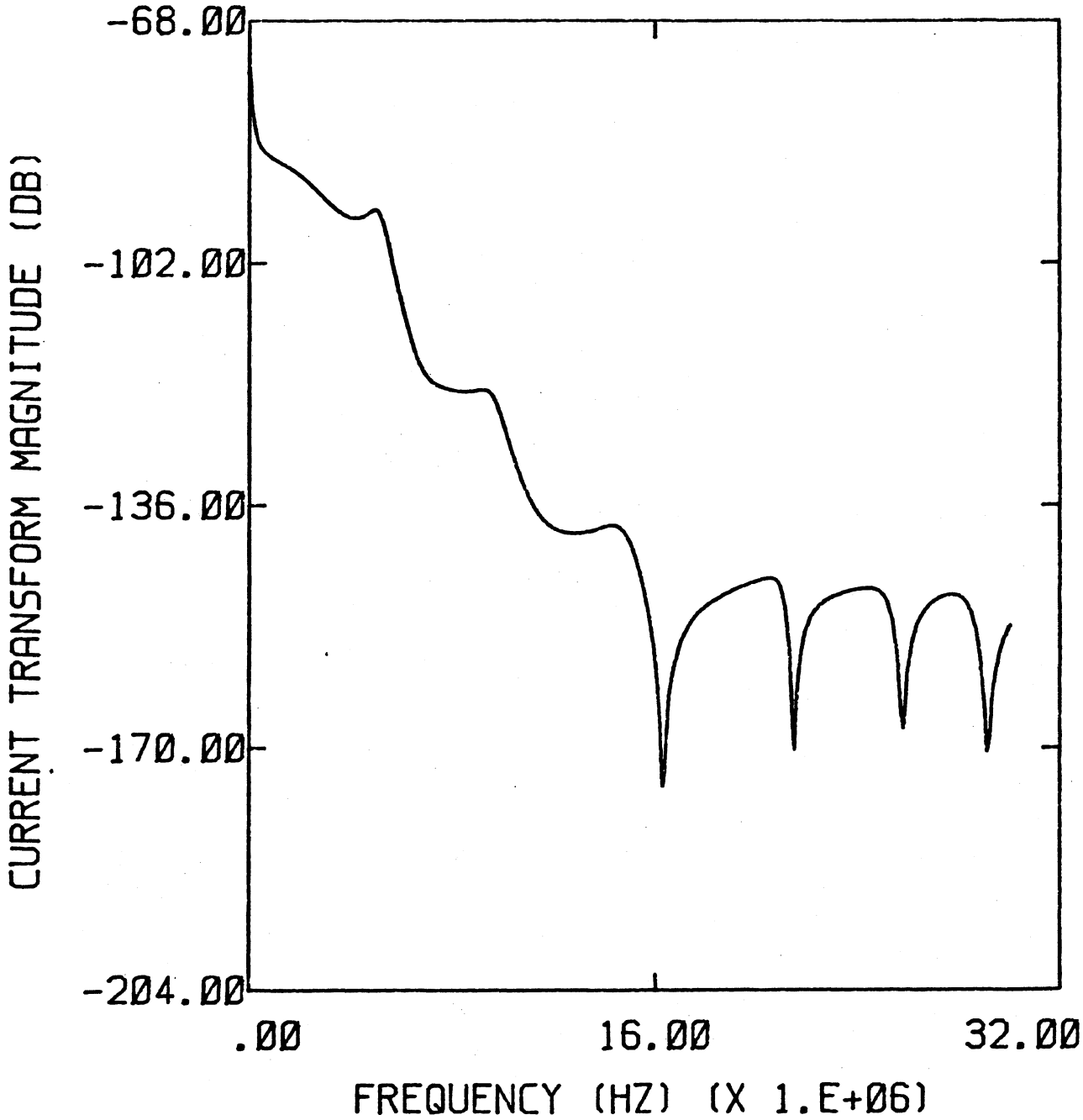

FIGURE 5.22 FOURIER TRANSFORM MAGNITUDE FOR THE CURRENT RESPONSE SHOWN IN FIGURE 5.20

transforms. The responses were calculated on the aircraft in approximately equivalent locations to those on the F106B. The biggest difference from the F106B responses is in the obvious resonant behavior of the C130. This is because the C130's lower frequency resonances are strongly excited by the air breakdown event. The widely variant behavior of the C130 and F106B responses illustrates the necessity of treating each aircraft individually when dealing with triggered lightning. Both the ambient field needed to trigger and the response after air breakdown are a strong function of aircraft geometry.

CHAPTER 6

ENHANCED NONLINEAR MODELING

This chapter reports on an extension to the nonlinear finite difference code which is currently being developed. The extension involves including fluid momentum and energy conservation equations to the particle conservation equations of the previous model. In that previous model heating of the electrons and ions in an air breakdown event was ignored, and organized motion of these charged particles was allowed for by an experimentally determined mobility. This mobility replaced the momentum conservation equation of the current model. Table 6.1 summarizes the major differences between the models. In what follows, the previous model will be referred to as model I and the newly developed model as model II.

Table 6.1 Differences Between Model I and Model II

Physical Quantity	Implementation in Previous Model (I)	Implementation in Current Model (II)
Charged particle number density	Particle conservation equations	Particle conservation equations
Charged particle motion	Mobility	Momentum conservation equations
Particle heating	Ignored	Energy conservation equations

The question naturally arises as to what is gained by using model II rather than model I, especially in view of the fact that model II is significantly larger than model I in terms of computer requirements. There are many more physical quantities to keep track of, and the numerical integration of the momentum and energy equations increases computer run time considerably. The answer is that the newer model is more complete,

providing self-consistent information about drift velocities and particle temperatures. These new predictions make it easier to compare the model to experimental results, where particle temperatures are often measured. The newer model is also more versatile, since it provides a framework for still more complete models, in which more energy and momentum sources and sinks are considered. If desirable, one can add more species of particles to the model by differentiating between the different types of heavy particles. This would allow one to implement more precise ionization, recombination, and excitation rates for each species, rather than an average over the gas as a whole, as is done presently.

Model II, like model I, is a fluid dynamic model, using fluid conservation equations to calculate charged particle densities, motions, and temperatures. The model contains three fluid equations for the electrons: conservation of particles, conservation of momentum, and conservation of energy. The heavy particles are a bit more complicated. There are particle conservation equations for positive and negative ions separately. There is a momentum conservation equation for the positive ions and an energy conservation equation for all the heavy particles together. The reason there are no separate energy equations for the heavy particles is that these particles are very strongly coupled by collisions because of their similar masses, resulting in a very rapid equipartition of energy.

The particle conservation equations for electrons, positive ions, and negative ions are shown below. At present the neutral gas particles are assumed to represent an unchanging background, so no equation is needed for them.

$$\frac{\partial n_e}{\partial t} + \nabla \cdot (n_e \vec{v}_e) = Q + g n_e - \alpha_e n_e - \beta n_e n_+ + k_e$$

$$\frac{\partial n_+}{\partial t} + \nabla \cdot (n_+ \vec{v}_+) = Q + g n_e - \beta n_e n_+ - \gamma n_+ n_- \qquad (6.1)$$

$$\frac{\partial n_-}{\partial t} + \nabla \cdot (n_- \vec{v}_-) = \alpha_e n_e - \gamma n_+ n_-$$

These equations determine the time evolution of the charged particle number densities (n_e, n_+, n_-) at a given point in space. The left hand side of each equation is the total time rate of change of the density at a point and takes into account organized motion of the particles through the convective derivative. The right hand sides represent sources and sinks of particles. Q is the ambient ionization rate from such sources as cosmic rays. gn_e is the ionization rate due to avalanching in the electric field. This provides electrons and positive ions and depends on the strength of the electric field and the air density. $\alpha_e n_e$ represents attachment of electrons to neutral particles to form negative ions. Hence it represents a sink for electrons and a source for negative ions. $\beta n_e n_+$ is the rate of electron positive ion recombination, and $\gamma n_+ n_-$ is negative ion-positive ion recombination. The last term in the electron density equation, k_e, represents diffusion of electrons from one location to another because of a temperature or density gradient.

The details of most of these terms have been documented in previous reports [3,4]. k_e has not been documented before, so a simple derivation of its form will be given here. Consider a surface separating two volumes of fluid with different densities and temperatures as shown in Figure 6.1.

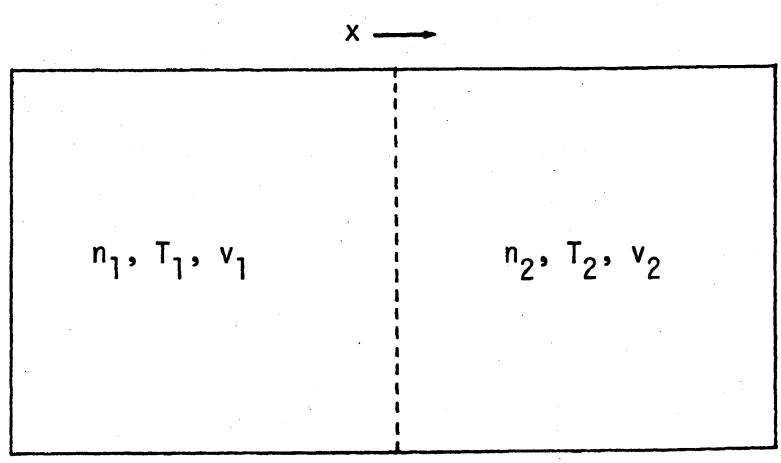

Figure 6.1 Two Equal Volumes of Fluid Separated by a Mathematical Surface for Use in Calculating k_e.

It will be assumed for simplicity that all particles in a given volume are moving at the speed appropriate to that temperature. In reality, of course, there is a distribution of velocities, but this merely complicates the analysis, without contributing to a physical understanding of the process.

The first step in the analysis is to calculate the net flux of particles across the surface. Only the velocities in the x direction need be considered, since the other components do not contribute to the flux. Hence,

$$\begin{aligned} \frac{1}{2} m v_{x_1}^{\ 2} &= \frac{1}{2} kT_1 \\ \frac{1}{2} m v_{x_2}^{\ 2} &= \frac{1}{2} kT_2, \end{aligned} \tag{6.2}$$

where m is the particle mass and k is Boltzman's constant.

$$\begin{aligned} v_{x_1} &= \sqrt{\frac{kT_1}{m}} \\ v_{x_2} &= \sqrt{\frac{kT_2}{m}} \ . \end{aligned} \tag{6.3}$$

To calculate the flux it must be assumed that half of the particles in each volume are moving in the +x direction and half in the -x direction. Then the number of particles crossing the surface per unit area per unit time can be written,

$$F = \frac{1}{2} n_1 \ v_{x_1} - \frac{1}{2} n_2 \ v_{x_2} = \frac{1}{2} \sqrt{\frac{k}{m}} \left(n_1 \sqrt{T_1} - n_2 \sqrt{T_2} \right). \tag{6.4}$$

The change in density per unit time because of this flux can now be written,

$$\frac{\Delta n}{\Delta t} = F \frac{\Delta A}{\Delta V} = \pm \frac{1}{2} \sqrt{\frac{k}{m}} \ \frac{\Delta A}{\Delta V} \left(n_1 \sqrt{T_1} - n_2 \sqrt{T_2} \right), \tag{6.5}$$

where ΔA is the area of the surface, and it has been assumed that $V_1 = V_2 = \Delta V$. The ambiguity in sign refers to the fact that one of the volumes gains density while the other loses density. In differential form Equation

(6.5) can be written,

$$\left.\frac{\partial n_e}{\partial t}\right|_{diffusion} = \pm \frac{1}{2}\sqrt{\frac{k}{m}}\ \frac{\partial}{\partial x}\,(n\ \sqrt{T}). \tag{6.6}$$

This is the desired form for k_e. Note that it depends both on a density and temperature gradient. The effects of each can be separated by expanding the derivative,

$$k_e = \pm \frac{1}{2}\sqrt{\frac{k}{m}}\left(\sqrt{T}\,\frac{\partial n}{\partial x} + \frac{n}{2\sqrt{T}}\ \frac{\partial T}{\partial x}\right). \tag{6.7}$$

Here the first term in parentheses is the effect of a density gradient with uniform temperature, and the second is the effect of a temperature gradient with uniform density. Note that k_e depends on $m^{-1/2}$, and is therefore much more important for electrons than for the heavy particles. That is why Equations (6.1) only include a diffusion term for electrons.

The momentum conservation equations for the three species are shown below.

$$n_\alpha\ \frac{\partial \vec{v}_\alpha}{\partial t} + n_\alpha(\vec{v}_\alpha\cdot\nabla)\vec{v}_\alpha = \frac{n_\alpha q_\alpha}{m_\alpha}\ (\vec{E} + \frac{1}{c}\,\vec{v}_\alpha \times \vec{B}) - \frac{1}{m_\alpha}\,\nabla p_\alpha - n_\alpha\,\vec{v}_\alpha\,\upsilon_c\ . \tag{6.8}$$

Here α refers to species type; electrons or positive ions.

Model II ignores the motion of negative ions, making the assumption that virtually all of the transfer of negative charge is accomplished by electrons. This is especially true during the active early portions of a discharge. Only when the discharge is dying away does negative ion motion become important.

Note that Equation (6.8) is a vector equation, and that the convective derivative on the left hand side couples the different components of $\vec{v}_\alpha$ together. This term is an additional source of nonlinearity in the problem, beyond the introduction of electric field dependent conductivity.

The left hand side of Equation (6.8) is the total rate of change of the fluid momentum per unit mass, including that due to organized particle flow. The first term on the right is the force per unit mass exerted

on the fluid by the electric and magnetic fields. Because of the factor v_α/c, where c is the speed of light in a vacuum, the magnetic force term is expected to be much smaller than the electric force term. The second term on the right represents the force per unit mass exerted on the fluid by the partial pressure gradient. The force is directed from high pressure regions to low pressure regions, thus tending to equalize the pressure. The third term on the right is the force per unit mass exerted on the fluid because of collisions. At the present time only collisions with neutral particles are considered because of the low level of ionization, and the collision frequency is assumed to be a constant. These approximations can be improved in the future if results warrant. The force due to collisions is always oriented opposite to the direction of the velocity. Hence the drift velocity ($\vec{v}_\alpha$ in steady state) is usually a balance between the driving force of the electric field and the damping of the collisions. A crude approximation to $\vec{v}_\alpha^{\,drift}$ is found to be,

$$\vec{v}_\alpha^{\,drift} = \frac{q_\alpha}{m_\alpha \upsilon_c} \vec{E} . \qquad (6.9)$$

Note that in model I a mobility was defined such that $\vec{v}_\alpha^{\,drift} = u_\alpha \vec{E}$. Then Equation (6.9) implies that an approximation to u_α is $\frac{q_\alpha}{m_\alpha \upsilon_c}$. This approximation can also help to fix υ_c if u_α is known.

The energy conservation equations are the most complex of the fluid equations used in model II. At present there are only two, one for electrons and one for heavy particles, but it may be necessary to include more eventually. Energy reservoirs that may need to be considered are vibrational and rotational states of molecules, and excited states of molecules, atoms, and ions. These states can take energy from particle motion, retain it for some period of time, and then release it as kinetic or electromagnetic energy. The present model II only begins to account for these effects.

The present energy balance equations are shown in Equations (6.10). As was stated earlier, the reason the heavy particles are all lumped together in one equation is that they are strongly coupled by

collisions, resulting in rapid equipartition of energy. In an electron-heavy particle collision, the electron retains most of its energy, hence electrons may have a different temperature than the heavy particles. However, when two heavy particles collide, a large fraction of the kinetic energy available can be transferred. Therefore, equipartition of energy occurs in at most a few collision times. This is much less than the time step used for model II, so the heavy particles can all be considered to have the same temperature, and one energy balance equation used for all.

$$\frac{\partial \varepsilon_e}{\partial t} + (\vec{v}_e \cdot \nabla)\, \varepsilon_e = q_e n_e \vec{E} \cdot \vec{v}_e - \frac{m_e}{m_H} \upsilon_c (\varepsilon_e - \varepsilon_e^{\,o}) + g n_e \left(\frac{1}{2} m_e v_+^{\,2} - \varepsilon_{ion}\right)$$

$$+ \varepsilon_Q - \alpha_e \varepsilon_e - \beta n_+ \varepsilon_e + H_e - k_{excitation} \tag{6.10}$$

$$\frac{\partial \varepsilon_H}{\partial t} + (\vec{v}_+ \cdot \nabla)\, \varepsilon_H = q_+ (n_+ + n_-) \vec{E} \cdot \vec{v}_+ + \frac{m_e}{m_H} \upsilon_c (\varepsilon_e - \varepsilon_e^{\,o})$$

$$- \frac{1}{2} g m_e n_e v_+^{\,2} + k_{excitation}.$$

Each of the terms in the above two equations will now be discussed individually, with the approximations used in each indicated.

The left hand side of each equation is the total rate of change of the energy density of the species. This includes changes due to organized flow of the particles, through the convective derivative term. The energy density is defined as the sum of the energy densities included in organized motion (particle flow) and internal energy (temperature). Note that the heavy particle equation uses the velocity of the positive ions, $\vec{v}_+$, in the convective derivative and throughout the rest of the equation. This is done because the positive ions appear in the early stages of air breakdown, before the electrons are able to attach to neutrals to form the negative ions. Hence it is necessary to use $\vec{v}_+$ in the first part of a discharge, and the approximation is made that this is the flow velocity of the heavy fluid at all times.

The first term on the right in the electron equation, $q_e n_e \vec{E} \cdot \vec{v}_e$ is the energy density transferred to the electron fluid per unit time by the action of the electric field on the electrons. Because $\vec{v}_e$ is nearly

always oppositely directed to $\vec{E}$, and q_e is negative, it is generally the case that energy flow is from the field to the electrons. However, it is at least mathematically possible (with large pressure gradients, for instance) for $\vec{v}_e$ to be in the same direction as $\vec{E}$, in which case energy is transferred from the electron fluid to the field. It may be noted here that the magnetic field makes no contribution to the energy density because of the nature of the force. The energy transferred from the magnetic field contains a term of the form $(\vec{v}_e \times \vec{B}) \cdot \vec{v}_e$ which is, of course, identically zero.

The second term on the right of the electron equation, $\frac{m_e}{m_H} \upsilon_c (\varepsilon_e - \varepsilon_e^o)$ represents energy transfer from the electrons to the heavy fluid because of collisions. These are electron-neutral collisions in general since the degree of ionization is assumed to be quite low, at least initially. In this term υ_c is the collision frequency, and ε_e^o is the ambient electron energy density. ε_e^o is a lower limit for the electron energy density, below which ε_e is not allowed to drop. Note that the energy transfer due to collisions is proportional to the electron energy, the collision frequency, and the ratio of the masses. The latter proportionality comes about because of the dynamics of a single electron-heavy particle collision. Less energy is transferred as the ratio of the masses becomes smaller. An approximation is made in this term that all heavy particles can be assigned some average mass, m_H.

The third term on the right, $gn_e \left(\frac{1}{2} m_e v_+^2 - \varepsilon_{ion}\right)$, represents the energy gained (or lost) by the electron fluid because of avalanching. In avalanching, electrons are liberated from neutral particles by collisions between the neutrals and energetic electrons. The energetic electron loses an amount of energy equal to the ionization potential of the neutral, ε_{ion}, and it is assumed that the new electron is born with a kinetic energy appropriate to the motion of the heavy fluid. Both of these energies are approximations, as in reality, a statistical distribution is to be expected in the energetics of ionizing collisions.

ε_Q represents the energy gained by the electron fluid because of the ambient ionization rate. This may be an energy over and above that added simply by the liberation of an electron. For instance, cosmic ray ionization may result in an electron released with a large amount of kinetic energy,

which is eventually distributed throughout the electron and heavy particle fluids.

The next two terms in the electron equation, $\alpha_e \varepsilon_e$ and $\beta n_+ \varepsilon_e$, represent the energy lost to the electrons because of attachment to neutral particles and because of electron-positive ion recombination. Both of these processes are assumed here to be a simple loss of the total energy of the electron engaged in the process. That is, for example, in the case of an attachment, the energy of the electron involved is assumed to be released in the form of a photon, which is then lost from the gas. That is not necessarily the case, because the energy may be transferred to heavy particle kinetic energy or stored in an excited state of the heavy particle. The probability of these processes may be explored in future enhancements to model II.

The term H_e in the electron equation is not a source or sink term as such but represents a transfer of energy from location to location analogous to the k_e term in the particle conservation equations. Its form is similar to the form derived there. The term is nonzero only in the presence of temperature or density gradients.

$k_{excitation}$ represents a process which has not yet been included in model II, but is felt to be essential to its proper functioning, and will be added shortly. The process is excitation of vibrational modes of molecules in the gas by electron collisions. The vibrational modes eventually decay into kinetic energy of the molecules, hence providing a significant path for energy transfer from electron to heavy particle kinetic energy. Direct collisions cannot accomplish this because of the great disparity in mass of the two types of particles. In results to be presented later it is seen that calculated electron temperatures are quite a lot higher than is seen experimentally. This occurs because in the present model II the electron fluid has no efficient way to transfer its internal energy to the heavy fluid. The addition of $k_{excitation}$ to the model will remedy this and hold down the electron temperature. The actual form to be used for $k_{excitation}$ is yet to be developed. Initially, at least, it is expected that the transfer of energy through the vibrational modes will be instantaneous, with no energy stored in the modes. This may be changed to

allow some time delay from excitation of the modes to deexcitation if this is found to be necessary.

On the right hand side of the heavy particle energy equation, it can be seen that many of the same terms as in the electron equation are present. The only new term is the first on the right hand side, $q_+ (n_+ + n_-) \vec{E} \cdot \vec{v}_+$. This represents the energy provided to the heavy particles by interaction with the electric field. Notice that this includes the contributions from both positive and negative ions. Strictly speaking, the contribution from the negative ions should be written $q_- n_- \vec{E} \cdot \vec{v}_-$, but if $|\vec{v}_-| \approx |\vec{v}_+|$, and $q_+ = -q_-$, the form shown in Equations (6.10) is very nearly correct.

Equations (6.10) are a simplification of the actual energy balance in an electrical discharge. As stated earlier, there are many other processes and energy reservoirs that could be included in model II. Some of these include energy stored in vibrational molecular states, excited atomic and molecular states, and a photon fluid arising from the statistical decay of excited states and recombinations. These have not been modeled at the present time in order to keep the model as simple as possible. They can be added in the future if it becomes necessary.

Figure 6.2 shows the physical situation to which model II has been applied. This is similar to the experimental setup of Collins and Meek [7] which has been investigated in previous reports [3,4]. However, the apparatus of Collins and Meek was significantly larger in the radial dimension. A smaller problem space has been used here because of run time considerations.

The problem space shown in Figure 6.2 was gridded with a spatial resolution of one centimeter in both the radial and axial directions. The time resolution was 20 picoseconds. The source was a voltage of 7×10^5 volts applied across the plates having the form of a step function with a risetime of 100 nanoseconds. Air parameters chosen are shown in Table 6.2. These are intended to be representative rather than exact values. For example, the mass of the heavy particles in air is not well defined, so the

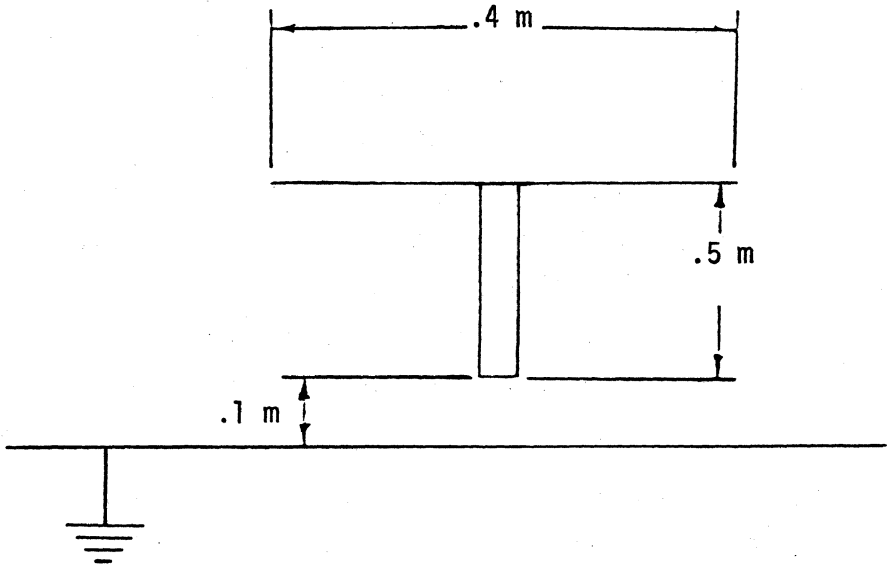

Figure 6.2 Schematic of Problem Space Modeled by Enhanced Nonlinear Air Chemistry Code

Table 6.2 Parameter Values Chosen for Model II Results

Relative air density = 1.

Percentage water content = 6.

Collision frequency = 1×10^{13} sec^{-1}.

Heavy particle mass = 2.34×10^{-26} kg.

Ionization energy = 2.4×10^{-18} joules.

Ambient temperature = $300^{o}k$.

Ambient neutral particle density = 1×10^{24} m^{-3}.

mass chosen is intended to be in some sense an average value.

The results from model II are shown in Figures 6.3 to 6.9. In Figure 6.3 is presented the electric field behavior at the tip of the rod. The reader will note that the field at breakdown drops essentially to zero and then rises again at a later time. The second rise occurs because of the constant voltage source across the plates. After the initial breakdown, the electrons which provide the local conductivity begin to attach to neutrals to form negative ions and also to recombine with positive ions. This drastically lowers the conductivity and allows the voltage source to put energy back into the electric field.

Figures 6.4 and 6.5 show the radial and axial electron velocities, respectively, near the tip of the rod. Note that these drop to zero as the electric field disappears. Figure 6.6 shows the electron temperature. This figure is somewhat deceptive, as the temperature is large at times when the electron density is small. The temperature is not really a significant quantity when there are only a few electrons present. Nevertheless, the predicted electron temperature is too high, and it is expected that the inclusion of the $k_{excitation}$ term in the electron and heavy particle energy equations will hold the value within acceptable limits.

Figure 6.7 shows the electron density at the tip of the rod. Notice the growth due to avalanching and the almost equally rapid decay because of attachment. The positive ion density is shown in Figure 6.8. Here again the growth is because of avalanching. However, the decay is from recombinations, a much slower process than attachment, so the positive ion density stays high. Figure 6.9 shows the heavy particle temperature, which is virtually unchanged from the ambient value. This is another indication that $k_{excitation}$ is needed in the energy equations to transfer energy from the electrons to the heavy particles.

Future plans for model II include a study to determine which terms are most important in the conservation equations. This will possibly allow a reduction in size of the final version. The model must also be checked in as many experimental situations as possible to increase confidence in its validity. Finally, it would be desirable if model II could in some way be

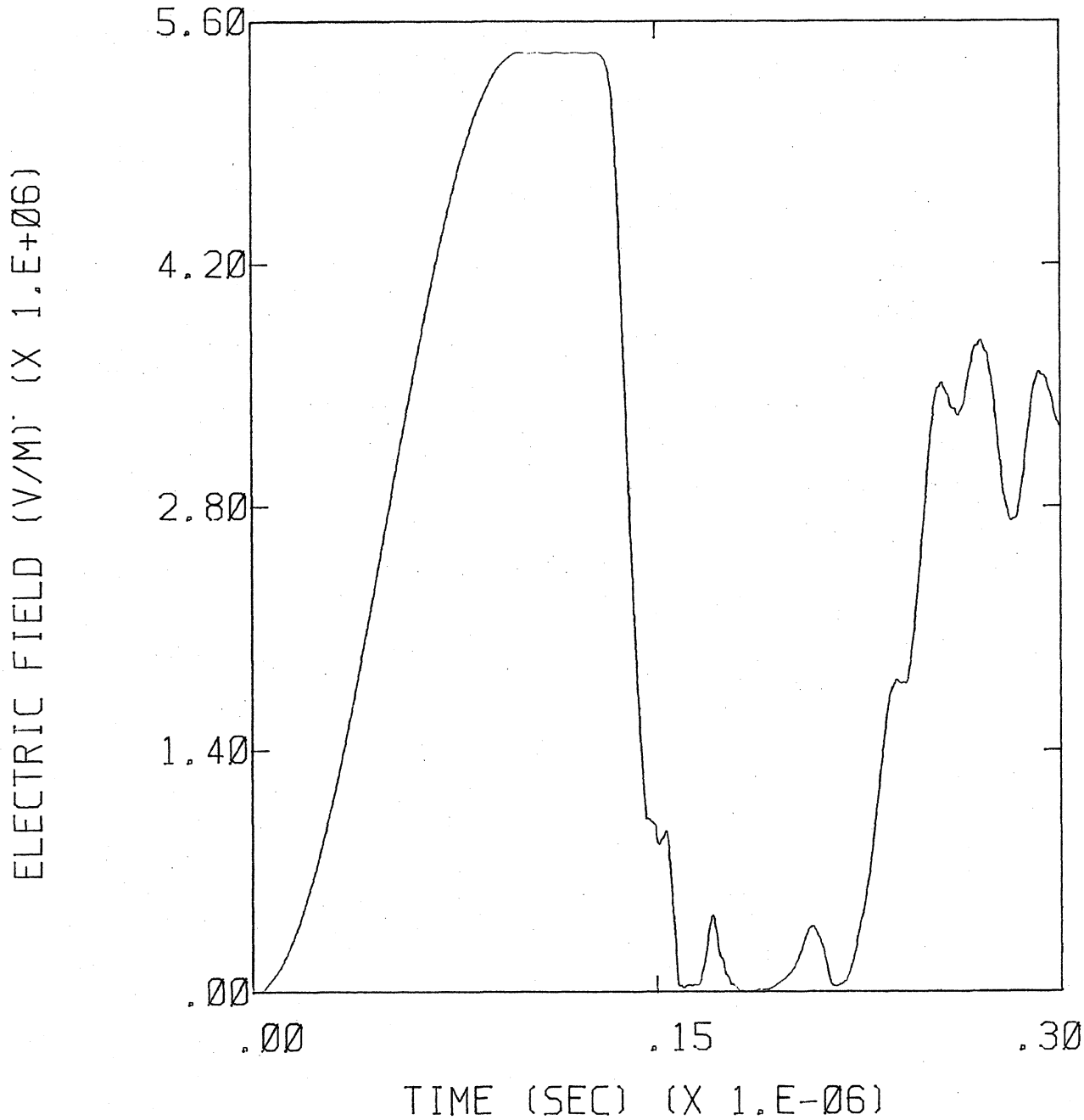

FIGURE 6.3 AXIAL ELECTRIC FIELD BEHAVIOR AT THE TIP OF THE ROD

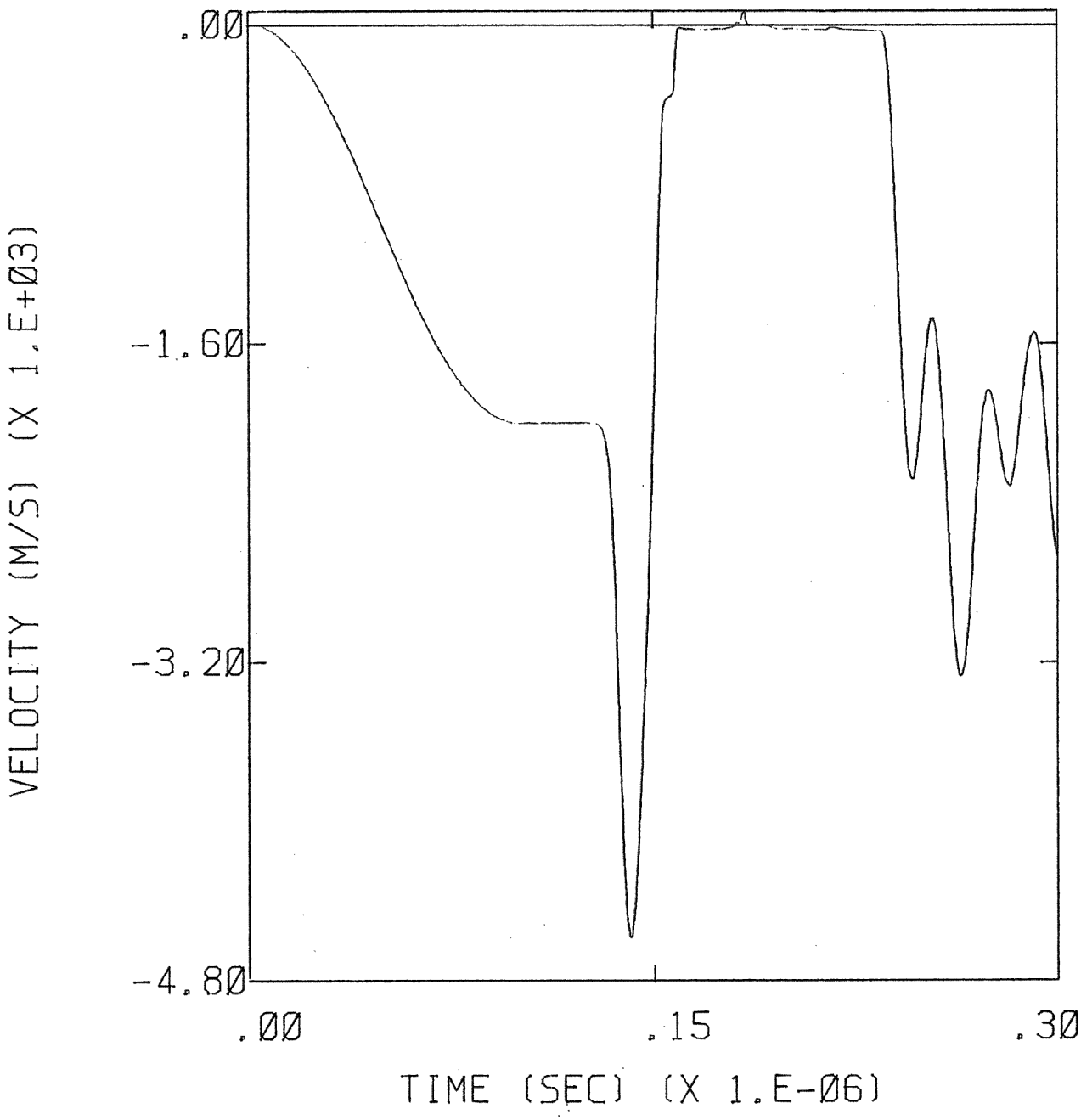

FIGURE 6.4 THE ELECTRON FLUID RADIAL VELOCITY NEAR THE TIP OF THE ROD

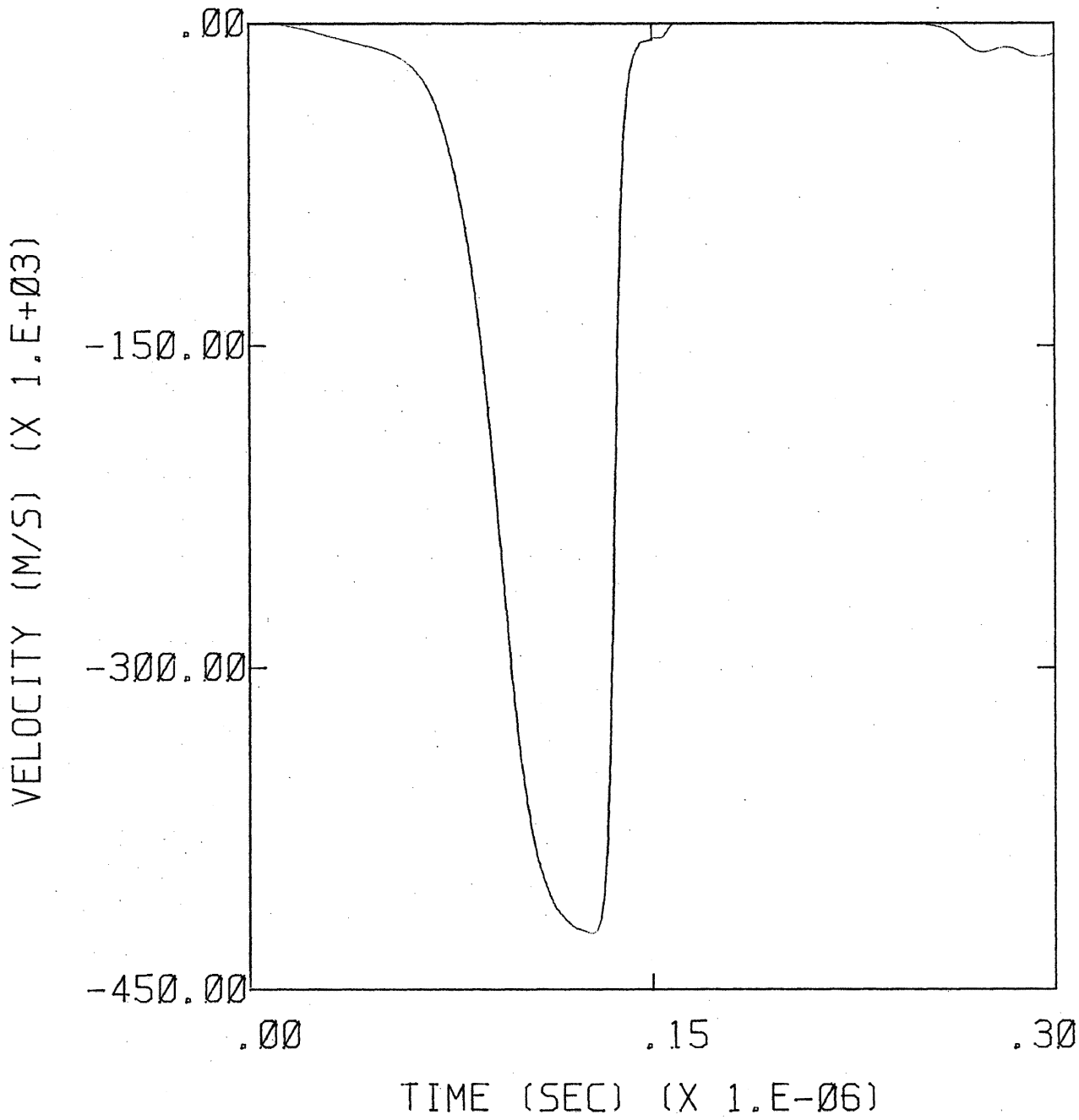

FIGURE 6.5 THE ELECTRON FLUID AXIAL VELOCITY NEAR THE TIP OF THE ROD

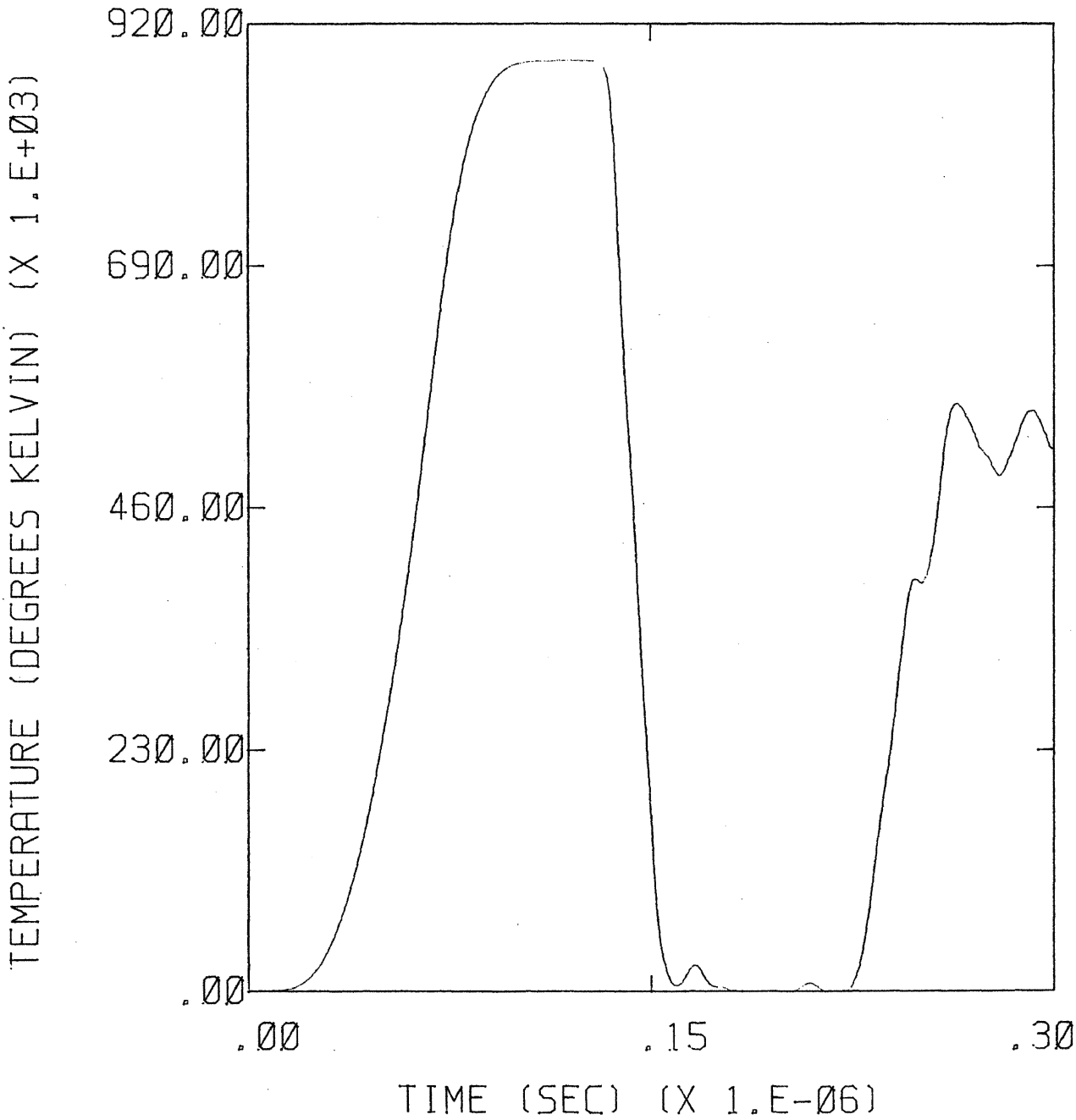

FIGURE 6.6 TEMPERATURE OF THE ELECTRON FLUID NEAR THE TIP OF THE ROD

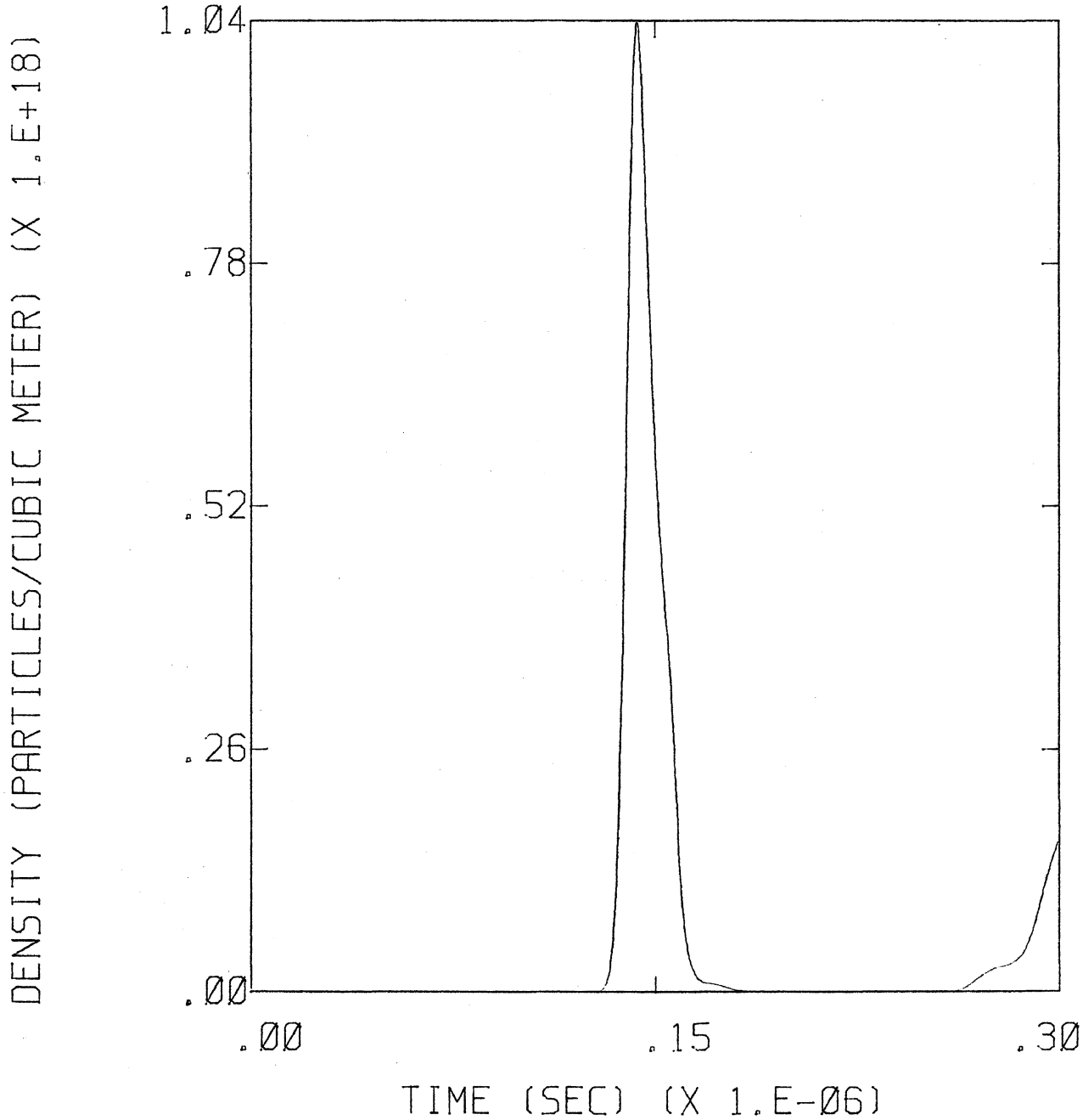

FIGURE 6.7 NUMBER DENSITY OF ELECTRONS NEAR THE TIP OF THE ROD

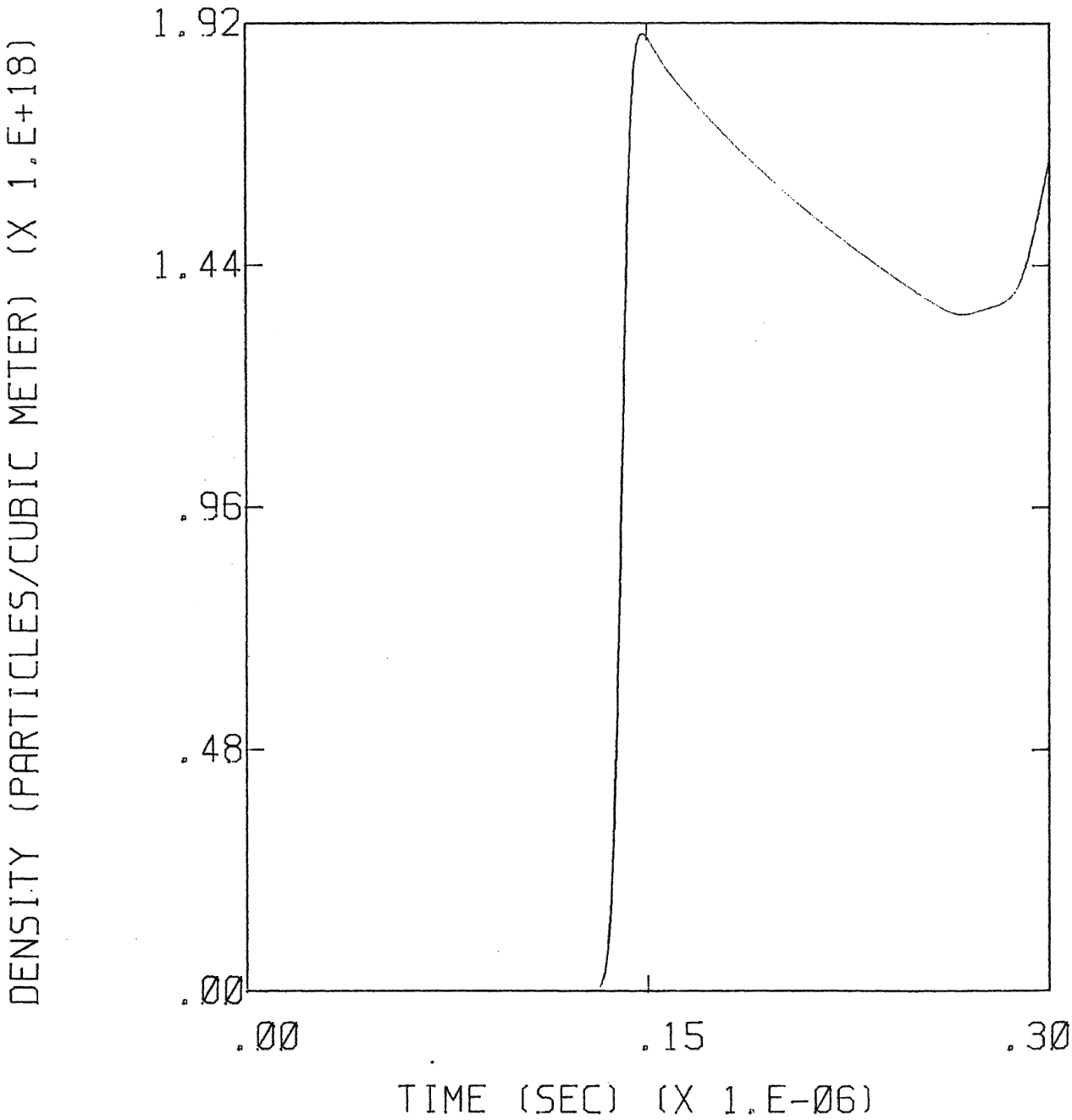

FIGURE 6.8 NUMBER DENSITY OF POSITIVE IONS NEAR THE TIP OF THE ROD

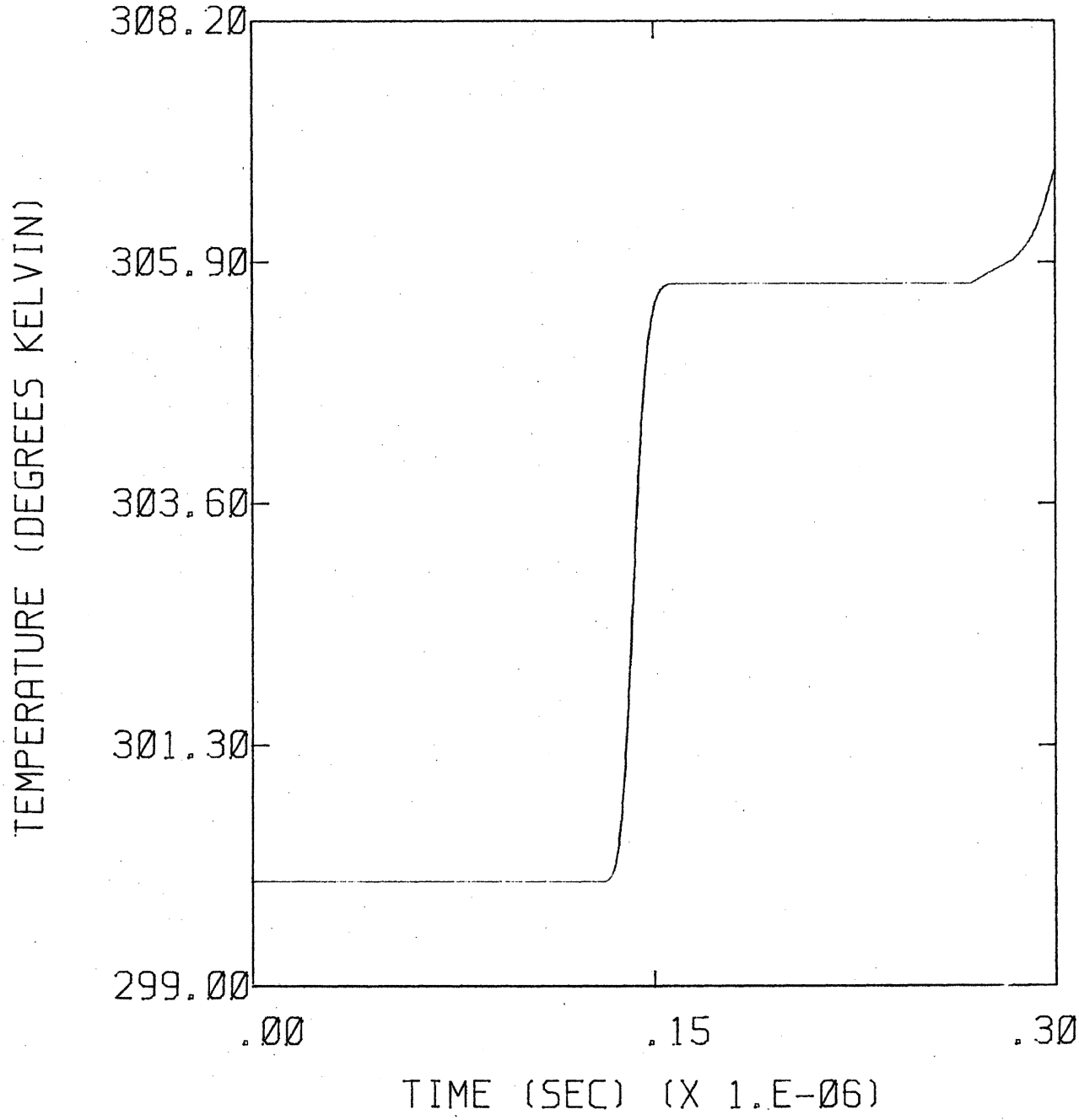

FIGURE 6.9 TEMPERATURE OF THE HEAVY PARTICLE FLUID NEAR THE TIP OF THE ROD

incorporated into the three dimensional code containing the F1O6B. There are two possibilities for accomplishing this. The first depends on the final size of model II. If it is small enough, the model can be made three dimensional and incorporated directly into the nonlinear finite code. In this case it may be that only selected regions (nose, wing tips, etc.) would be considered for nonlinearities. The second possibility concerns interfacing the present two dimensional model II with the three dimensional code. This could only be done around regions of the F1O6B which exhibit two dimensional symmetry, such as the nose. Details of how the interface would work are not yet available.

CHAPTER 7

SUBGRID THEORY AND DEVELOPMENT

7.1 Introduction

In standard applications of explicit finite difference techniques to solving Maxwell's equations the fundamental limit of spatial resolution is the largest spatial grid interval. In fact, because of problems with error propagation at short wavelengths, the rule of thumb limit of spatial resolution is normally taken to be that approximately five of the largest spatial grid intervals are required to resolve the wavelength of the highest frequency of interest. While this resolution is usually sufficient for problems involving the large scale response of a scattering object to electromagnetic fields, it is known that such coarse resolution results underestimate the magnitude of the charge densities and currents on a scatterer in the vicinity of sharp edges or points such as the nose of an aircraft. One way to understand this is to consider the finite difference solution as a volume average over the coarse grid unit cell. The larger this volume is, the lower the volume average is relative to the continuum results near a discontinuity.

This is of particular importance when applied to the nonlinear corona model of the F106B. Corona and air breakdown are strongly dependent on the absolute magnitude of the electric field in a local region. Because the pitot boom of the F106B is very sharply pointed, large electric fields will exist near the tip. These large fields, however, will not extend very far from the tip. In fact the field will vary approximately as $1/r^2$, where r is the distance from the tip of the boom. This is a very rapid variation which is impossible to model accurately in a nonlinear code with cell sizes of .5m x 1m x .5m. This is not to say that air breadown will not occur in this model. It will, but it will occur at a larger ambient field level for the model than for the real aircraft. This may alter the D-dot and B-dot waveforms as predicted by the code. Therefore, it is necessary to attempt to achieve a better spatial resolution of the sharp points and edges of the aircraft. This needs to be accomplished without increasing the resolution at all points, because that leads to codes which become

rapidly unwieldy in size. One solution to this problem is to grid a portion of the aircraft (such as the nose) with a fine grid and then integrate that fine grid into the rest of the code. In many cases the nonlinear portion of the code can fit entirely into the fine grid, with the larger grid being linear. The details of this "subgrid" model are explained in the rest of this chapter.

7.2 General Description

In the model discussed in this report it is necessary to consider a rectilinear volume of space within which one wishes to obtain a finite difference approximation (f.d.a) to the solution of Maxwell's equations. Well posed solutions require the specification of the vector fields over the entire volume initially and specification of the boundary values of the fields at all times. The f.d.a. used is an explicit, second order, centered difference procedure. In this procedure the Cartesian components of the vector $\underline{E}$ and $\underline{H}$ fields are assigned staggered grid locations. The bounding planes of the problem volume are assumed to coincide with surfaces containing the H field components tangential to the bounding surface. Contained within this volume is a small rectilinear volume in which the finite difference grid intervals are some even integer ratio of the larger problem volume grid interval. The bounding surfaces of the smaller volume also coincide with surfaces containing both the coarse grid resolution and the fine grid resolution tangential H field components. Conceptually, the boundary between the two volumes is the same as the inner boundary of the larger problem volume. The fields on this boundary must be specified at all times in order to obtain a well posed solution to either the coarse or fine resolution f.d.a.'s to Maxwell's equations. The details of these specifications are discussed in the section on boundary conditions. The essential point of the specification is that it must also be consistent with both the coarse and fine grid solutions.

7.3 Details of the Fine Resolution Field Lattice and its Relationship to the Coarse Resolution Field Lattice

As mentioned in the previous subsection, the boundary between the coarse and fine resolution grids is equivalent to any other boundary of the problem volume. In effect, it is the interface between two separate f.d.a. solutions to Maxwell's equations.

In the volume containing the fine resolution grid, the f.d.a. imposed is again a centered difference staggered grid lattice. The grid interval is the fine resolution grid size. In Figure 7.1, a diagram of this lattice for a single field component (E_Z) is shown in relation to a coarse grid field component. The expansion factor is 2, with the origin of the fine resolution grid corresponding to the origin of a given unit cell in the coarse grid. For this expansion factor, the x-y planes (planes normal to the z axis) between two full coarse grid x-y planes contain fine grid fields which are shared by coarse grid fields above and below this plane. Only those fine grid fields on the same x-y plane as the coarse grid are associated with a single field in the coarse grid.

In order to avoid the uncertainties involved in extrapolating the boundary fields in time, both the coarse grid and fine grid fields are evaluated at the same times. The Courant stability criterion then requires a time step which is stable for the fine resolution grid.

It has been found that to obtain equivalent coarse grid fields from their fine grid counterparts, it is necessary to do a surface average. Consider a particular coarse grid electric field which is within the subgrid and therefore also represented by fine grid electric fields. For concreteness, assume that it is oriented in the X direction. The appropriate method for deriving the coarse grid field from the fine grid fields associated with it is the following:

1) Determine the y-z plane which is at the same X location as the coarse grid field.
2) Arithmetically average those fine grid fields which are located on that same plane and within a half cell spacing of the coarse grid field in the y and z directions.

This average is the appropriate value to use in the coarse grid finite difference scheme. In equation form, the average can be expressed,

$$F_x^{coarse} = \left(\frac{1}{X_y X_z}\right) \sum f_x^{fine} \text{ associated with the coarse grid field} \qquad (7.1)$$

where X_y and X_z are the expansion factors in the Y and Z directions and F_x^{coarse} and f_x^{fine} are general coarse and fine grid x directed fields, respectively. The effect of this averaging process is to reduce the amplitude of Fourier components with wavelengths smaller than the coarse grid interval in coarse grid fields.

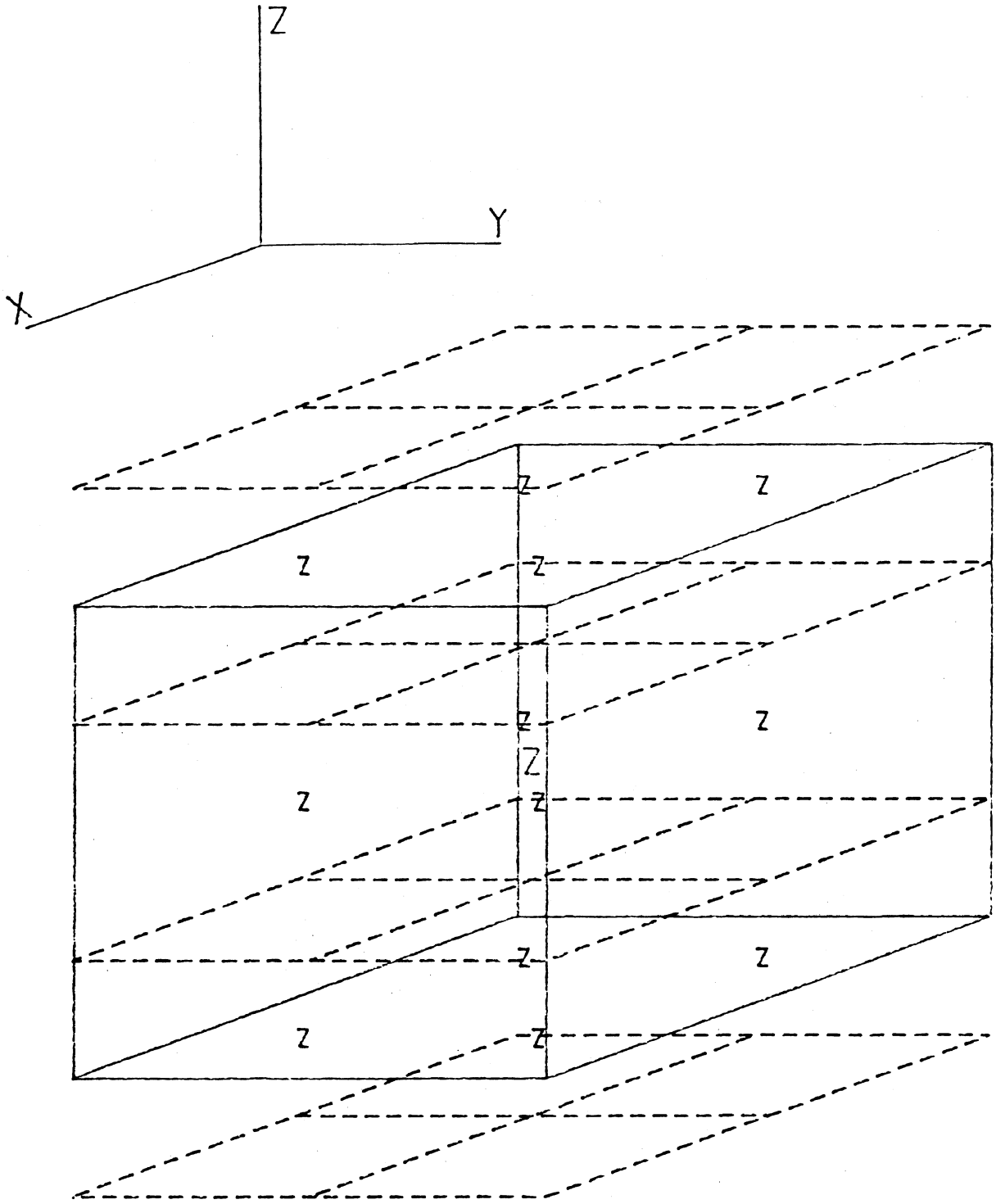

Figure 7.1 Distribution of Coarse (Z) and Fine (z) Grid Ez Fields for an Expansion Factor of 2 in all Three Coordinate Directions. The Solid Cube is a Coarse Grid Unit Cell. The Four Dashed Horizontal Planes Represent the Vertical Plane Boundaries of the Fine Grid Unit Cells. The Crossed Dashed Lines on Each Plane Correspond to the Projections of the Other Fine Grid Unit Cell Boundaries

7.4 Details of the Specification of H Fields Tangential to the Fine Grid - Coarse Grid Interface

The general philosophy for specification of H fields tangential to the coarse grid-fine grid interface is as follows:

(i) Obtain the coarse grid H fields (tangential to the interface) at time $t = n \Delta t$ by using the coarse grid advance equations.

(ii) Interpolate the coarse grid H fields to obtain the fine grid tangential H fields on the interface.

(iii) Advance the fine grid H and E fields in the interior.

(iv) Volume average the fine grid E fields tangential to the interface to obtain corresponding coarse grid E fields.

This procedure completes one time step. The coarse grid determines the boundary for the fine grid by providing a distribution of tangential H fields which are used to obtain the fine grid H fields by interpolation. The fine grid then couples back into the coarse grid by providing volume averaged E fields which are used in the coarse grid H field advance equations on the next time step.

It is necessary to distinguish between interfaces which are penetrated by a scatterer and those which are not. When a scattering object crosses the fine grid boundary special care must be exercised in determining the H fields tangential to the interface.

For interfaces which are not penetrated by a scattering object it is usually sufficient to perform a simple four point planar interpolation to obtain the components tangential to the surface. In the current implementation of the interface interpolation procedure the four point interpolation used is:

$$f_{fine}(x,y) = D + A\,(x-x_0) + B(y-y_0) + C\,(x-x_0)(y-y_0) \qquad (7.2)$$

where $x_0 \le x < x_0 + \Delta x_{c(coarse)}$ & $y_0 \le y < y_0 + \Delta y_c$

and $D \equiv F_c(x_0, y_0)$

$$A \equiv \frac{F_c(x_o + \Delta x_c, y_o) - F_c(x_o, y_o)}{\Delta x_c}$$

$$B \equiv \frac{F_c(x_o, y_o + \Delta y_c) - F_c(x_o, y_o)}{\Delta y_c} \tag{7.3}$$

$$C \equiv \frac{\left[F(x_o + \Delta x_c, y_o + \Delta y_c) + F(x_o, y_o) - F(x_o + \Delta x_c, y_o) - F(x_o, y_o + \Delta y_c)\right]}{\Delta x_c \, \Delta y_c}$$

It is clear by implication that these boundaries assume that the coarse grid field variation is relatively smooth (i.e., bilinear), and that the fine grid will follow this behavior. This is not the case when a scatterer penetrates the boundary. In order to match solutions across the coarse-fine grid interface, it is necessary to force a linear variation in fine grid magnetic fields inward into the fine grid subvolume. This is done by a linear interpolation of the outermost subgrid magnetic fields between the boundary and the corresponding subgrid field which is an expansion factor number of cells inside the subgrid volume.

When a scatterer penetrates the interface the four point interpolation procedure does not accurately predict the tangential H field's magnitude or distribution near the surface of the conductor in the fine resolution grid. In order to obtain a better estimate of the tangential H fields, a method that uses Maxwell's equations is required. For cases where the field distribution is approximately two-dimensional, that is

$$\frac{\partial H_x}{\partial x} + \frac{\partial H_y}{\partial y} \sim 0$$

one makes use of Euler potentials to obtain a solution for the distribution of tangential H fields in the fine grid at the interface.

Define two scalar fields $\alpha(x,y)$ and $\beta(z) = z$;

then $\underline{H} = \underline{\nabla} \times (\alpha \underline{\nabla} \beta) = -\hat{z} \times \underline{\nabla}\alpha = \frac{\partial x}{\partial y} \hat{x} - \frac{\partial \alpha}{\partial x} \hat{y}$ (7.4)

also

$$\hat{z} \cdot (\underline{\nabla} \times \underline{H}) = -\frac{\partial^2 \alpha}{\partial x^2} - \frac{\partial^2 \alpha}{\partial y^2} = \varepsilon \frac{\partial E_z}{\partial t} \tag{7.5}$$

or

$$\frac{\partial^2 \alpha}{\partial x^2} + \frac{\partial^2 \alpha}{\partial y^2} = -\varepsilon \frac{\partial E_z}{\partial t} \cdot \tag{7.6}$$

By specifying Neumann boundary conditions sufficiently distant from the surface of the conductor and interpolating to obtain the source terms for the fine grid resolution the α's can be solved for at the normal E-field positions in the fine grid. Note that the value of α on a conductor is set to zero. At present, the Poisson equation is solved by the method of successive over-relaxation. [8].

Given the boundary values of the tangential H fields in the fine grid the interior points in the fine grid are advanced. The coarse grid E fields contained entirely within the fine grid are then computed by taking the volume average of their associated fine grid fields. These fields are then used to advance the coarse grid H fields tangential to the coarse grid - fine grid interface.

7.5 Gridding of Scatterers in the Fine Resolution Mesh

When gridding a scatterer in the fine resolution grid some care must be exercised, particularly at the interface between the coarse grid and fine grid. The essential point is that all fine grid fields which contribute to the volume average of a coarse grid field must be zeroed. Hence all fine grid E fields contained within a unit cell of a zeroed coarse grid E field, as well as those shared by a zeroed coarse grid field and one which is not zeroed must be zeroed. It is often useful to diagram the fine grid and coarse grid fields in order to determine which fields are zeroed, since complicated scatterers may be hard to automate.

7.6 Results

An example of the utility and efficacy of this technique is a comparison of the normal electric field above one end of a 9m x 3m x 3m bar in a pure coarse grid and the same fields for a hybrid coarse-fine grid with the bar tapered to a 1m x 1m cross section. The pure coarse grid has a spatial grid interval of 1m in all three Cartesian coordinates. The coarse resolution part of the hybrid has the same grid interval while the fine resolution part has a spatial grid interval of .5m in all three Cartesian coordinates. In all cases the bar is illuminated by a normally incident electromagnetic plane wave which rises to a constant 50 kV/m in 40 ns with a $\sin^2$ leading edge. The incident electric field is polarized parallel to the bar's length.

Figure 7.2a shows the waveform associated with the normal electric field in the pure coarse grid solution, while Figure 7.2b shows the normal electric field for the hybrid coarse-fine grid solution. Figure 7.3 shows the waveform for the normal electric field when the bar cross section is tapered to 1m. Note that the hybrid enhances the normal electric field because of the improved resolution. The tapered bar could not be gridded in the pure coarse grid, but this is possible in the hybrid.

The subgrid model has not yet been incorporated into the F106 finite difference model or corona model. This will occur during the next year's effort.

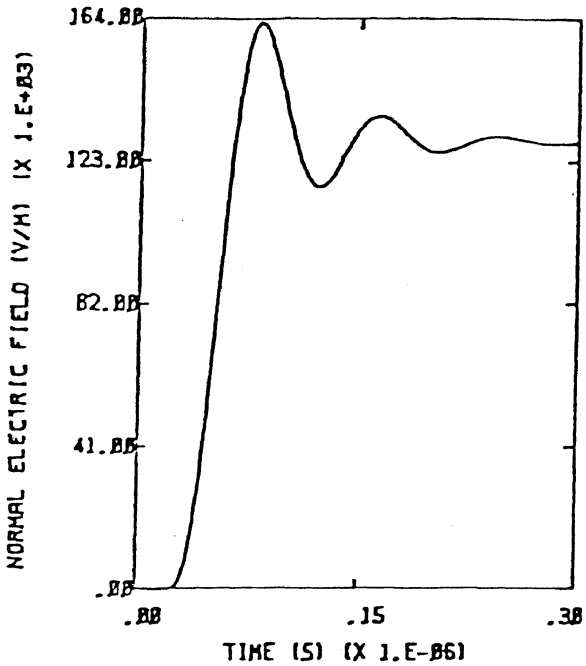

Figure 7.2a Normal Electric Field Above the End of the Bar in the Pure Coarse Grid Solution

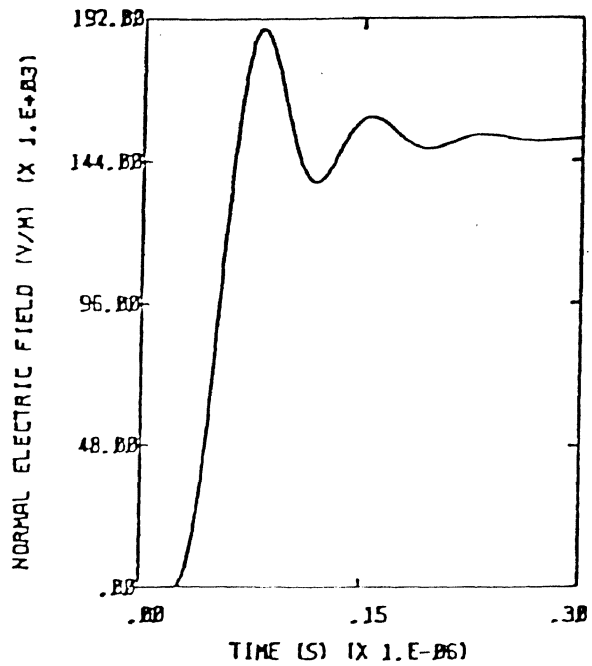

Figure 7.2b Normal Electric Field Above the End of the Bar in the Hybrid Coare-Fine Grid Solution

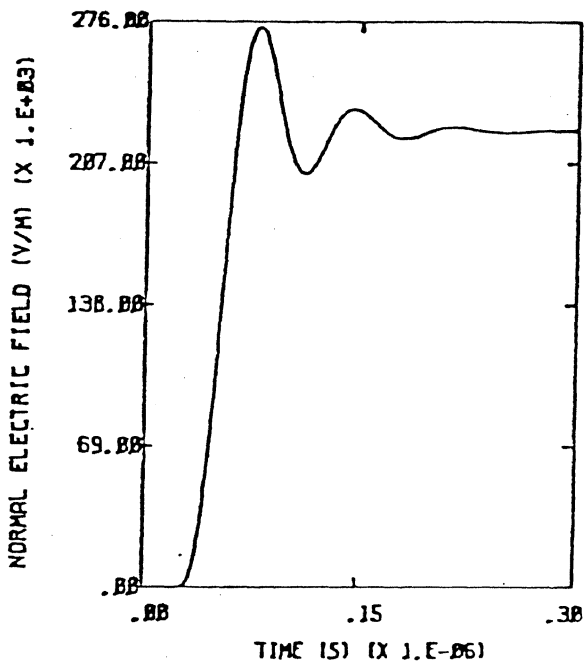

Figure 7.3 Normal Electric Field Above the Tapered End of the Bar in the Hybrid Coarse-Fine Grid Solution

CHAPTER 8

F106B TRANSFER FUNCTIONS FOR THREE CURRENT INJECTION CONFIGURATIONS

As an aid to a possible current injection test of the F106B, transfer functions have been calculated for three different configurations of the aircraft. The transfer functions were calculated between a current injected at the nose of the F106B and the D-dot and B-dot responses at the positions of the sensors. The three configurations used were:

i) aircraft in free space,
ii) aircraft resting on perfect ground plane,
iii) aircraft elevated ten meters above a perfect ground plane.

The purpose of the proposed test was to determine the transfer function between an injected nose current and the D-dot forward and B-dot longitudinal responses of the F106B in flight. This of course, was not possible experimentally, so the calculations were performed in order to determine what the effect the presence of the ground plane had on the transfer function, and whether elevating the aircraft ten meters above the ground significantly removed the effect of the ground plane. Also, in principle, the calculations allow the free space transfer function to be determined from the measured transfer function in the presence of the ground plane, because the differences are known.

The D-dot and B-dot responses were calculated using a three-dimensional finite difference code including a thin wire channel for current injection [6]. The wire injected current at the nose of the aircraft and removed it from the base of the tail. The three configurations of aircraft, thin wire, and ground plane are shown in Figure 8.1. In the free space configuration, the thin wire runs directly into the problem space boundary and is driven by a voltage source at the edge of the problem space. The intent of this is to make the thin wire appear to be infinitely long on both the front and back of the aircraft. For the other two configurations the thin wire was connected to the ground plane on both the front and back in order to use the ground as a return path for the current. The voltage

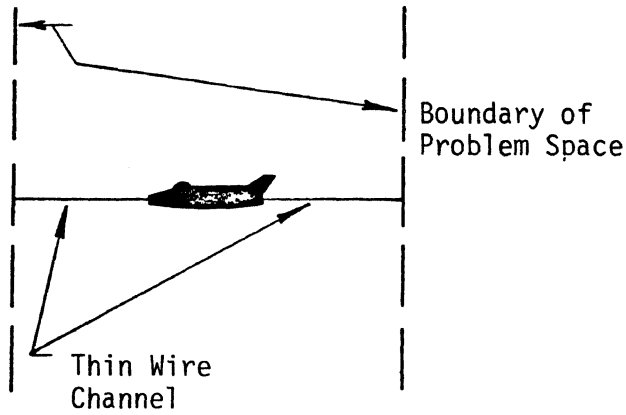

(a) Free Space

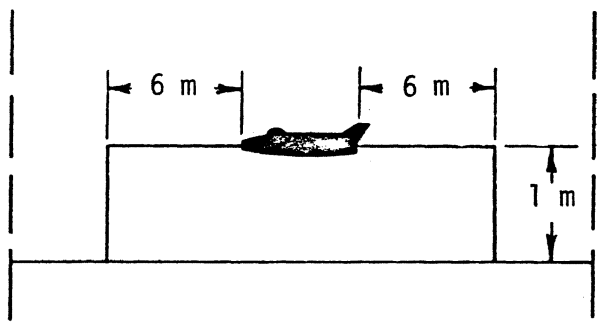

(b) Resting on Ground Plane

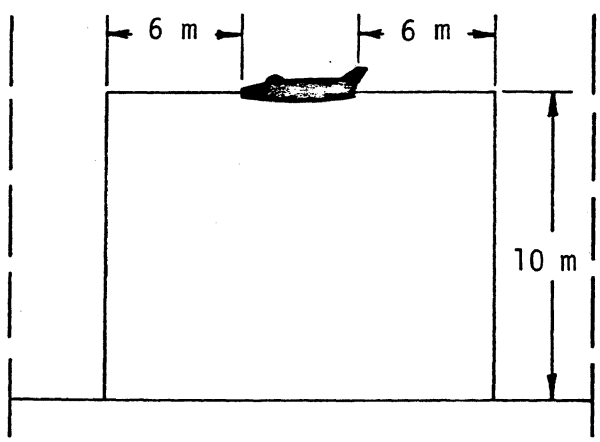

(c) Ten Meters Above Ground Plane

Figure 8.1 The Three Current Injection Configurations Used in the Calculation of Transfer Functions

source for these configurations was placed at the junction of the wire and the ground at the front of the aircraft. In all cases the thin wire had a characteristic impedance of 96Ω and a velocity of propagation of 3×10^8 m/sec.

The transfer functions were calculated between the D-dot and B-dot responses and the current injected at the nose of the aircraft according to $T = \tilde{R}/\tilde{I}$, where T is the transfer function, $\tilde{R}$ is the response in question, $\tilde{I}$ is the injected current, and tildes denote Fourier transforms. In the following the subscripts FS, GP and EL refer to the free space, ground plane, and elevated above ground plane cases, respectively. The transfer functions then may be designated T_{FS} (D-dot), T_{GP}(D-dot), T_{EL}(D-dot), T_{FS}(B-dot), T_{GP}(B-dot), and T_{EL}(B-dot). These transfer functions are, of course, complex functions of frequency. The frequency dependence is suppressed in the notation.

Although the transfer functions themselves were calculated, it is more instructive to present ratios of the transfer functions. The ratio of the GP and EL cases to the FS case graphically illustrates the distortion in the transfer function caused by the ground plane. Figures 8.2 - 8.5 show the four possible ratios of the magnitudes of the transfer functions. The vertical scale is in dB and the horizontal scale is the base ten log of the frequency from 100 kHz to 50 MHz. Note that this means that the value of zero on the graphs indicates that the transfer function magnitudes are equal at that frequency. The figures also show that, as expected, the ratios are larger for the GP case than the EL case by amounts ranging up to 20 dB. Therefore, the effect of the ground plane is much reduced by elevating the aircraft, but it should also be noted that ratios of the order of 12 dB still exist for the EL case. The largest peaks in the ratio graphs are at approximately 2 MHz for Figures 8.2 and 8.3 and at 1 MHz for Figures 8.4 and 8.5. These appear to be characteristic frequencies of aircraft, wire, ground plane systems for the two configurations. As a caution in using the graphs, it must be remembered that the presence of a dielectric beneath the aircraft, such as wood support structure, could alter the transfer functions. The calculations were performed assuming the support had the same electrical properties as air.

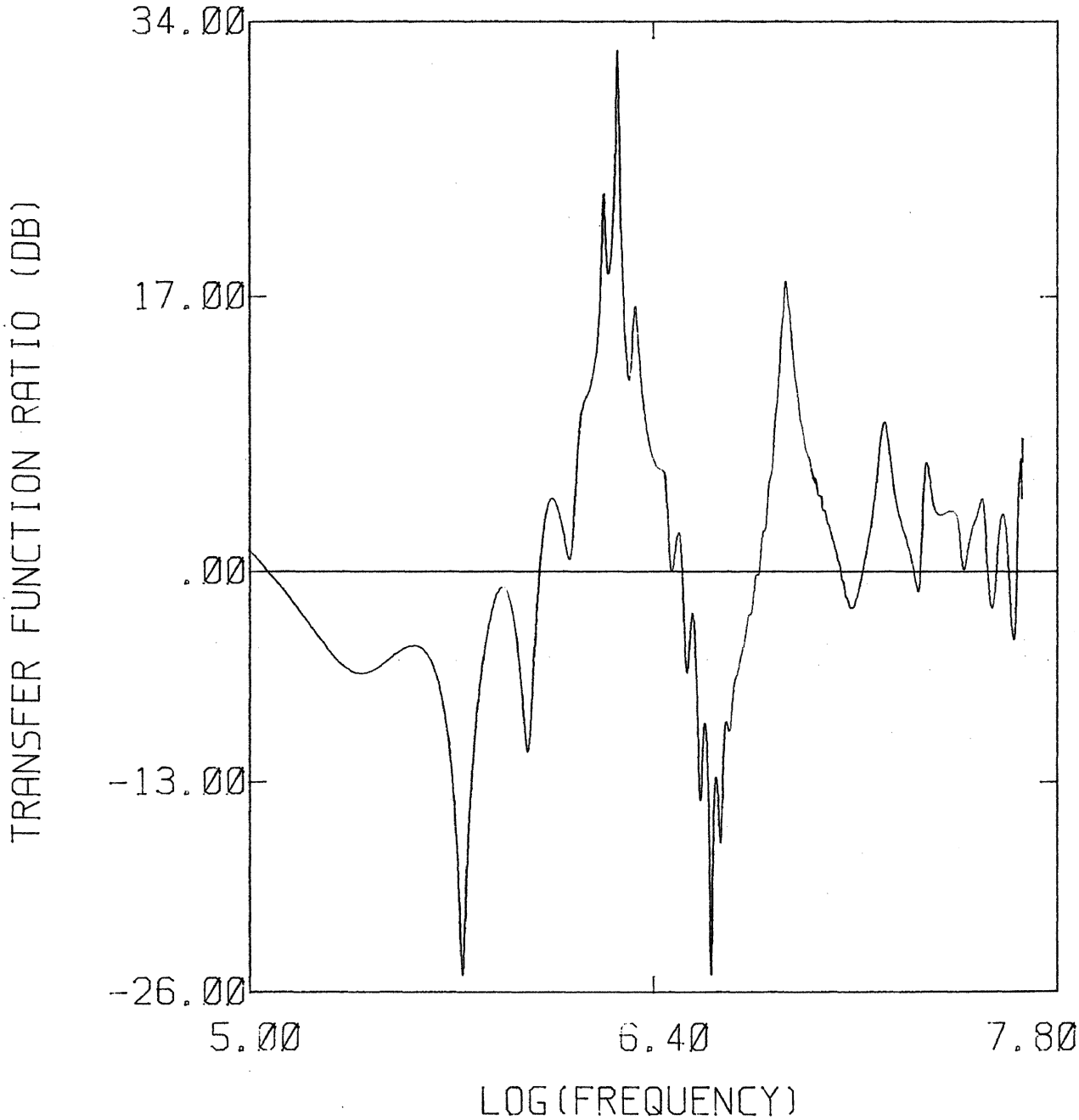

FIGURE 8.2 RATIO OF THE D-DOT TRANSFER FUNCTION FOR THE GROUND PLANE CONFIGURATION (GP) TO THE D-DOT TRANSFER FUNCTION FOR THE FREE SPACE CONFIGURATION (FS)

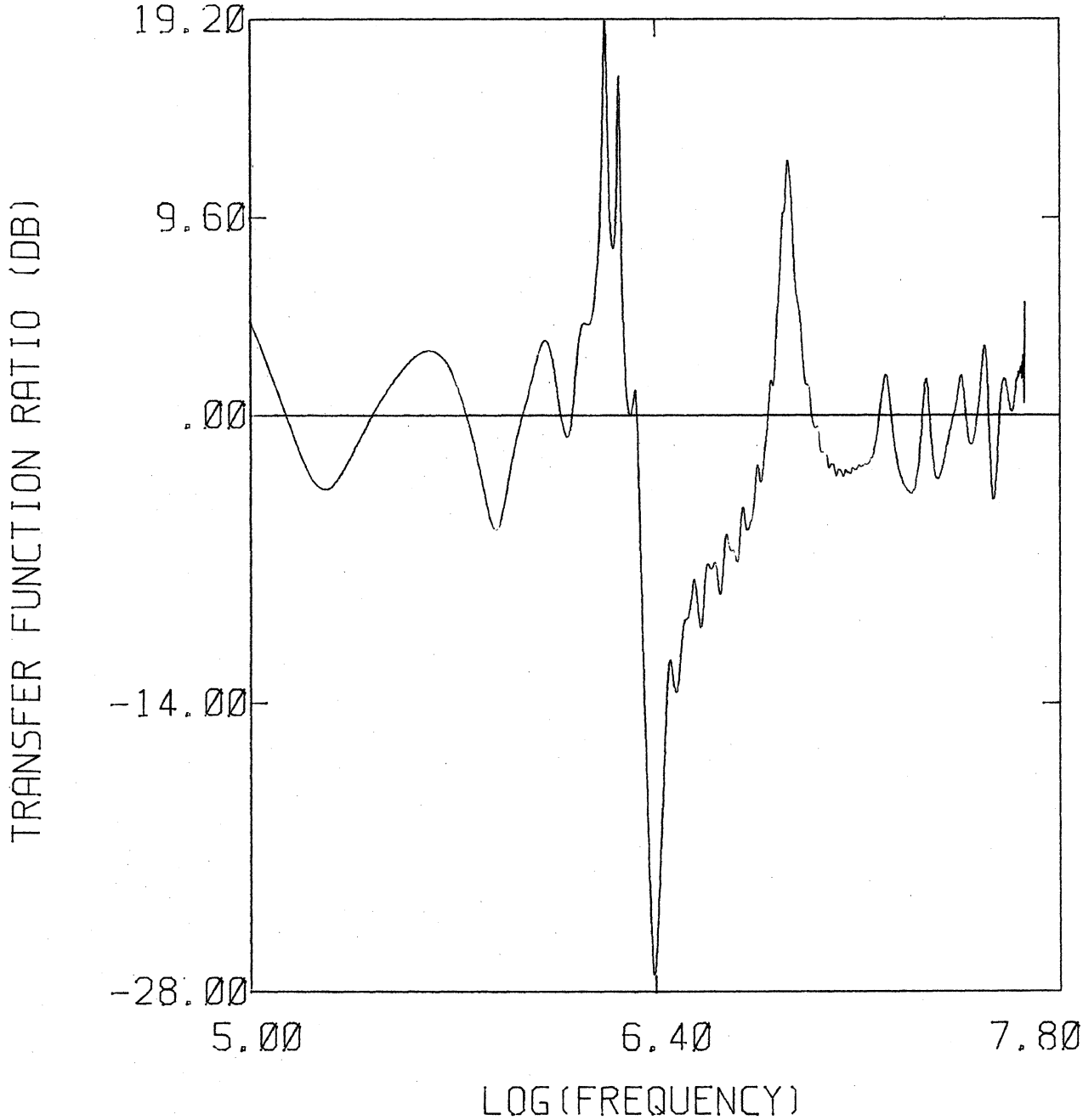

FIGURE 8.3 RATIO OF THE B-DOT TRANSFER FUNCTION FOR THE GROUND PLANE CONFIGURATION (GP) TO THE B-DOT TRANSFER FUNCTION FOR THE FREE SPACE CONFIGURATION (FS)

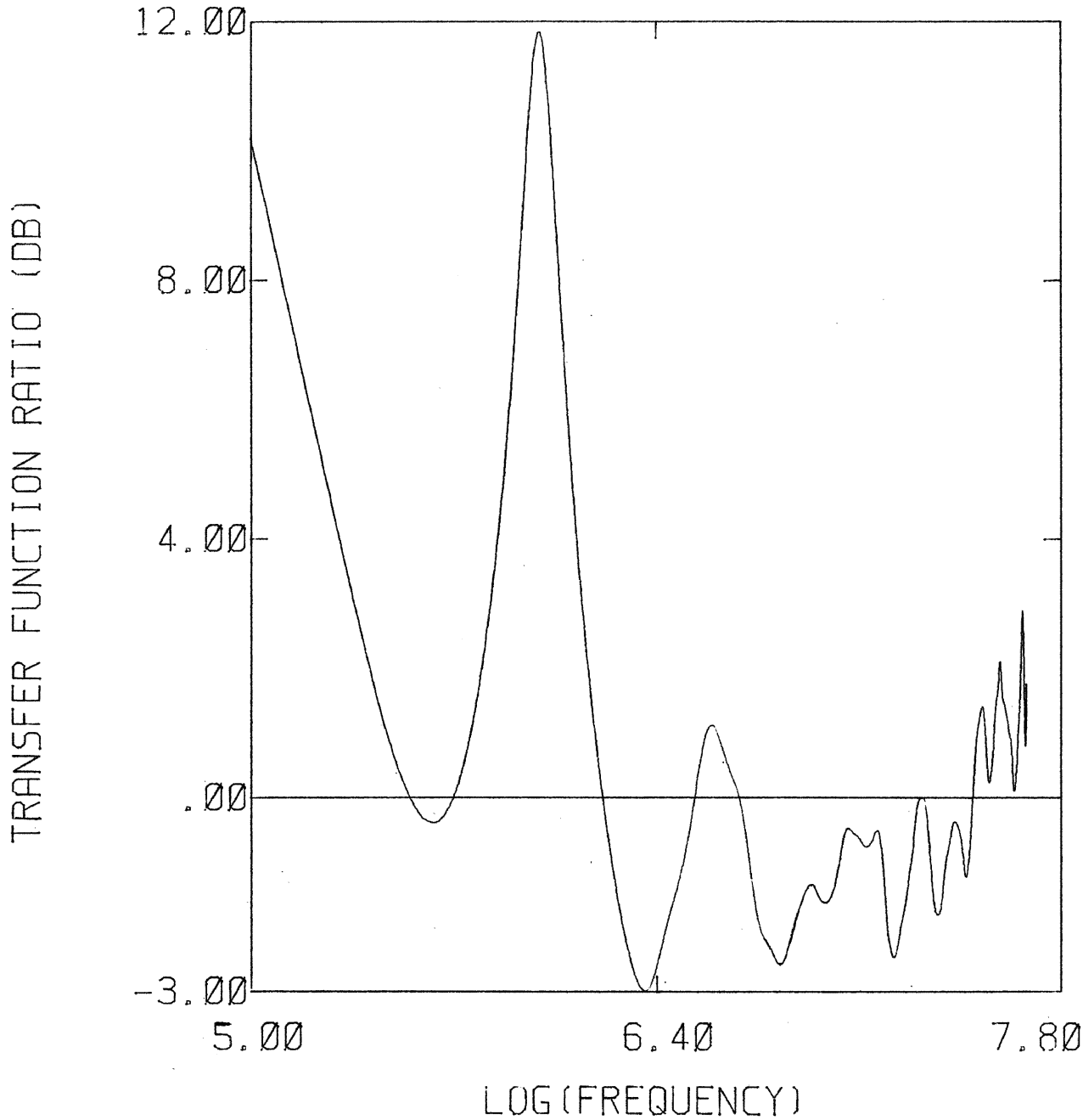

FIGURE 8.4 RATIO OF THE D-DOT TRANSFER FUNCTION FOR THE ELEVATED CONFIGURATION (EL) TO THE D-DOT TRANSFER FUNCTION FOR THE FREE SPACE CONFIGURATION (FS)

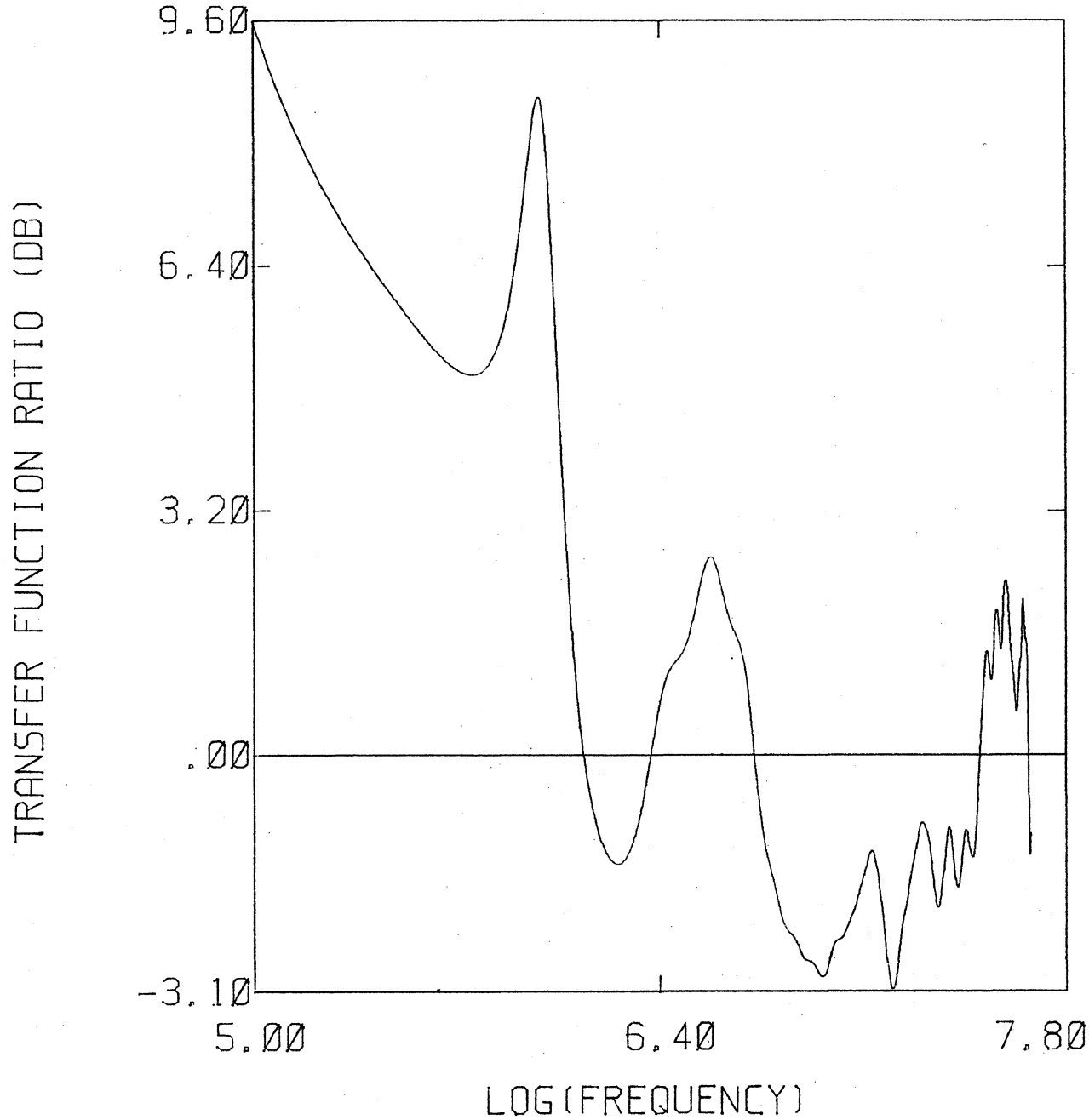

FIGURE 8.5 RATIO OF THE B-DOT TRANSFER FUNCTION FOR THE ELEVATED CONFIGURATION (EL) TO THE B-DOT TRANSFER FUNCTION FOR THE FREE SPACE CONFIGURATION (FS)

CHAPTER 9

SUMMARY AND CONCLUSIONS

The work reported here has concentrated on analysis of the 1982 inflight lightning data and the development of analytical tools to better understand that data. Data classification has been made in the time domain, involving the sorting of waveforms into groups having similar characteristics. Although somewhat subjective, this process may give some insight into similar lightning events that could be occurring on the F106B. Data analysis has also been done in the frequency domain by a numerical search for recurring resonances in the measured responses.

The possibility that triggered lightning is responsible for much, if not all, of the direct strike data has prompted an investigation into this area. The expected behavior of triggered lightning and its effect on the F106B have been studied both intuitively and numerically. Calculated responses have been compared with actual measured responses.

A pair of new analytical tools have been developed to help in the data interpretation process. The first is an enhanced nonlinear model, which, when finalized, will predict in much greater detail the evolution of a static discharge. Also developed was a subgrid model, which allows the analyst to spatially resolve a portion of a finite difference problem space in much greater detail than was previously possible. It is expected that both of these tools will be further developed and applied in following efforts.

REFERENCES

1. Thomas, M.E., and F.L. Pitts, "1982 Direct Strike Lightning Data," NASA TM-84626, March 1983.

2. Le Vine, D.M., and V. Mazur, "Correlated Measurements of UHF Radar Signatures, RF Radiation, and Electric Field Changes from Lightning," Proc. of the 8th Int. Aerospace and Ground Conf. on Lightning and Static Electricity, June 1983.

3. Rudolph, T., and R.A. Perala, "Interpretation Methodology and Analysis of Inflight Lightning Data," NASA CR-3590, October 1982.

4. Rudolph, T., and R. A. Perala, "Linear and Nonlinear Interpretation of the Direct Strike Lightning Response of the NASA F106B Thunderstorm Research Aircraft," NASA CR-3746, March 1983.

5. Malan, D.J., "Physics of Lightning," The English Universities Press Ltd., London, 1963.

6. Merewether, D.E. and R. Fisher, "Finite Difference Solution of Maxwell's Equation for EMP Applications, "Report EMA-79-R-4 (Revised), Electro Magnetic Applications, Inc. (EMA), P.O.Box 8482, Albuquerque, NM 87198, 22 April 1980.

7. Collins, M.M.C., and J.M. Meek, "Measurement of Field Changes Preceding Impulse Breakdown of Rod-Plane Gaps," Proceedings of the Seventh International Conference on Phenomena in Ionized Bases, August 22-27, Gradevinska Kujiga Publishing House, Belgrade, 22-27 August 1965.

8. Roache, P.J., "Computational Fluid Dynamics," Hermosa Publishers, Albuquerque, 1976.

APPENDIX A

D-Dot and B-Dot Records

The legend beneath each plot gives the flight and run number, strike attach and detach points, strike altitude, and ambient temperature. The attach and detach points were determined by NASA and LTI personnel from pilot's comments and the appearance of pit marks on the aircraft. The code for attach-detach locations is the following:

U - Unknown
N - Nose
T - Tail
LW - Left Wing
RW - Right Wing
M - Multiple
N - Nearby

D-Dot Records

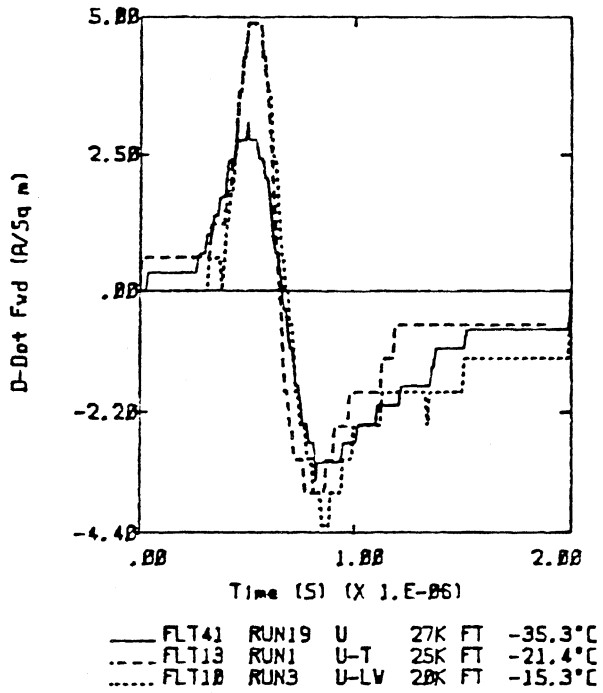
5.00
2.50
.00
-2.20
-4.40
D-Dot Fvd (A/Sq m)
.00
1.00
2.00
Time (S) (X 1.E-06)
FLT41 RUN19 U 27K FT -35.3°C
FLT13 RUN1 U-T 25K FT -21.4°C
FLT10 RUN3 U-LW 20K FT -15.3°C

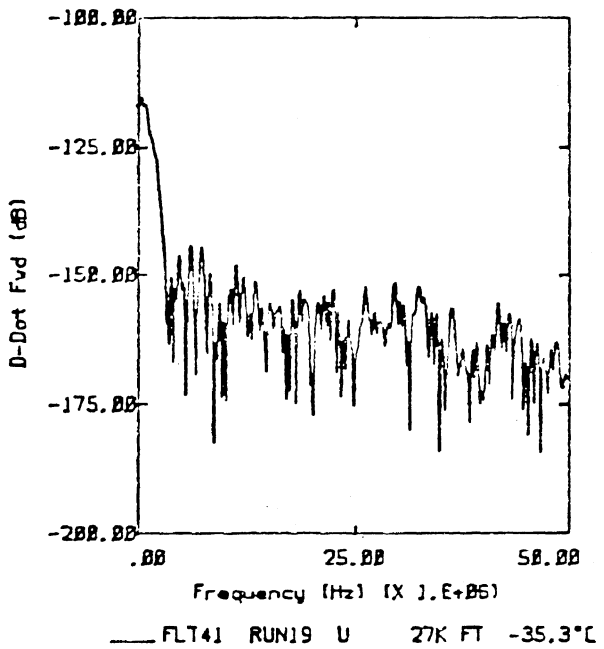
-100.00
-125.00
-150.00
-175.00
-200.00
D-Dot Fvd (dB)
.00
25.00
50.00
Frequency (Hz) (X 1.E+06)
FLT41 RUN19 U 27K FT -35.3°C

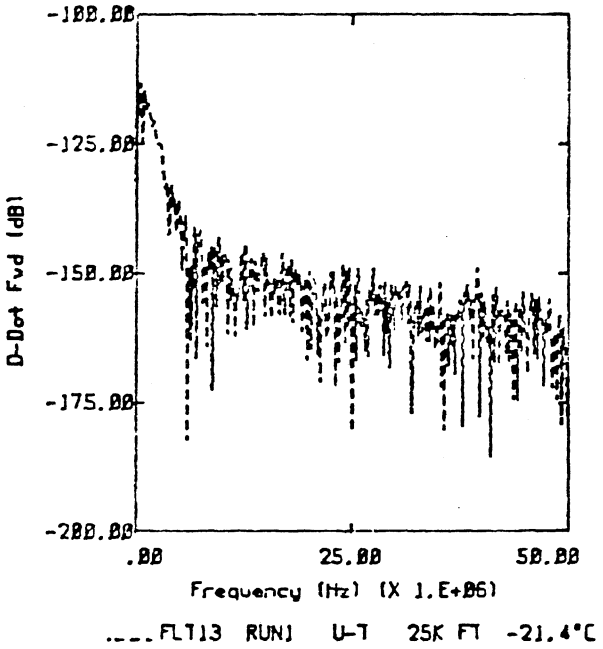
-100.00
-125.00
-150.00
-175.00
-200.00
D-Dot Fvd (dB)
.00
25.00
50.00
Frequency (Hz) (X 1.E+06)
FLT13 RUN1 U-T 25K FT -21.4°C

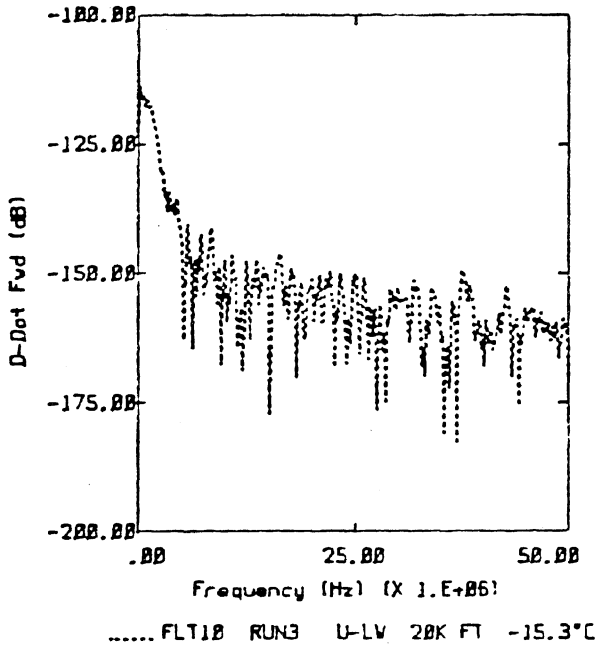
-100.00
-125.00
-150.00
-175.00
-200.00
D-Dot Fvd (dB)
.00
25.00
50.00
Frequency (Hz) (X 1.E+06)
FLT10 RUN3 U-LW 20K FT -15.3°C

Category 1

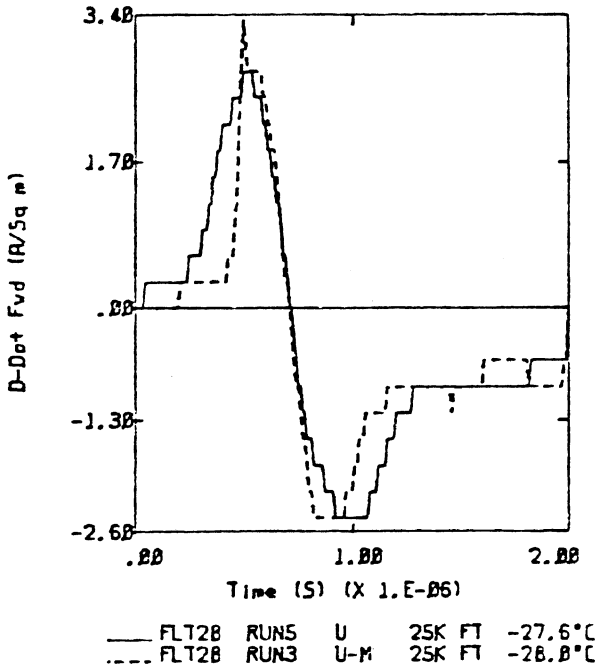
3.40
1.70
.00
-1.30
-2.60
D-Dot Fvd (A/Sq m)
.00
1.00
2.00
Time (S) (X 1.E-06)
FLT28 RUN5 U 25K FT -27.6°C
FLT28 RUN3 U-M 25K FT -28.0°C

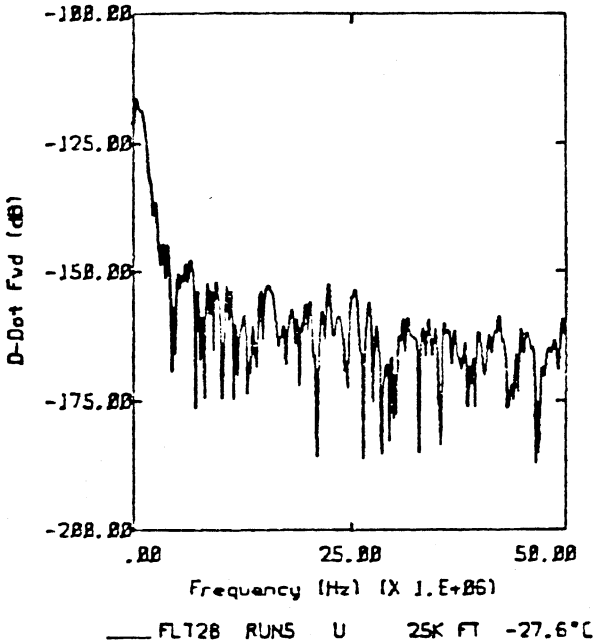
-100.00
-125.00
-150.00
-175.00
-200.00
D-Dot Fvd (dB)
.00
25.00
50.00
Frequency (Hz) (X 1.E+06)
FLT28 RUN5 U 25K FT -27.6°C

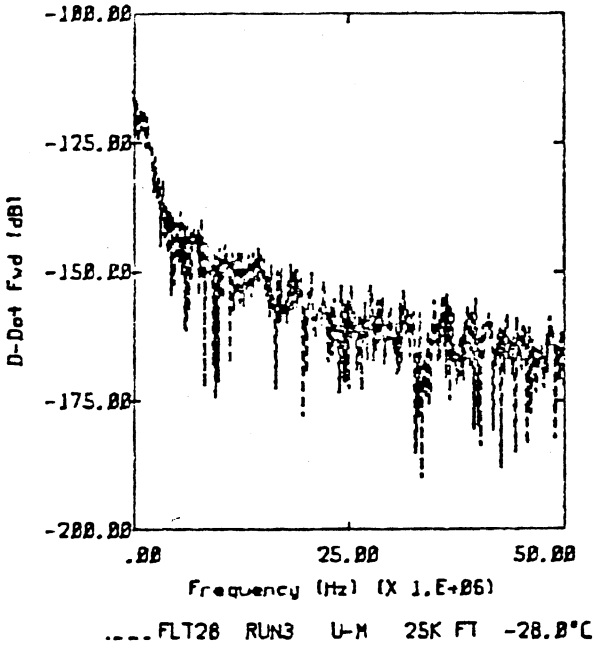
-100.00
-125.00
-150.00
-175.00
-200.00
D-Dot Fvd (dB)
.00
25.00
50.00
Frequency (Hz) (X 1.E+06)
FLT28 RUN3 U-M 25K FT -28.0°C

Category 1

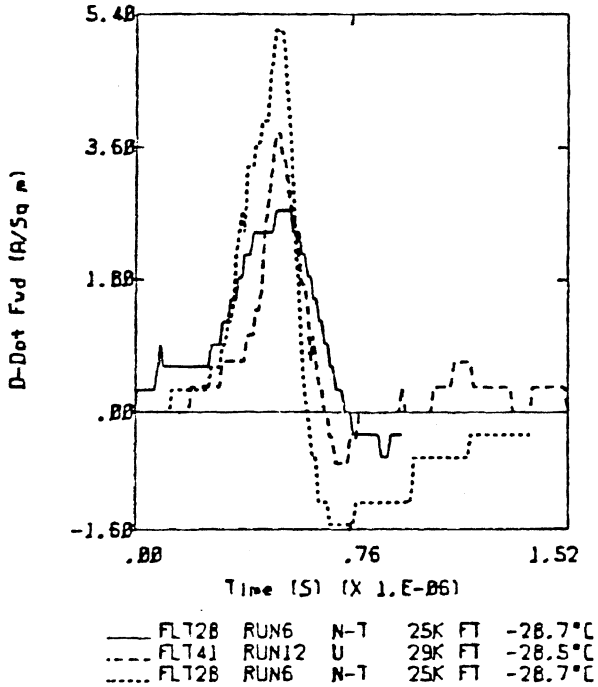
5.40
3.60
1.80
.00
-1.60
D-Dot Fvd (A/Sq m)
.00
.76
1.52
Time (S) (X 1.E-06)
FLT28 RUN6 N-T 25K FT -28.7°C
FLT41 RUN12 U 29K FT -28.5°C
FLT28 RUN6 N-T 25K FT -28.7°C

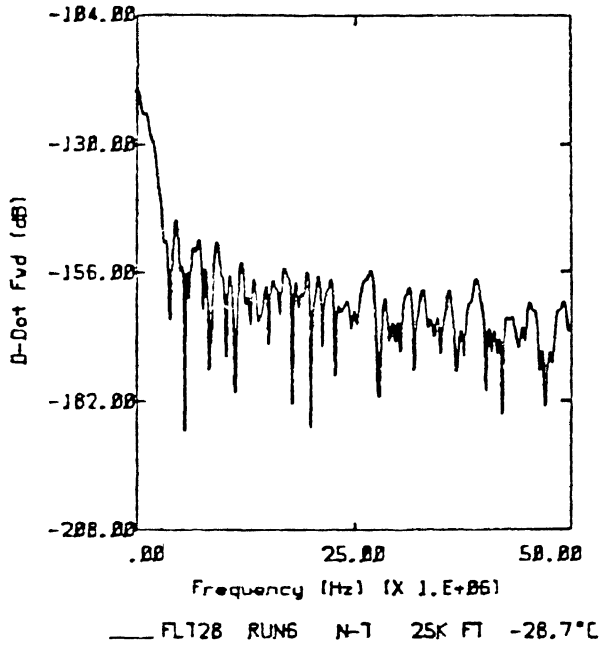
-104.00
-130.00
-156.00
-182.00
-208.00
D-Dot Fvd (dB)
.00
25.00
50.00
Frequency (Hz) (X 1.E+06)
FLT28 RUN6 N-T 25K FT -28.7°C

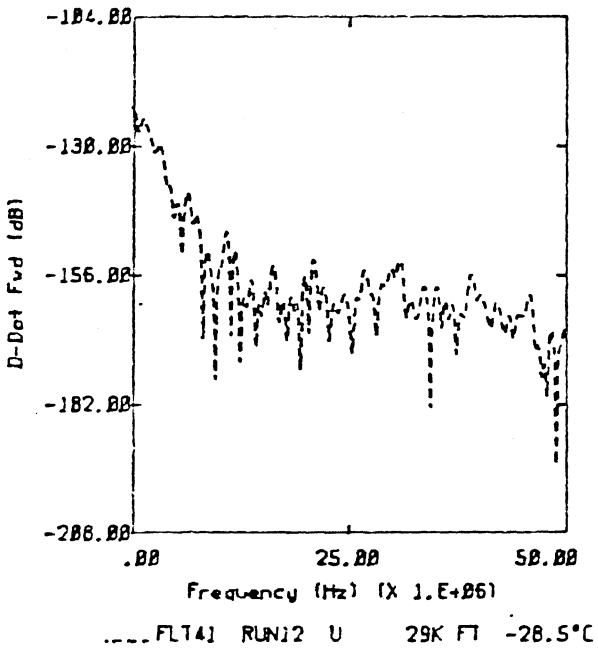
-104.00
-130.00
-156.00
-182.00
-208.00
D-Dot Fvd (dB)
.00
25.00
50.00
Frequency (Hz) (X 1.E+06)
FLT41 RUN12 U 29K FT -28.5°C

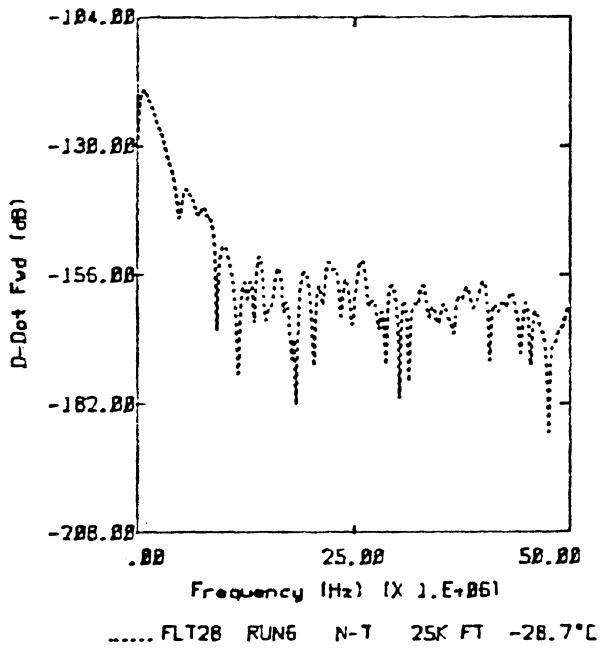
-104.00
-130.00
-156.00
-182.00
-208.00
D-Dot Fvd (dB)
.00
25.00
50.00
Frequency (Hz) (X 1.E+06)
FLT28 RUN6 N-T 25K FT -28.7°C

Category 1

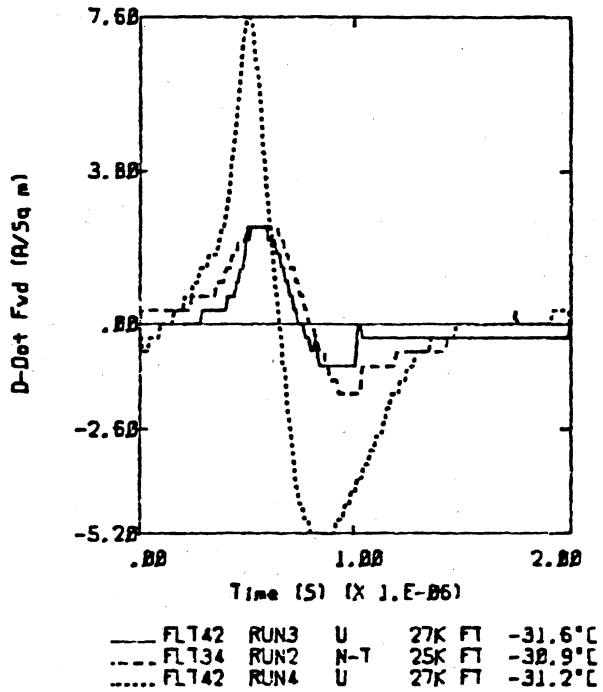
7.60
3.80
.00
-2.60
-5.20
D-Dot Fvd (A/Sq m)
.00
1.00
2.00
Time (S) (X 1.E-06)
FLT42 RUN3 U 27K FT -31.6°C
FLT34 RUN2 N-T 25K FT -30.9°C
FLT42 RUN4 U 27K FT -31.2°C

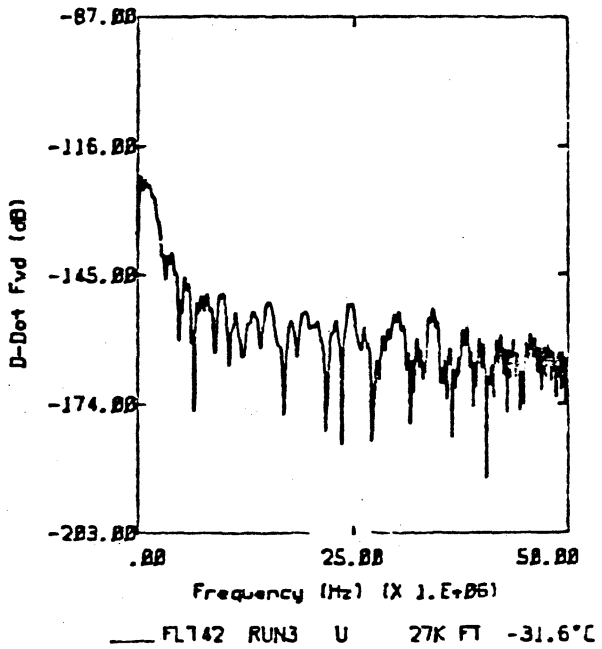
-87.00
-116.00
-145.00
-174.00
-203.00
D-Dot Fvd (dB)
.00
25.00
50.00
Frequency (Hz) (X 1.E+06)
FLT42 RUN3 U 27K FT -31.6°C

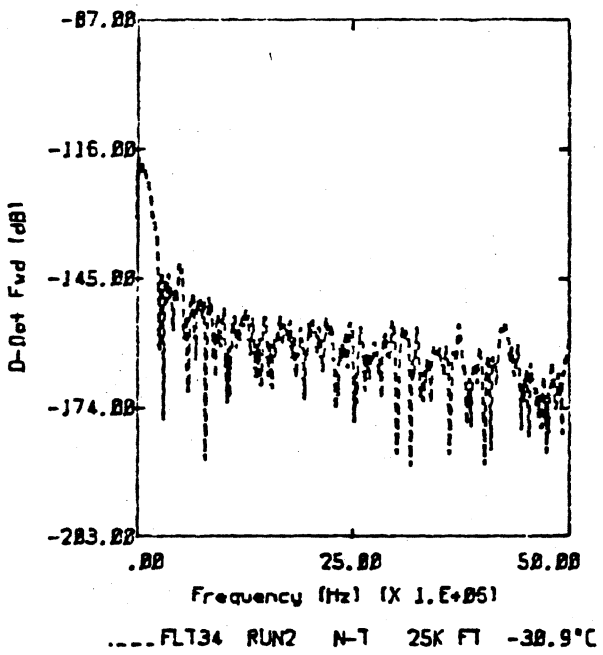
-87.00
-116.00
-145.00
-174.00
-203.00
D-Dot Fvd (dB)
.00
25.00
50.00
Frequency (Hz) (X 1.E+06)
FLT34 RUN2 N-T 25K FT -30.9°C

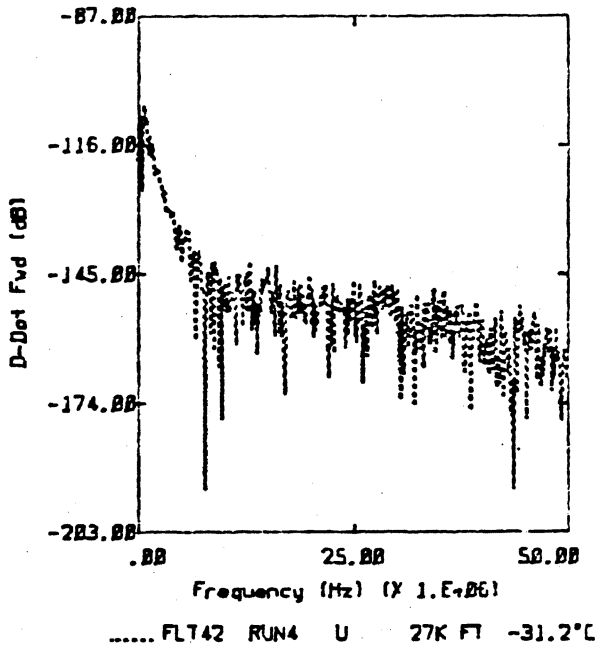
-87.00
-116.00
-145.00
-174.00
-203.00
D-Dot Fvd (dB)
.00
25.00
50.00
Frequency (Hz) (X 1.E+06)
FLT42 RUN4 U 27K FT -31.2°C

Category 1

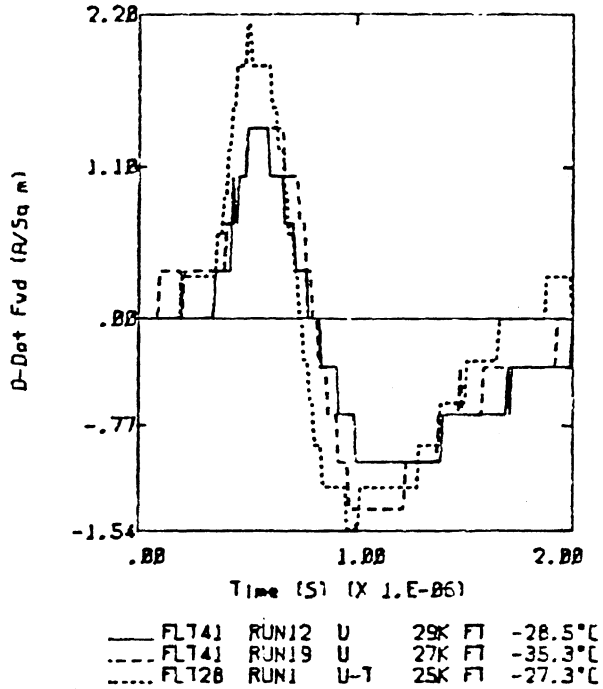
2.20
1.10
.00
-.77
-1.54
D-Dot Fvd (A/Sq m)
.00
1.00
2.00
Time (S) (X 1.E-06)
FLT41 RUN12 U 29K FT -28.5°C
FLT41 RUN19 U 27K FT -35.3°C
FLT28 RUN1 U-T 25K FT -27.3°C

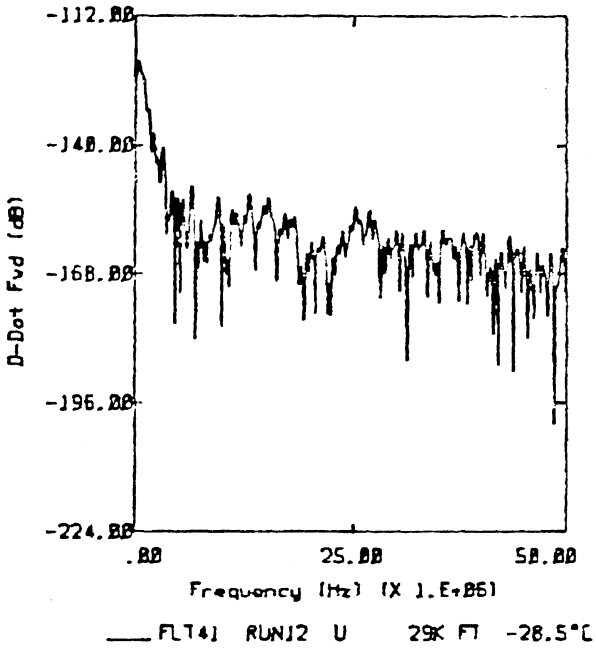
-112.00
-140.00
-168.00
-196.00
-224.00
D-Dot Fvd (dB)
.00
25.00
50.00
Frequency (Hz) (X 1.E+06)
FLT41 RUN12 U 29K FT -28.5°C

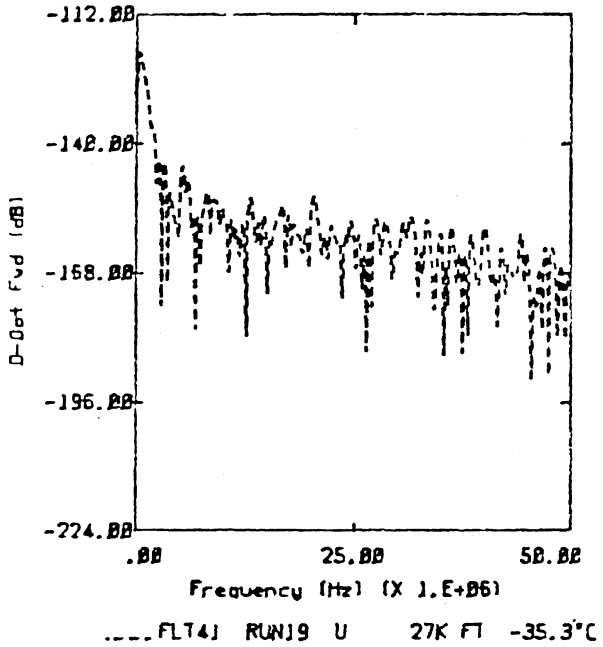
-112.00
-140.00
-168.00
-196.00
-224.00
D-Dot Fvd (dB)
.00
25.00
50.00
Frequency (Hz) (X 1.E+06)
FLT41 RUN19 U 27K FT -35.3°C

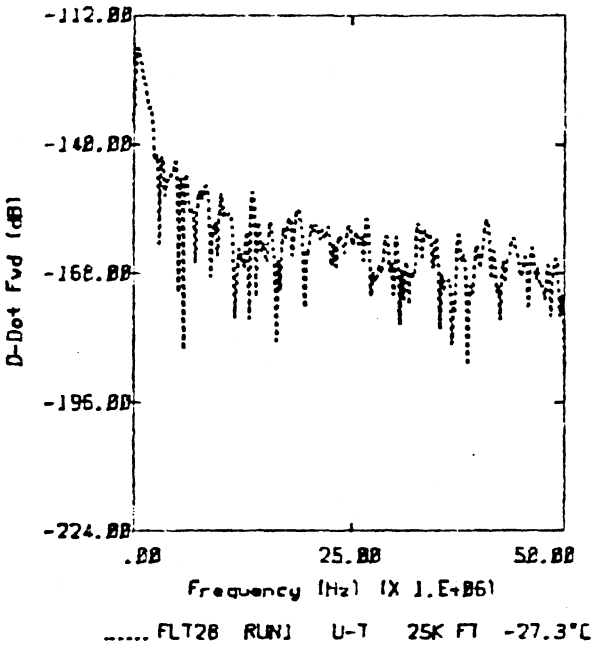
-112.00
-140.00
-168.00
-196.00
-224.00
D-Dot Fvd (dB)
.00
25.00
50.00
Frequency (Hz) (X 1.E+06)
FLT28 RUN1 U-T 25K FT -27.3°C

Category 1

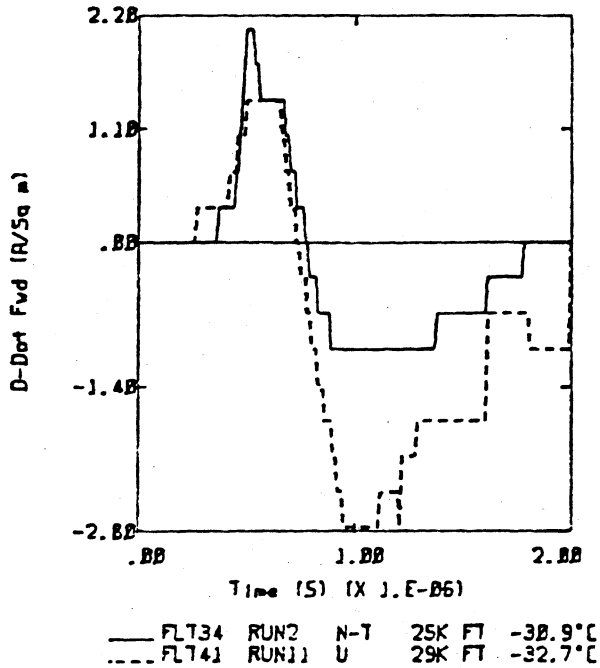
2.2B
1.1B
.BB
-1.4B
-2.8B
D-Dot Fvd (R/Sq m)
.BB
1.BB
2.BB
Time (S) (X 1.E-B6)
FLT34 RUN2 N-T 25K FT -3B.9°C
FLT41 RUN11 U 29K FT -32.7°C

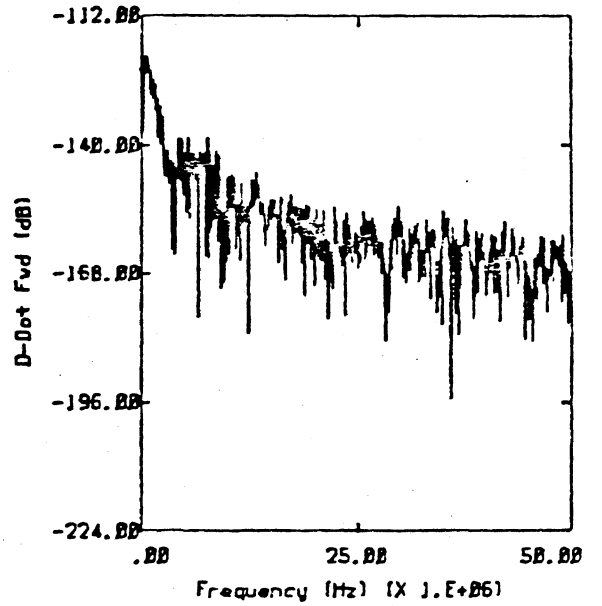
-112.BB
-14B.BB
-168.BB
-196.BB
-224.BB
D-Dot Fvd (dB)
.BB
25.BB
5B.BB
Frequency (Hz) (X 1.E+B6)
FLT34 RUN2 N-T 25K FT -3B.9°C

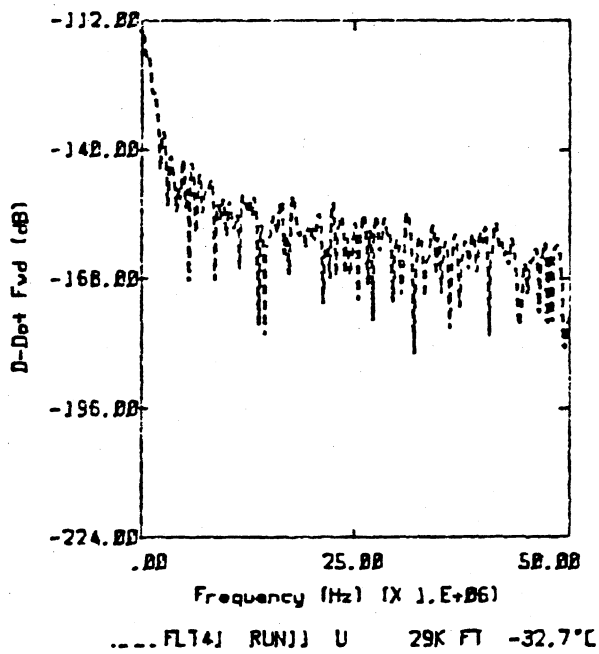
-112.BB
-14B.BB
-168.BB
-196.BB
-224.BB
D-Dot Fvd (dB)
.BB
25.BB
5B.BB
Frequency (Hz) (X 1.E+B6)
FLT41 RUN11 U 29K FT -32.7°C

Category 1

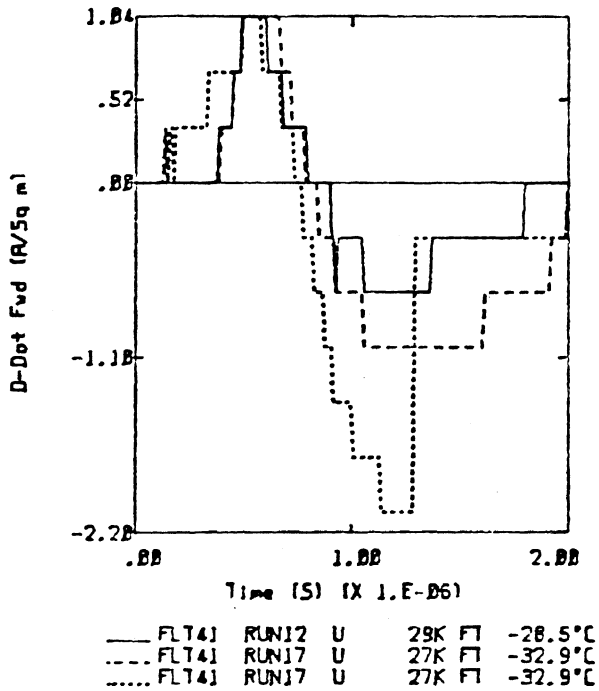
1.04
.52
.00
-1.10
-2.20
D-Dot Fwd (V/sq m)
.00
1.00
2.00
Time (S) (X 1.E-06)
FLT41 RUN12 U 29K FT -28.5°C
FLT41 RUN17 U 27K FT -32.9°C
FLT41 RUN17 U 27K FT -32.9°C

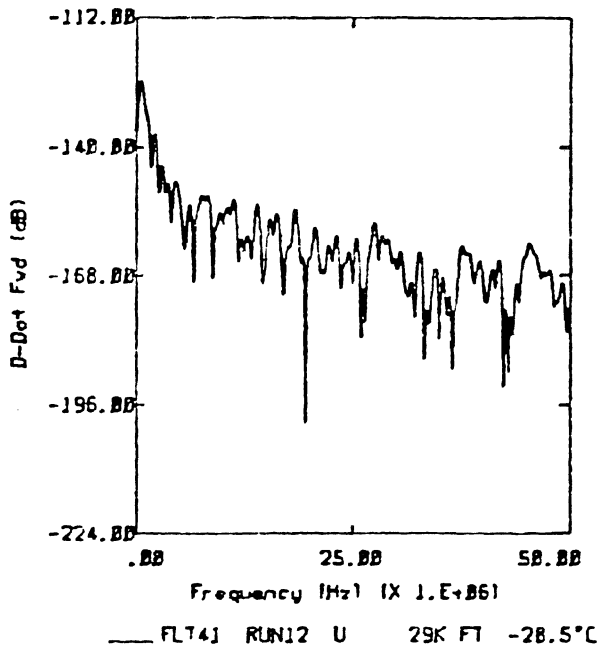
-112.00
-140.00
-168.00
-196.00
-224.00
D-Dot Fwd (dB)
.00
25.00
50.00
Frequency (Hz) (X 1.E+06)
FLT41 RUN12 U 29K FT -28.5°C

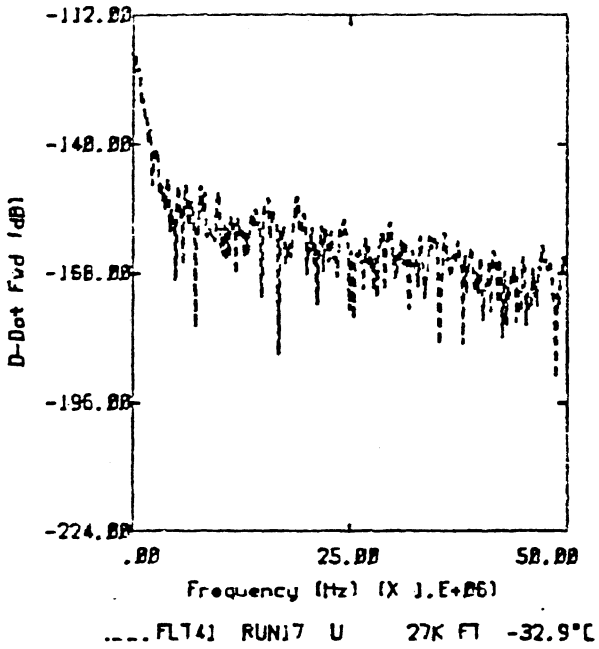
-112.00
-140.00
-168.00
-196.00
-224.00
D-Dot Fwd (dB)
.00
25.00
50.00
Frequency (Hz) (X 1.E+06)
FLT41 RUN17 U 27K FT -32.9°C

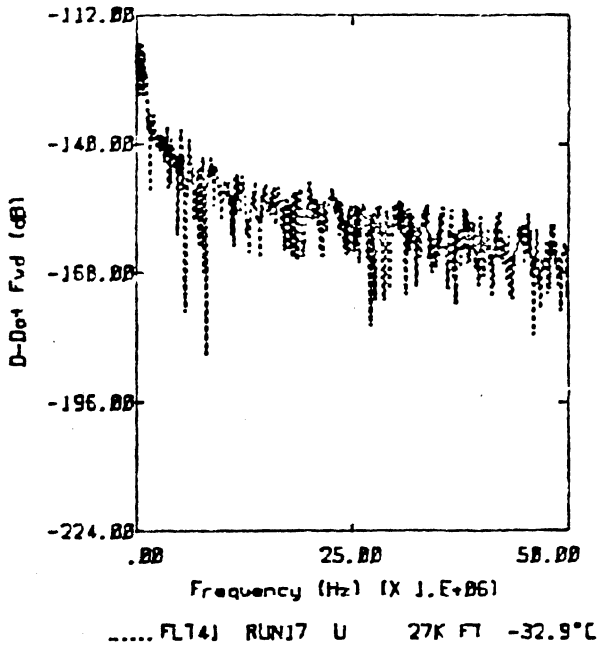
-112.00
-140.00
-168.00
-196.00
-224.00
D-Dot Fwd (dB)
.00
25.00
50.00
Frequency (Hz) (X 1.E+06)
FLT41 RUN17 U 27K FT -32.9°C

Category 1

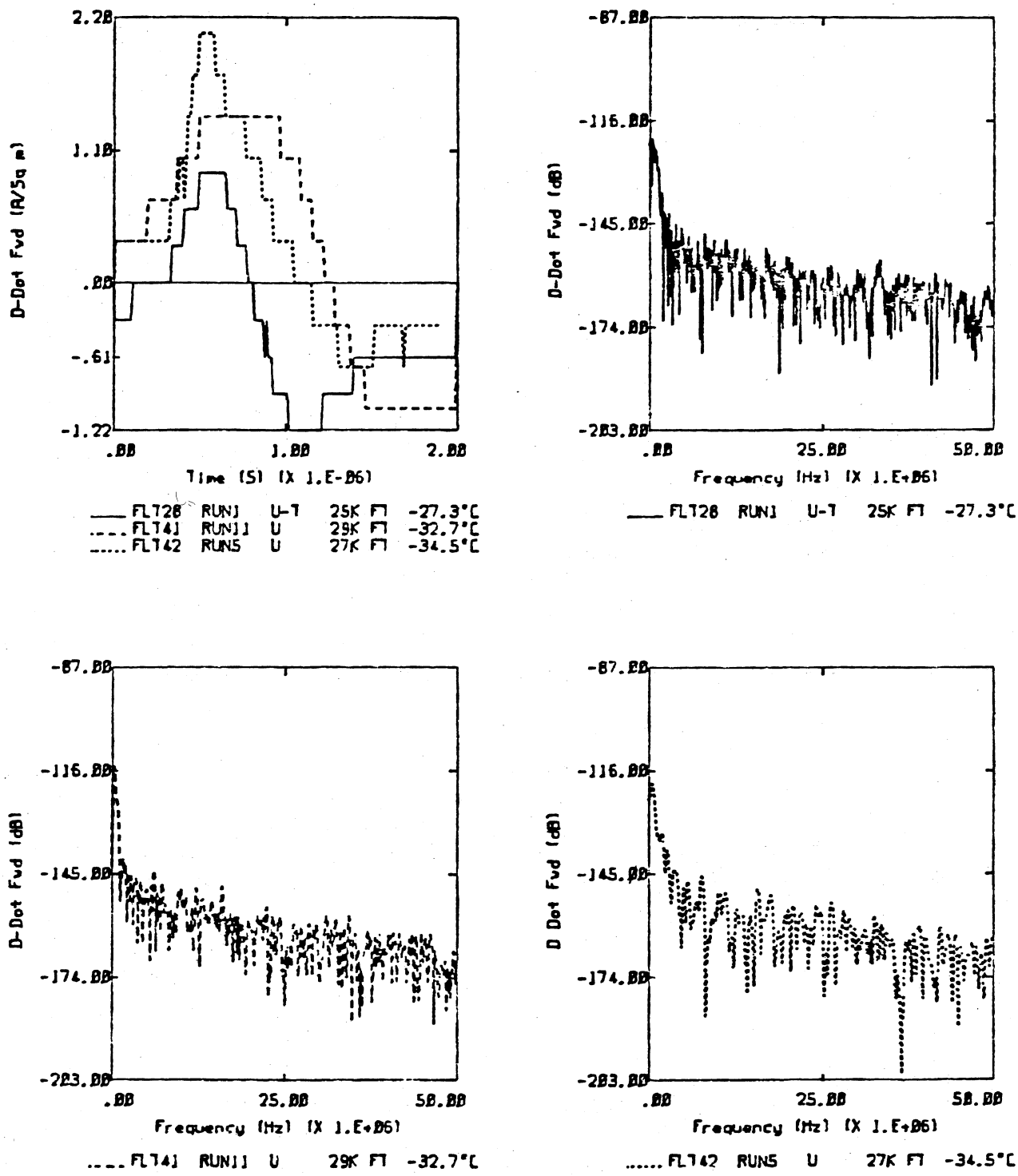
2.20
1.10
.00
-.61
-1.22
D-Dot Fvd (R/Sq m)
.00
1.00
2.00
Time (S) (X 1.E-06)
FLT28 RUN1 U-T 25K FT -27.3°C
FLT41 RUN11 U 29K FT -32.7°C
FLT42 RUN5 U 27K FT -34.5°C
-87.00
-116.00
-145.00
-174.00
-203.00
D-Dot Fvd (dB)
.00
25.00
50.00
Frequency (Hz) (X 1.E+06)
FLT28 RUN1 U-T 25K FT -27.3°C
-87.00
-116.00
-145.00
-174.00
-203.00
D-Dot Fvd (dB)
.00
25.00
50.00
Frequency (Hz) (X 1.E+06)
FLT41 RUN11 U 29K FT -32.7°C
-87.00
-116.00
-145.00
-174.00
-203.00
D Dot Fvd (dB)
.00
25.00
50.00
Frequency (Hz) (X 1.E+06)
FLT42 RUN5 U 27K FT -34.5°C

Category 1

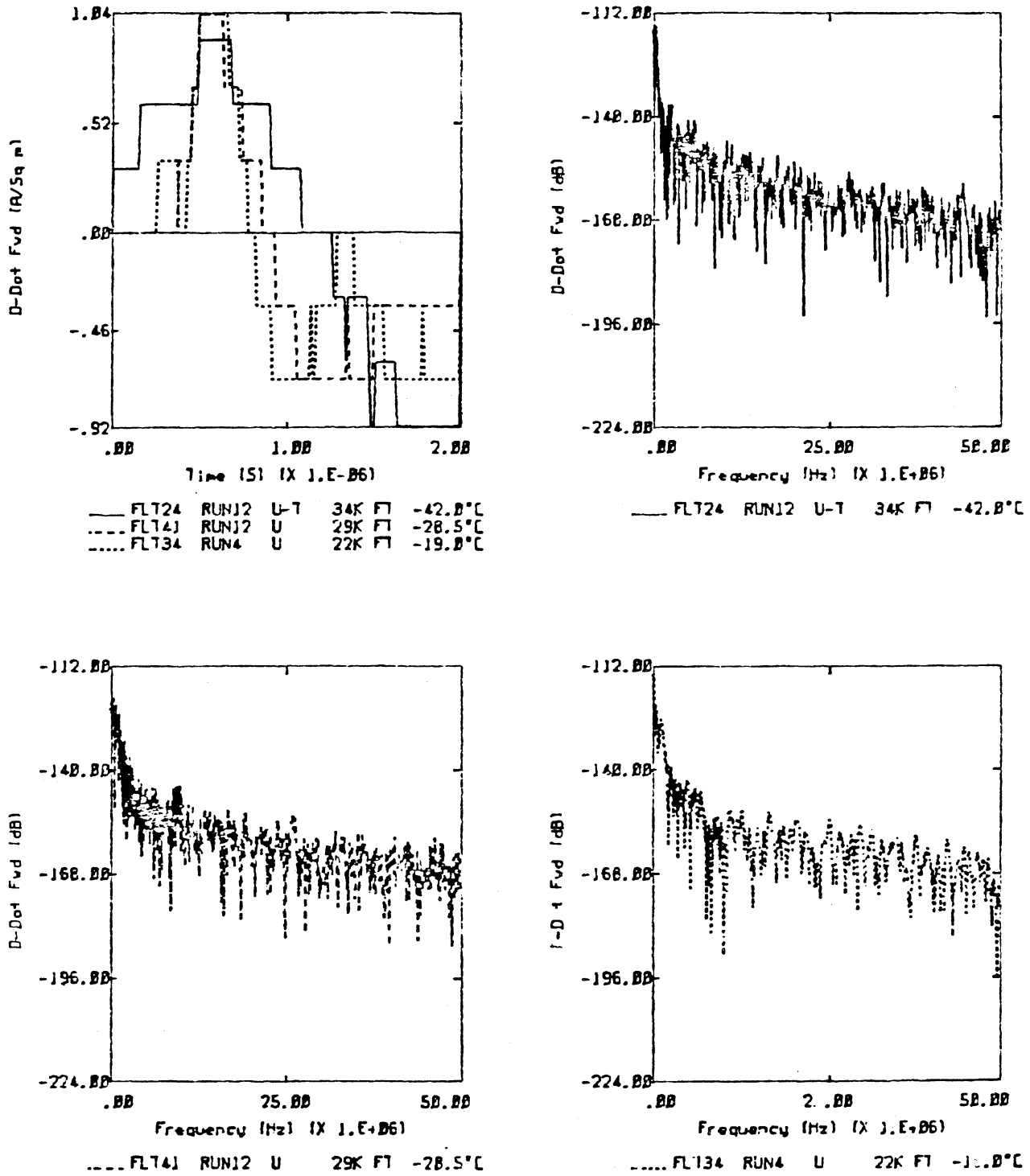
1.04
.52
.00
-.46
-.92
D-Dot Fwd (A/Sq m)
.00
1.00
2.00
Time (S) (X 1.E-06)
FLT24 RUN12 U-T 34K FT -42.0°C
FLT41 RUN12 U 29K FT -28.5°C
FLT34 RUN4 U 22K FT -19.0°C
-112.00
-140.00
-168.00
-196.00
-224.00
D-Dot Fwd (dB)
.00
25.00
50.00
Frequency (Hz) (X 1.E+06)
FLT24 RUN12 U-T 34K FT -42.0°C
-112.00
-140.00
-168.00
-196.00
-224.00
D-Dot Fwd (dB)
.00
25.00
50.00
Frequency (Hz) (X 1.E+06)
FLT41 RUN12 U 29K FT -28.5°C
-112.00
-140.00
-168.00
-196.00
-224.00
D-Dot Fwd (dB)
.00
50.00
Frequency (Hz) (X 1.E+06)
FLT34 RUN4 U 22K FT

Category 1

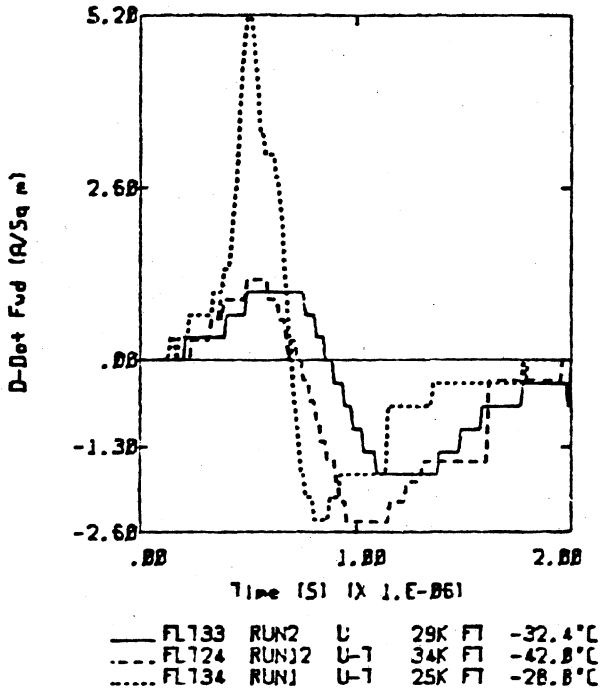
5.2Ø
2.6Ø
.ØØ
-1.3Ø
-2.6Ø
D-Dot Fvd (R/Sq m)
.ØØ
1.ØØ
2.ØØ
Time (S) (X 1.E-Ø6)
FL733 RUN2 U 29K FT -32.4°C
FL724 RUN12 U-T 34K FT -42.8°C
FL734 RUN1 U-T 25K FT -28.8°C

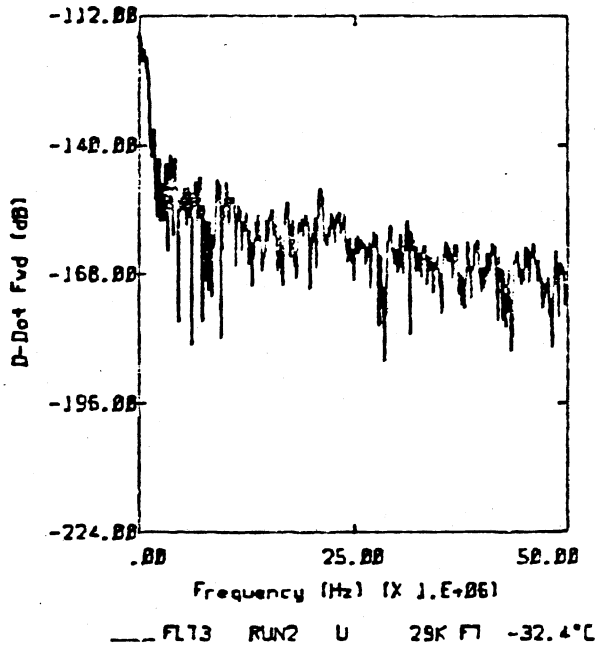
-112.ØØ
-14Ø.ØØ
-168.ØØ
-196.ØØ
-224.ØØ
D-Dot Fvd (dB)
.ØØ
25.ØØ
5Ø.ØØ
Frequency (Hz) (X 1.E+Ø6)
FL73 RUN2 U 29K FT -32.4°C

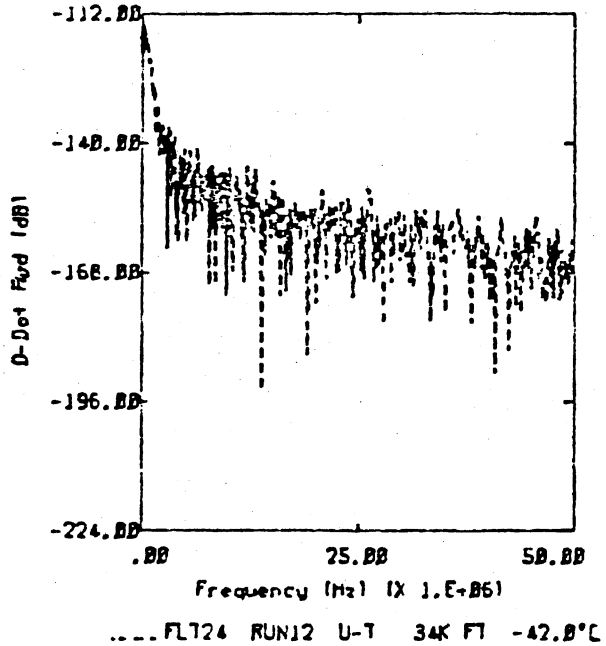
-112.ØØ
-14Ø.ØØ
-168.ØØ
-196.ØØ
-224.ØØ
D-Dot Fvd (dB)
.ØØ
25.ØØ
5Ø.ØØ
Frequency (Hz) (X 1.E+Ø6)
FL724 RUN12 U-T 34K FT -42.8°C

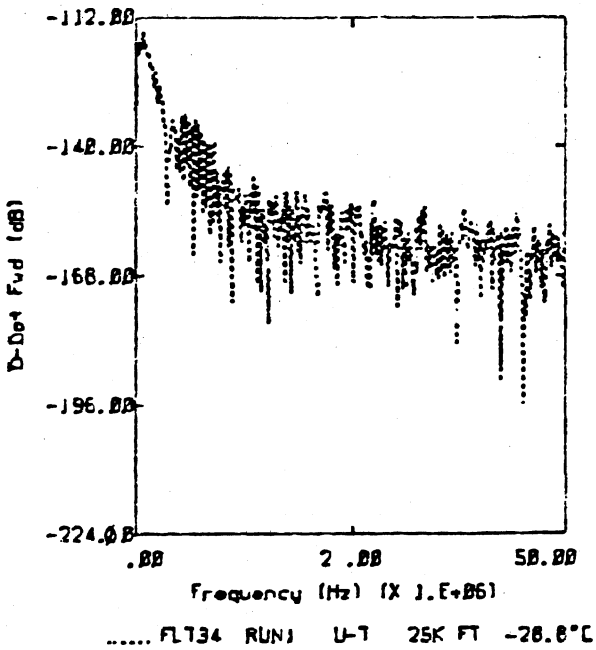
-112.ØØ
-14Ø.ØØ
-168.ØØ
-196.ØØ
-224.ØØ
D-Dot Fvd (dB)
.ØØ
2 .ØØ
5Ø.ØØ
Frequency (Hz) (X 1.E+Ø6)
FL734 RUN1 U-T 25K FT -28.8°C

Category 1

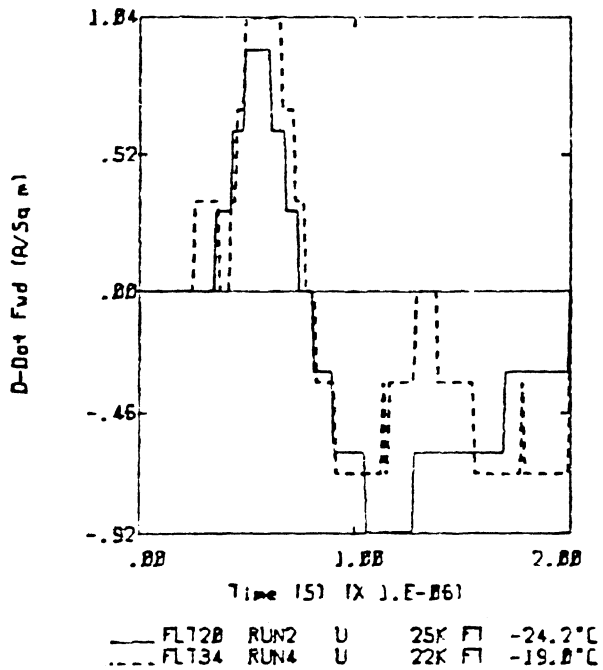
1.04
.52
.00
-.46
-.92
D-Dot Fwd (A/Sq m)
.00
1.00
2.00
Time (S) (X 1.E-06)
FLT20 RUN2 U 25K FT -24.2°C
FLT34 RUN4 U 22K FT -19.0°C

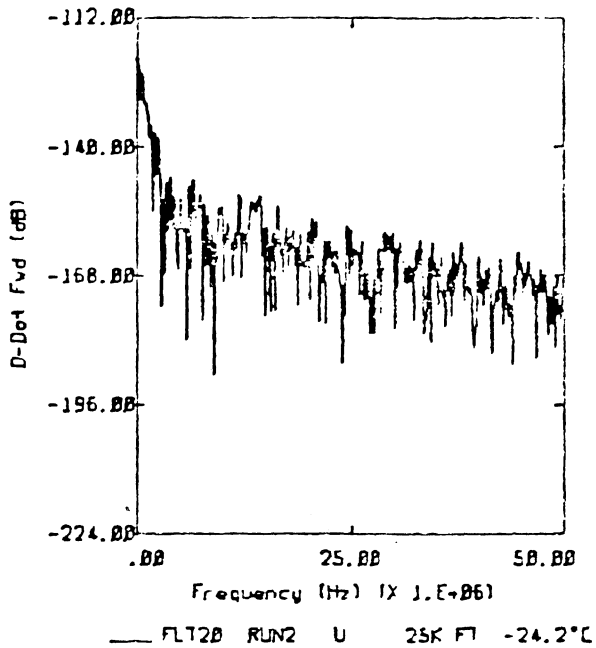
-112.00
-140.00
-168.00
-196.00
-224.00
D-Dot Fwd (dB)
.00
25.00
50.00
Frequency (Hz) (X 1.E+06)
FLT20 RUN2 U 25K FT -24.2°C

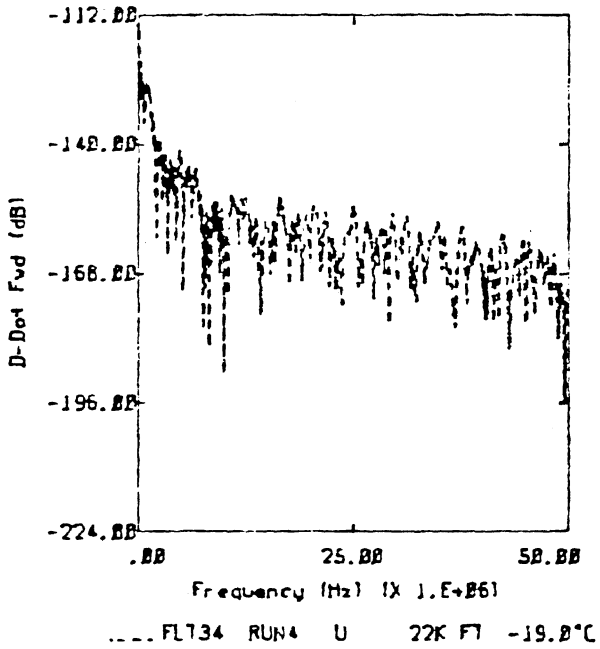
-112.00
-140.00
-168.00
-196.00
-224.00
D-Dot Fwd (dB)
.00
25.00
50.00
Frequency (Hz) (X 1.E+06)
FLT34 RUN4 U 22K FT -19.0°C

Category 1

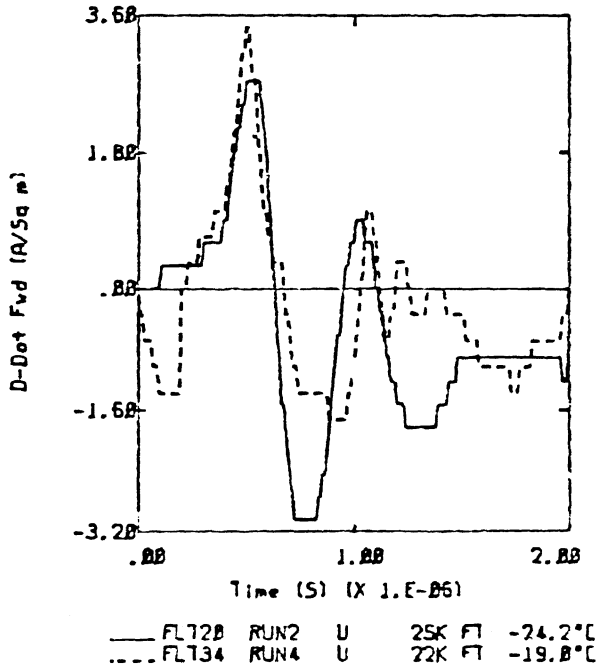
3.60
1.80
.00
-1.60
-3.20
D-Dot Fwd (A/Sq m)
.00
1.00
2.00
Time (S) (X 1.E-06)
FLT20 RUN2 U 25K FT -24.2°C
FLT34 RUN4 U 22K FT -19.0°C

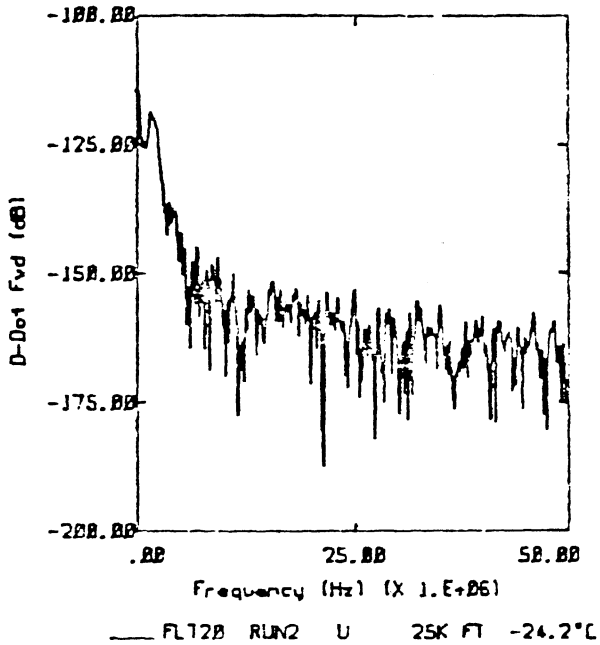
-100.00
-125.00
-150.00
-175.00
-200.00
D-Dot Fwd (dB)
.00
25.00
50.00
Frequency (Hz) (X 1.E+06)
FLT20 RUN2 U 25K FT -24.2°C

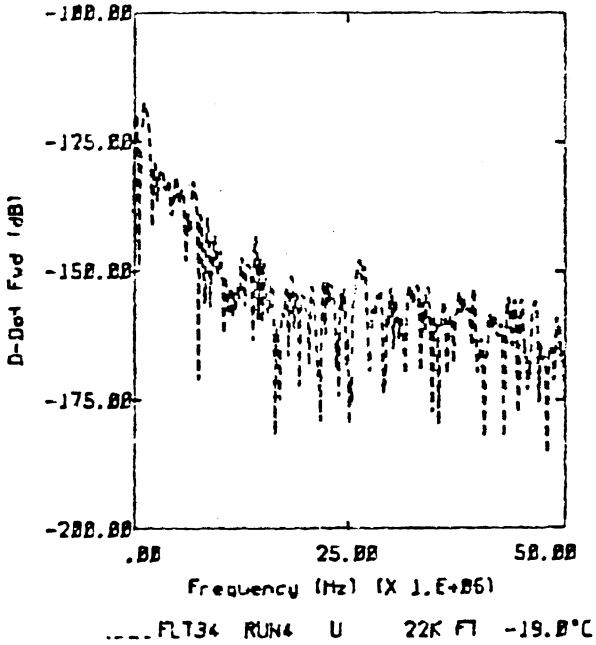
-100.00
-125.00
-150.00
-175.00
-200.00
D-Dot Fwd (dB)
.00
25.00
50.00
Frequency (Hz) (X 1.E+06)
FLT34 RUN4 U 22K FT -19.0°C

Category 1

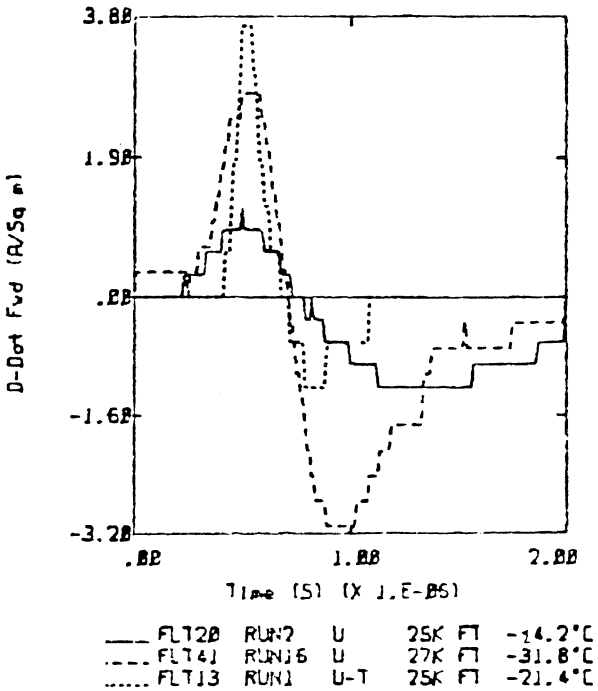
3.00
1.90
.00
-1.60
-3.20
D-Dot Fwd (A/Sq m)
.00
1.00
2.00
Time (S) (X 1.E-06)
FLT20 RUN2 U 25K FT -14.2°C
FLT41 RUN16 U 27K FT -31.8°C
FLT13 RUN1 U-T 25K FT -21.4°C

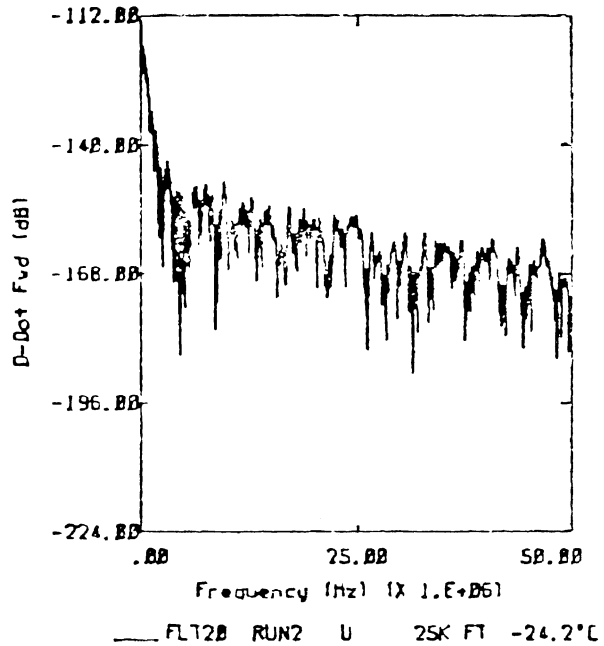
-112.00
-140.00
-168.00
-196.00
-224.00
D-Dot Fwd (dB)
.00
25.00
50.00
Frequency (Hz) (X 1.E+06)
FLT20 RUN2 U 25K FT -24.2°C

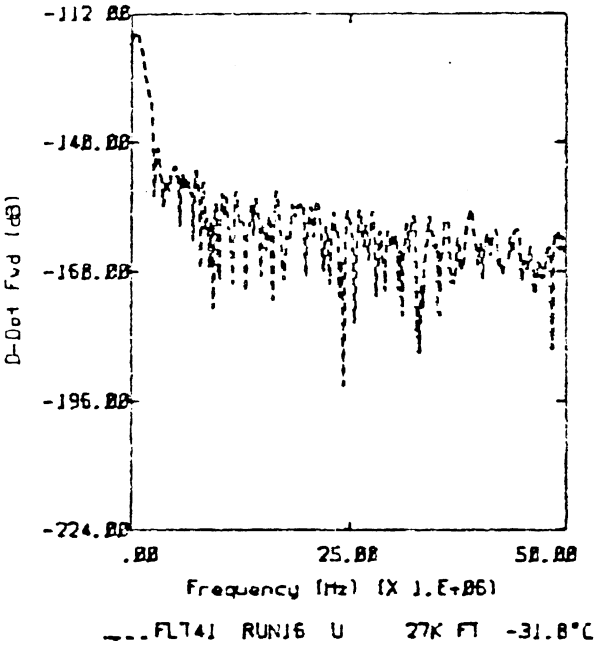
-112.00
-140.00
-168.00
-196.00
-224.00
D-Dot Fwd (dB)
.00
25.00
50.00
Frequency (Hz) (X 1.E+06)
FLT41 RUN16 U 27K FT -31.8°C

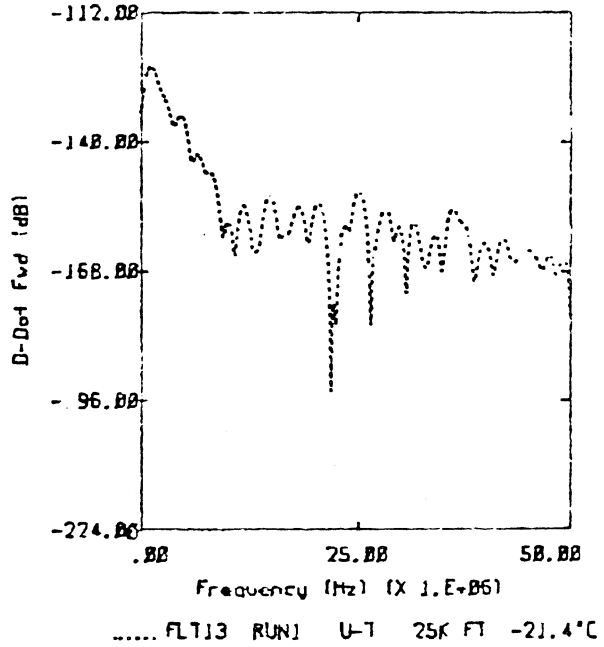
-112.00
-140.00
-168.00
-196.00
-224.00
D-Dot Fwd (dB)
.00
25.00
50.00
Frequency (Hz) (X 1.E+06)
FLT13 RUN1 U-T 25K FT -21.4°C

Category 1

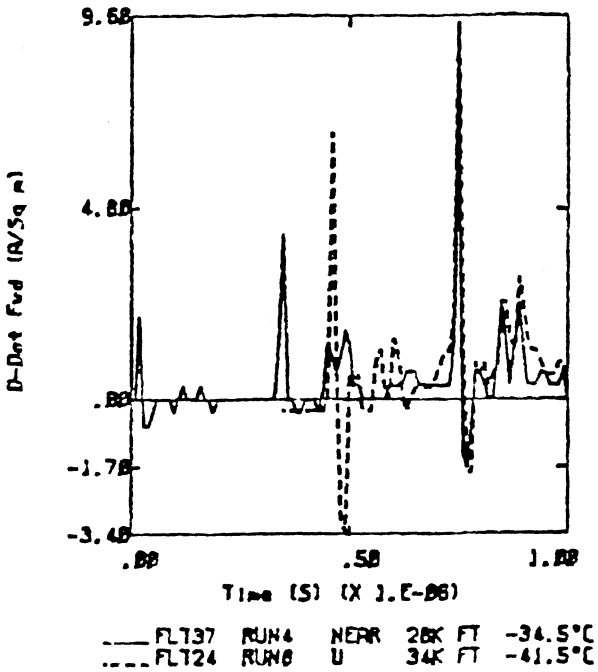
9.60
4.80
.00
-1.70
-3.40
D-Dot Fwd (V/Sq m)
.00
.50
1.00
Time (S) (X 1.E-06)
FLT37 RUN4 NEAR 28K FT -34.5°C
FLT24 RUN8 U 34K FT -41.5°C

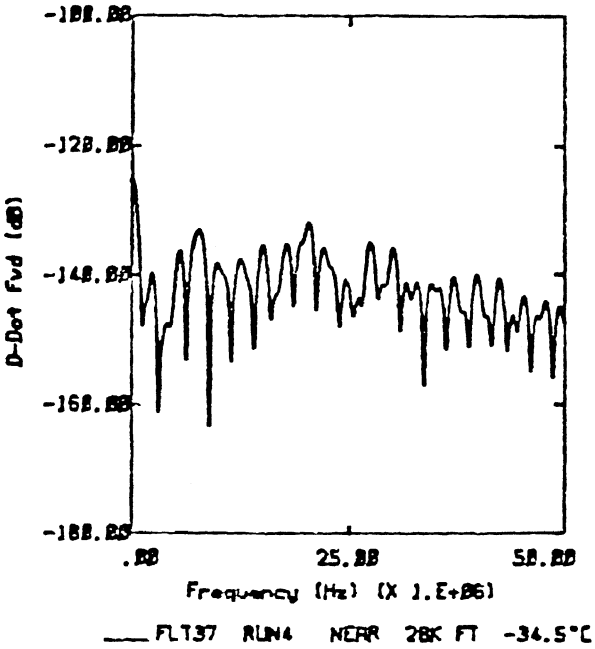
-100.00
-120.00
-140.00
-160.00
-180.00
D-Dot Fwd (dB)
.00
25.00
50.00
Frequency (Hz) (X 1.E+06)
FLT37 RUN4 NEAR 28K FT -34.5°C

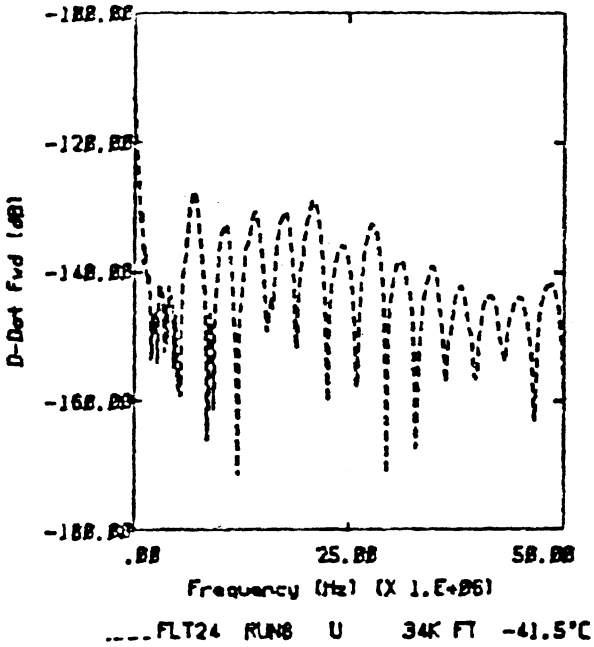
-100.00
-120.00
-140.00
-160.00
-180.00
D-Dot Fwd (dB)
.00
25.00
50.00
Frequency (Hz) (X 1.E+06)
FLT24 RUN8 U 34K FT -41.5°C

Category 2

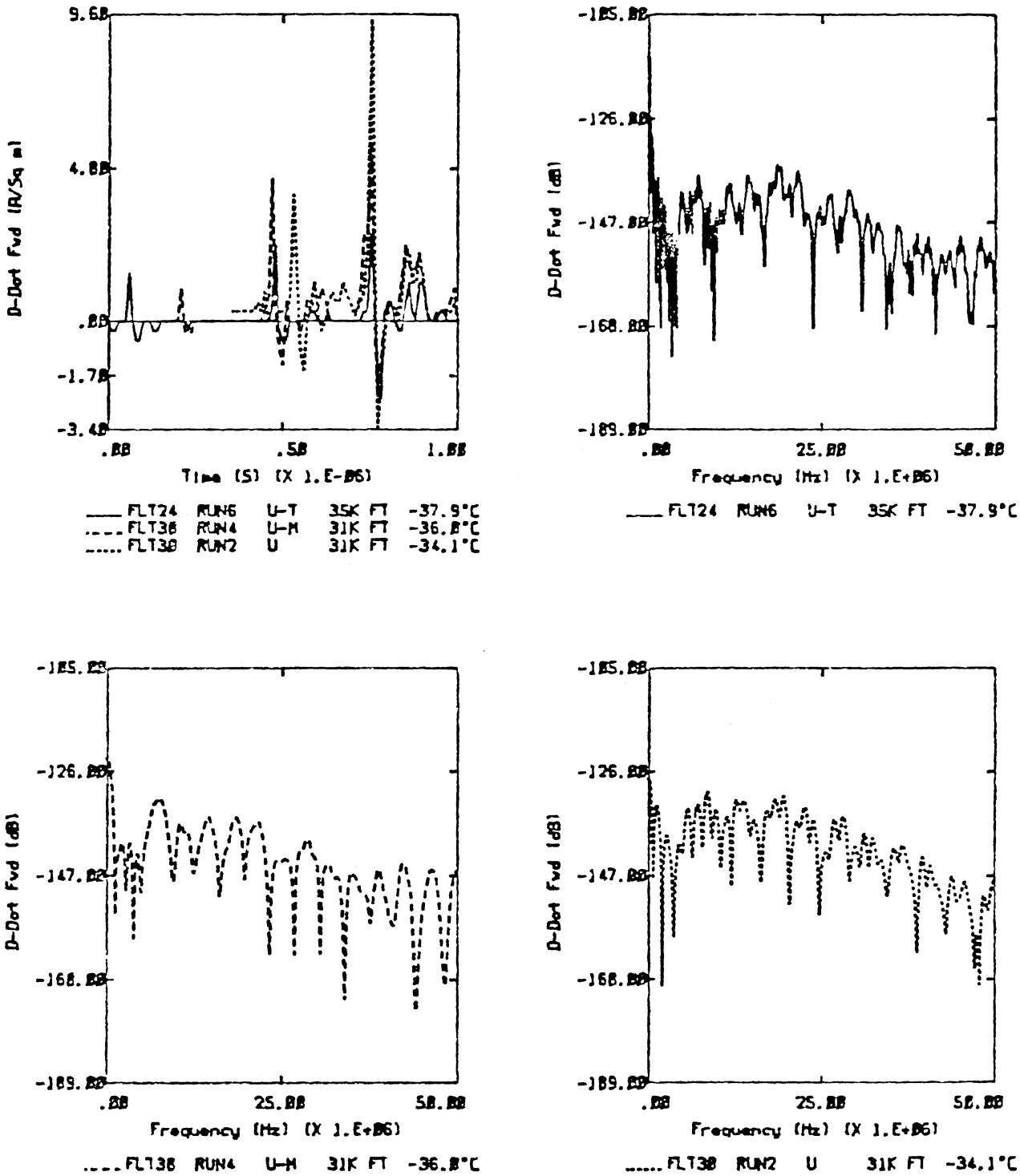
9.6B
4.BB
.BB
-1.7B
-3.4B
D-Dot Fvd (R/Sq m)
.BB
.5B
1.BB
Time (S) (X 1.E-B6)
FLT24 RUN6 U-T 35K FT -37.9°C
FLT38 RUN4 U-M 31K FT -36.B°C
FLT38 RUN2 U 31K FT -34.1°C
-185.BB
-126.BB
-147.BB
-168.BB
-189.BB
D-Dot Fvd (dB)
.BB
25.BB
5B.BB
Frequency (Hz) (X 1.E+B6)
FLT24 RUN6 U-T 35K FT -37.9°C
-185.BB
-126.BB
-147.BB
-168.BB
-189.BB
D-Dot Fvd (dB)
.BB
25.BB
5B.BB
Frequency (Hz) (X 1.E+B6)
FLT38 RUN4 U-M 31K FT -36.B°C
-185.BB
-126.BB
-147.BB
-168.BB
-189.BB
D-Dot Fvd (dB)
.BB
25.BB
5B.BB
Frequency (Hz) (X 1.E+B6)
FLT38 RUN2 U 31K FT -34.1°C

Category 2

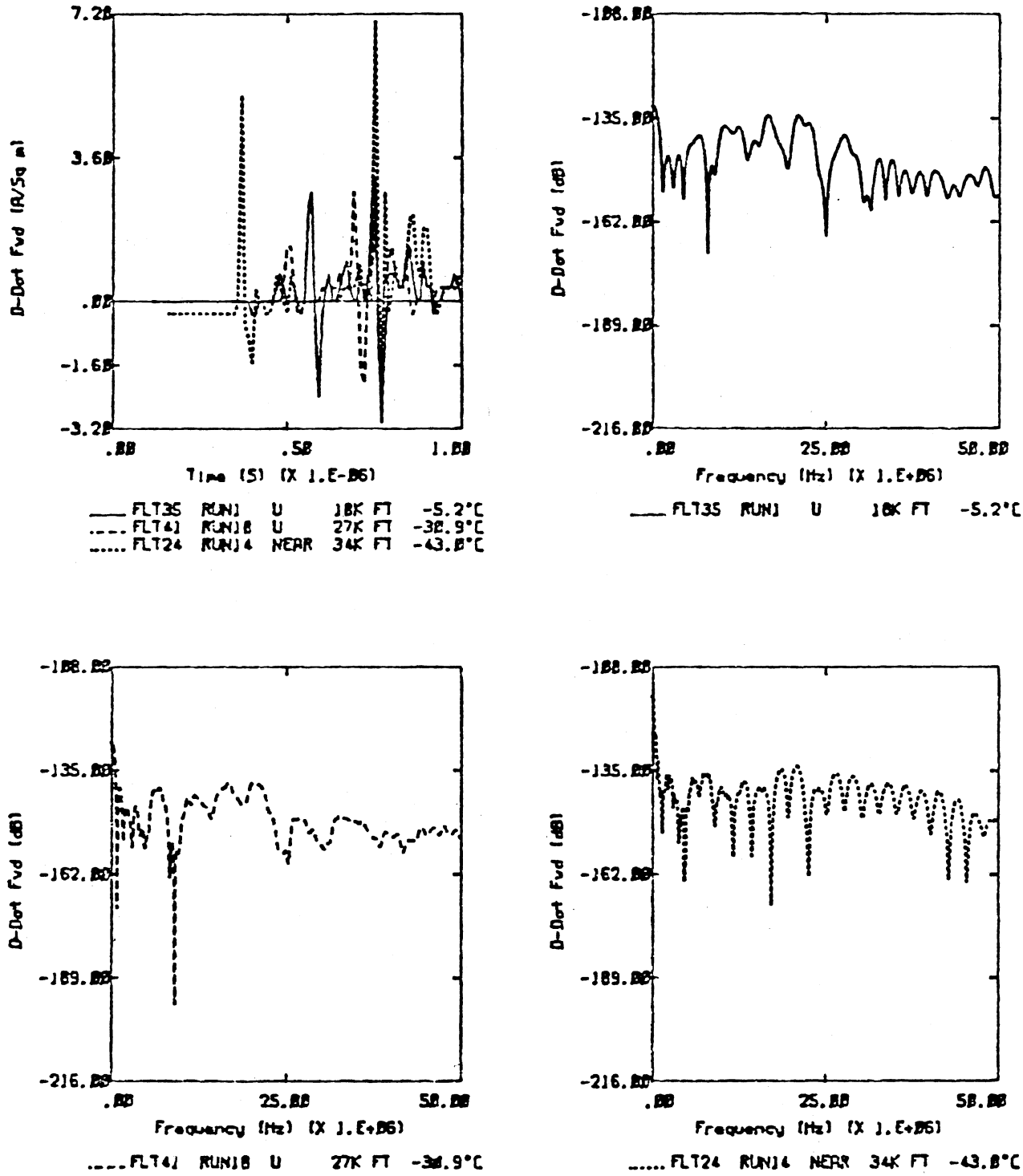
7.20
3.60
.00
-1.60
-3.20
D-Dot Fvd (A/Sq m)
.00
.50
1.00
Time (S) (X 1.E-06)
FLT35 RUN1 U 18K FT -5.2°C
FLT41 RUN18 U 27K FT -30.9°C
FLT24 RUN14 NEAR 34K FT -43.0°C
-108.00
-135.00
-162.00
-189.00
-216.00
D-Dot Fvd (dB)
.00
25.00
50.00
Frequency (Hz) (X 1.E+06)
FLT35 RUN1 U 18K FT -5.2°C
FLT41 RUN18 U 27K FT -30.9°C
FLT24 RUN14 NEAR 34K FT -43.0°C

Category 2

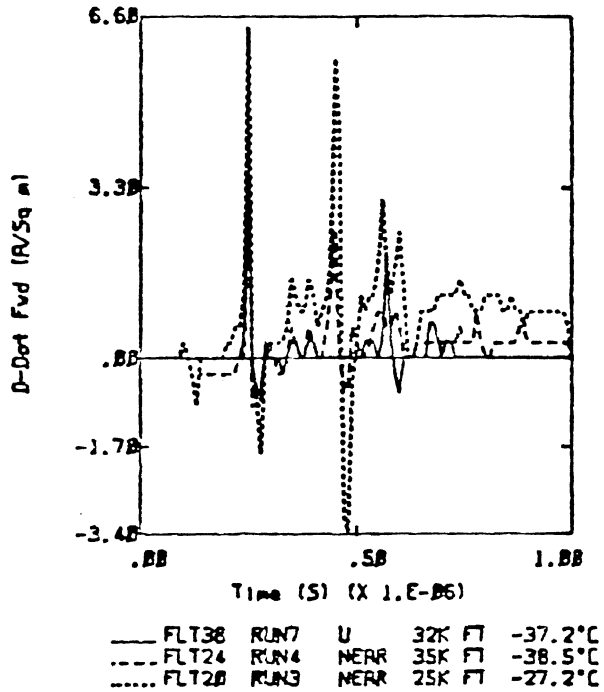
6.6B
3.3B
.BB
-1.7B
-3.4B
D-Dot Fvd (A/Sq m)
.BB
.5B
1.BB
Time (S) (X 1.E-B6)
FLT38 RUN7 U 32K FT -37.2°C
FLT24 RUN4 NEAR 35K FT -38.5°C
FLT2B RUN3 NEAR 25K FT -27.2°C

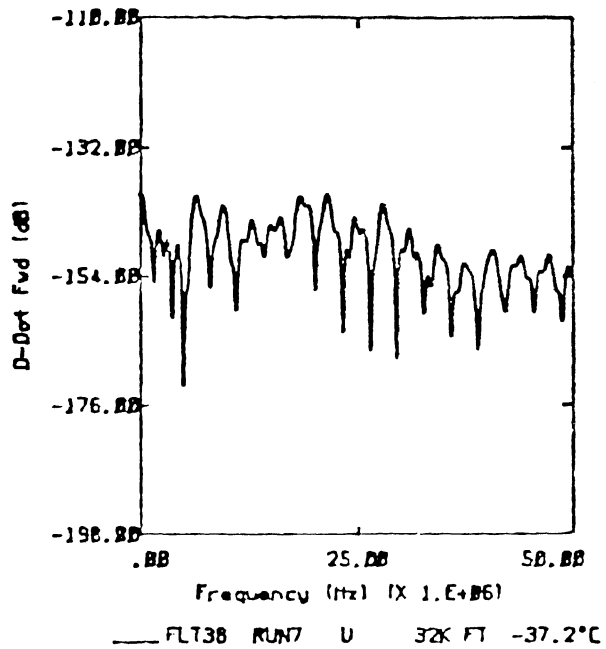
-11B.BB
-132.BB
-154.BB
-176.BB
-198.BB
D-Dot Fvd (dB)
.BB
25.BB
5B.BB
Frequency (Hz) (X 1.E+B6)
FLT38 RUN7 U 32K FT -37.2°C

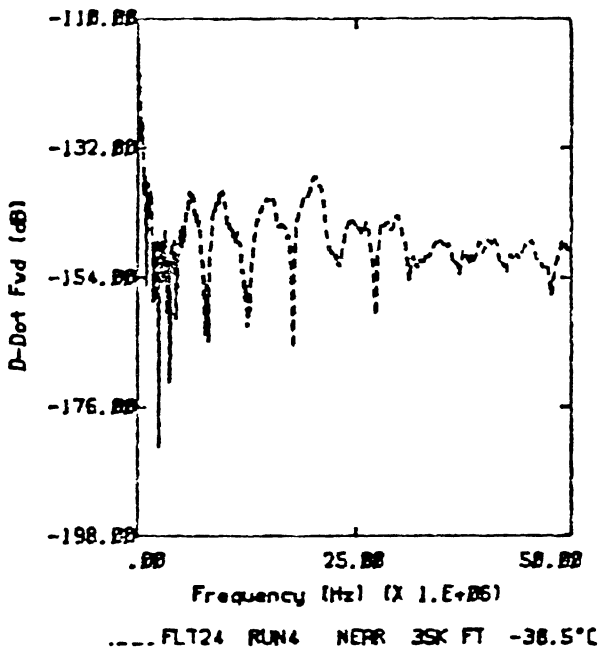
-11B.BB
-132.BB
-154.BB
-176.BB
-198.BB
D-Dot Fvd (dB)
.BB
25.BB
5B.BB
Frequency (Hz) (X 1.E+B6)
FLT24 RUN4 NEAR 35K FT -38.5°C

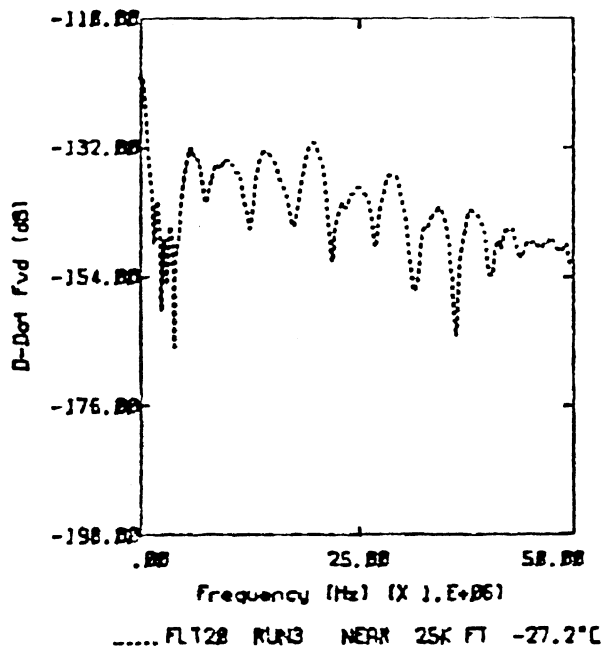
-11B.BB
-132.BB
-154.BB
-176.BB
-198.BB
D-Dot Fvd (dB)
.BB
25.BB
5B.BB
Frequency (Hz) (X 1.E+B6)
FLT2B RUN3 NEAR 25K FT -27.2°C

Category 2

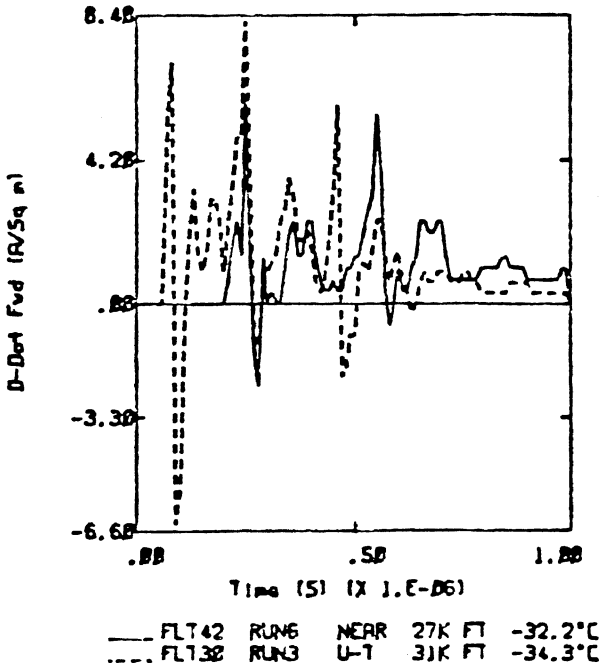
8.40
4.20
.00
-3.30
-6.60
D-Dot Fvd (A/Sq m)
.00
.50
1.00
Time (S) (X 1.E-06)
FLT42 RUN6 NEAR 27K FT -32.2°C
FLT38 RUN3 U-T 31K FT -34.3°C

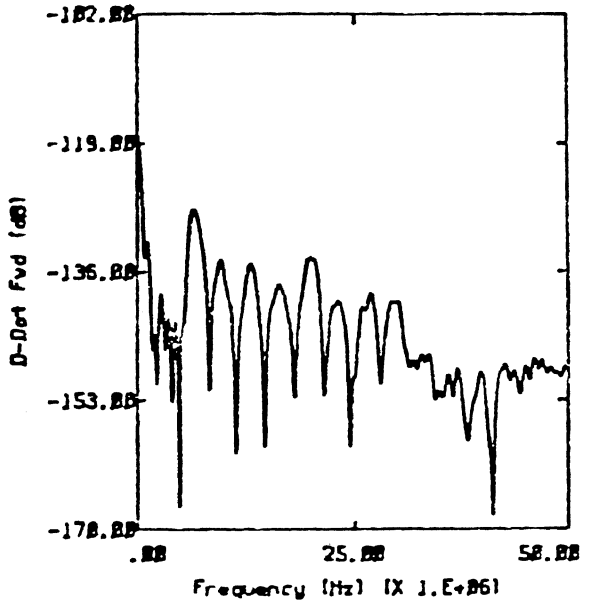
-102.00
-119.00
-136.00
-153.00
-170.00
D-Dot Fvd (dB)
.00
25.00
50.00
Frequency (Hz) (X 1.E+06)
FLT42 RUN6 NEAR 27K FT -32.2°C

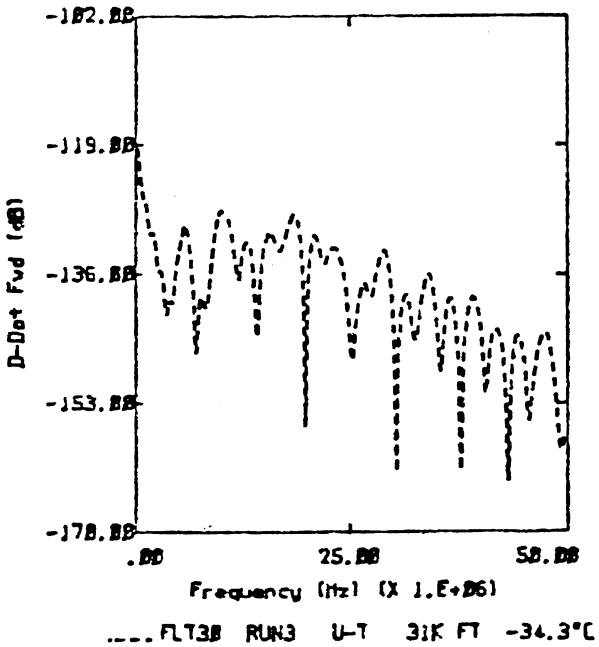
-102.00
-119.00
-136.00
-153.00
-170.00
D-Dot Fvd (dB)
.00
25.00
50.00
Frequency (Hz) (X 1.E+06)
FLT38 RUN3 U-T 31K FT -34.3°C

Category 2

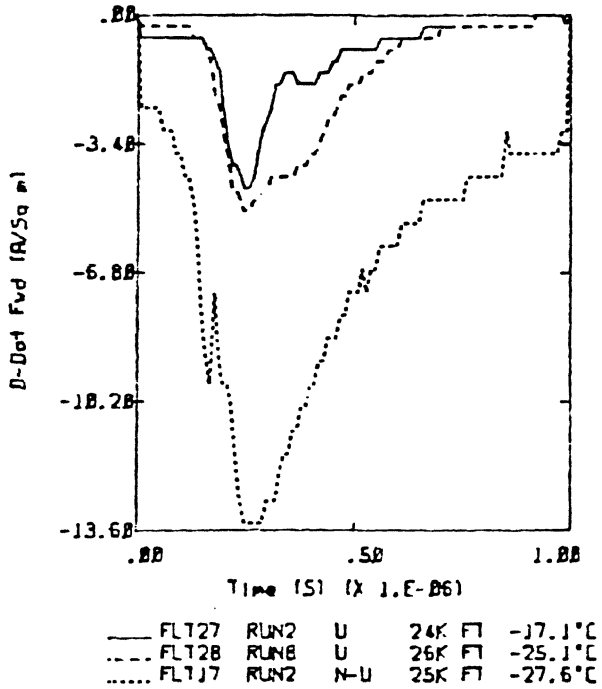
.00
-3.40
-6.80
-10.20
-13.60
D-Dot Fwd (A/Sq m)
.00
.50
1.00
Time (S) (X 1.E-06)
FLT27 RUN2 U 24K FT -17.1°C
FLT28 RUN8 U 26K FT -25.1°C
FLT17 RUN2 N-U 25K FT -27.6°C

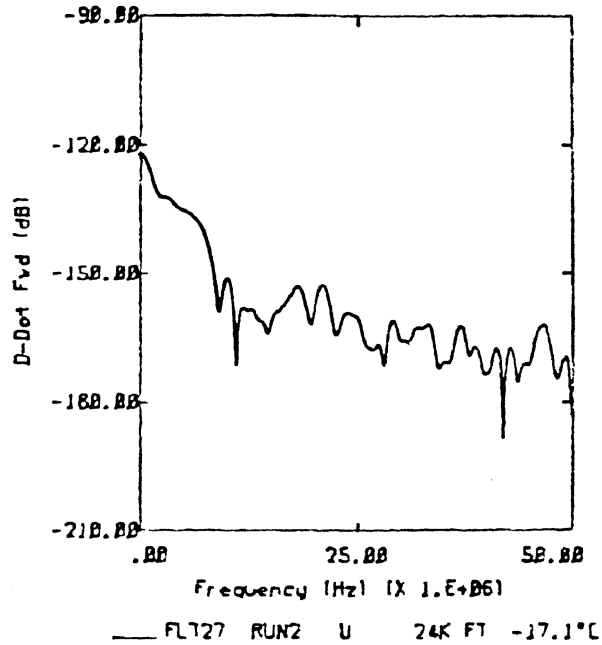
-90.00
-120.00
-150.00
-180.00
-210.00
D-Dot Fwd (dB)
.00
25.00
50.00
Frequency (Hz) (X 1.E+06)
FLT27 RUN2 U 24K FT -17.1°C

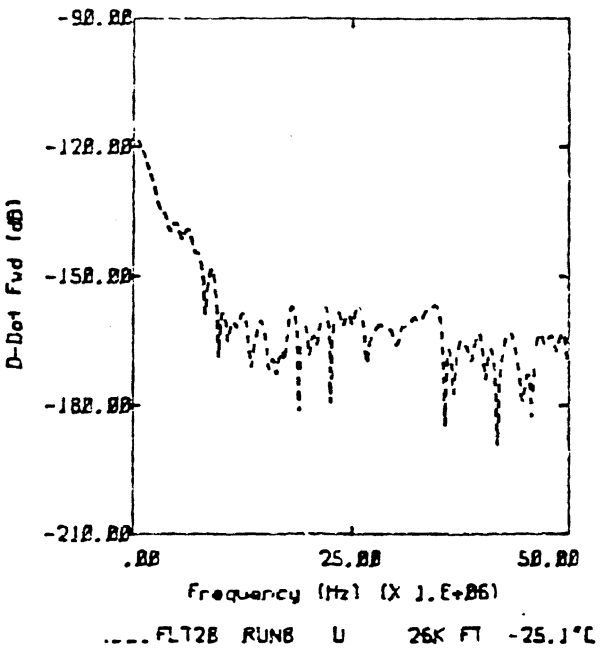
-90.00
-120.00
-150.00
-180.00
-210.00
D-Dot Fwd (dB)
.00
25.00
50.00
Frequency (Hz) (X 1.E+06)
FLT28 RUN8 U 26K FT -25.1°C

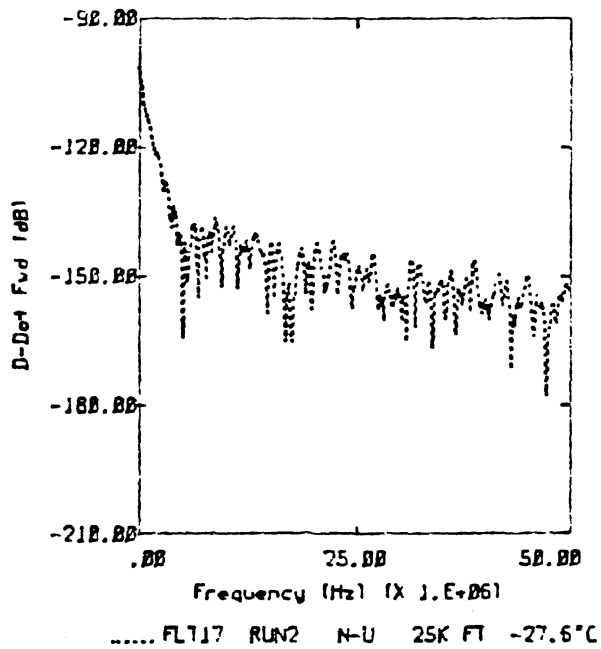
-90.00
-120.00
-150.00
-180.00
-210.00
D-Dot Fwd (dB)
.00
25.00
50.00
Frequency (Hz) (X 1.E+06)
FLT17 RUN2 N-U 25K FT -27.6°C

Category 3

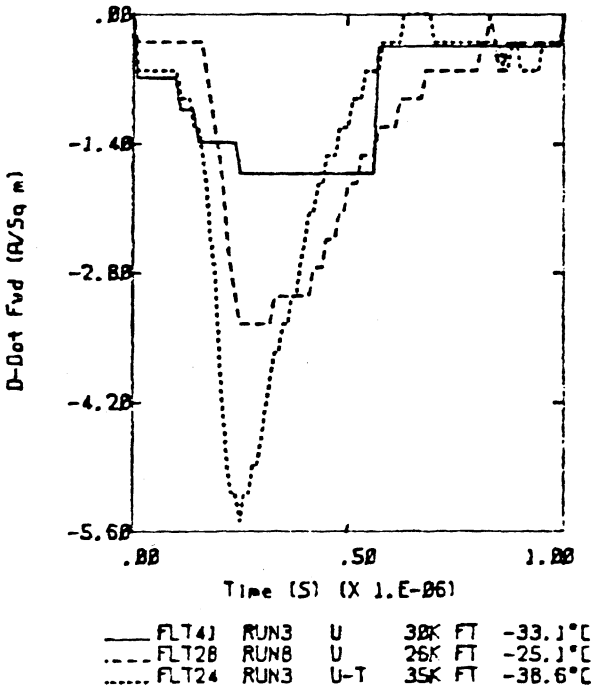
.00
-1.40
-2.80
-4.20
-5.60
D-Dot Fvd (A/Sq m)
.00
.50
1.00
Time (S) (X 1.E-06)
FLT41 RUN3 U 30K FT -33.1°C
FLT28 RUN8 U 26K FT -25.1°C
FLT24 RUN3 U-T 35K FT -38.6°C

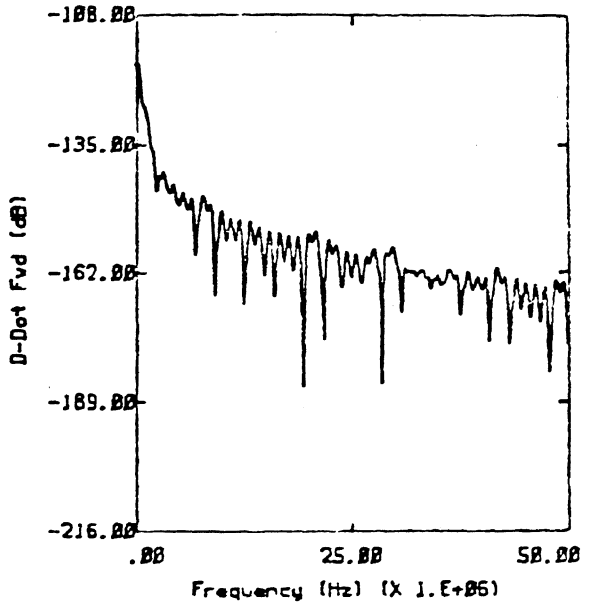
-108.00
-135.00
-162.00
-189.00
-216.00
D-Dot Fvd (dB)
.00
25.00
50.00
Frequency (Hz) (X 1.E+06)
FLT41 RUN3 U 30K FT -33.1°C

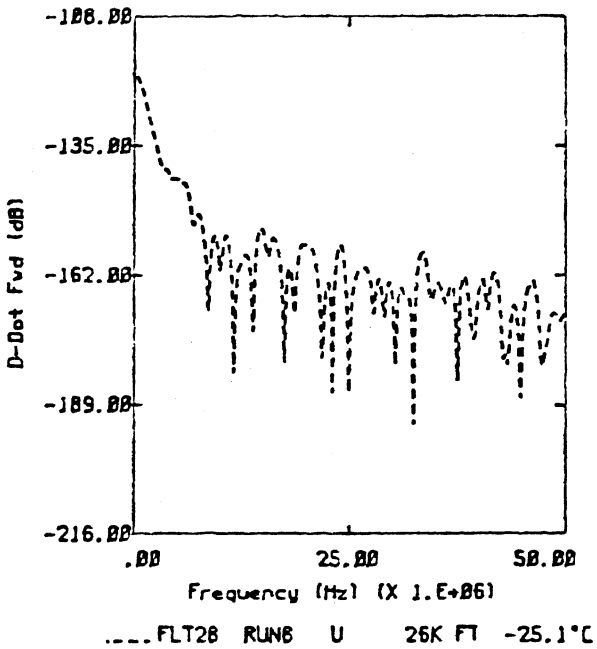
-108.00
-135.00
-162.00
-189.00
-216.00
D-Dot Fvd (dB)
.00
25.00
50.00
Frequency (Hz) (X 1.E+06)
FLT28 RUN8 U 26K FT -25.1°C

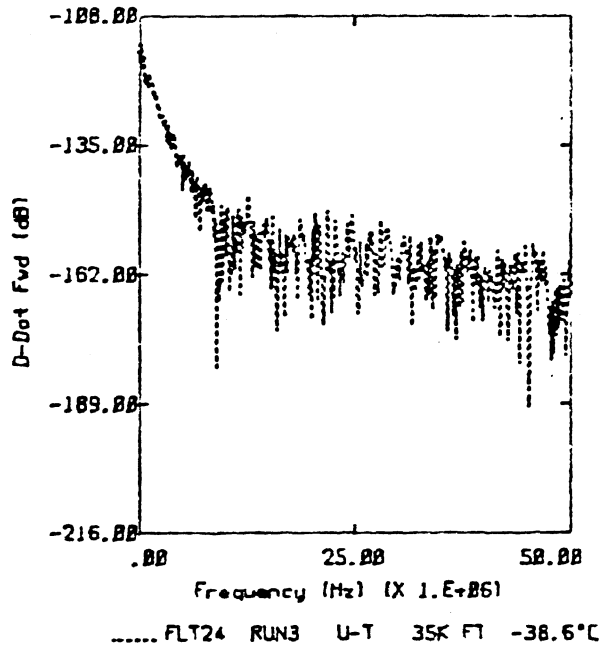
-108.00
-135.00
-162.00
-189.00
-216.00
D-Dot Fvd (dB)
.00
25.00
50.00
Frequency (Hz) (X 1.E+06)
FLT24 RUN3 U-T 35K FT -38.6°C

Category 3

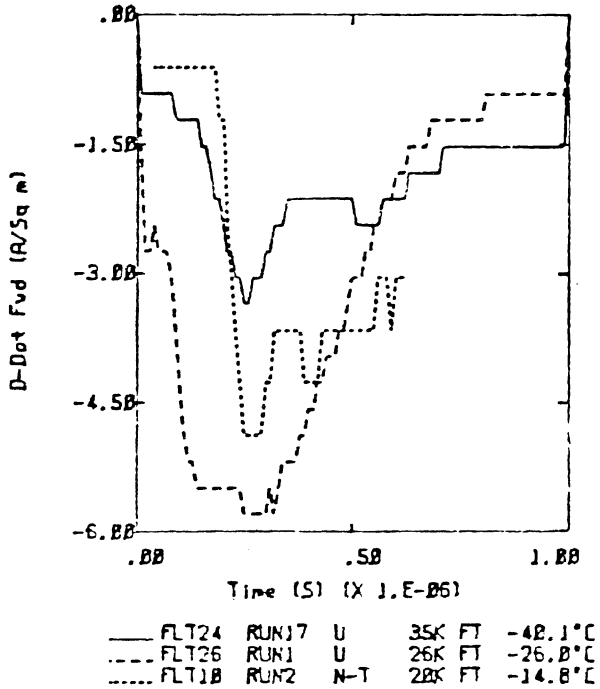
.00
-1.50
-3.00
-4.50
-6.00
D-Dot Fvd (A/Sq m)
.00
.50
1.00
Time (S) (X 1.E-06)
FLT24 RUN17 U 35K FT -40.1°C
FLT26 RUN1 U 26K FT -26.0°C
FLT18 RUN2 N-T 20K FT -14.8°C

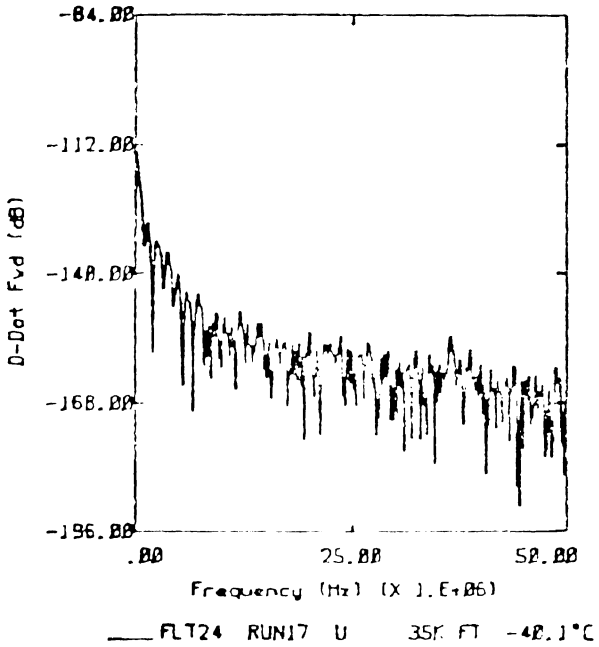
-84.00
-112.00
-140.00
-168.00
-196.00
D-Dot Fvd (dB)
.00
25.00
50.00
Frequency (Hz) (X 1.E+06)
FLT24 RUN17 U 35K FT -40.1°C

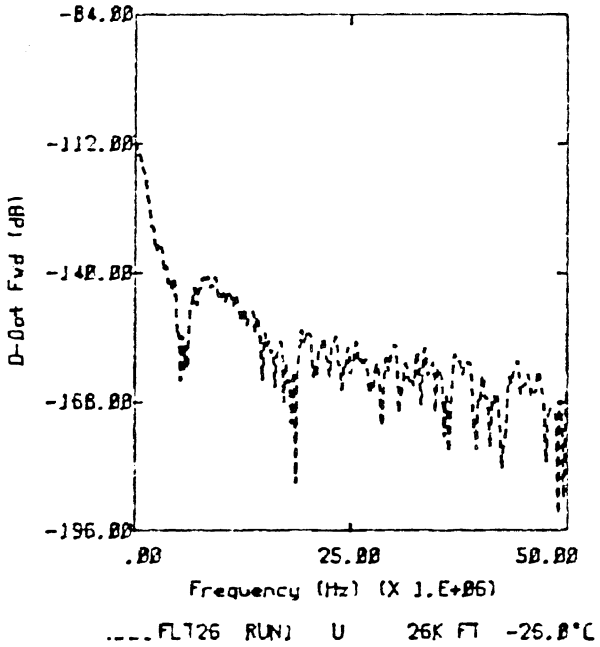
-84.00
-112.00
-140.00
-168.00
-196.00
D-Dot Fvd (dB)
.00
25.00
50.00
Frequency (Hz) (X 1.E+06)
FLT26 RUN1 U 26K FT -26.0°C

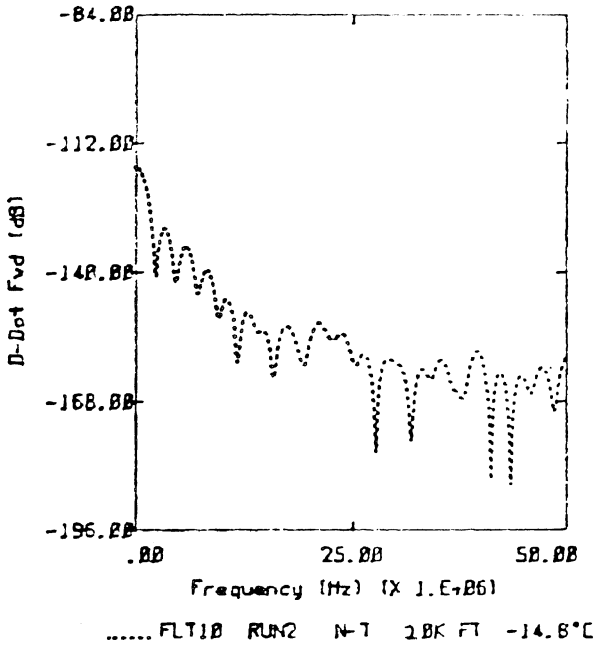
-84.00
-112.00
-140.00
-168.00
-196.00
D-Dot Fvd (dB)
.00
25.00
50.00
Frequency (Hz) (X 1.E+06)
FLT18 RUN2 N-T 20K FT -14.8°C

Category 3

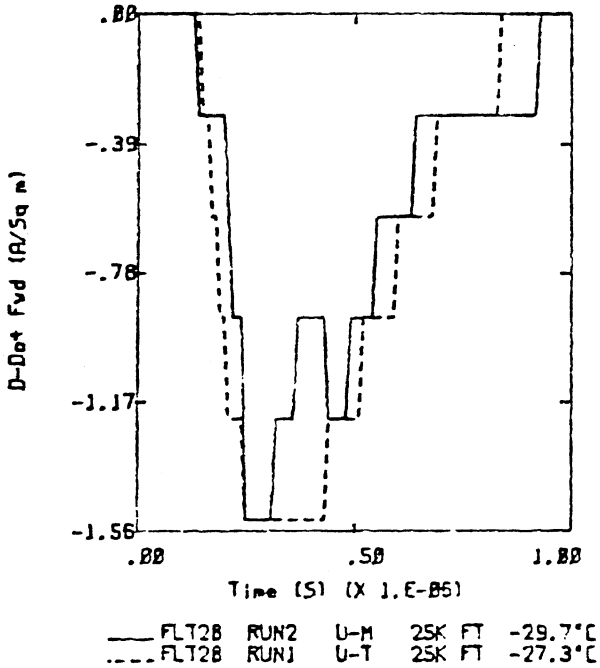
.00
-.39
-.78
-1.17
-1.56
D-Dot Fvd (A/Sq m)
.00
.50
1.00
Time (S) (X 1.E-06)
FLT28 RUN2 U-M 25K FT -29.7°C
FLT28 RUN1 U-T 25K FT -27.3°C

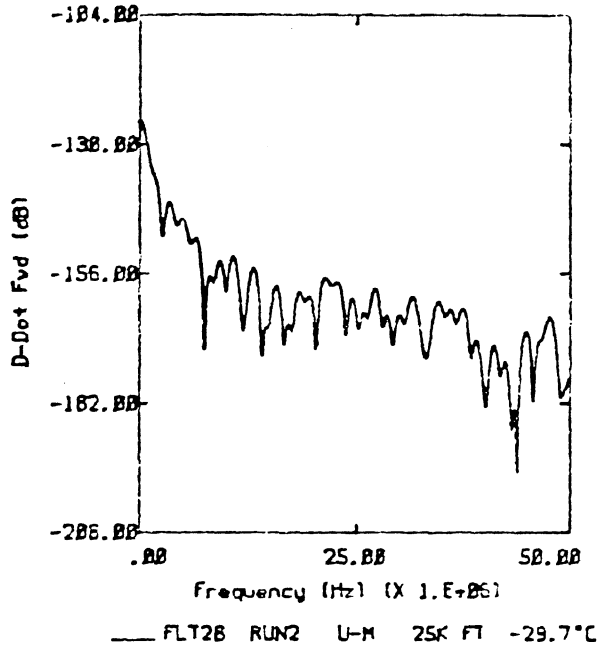
-104.00
-130.00
-156.00
-182.00
-208.00
D-Dot Fvd (dB)
.00
25.00
50.00
Frequency (Hz) (X 1.E+06)
FLT28 RUN2 U-M 25K FT -29.7°C

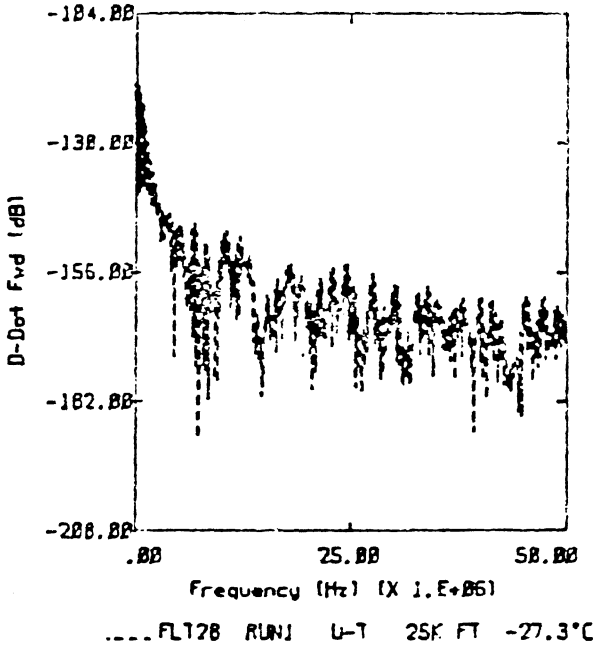
-104.00
-130.00
-156.00
-182.00
-208.00
D-Dot Fvd (dB)
.00
25.00
50.00
Frequency (Hz) (X 1.E+06)
FLT28 RUN1 U-T 25K FT -27.3°C

Category 3

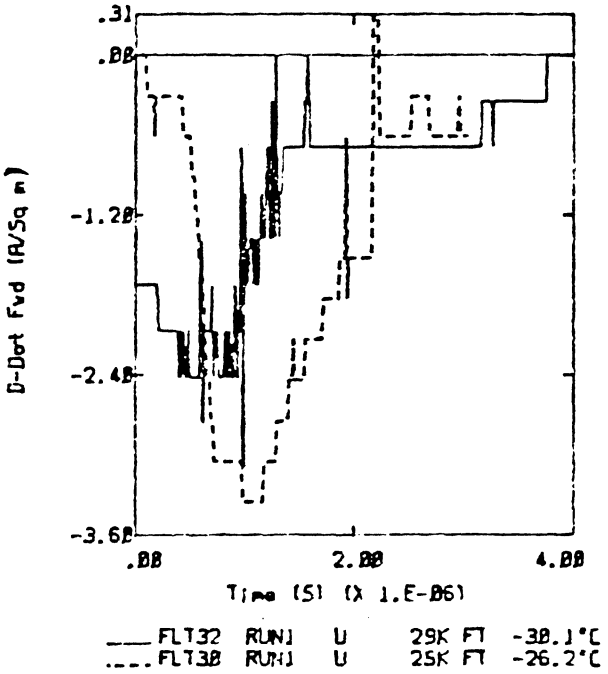
.31
.00
-1.20
-2.40
-3.60
.00
2.00
4.00
D-Dot Fwd (A/Sq m)
Time (S) (X 1.E-06)
FLT32 RUN1 U 29K FT -30.1°C
FLT30 RUN1 U 25K FT -26.2°C

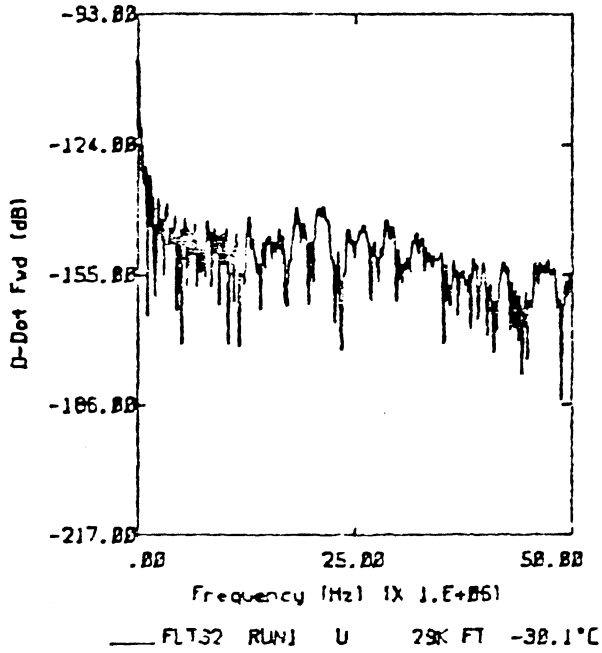
-93.00
-124.00
-155.00
-186.00
-217.00
.00
25.00
50.00
D-Dot Fwd (dB)
Frequency (Hz) (X 1.E+06)
FLT32 RUN1 U 29K FT -30.1°C

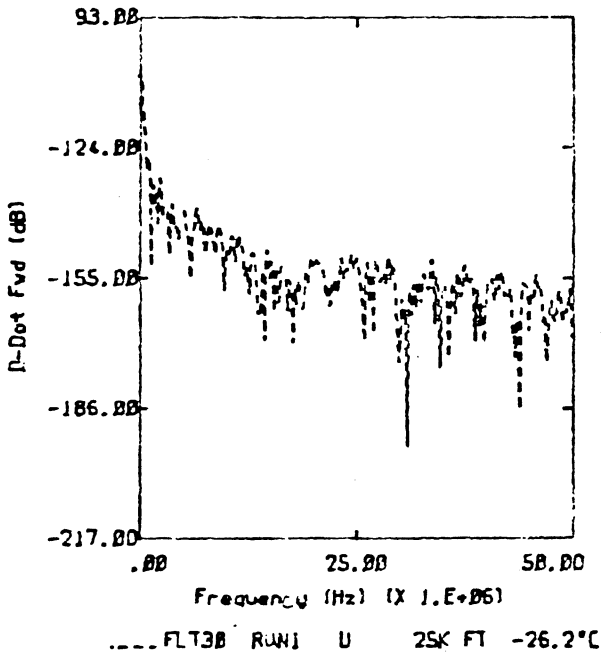
93.00
-124.00
-155.00
-186.00
-217.00
.00
25.00
50.00
D-Dot Fwd (dB)
Frequency (Hz) (X 1.E+06)
FLT30 RUN1 U 25K FT -26.2°C

Category 3

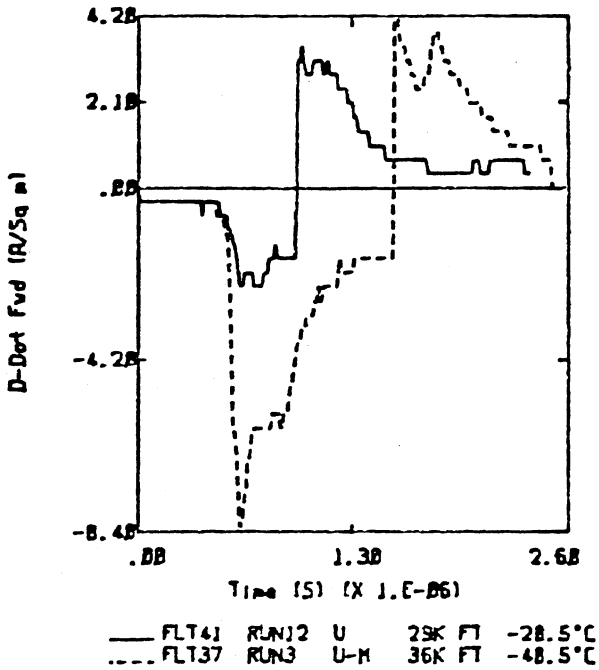
4.2B
2.1B
.BB
-4.2B
-8.4B
D-Dot Fvd (R/Sq m)
.BB
1.3B
2.6B
Time (S) (X 1.E-B6)
FLT41 RUN12 U 29K FT -28.5°C
FLT37 RUN3 U-M 36K FT -48.5°C

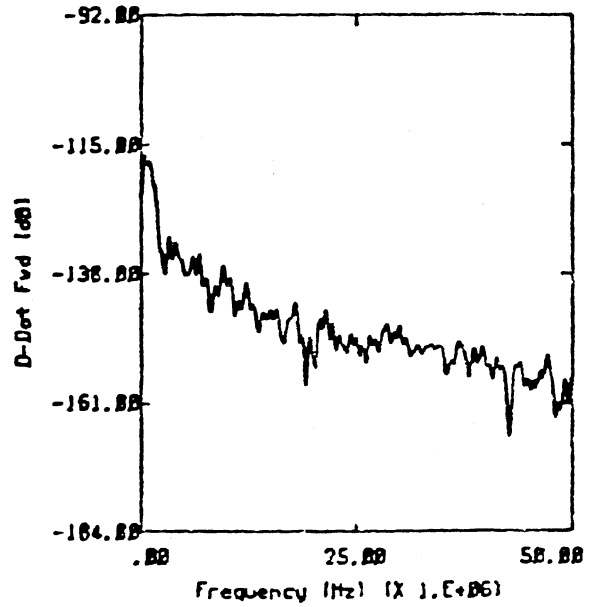
-92.BB
-115.BB
-138.BB
-161.BB
-184.BB
D-Dot Fvd (dB)
.BB
25.BB
5B.BB
Frequency (Hz) (X 1.E+B6)
FLT41 RUN12 U 29K FT -28.5°C

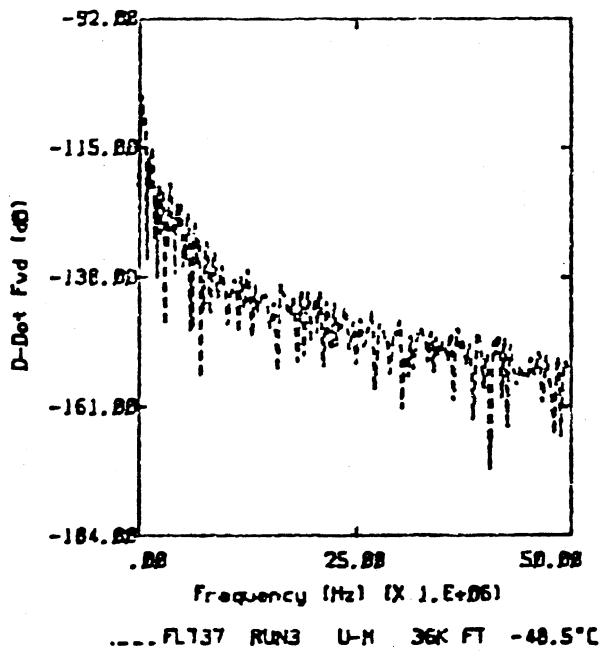
-92.BB
-115.BB
-138.BB
-161.BB
-184.BB
D-Dot Fvd (dB)
.BB
25.BB
5B.BB
Frequency (Hz) (X 1.E+B6)
FLT37 RUN3 U-M 36K FT -48.5°C

Category 4

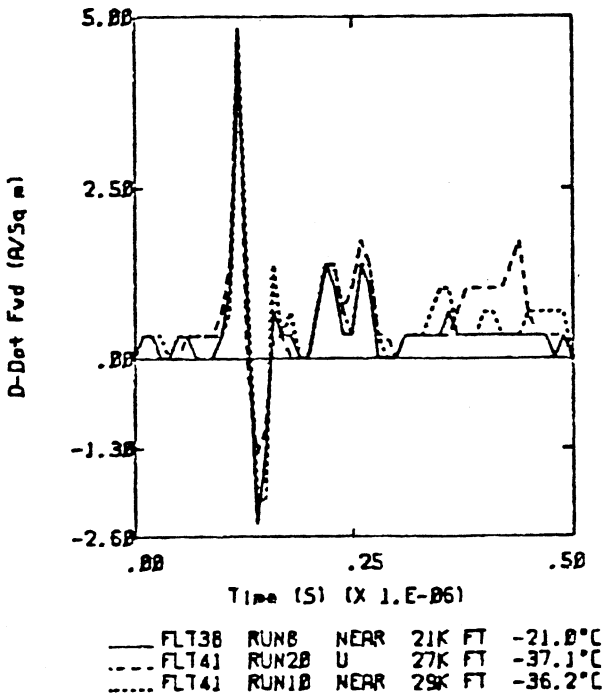
5.00
2.50
.00
-1.30
-2.60
.00
.25
.50
D-Dot Fvd (A/Sq m)
Time (S) (X 1.E-06)
FLT38 RUN8 NEAR 21K FT -21.0°C
FLT41 RUN20 U 27K FT -37.1°C
FLT41 RUN10 NEAR 29K FT -36.2°C

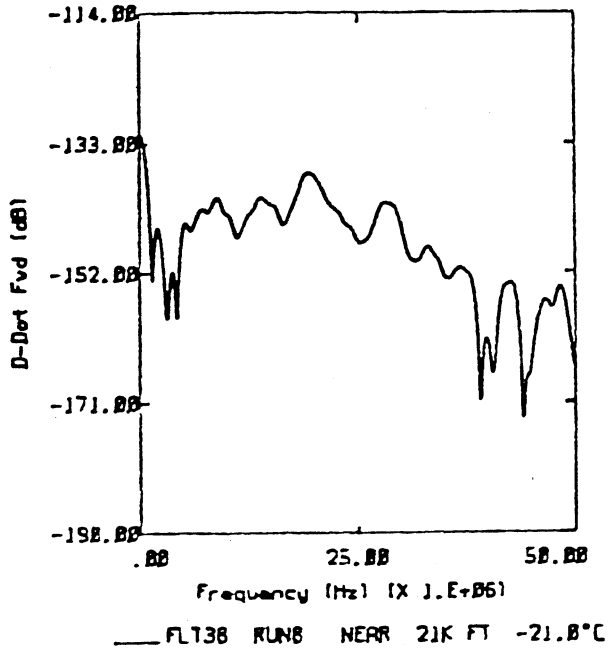
-114.00
-133.00
-152.00
-171.00
-190.00
.00
25.00
50.00
D-Dot Fvd (dB)
Frequency (Hz) (X 1.E+06)
FLT38 RUN8 NEAR 21K FT -21.0°C

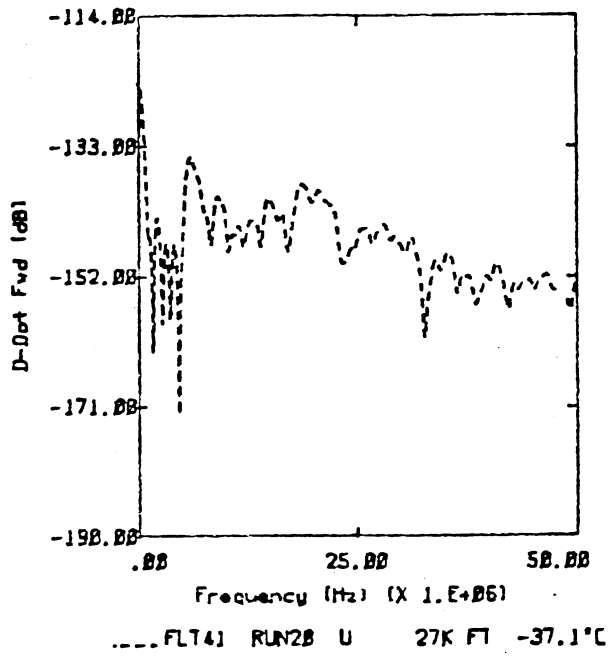
-114.00
-133.00
-152.00
-171.00
-190.00
.00
25.00
50.00
D-Dot Fvd (dB)
Frequency (Hz) (X 1.E+06)
FLT41 RUN20 U 27K FT -37.1°C

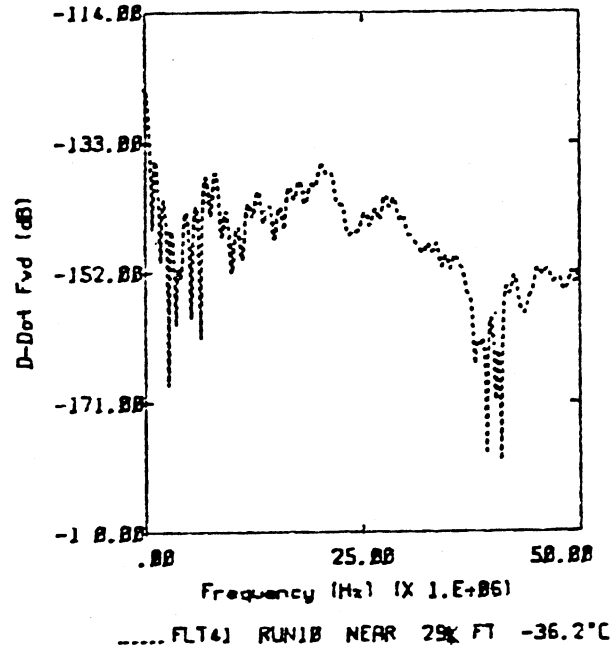
-114.00
-133.00
-152.00
-171.00
-1 0.00
.00
25.00
50.00
D-Dot Fvd (dB)
Frequency (Hz) (X 1.E+06)
FLT41 RUN10 NEAR 29K FT -36.2°C

Category 5

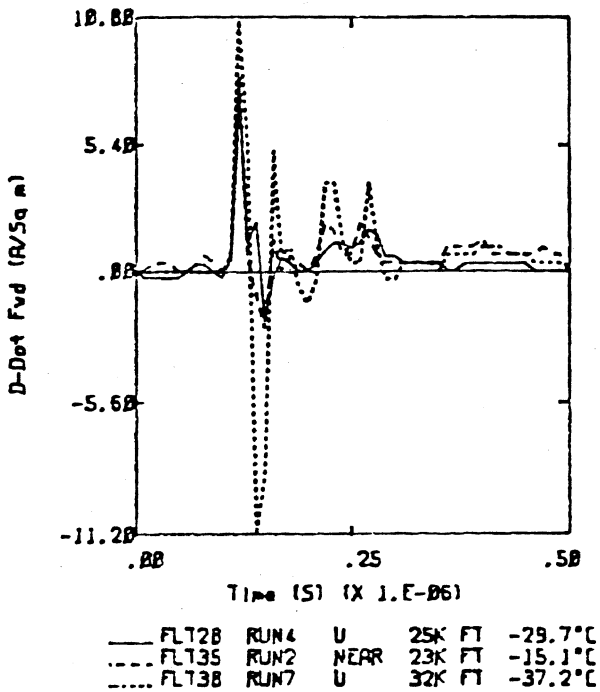
10.00
5.40
.00
-5.60
-11.20
D-Dot Fvd (A/Sq m)
.00
.25
.50
Time (S) (X 1.E-06)
FLT28 RUN4 U 25K FT -29.7°C
FLT35 RUN2 NEAR 23K FT -15.1°C
FLT38 RUN7 U 32K FT -37.2°C

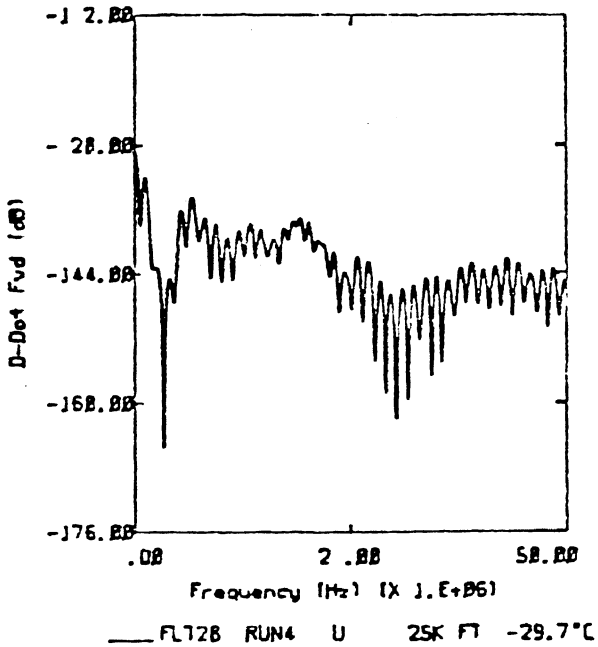
-112.00
-128.00
-144.00
-160.00
-176.00
D-Dot Fvd (dB)
.00
25.00
50.00
Frequency (Hz) (X 1.E+06)
FLT28 RUN4 U 25K FT -29.7°C

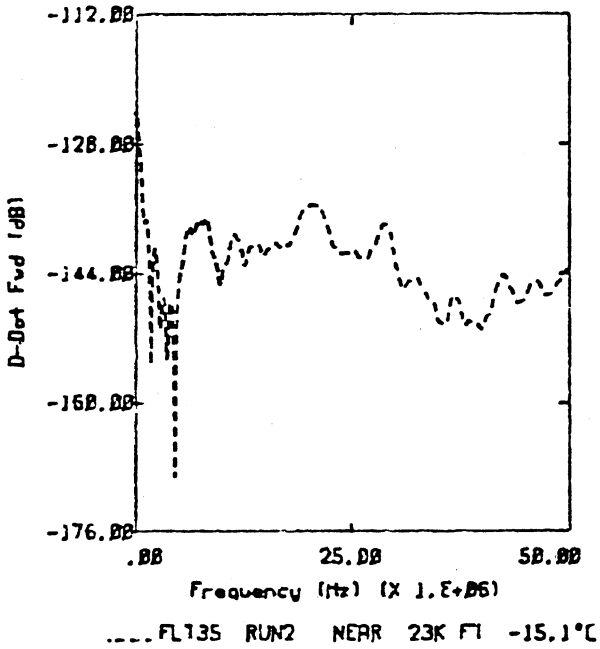
-112.00
-128.00
-144.00
-160.00
-176.00
D-Dot Fvd (dB)
.00
25.00
50.00
Frequency (Hz) (X 1.E+06)
FLT35 RUN2 NEAR 23K FT -15.1°C

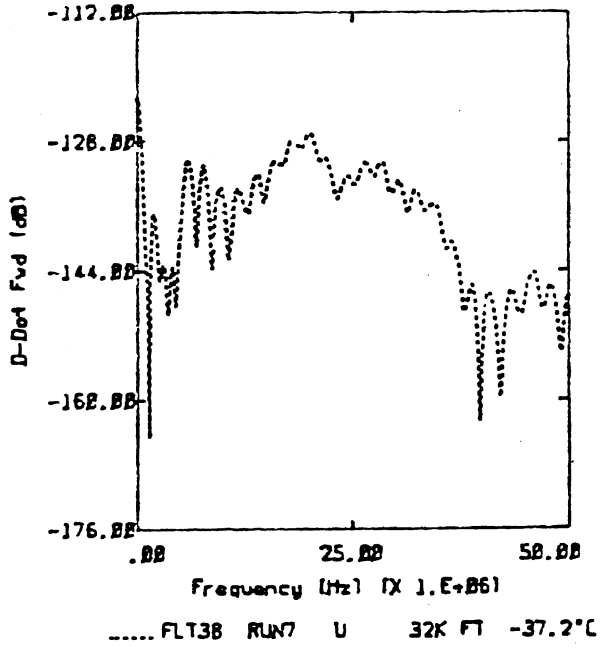
-112.00
-128.00
-144.00
-160.00
-176.00
D-Dot Fvd (dB)
.00
25.00
50.00
Frequency (Hz) (X 1.E+06)
FLT38 RUN7 U 32K FT -37.2°C

Category 5

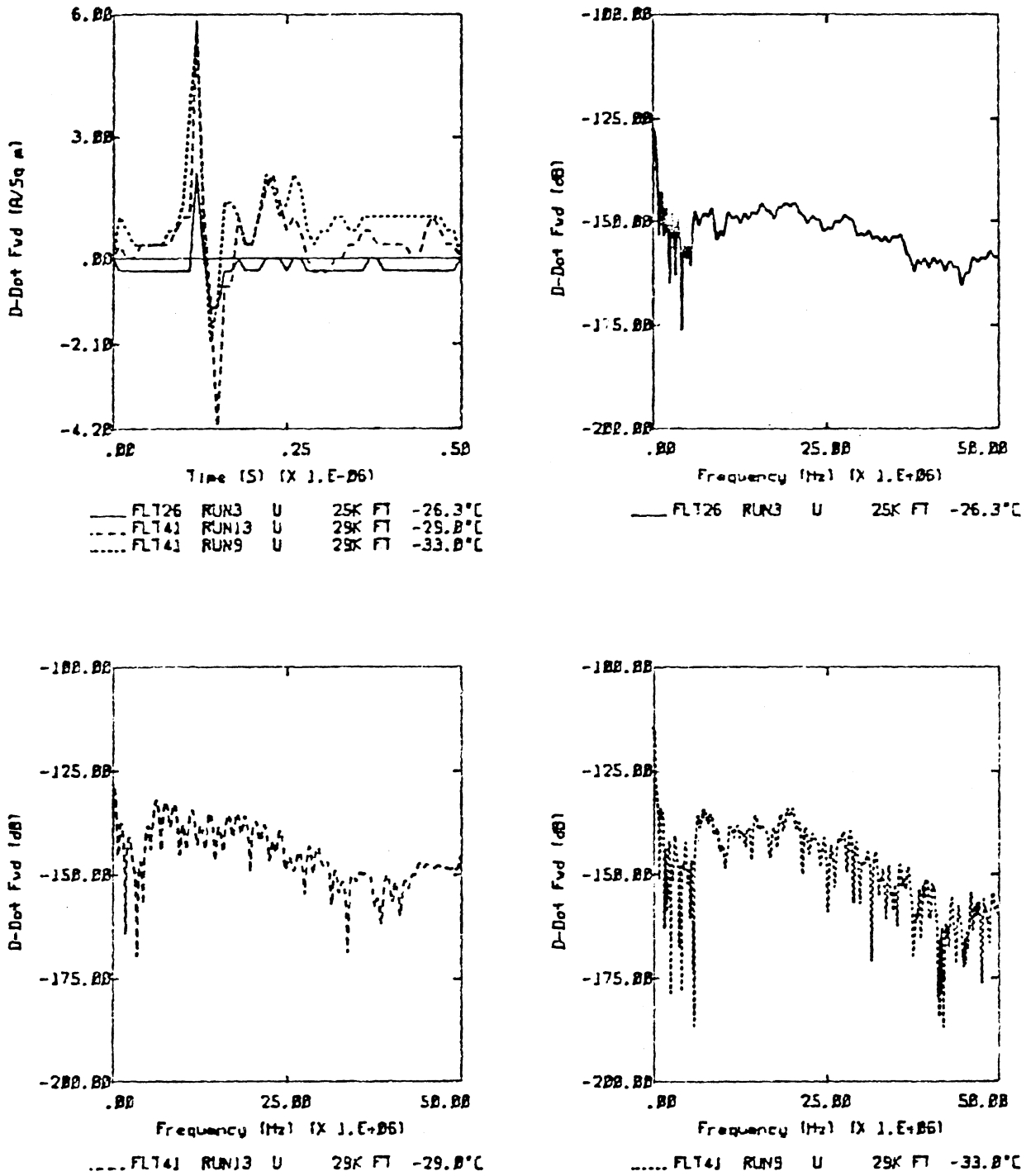
6.00
3.00
.00
-2.10
-4.20
D-Dot Fvd (A/Sq m)
.00
.25
.50
Time (S) (X 1.E-06)
FLT26 RUN3 U 25K FT -26.3°C
FLT41 RUN13 U 29K FT -29.0°C
FLT41 RUN9 U 29K FT -33.0°C
-100.00
-125.00
-150.00
-175.00
-200.00
D-Dot Fvd (dB)
.00
25.00
50.00
Frequency (Hz) (X 1.E+06)
FLT26 RUN3 U 25K FT -26.3°C
FLT41 RUN13 U 29K FT -29.0°C
FLT41 RUN9 U 29K FT -33.0°C

Category 5

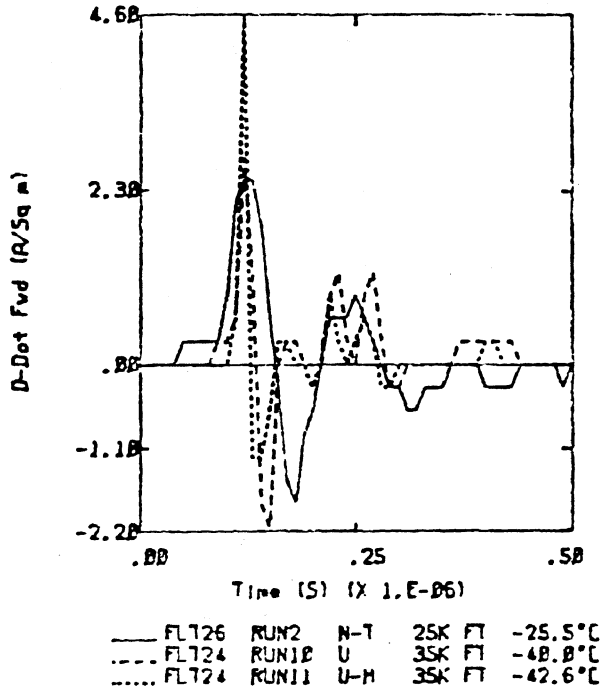
4.60
2.30
.00
-1.10
-2.20
D-Dot Fvd (A/Sq m)
.00
.25
.50
Time (S) (X 1.E-06)
FLT26 RUN2 N-T 25K FT -25.5°C
FLT24 RUN10 U 35K FT -40.0°C
FLT24 RUN11 U-M 35K FT -42.6°C

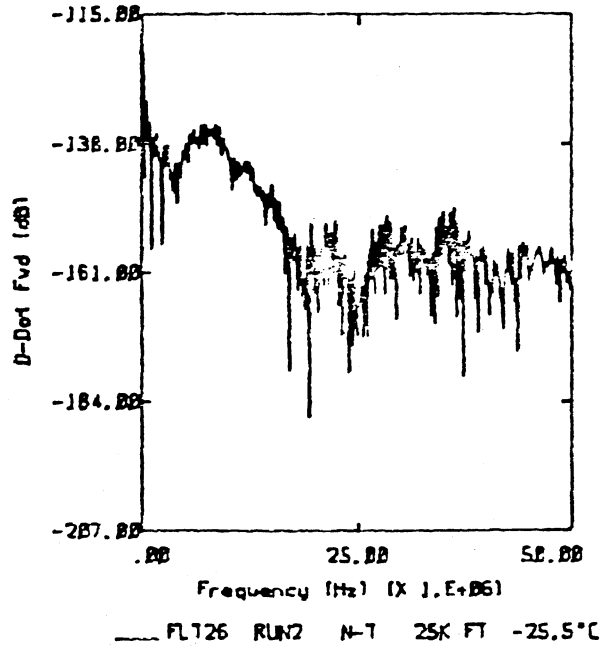
-115.00
-138.00
-161.00
-184.00
-207.00
D-Dot Fvd (dB)
.00
25.00
50.00
Frequency (Hz) (X 1.E+06)
FLT26 RUN2 N-T 25K FT -25.5°C

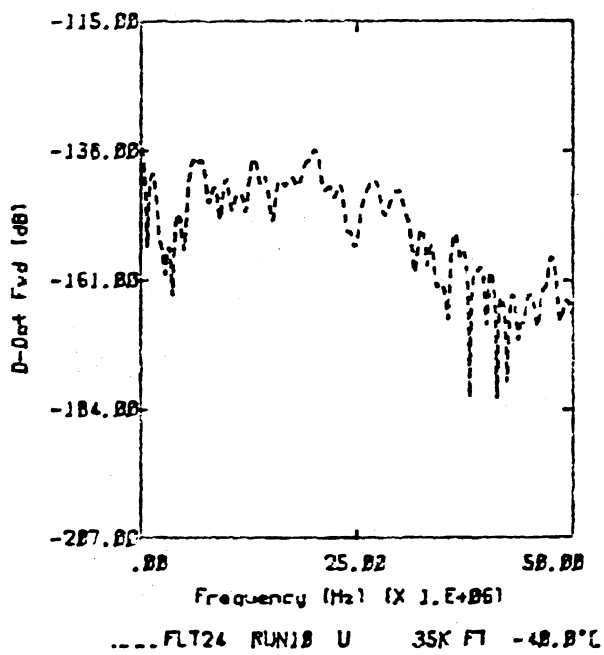
-115.00
-138.00
-161.00
-184.00
-207.00
D-Dot Fvd (dB)
.00
25.00
50.00
Frequency (Hz) (X 1.E+06)
FLT24 RUN10 U 35K FT -40.0°C

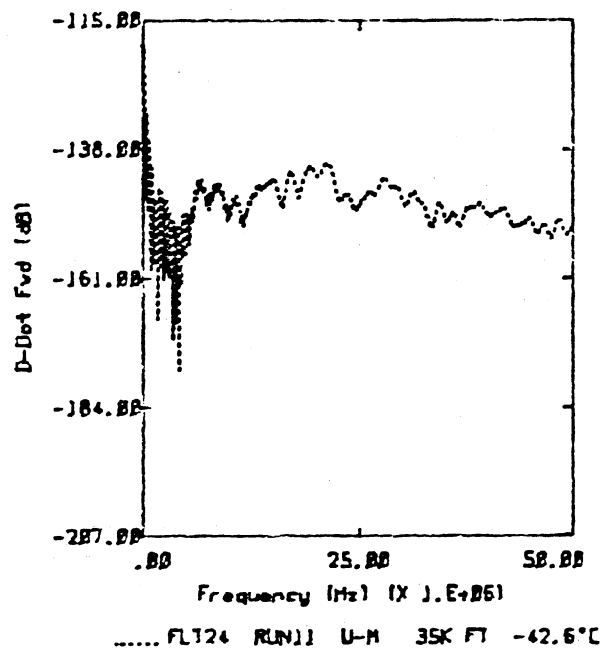
-115.00
-138.00
-161.00
-184.00
-207.00
D-Dot Fvd (dB)
.00
25.00
50.00
Frequency (Hz) (X 1.E+06)
FLT24 RUN11 U-M 35K FT -42.6°C

Category 5

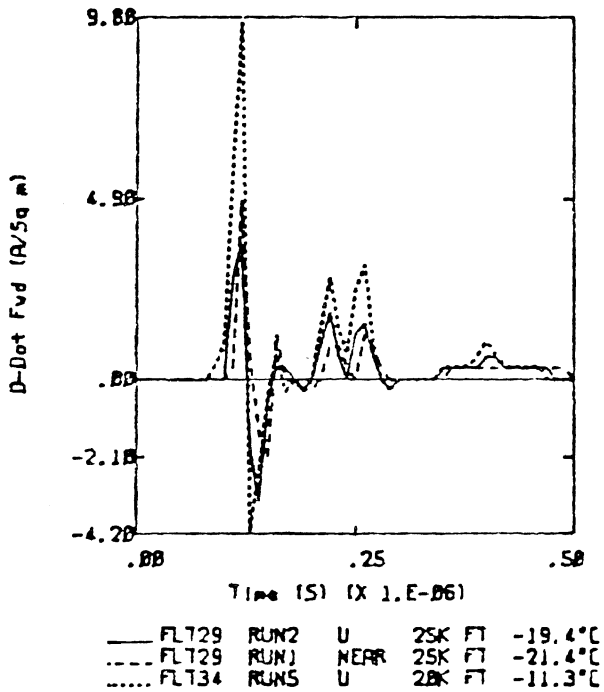
9.00
4.90
.00
-2.10
-4.20
D-Dot Fwd (A/Sq m)
.00
.25
.50
Time (S) (X 1.E-06)
FLT29 RUN2 U 25K FT -19.4°C
FLT29 RUN1 NEAR 25K FT -21.4°C
FLT34 RUN5 U 20K FT -11.3°C

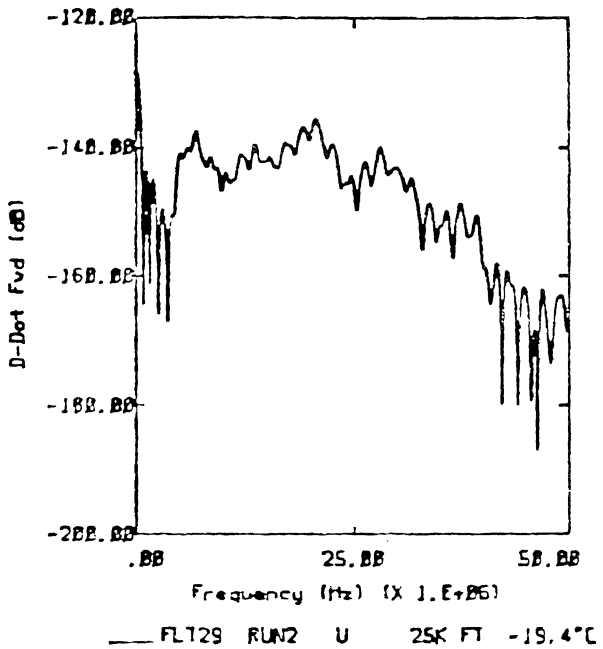
-120.00
-140.00
-160.00
-180.00
-200.00
D-Dot Fwd (dB)
.00
25.00
50.00
Frequency (Hz) (X 1.E+06)
FLT29 RUN2 U 25K FT -19.4°C

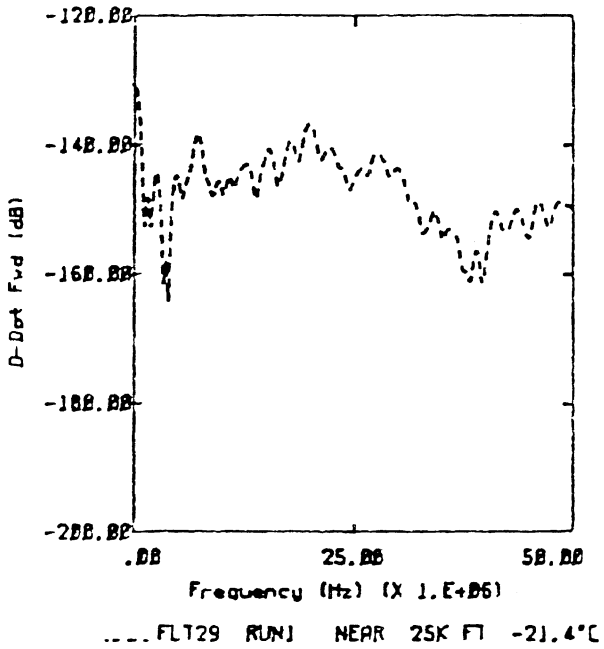
-120.00
-140.00
-160.00
-180.00
-200.00
D-Dot Fwd (dB)
.00
25.00
50.00
Frequency (Hz) (X 1.E+06)
FLT29 RUN1 NEAR 25K FT -21.4°C

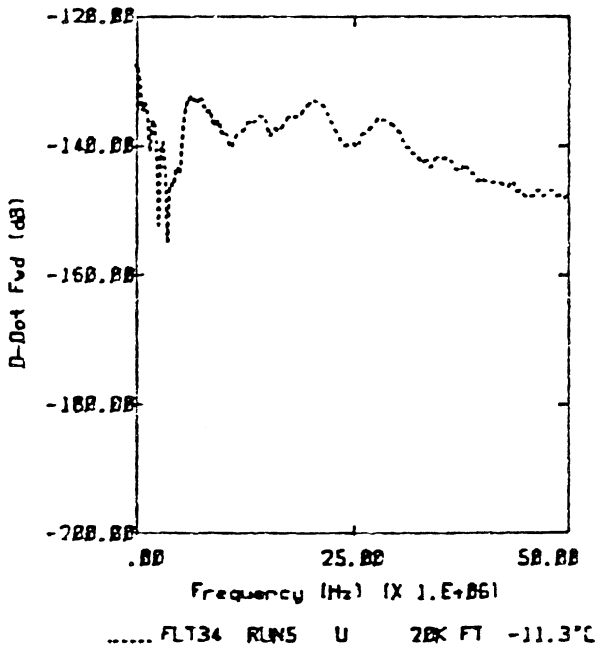
-120.00
-140.00
-160.00
-180.00
-200.00
D-Dot Fwd (dB)
.00
25.00
50.00
Frequency (Hz) (X 1.E+06)
FLT34 RUN5 U 20K FT -11.3°C

Category 5

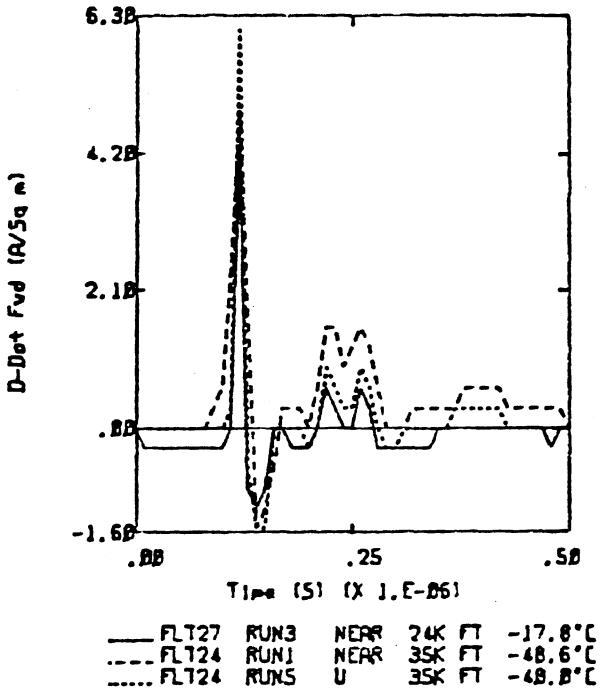
6.3B
4.2B
2.1B
.BB
-1.6B
D-Dot Fvd (A/Sq m)
.BB
.25
.5B
Time (S) (X 1.E-B6)
FLT27 RUN3 NEAR 24K FT -17.8°C
FLT24 RUN1 NEAR 35K FT -48.6°C
FLT24 RUN5 U 35K FT -48.B°C

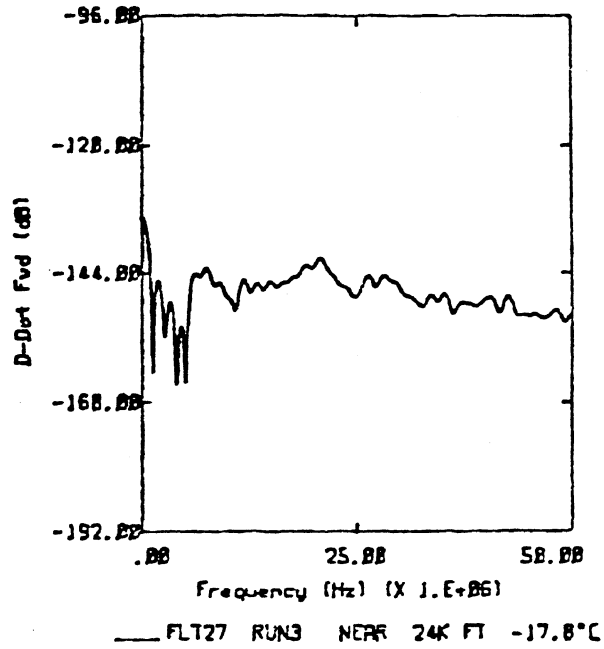
-96.BB
-12B.BB
-144.BB
-16B.BB
-192.BB
D-Dot Fvd (dB)
.BB
25.BB
5B.BB
Frequency (Hz) (X 1.E+B6)
FLT27 RUN3 NEAR 24K FT -17.8°C

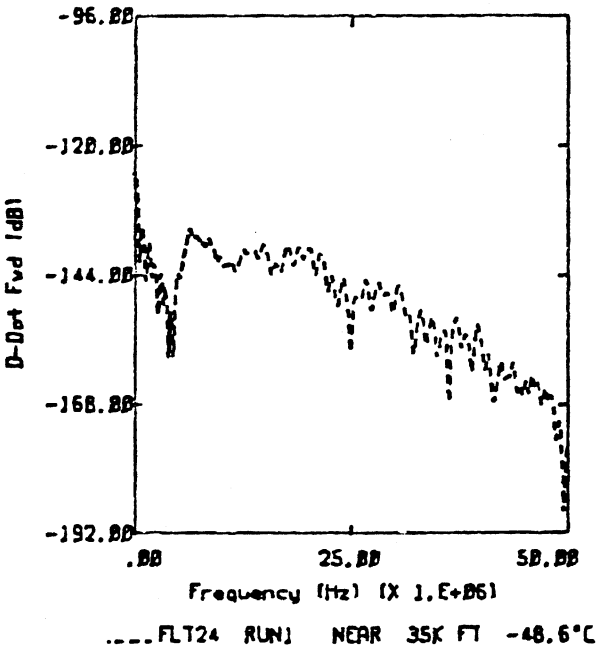
-96.BB
-12B.BB
-144.BB
-16B.BB
-192.BB
D-Dot Fvd (dB)
.BB
25.BB
5B.BB
Frequency (Hz) (X 1.E+B6)
FLT24 RUN1 NEAR 35K FT -48.6°C

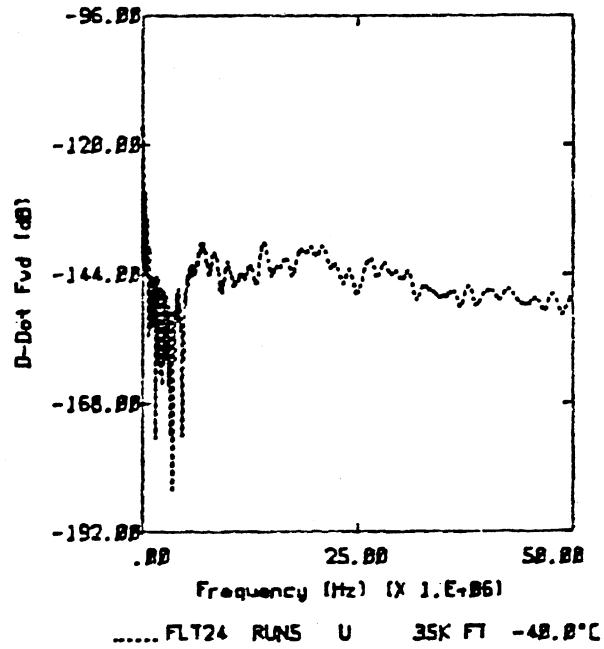
-96.BB
-12B.BB
-144.BB
-16B.BB
-192.BB
D-Dot Fvd (dB)
.BB
25.BB
5B.BB
Frequency (Hz) (X 1.E+B6)
FLT24 RUN5 U 35K FT -48.B°C

Category 5

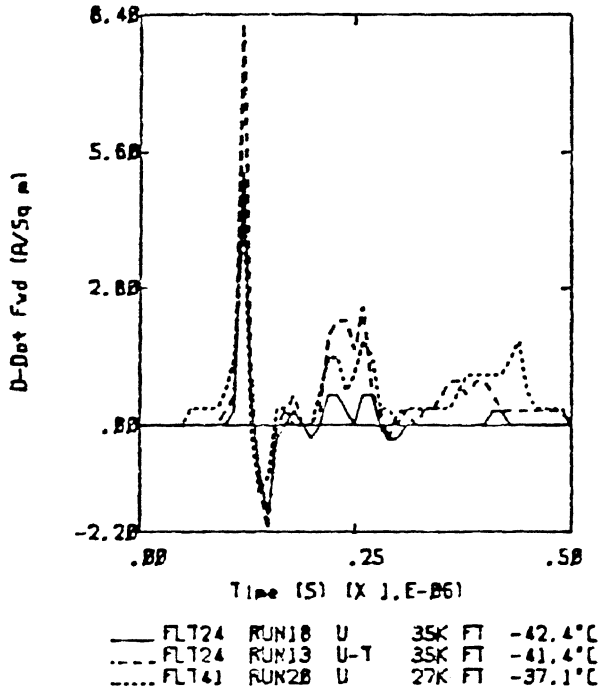
8.4B
5.6B
2.8B
.BB
-2.2B
D-Dot Fvd (A/Sq m)
.BB
.25
.5B
Time (S) (X 1.E-B6)
FLT24 RUN18 U 35K FT -42.4°C
FLT24 RUN13 U-T 35K FT -41.4°C
FLT41 RUN2B U 27K FT -37.1°C

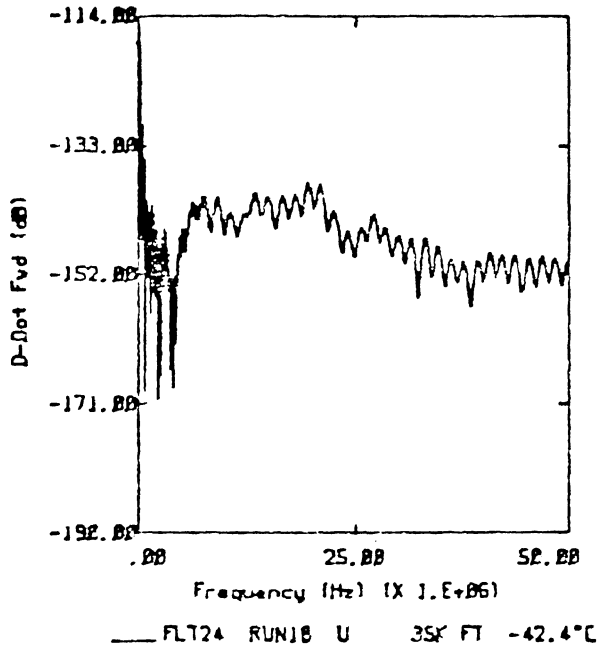
-114.BB
-133.BB
-152.BB
-171.BB
-19B.BB
D-Dot Fvd (dB)
.BB
25.BB
5B.BB
Frequency (Hz) (X 1.E+B6)
FLT24 RUN18 U 35K FT -42.4°C

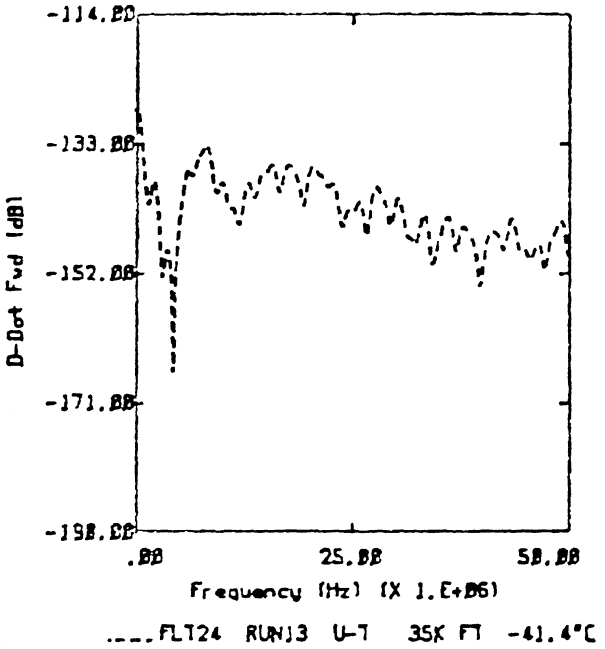
-114.BB
-133.BB
-152.BB
-171.BB
-19B.BB
D-Dot Fvd (dB)
.BB
25.BB
5B.BB
Frequency (Hz) (X 1.E+B6)
FLT24 RUN13 U-T 35K FT -41.4°C

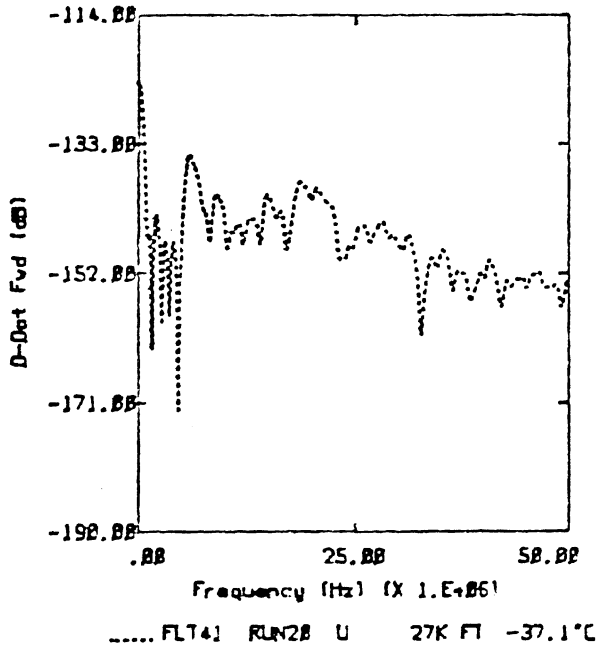
-114.BB
-133.BB
-152.BB
-171.BB
-19B.BB
D-Dot Fvd (dB)
.BB
25.BB
5B.BB
Frequency (Hz) (X 1.E+B6)
FLT41 RUN2B U 27K FT -37.1°C

Category 5

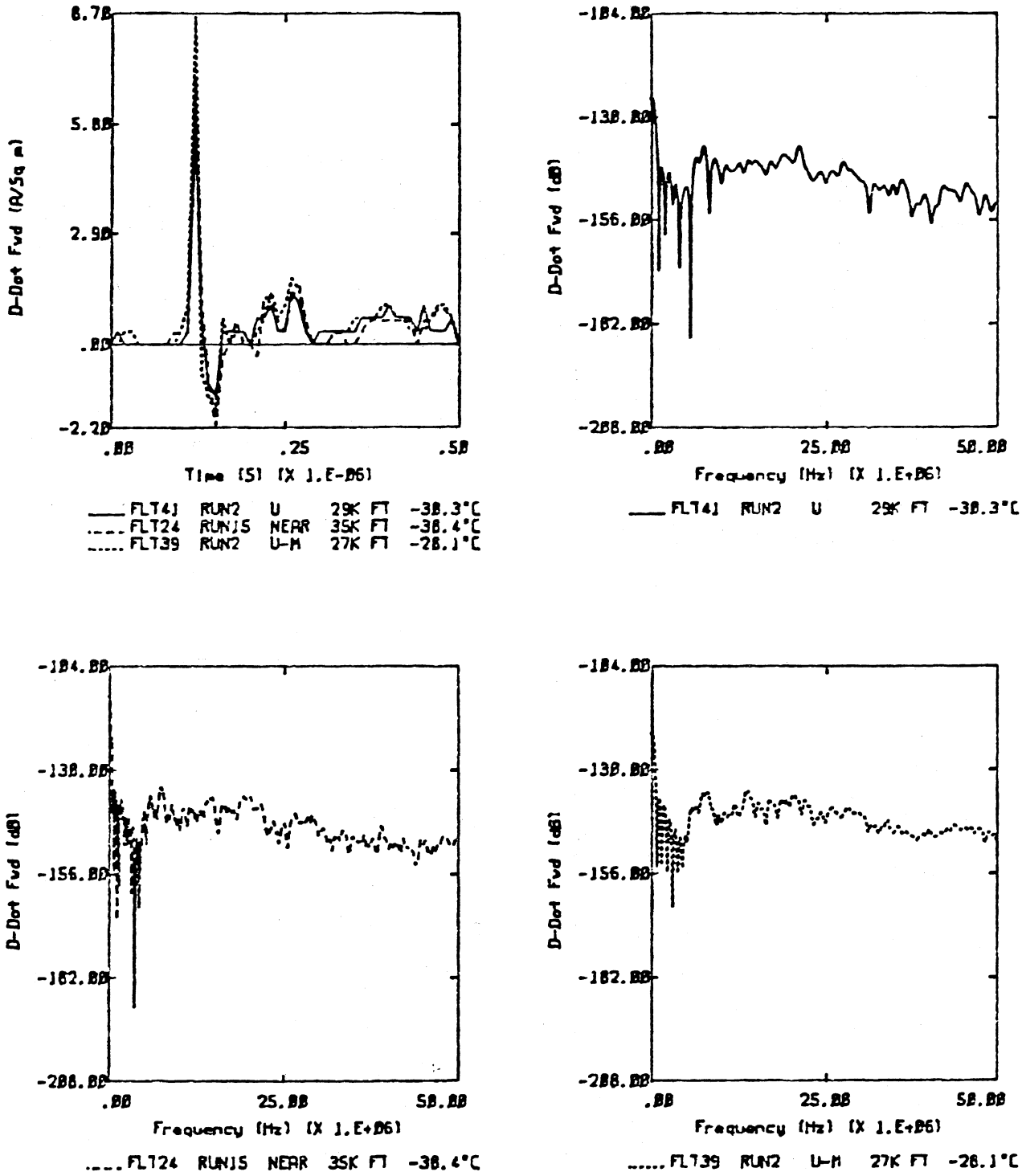
D-Dot Fvd (V/Sq m)
Time (S) (X 1.E-06)
FLT41 RUN2 U 29K FT -38.3°C
FLT24 RUN15 NEAR 35K FT -38.4°C
FLT39 RUN2 U-M 27K FT -28.1°C
D-Dot Fvd (dB)
Frequency (Hz) (X 1.E+06)
FLT41 RUN2 U 29K FT -38.3°C
FLT24 RUN15 NEAR 35K FT -38.4°C
FLT39 RUN2 U-M 27K FT -28.1°C

Category 5

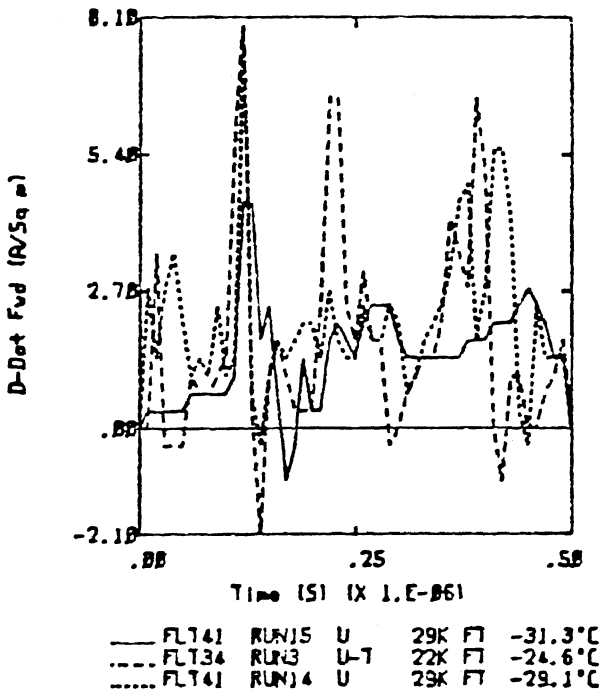
8.1B
5.4B
2.7B
.BB
-2.1B
D-Dot Fwd (R/Sq m)
.BB
.25
.5B
Time (S) (X 1.E-B6)
FLT41 RUN15 U 29K FT -31.3°C
FLT34 RUN3 U-T 22K FT -24.6°C
FLT41 RUN14 U 29K FT -29.1°C

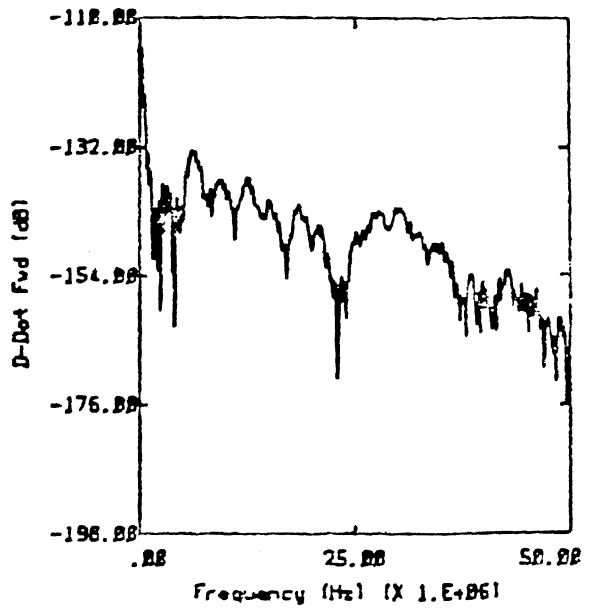
-11B.BB
-132.BB
-154.BB
-176.BB
-198.BB
D-Dot Fwd (dB)
.BB
25.BB
5B.BB
Frequency (Hz) (X 1.E+B6)
FLT41 RUN15 U 29K FT -31.3°C

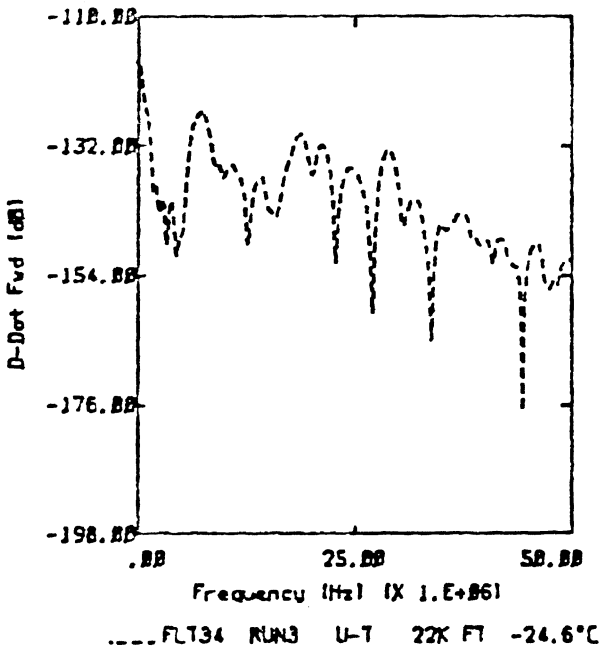
-11B.BB
-132.BB
-154.BB
-176.BB
-198.BB
D-Dot Fwd (dB)
.BB
25.BB
5B.BB
Frequency (Hz) (X 1.E+B6)
FLT34 RUN3 U-T 22K FT -24.6°C

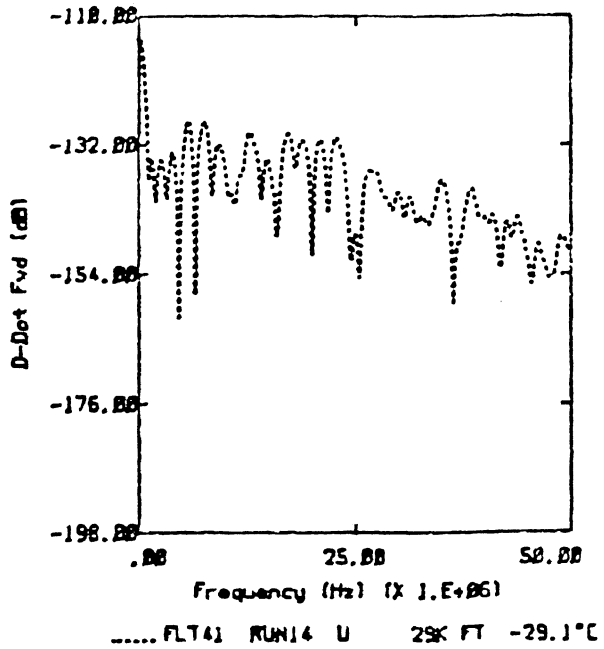
-11B.BB
-132.BB
-154.BB
-176.BB
-198.BB
D-Dot Fwd (dB)
.BB
25.BB
5B.BB
Frequency (Hz) (X 1.E+B6)
FLT41 RUN14 U 29K FT -29.1°C

Category 6

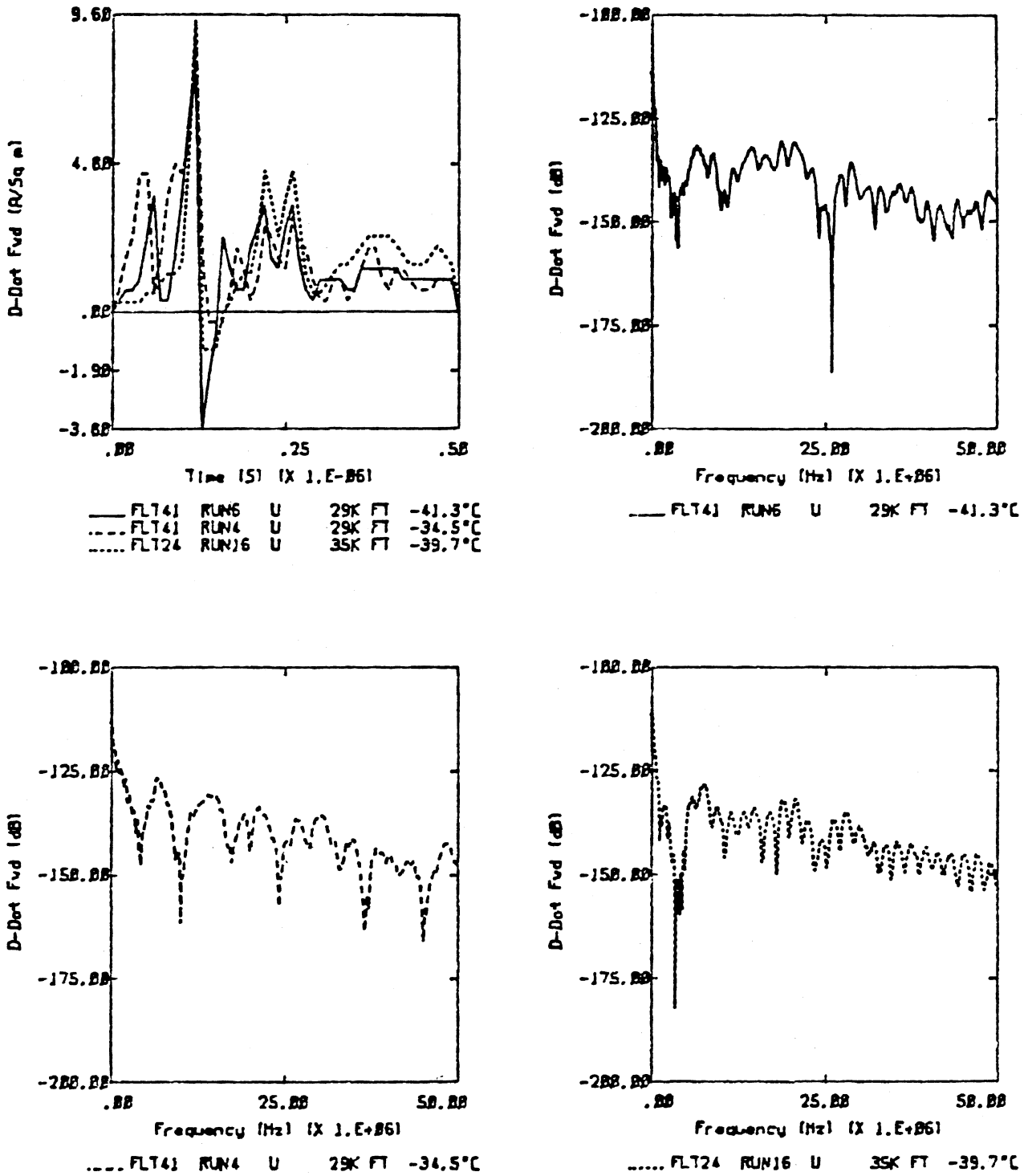
9.60
4.80
.00
-1.90
-3.80
D-Dot Fwd (A/Sq m)
.00
.25
.50
Time (S) (X 1.E-06)
FLT41 RUN6 U 29K FT -41.3°C
FLT41 RUN4 U 29K FT -34.5°C
FLT24 RUN16 U 35K FT -39.7°C
-100.00
-125.00
-150.00
-175.00
-200.00
D-Dot Fwd (dB)
.00
25.00
50.00
Frequency (Hz) (X 1.E+06)
FLT41 RUN6 U 29K FT -41.3°C
FLT41 RUN4 U 29K FT -34.5°C
FLT24 RUN16 U 35K FT -39.7°C

Category 6

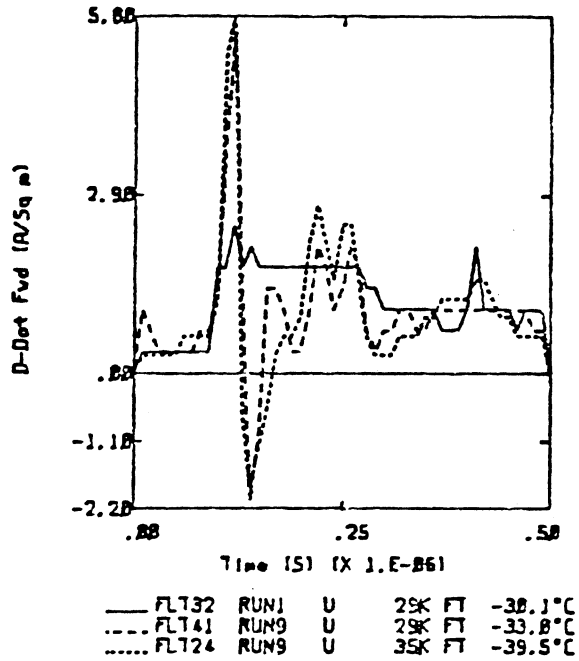
5.00
2.90
.00
-1.10
-2.20
D-Dot Fwd (V/Sq m)
.00
.25
.50
Time (S) (X 1.E-06)
FLT32 RUN1 U 29K FT -38.1°C
FLT41 RUN9 U 29K FT -33.0°C
FLT24 RUN9 U 35K FT -39.5°C

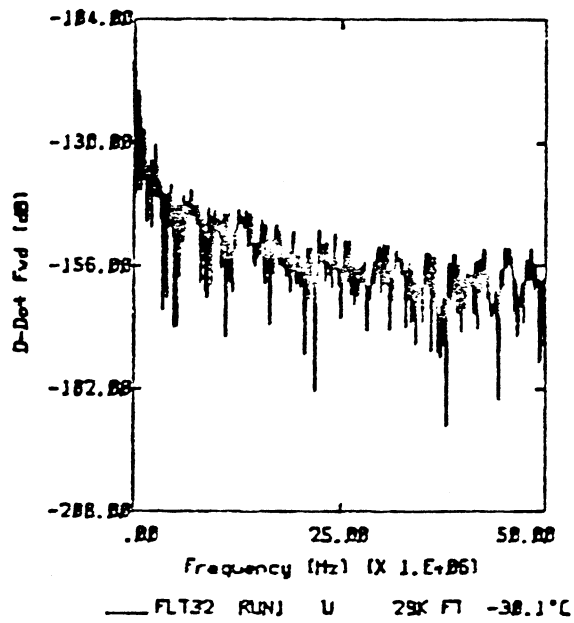
-104.00
-130.00
-156.00
-182.00
-208.00
D-Dot Fwd (dB)
.00
25.00
50.00
Frequency (Hz) (X 1.E+06)
FLT32 RUN1 U 29K FT -38.1°C

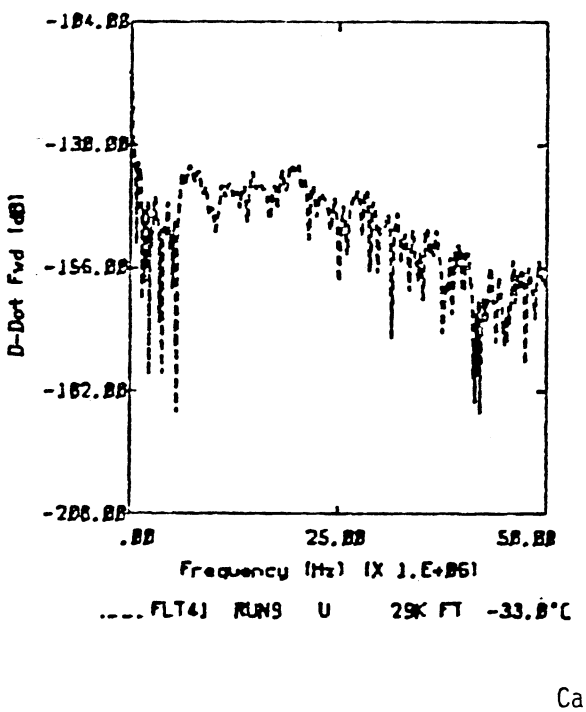
-104.00
-130.00
-156.00
-182.00
-208.00
D-Dot Fwd (dB)
.00
25.00
50.00
Frequency (Hz) (X 1.E+06)
FLT41 RUN9 U 29K FT -33.0°C

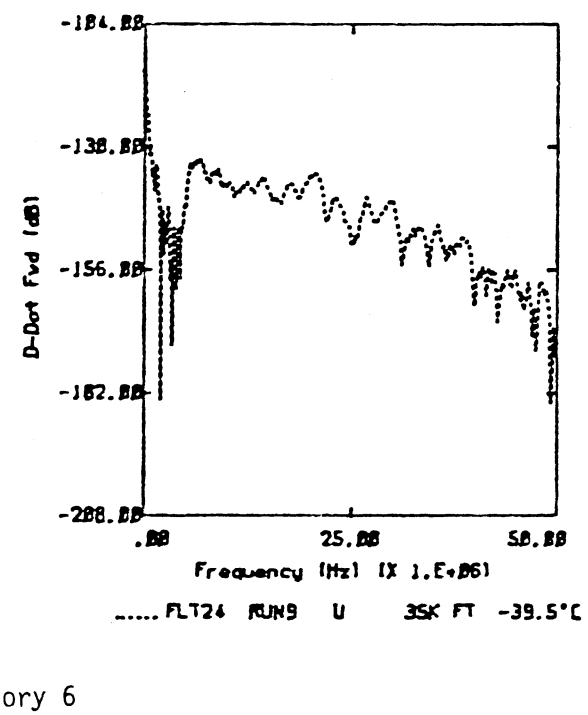
-104.00
-130.00
-156.00
-182.00
-208.00
D-Dot Fwd (dB)
.00
25.00
50.00
Frequency (Hz) (X 1.E+06)
FLT24 RUN9 U 35K FT -39.5°C

Category 6

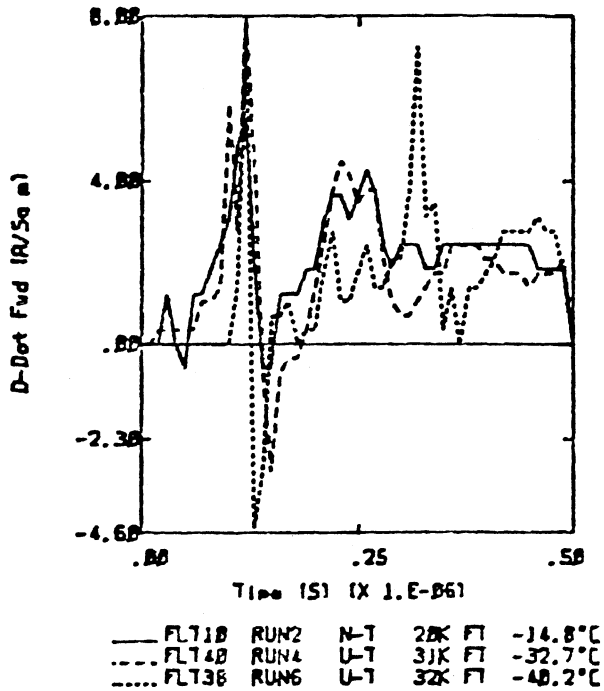
D-Dot Fwd (A/Sq m)
Time (S) (X 1.E-06)
FLT10 RUN2 N-T 28K FT -14.8°C
FLT40 RUN4 U-T 31K FT -32.7°C
FLT38 RUN6 U-T 32K FT -48.2°C

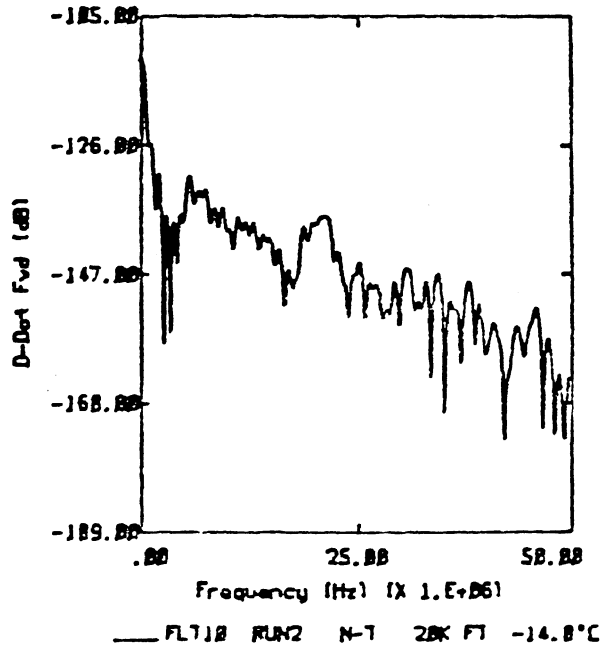
D-Dot Fwd (dB)
Frequency (Hz) (X 1.E+06)
FLT10 RUN2 N-T 28K FT -14.8°C

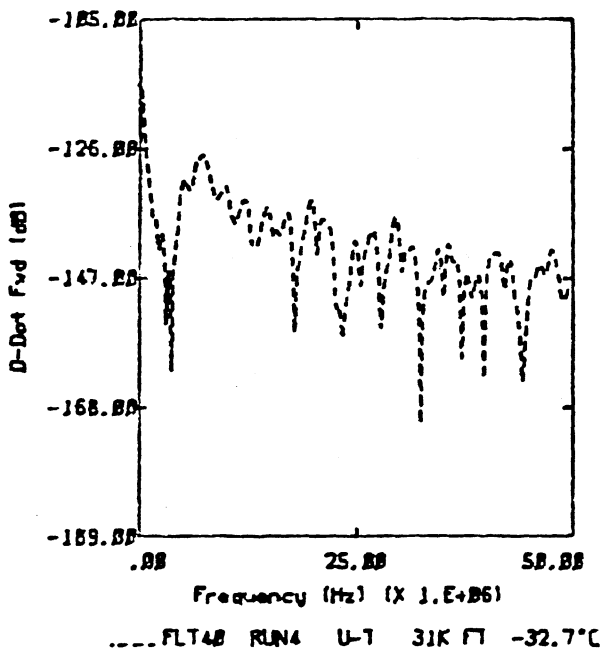
D-Dot Fwd (dB)
Frequency (Hz) (X 1.E+06)
FLT40 RUN4 U-T 31K FT -32.7°C

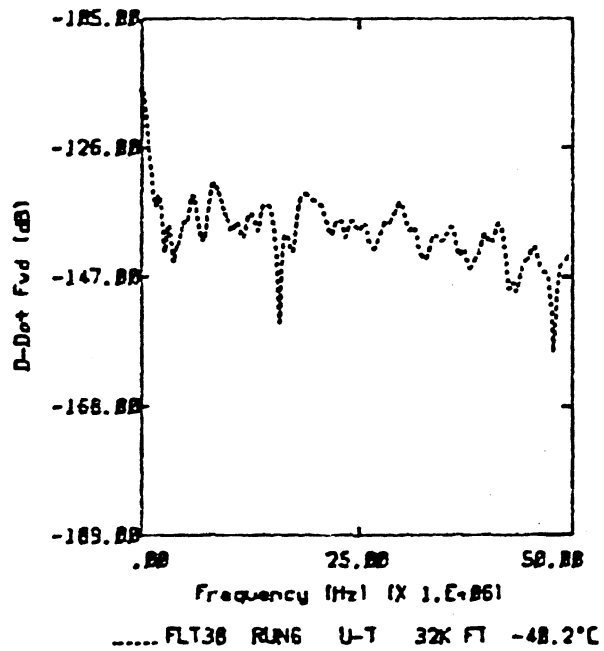
D-Dot Fwd (dB)
Frequency (Hz) (X 1.E+06)
FLT38 RUN6 U-T 32K FT -48.2°C

Category 6

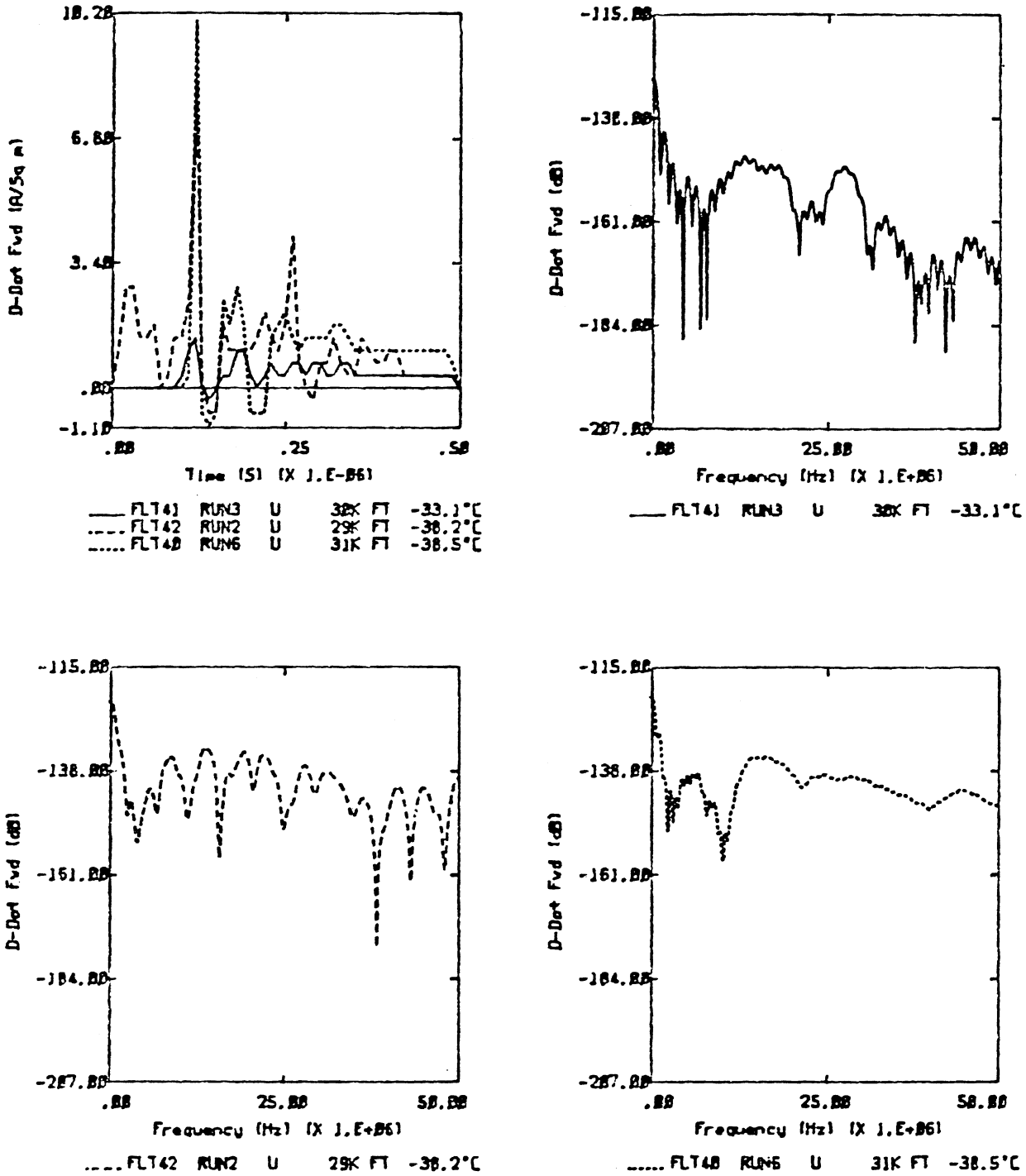
D-Dot Fvd (A/Sq m)
Time (S) (X 1.E-06)
FLT41 RUN3 U 38K FT -33.1°C
FLT42 RUN2 U 29K FT -38.2°C
FLT48 RUN6 U 31K FT -38.5°C
D-Dot Fvd (dB)
Frequency (Hz) (X 1.E+06)
FLT41 RUN3 U 38K FT -33.1°C
FLT42 RUN2 U 29K FT -38.2°C
FLT48 RUN6 U 31K FT -38.5°C

Category 6

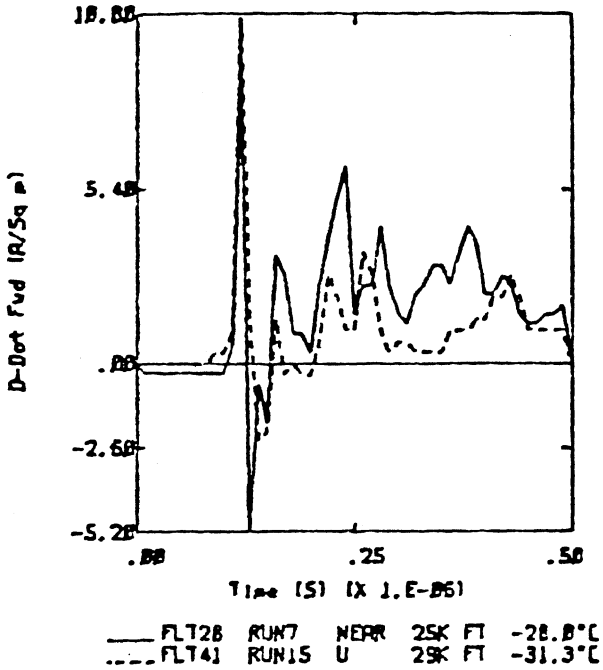
10.00
5.40
.00
-2.60
-5.20
.00
.25
.50
D-Dot Fvd (R/Sq m)
Time (S) (X 1.E-06)
FLT28 RUN7 NEAR 25K FT -28.0°C
FLT41 RUN15 U 29K FT -31.3°C

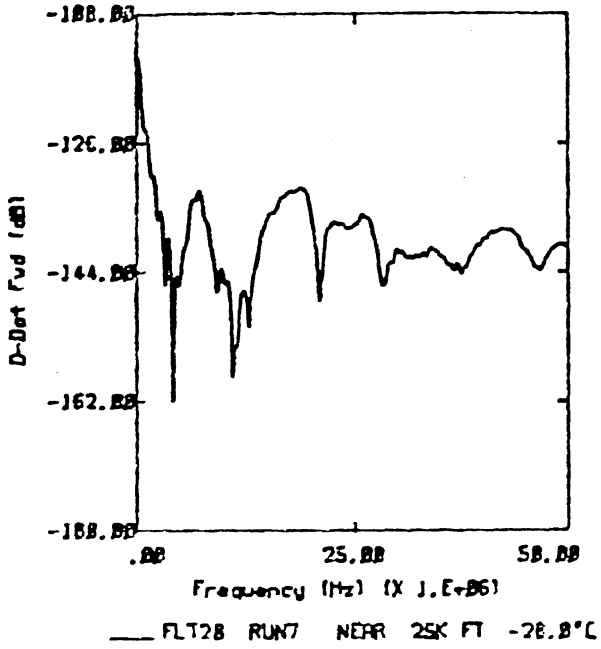
-108.00
-126.00
-144.00
-162.00
-180.00
.00
25.00
50.00
D-Dot Fvd (dB)
Frequency (Hz) (X 1.E+06)
FLT28 RUN7 NEAR 25K FT -28.0°C

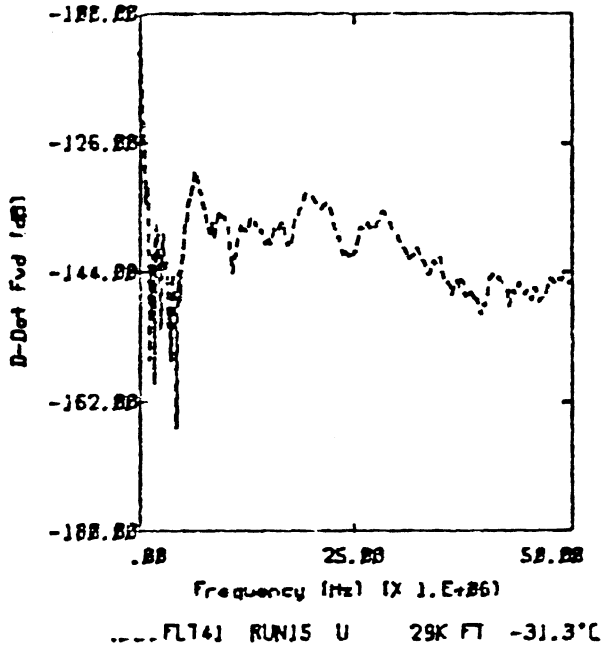
-108.00
-126.00
-144.00
-162.00
-180.00
.00
25.00
50.00
D-Dot Fvd (dB)
Frequency (Hz) (X 1.E+06)
FLT41 RUN15 U 29K FT -31.3°C

Category 6

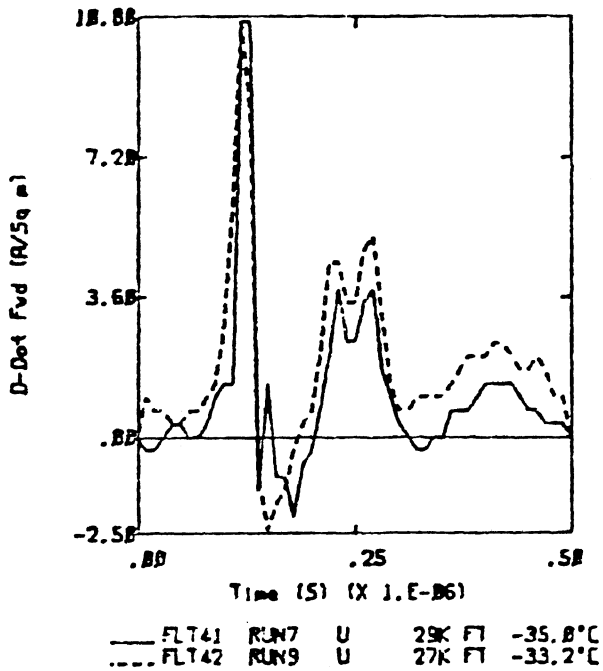
10.00
7.20
3.60
.00
-2.50
.00
.25
.50
D-Dot Fvd (A/Sq m)
Time (S) (X 1.E-06)
FLT41 RUN7 U 29K FT -35.0°C
FLT42 RUN9 U 27K FT -33.2°C

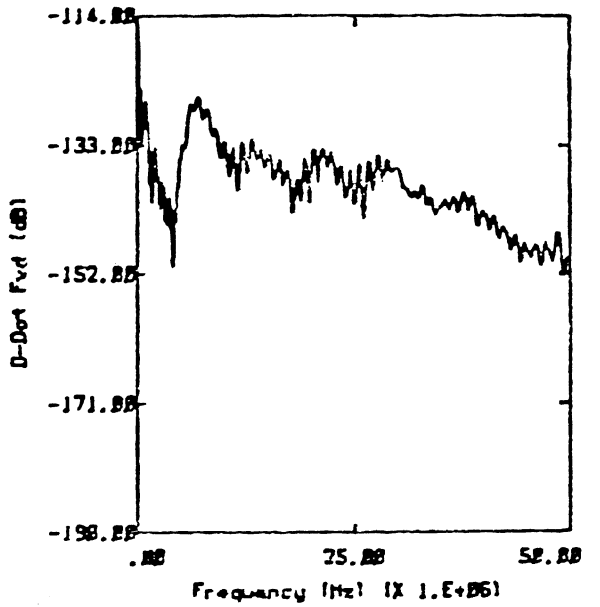
-114.00
-133.00
-152.00
-171.00
-190.00
.00
25.00
50.00
D-Dot Fvd (dB)
Frequency (Hz) (X 1.E+06)
FLT41 RUN7 U 29K FT -35.0°C

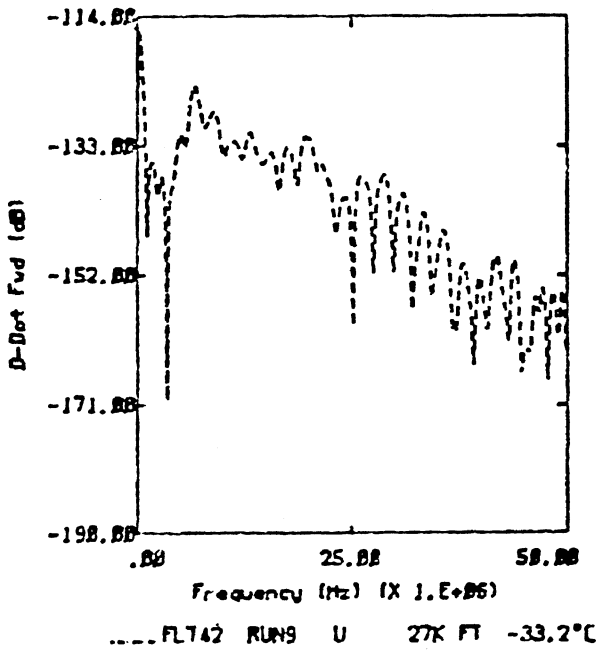
-114.00
-133.00
-152.00
-171.00
-190.00
.00
25.00
50.00
D-Dot Fvd (dB)
Frequency (Hz) (X 1.E+06)
FLT42 RUN9 U 27K FT -33.2°C

Category 6

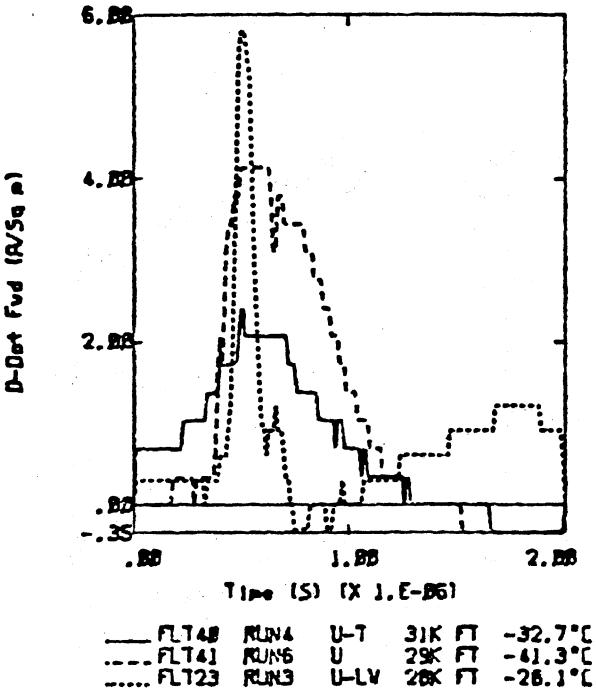
6.00
4.00
2.00
.00
-.35
D-Dot Fvd (A/Sq m)
.00
1.00
2.00
Time (S) (X 1.E-06)
FLT48 RUN4 U-T 31K FT -32.7°C
FLT41 RUN6 U 29K FT -41.3°C
FLT23 RUN3 U-LV 28K FT -28.1°C

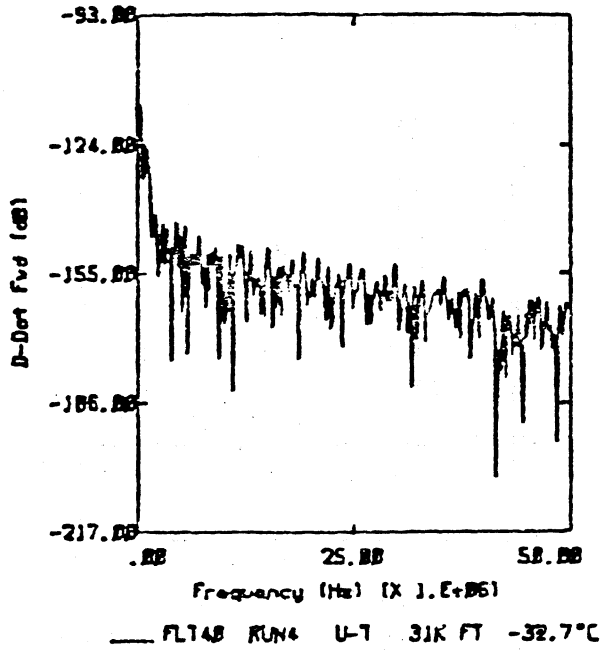
-93.00
-124.00
-155.00
-186.00
-217.00
D-Dot Fvd (dB)
.00
25.00
50.00
Frequency (Hz) (X 1.E+06)
FLT48 RUN4 U-T 31K FT -32.7°C

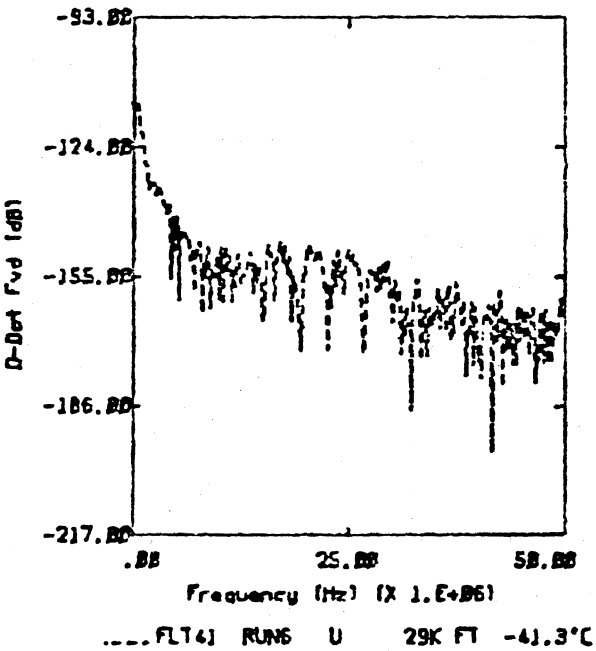
-93.00
-124.00
-155.00
-186.00
-217.00
D-Dot Fvd (dB)
.00
25.00
50.00
Frequency (Hz) (X 1.E+06)
FLT41 RUN6 U 29K FT -41.3°C

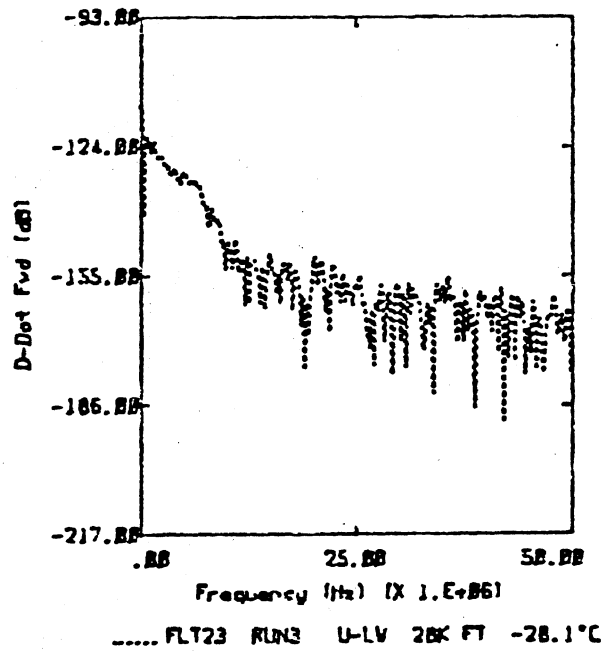
-93.00
-124.00
-155.00
-186.00
-217.00
D-Dot Fvd (dB)
.00
25.00
50.00
Frequency (Hz) (X 1.E+06)
FLT23 RUN3 U-LV 28K FT -28.1°C

Category 7

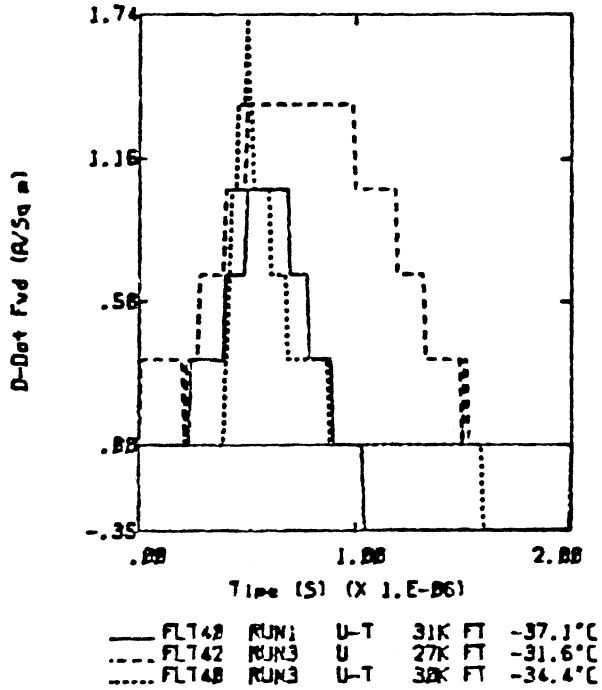
1.74
1.16
.58
.00
-.35
D-Dot Fvd (A/Sq m)
.00
1.00
2.00
Time (S) (X 1.E-06)
FLT40 RUN1 U-T 31K FT -37.1°C
FLT42 RUN3 U 27K FT -31.6°C
FLT48 RUN3 U-T 38K FT -34.4°C

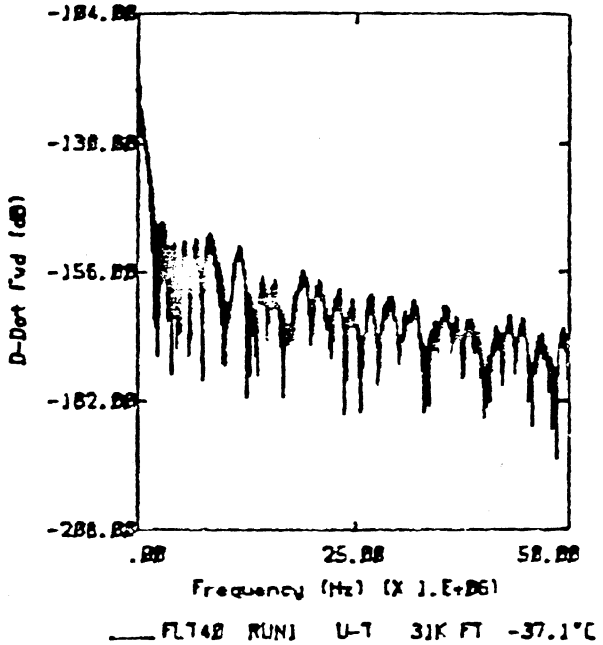
-104.00
-130.00
-156.00
-182.00
-208.00
D-Dot Fvd (dB)
.00
25.00
50.00
Frequency (Hz) (X 1.E+06)
FLT40 RUN1 U-T 31K FT -37.1°C

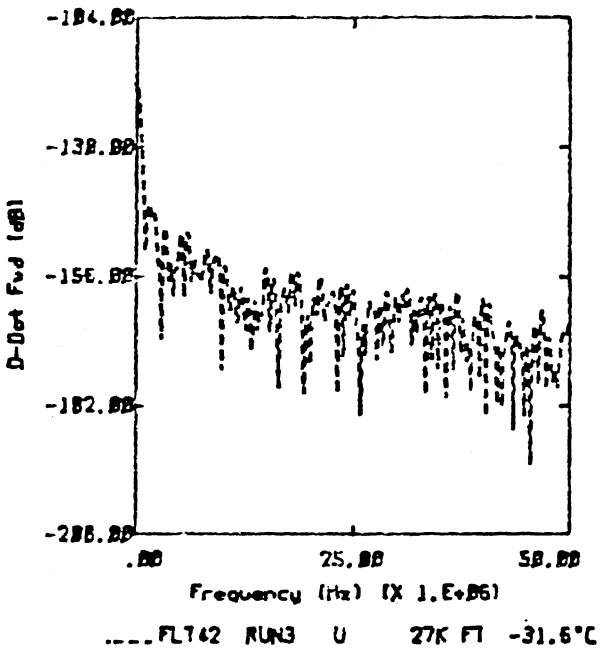
-104.00
-130.00
-156.00
-182.00
-208.00
D-Dot Fvd (dB)
.00
25.00
50.00
Frequency (Hz) (X 1.E+06)
FLT42 RUN3 U 27K FT -31.6°C

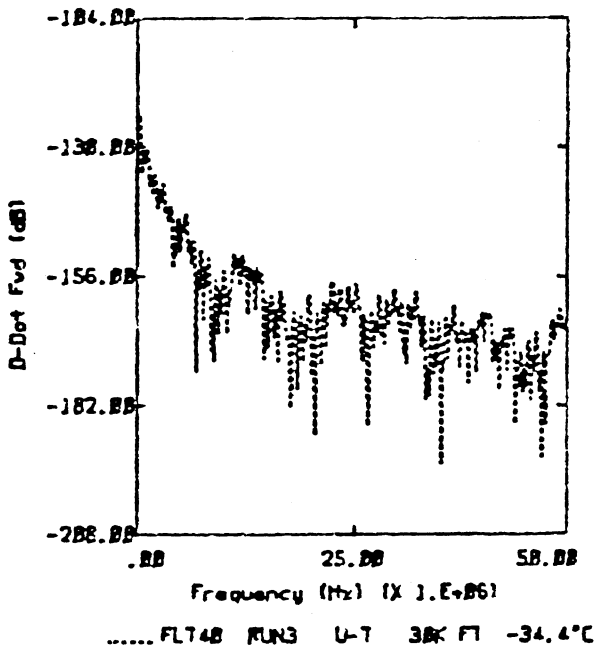
-104.00
-130.00
-156.00
-182.00
-208.00
D-Dot Fvd (dB)
.00
25.00
50.00
Frequency (Hz) (X 1.E+06)
FLT48 RUN3 U-T 38K FT -34.4°C

Category 7

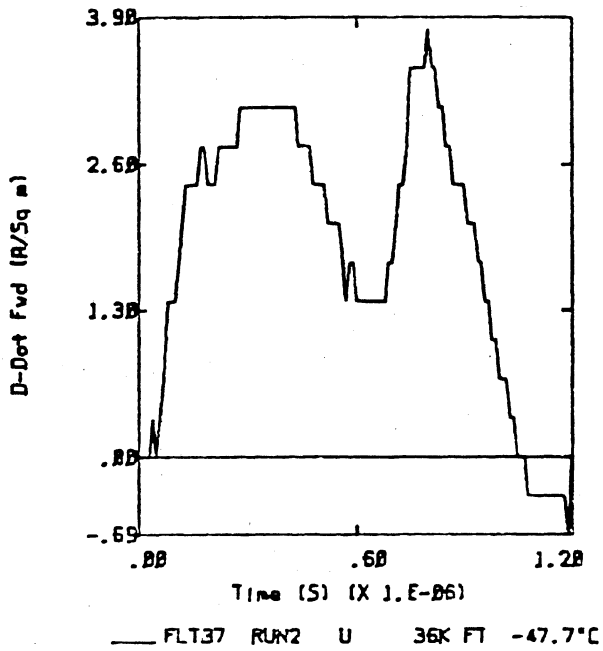
3.90
2.60
1.30
.00
-.69
D-Dot Fwd (R/Sq m)
.00
.60
1.20
Time (S) (X 1.E-06)
FLT37 RUN2 U 36K FT -47.7°C

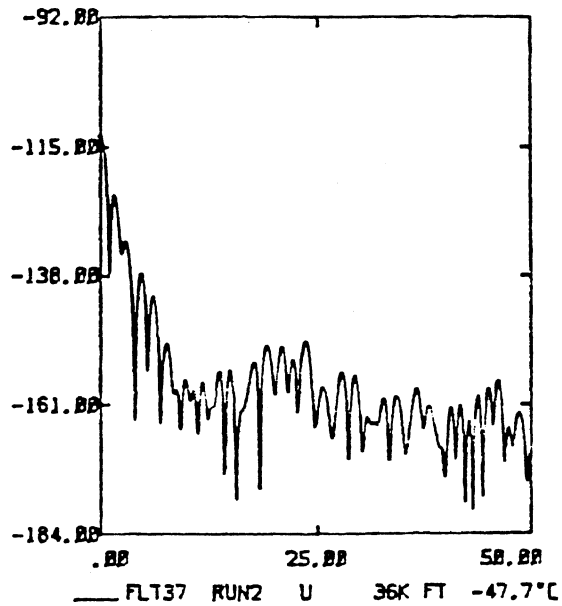
-92.00
-115.00
-138.00
-161.00
-184.00
.00
25.00
50.00
FLT37 RUN2 U 36K FT -47.7°C

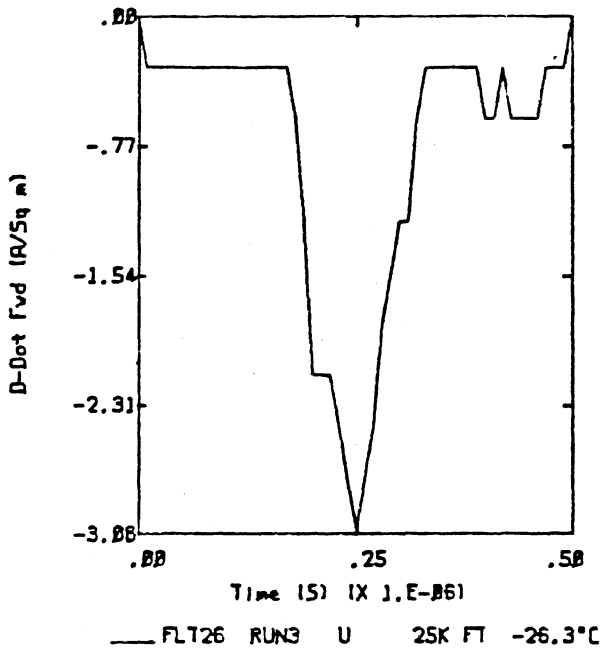
.00
-.77
-1.54
-2.31
-3.08
D-Dot Fwd (R/Sq m)
.00
.25
.50
Time (S) (X 1.E-06)
FLT26 RUN3 U 25K FT -26.3°C

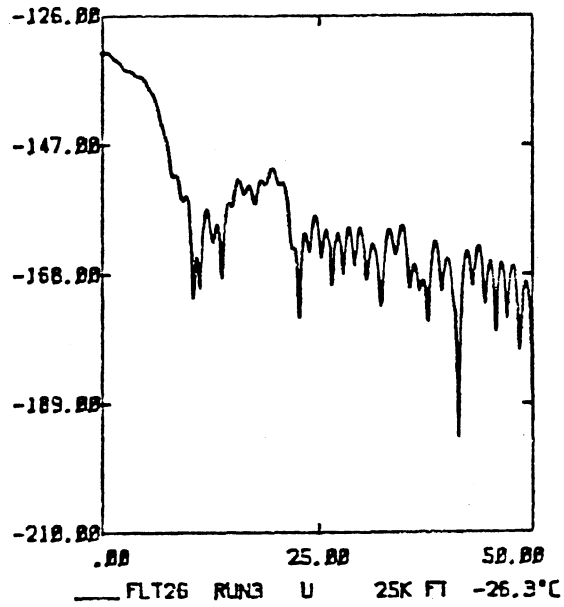
-126.00
-147.00
-168.00
-189.00
-210.00
.00
25.00
50.00
FLT26 RUN3 U 25K FT -26.3°C

Category 8

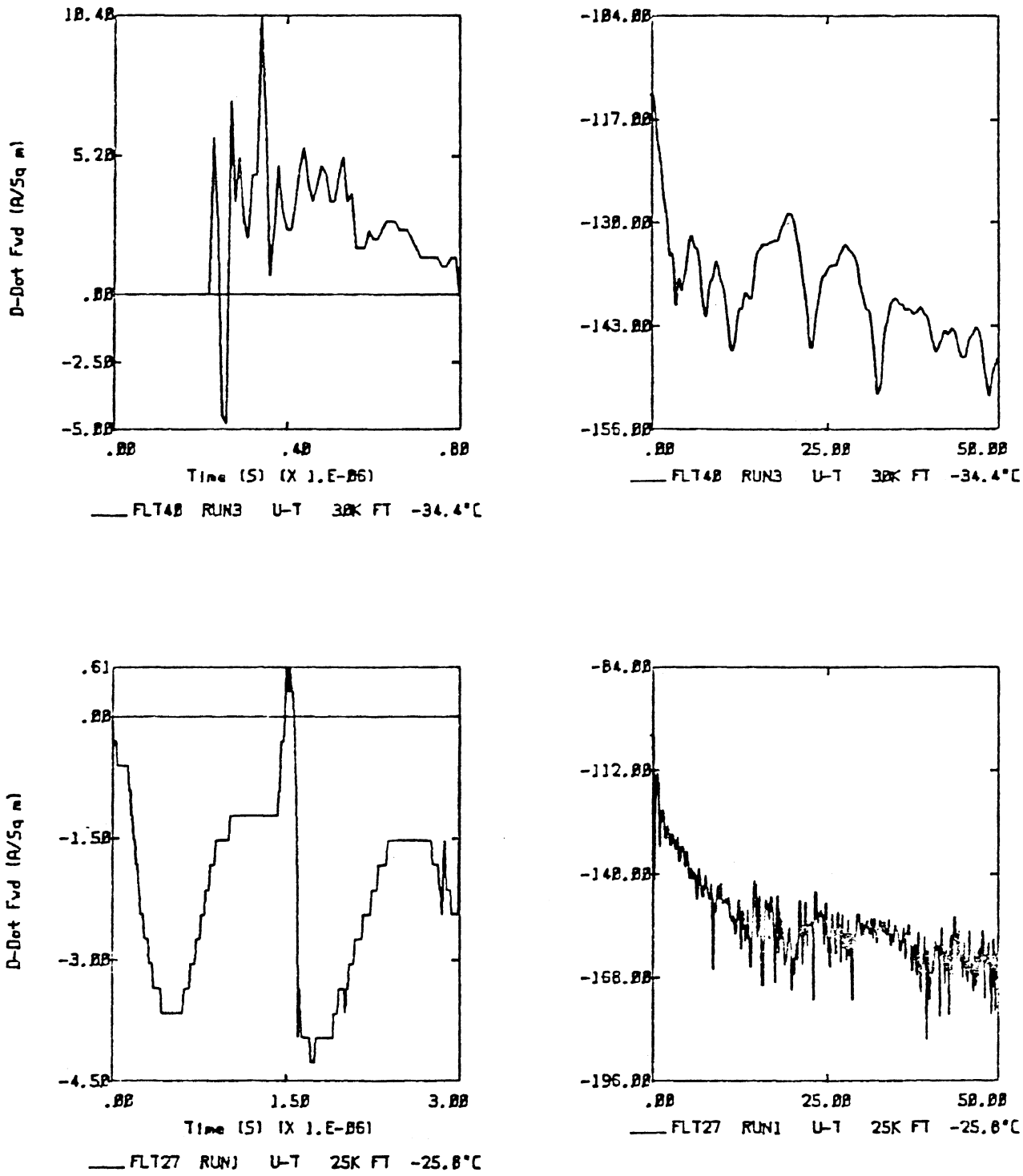
10.40
5.20
.00
-2.50
-5.00
.00
.40
.80
Time (S) (X 1.E-06)
D-Dot Fvd (A/Sq m)
FLT40 RUN3 U-T 30K FT -34.4°C
-104.00
-117.00
-130.00
-143.00
-156.00
.00
25.00
50.00
FLT40 RUN3 U-T 30K FT -34.4°C
.61
.00
-1.50
-3.00
-4.50
.00
1.50
3.00
Time (S) (X 1.E-06)
D-Dot Fvd (A/Sq m)
FLT27 RUN1 U-T 25K FT -25.8°C
-84.00
-112.00
-140.00
-168.00
-196.00
.00
25.00
50.00
FLT27 RUN1 U-T 25K FT -25.8°C

Category 8

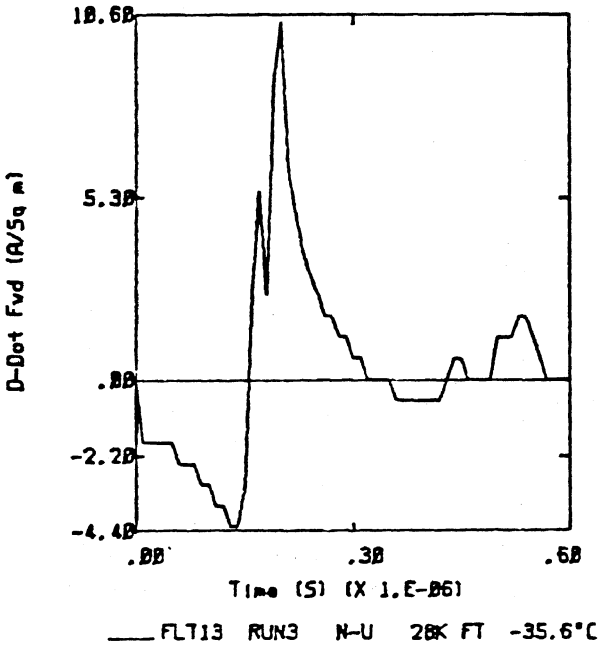
10.60
5.30
.00
-2.20
-4.40
D-Dot Fvd (A/Sq m)
.00
.30
.60
Time (S) (X 1.E-06)
FLT13 RUN3 N-U 28K FT -35.6°C

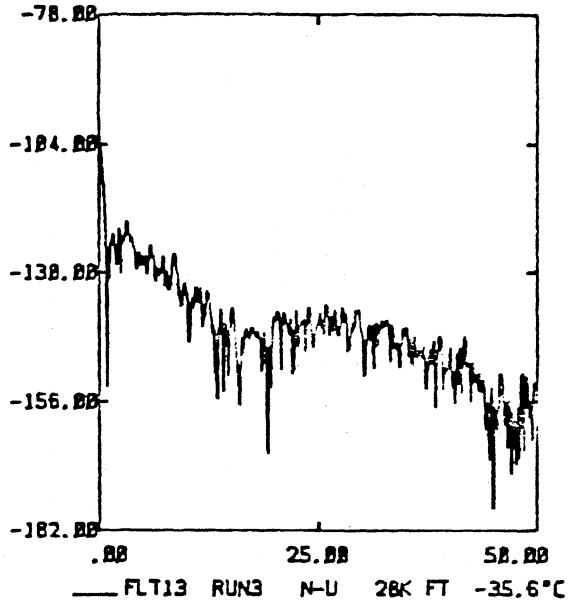
-78.00
-104.00
-130.00
-156.00
-182.00
.00
25.00
50.00
FLT13 RUN3 N-U 28K FT -35.6°C

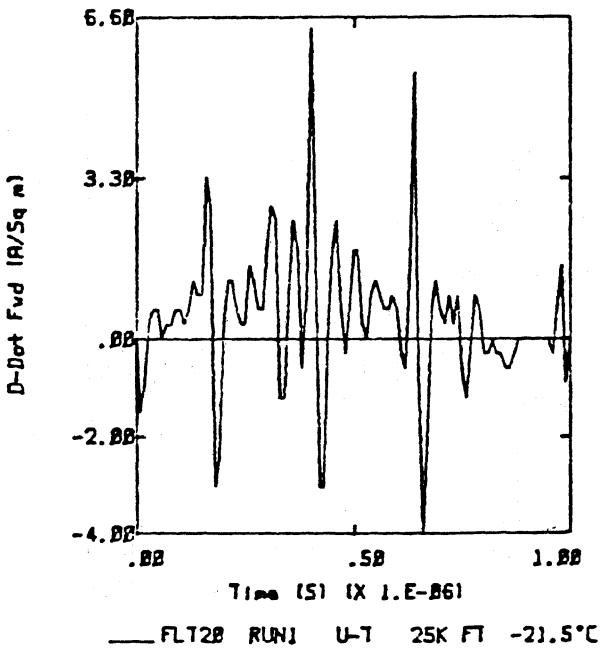
6.60
3.30
.00
-2.00
-4.00
D-Dot Fvd (A/Sq m)
.00
.50
1.00
Time (S) (X 1.E-06)
FLT28 RUN1 U-T 25K FT -21.5°C

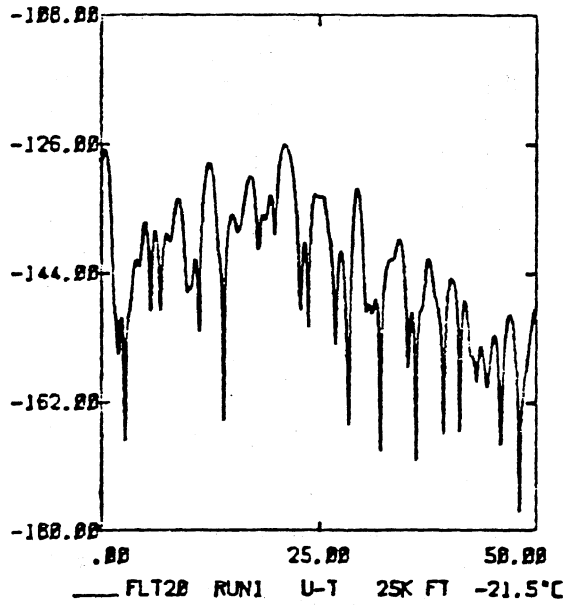
-108.00
-126.00
-144.00
-162.00
-180.00
.00
25.00
50.00
FLT28 RUN1 U-T 25K FT -21.5°C

Category 8

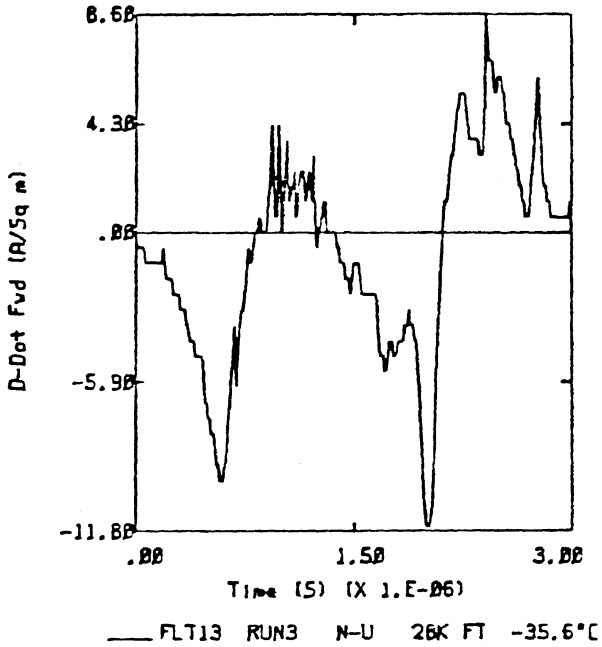
6.60
4.30
.00
-5.90
-11.80
D-Dot Fvd (A/Sq m)
.00
1.50
3.00
Time (S) (X 1.E-06)
FLT13 RUN3 N-U 28K FT -35.6°C

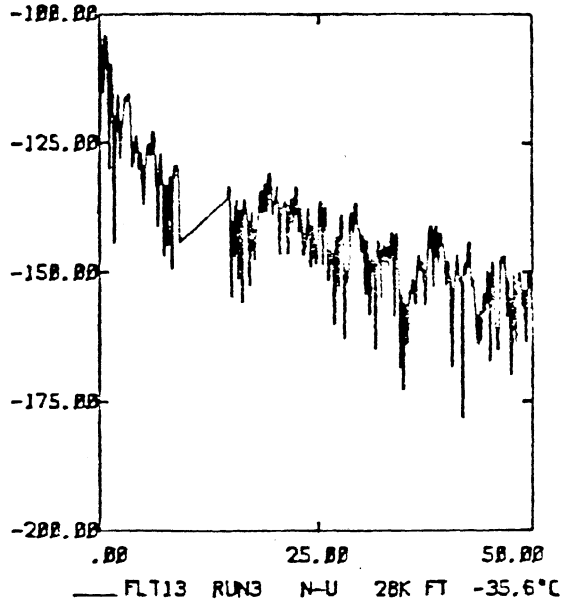
-100.00
-125.00
-150.00
-175.00
-200.00
.00
25.00
50.00
FLT13 RUN3 N-U 28K FT -35.6°C

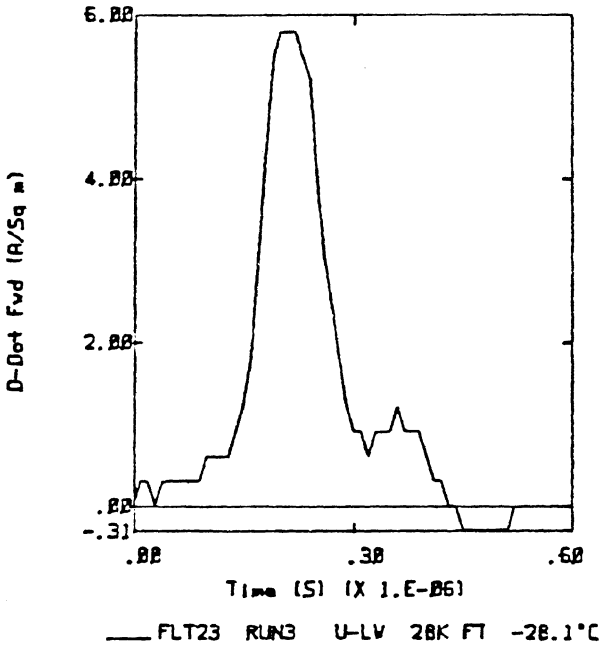
6.00
4.00
2.00
.00
-.31
D-Dot Fvd (A/Sq m)
.00
.30
.60
Time (S) (X 1.E-06)
FLT23 RUN3 U-LW 28K FT -28.1°C

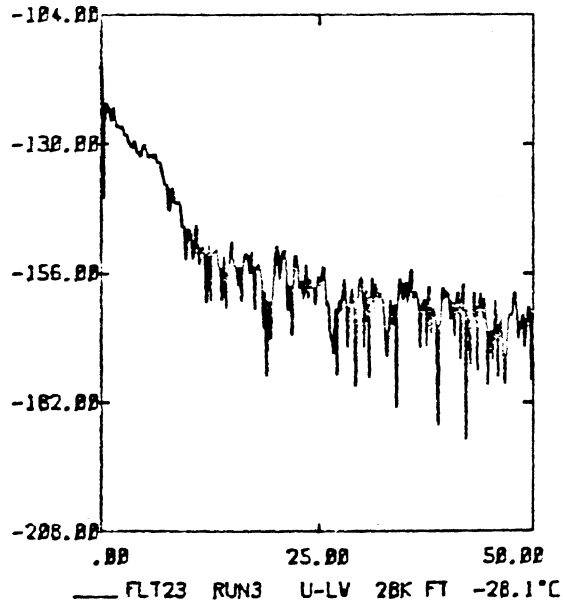
-104.00
-130.00
-156.00
-182.00
-208.00
.00
25.00
50.00
FLT23 RUN3 U-LW 28K FT -28.1°C

Category 8

B-Dot Records

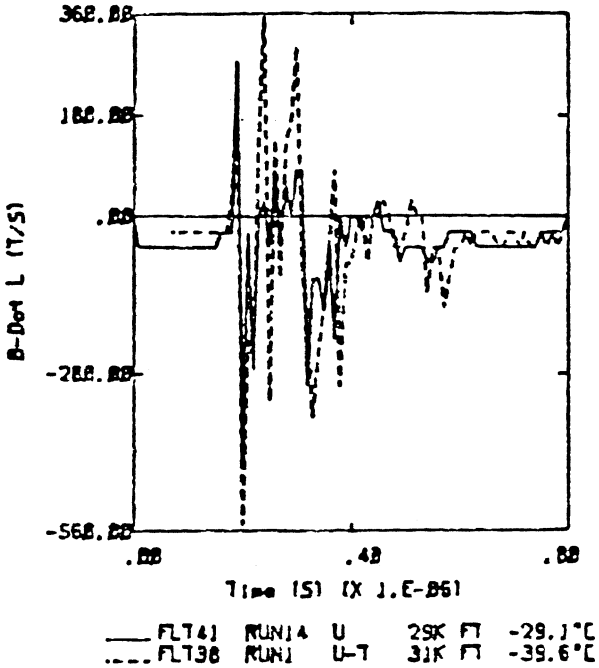
B-Dot L (T/S)
Time (S) (X 1.E-06)
FLT41 RUN14 U 29K FT -29.1°C
FLT38 RUN1 U-T 31K FT -39.6°C

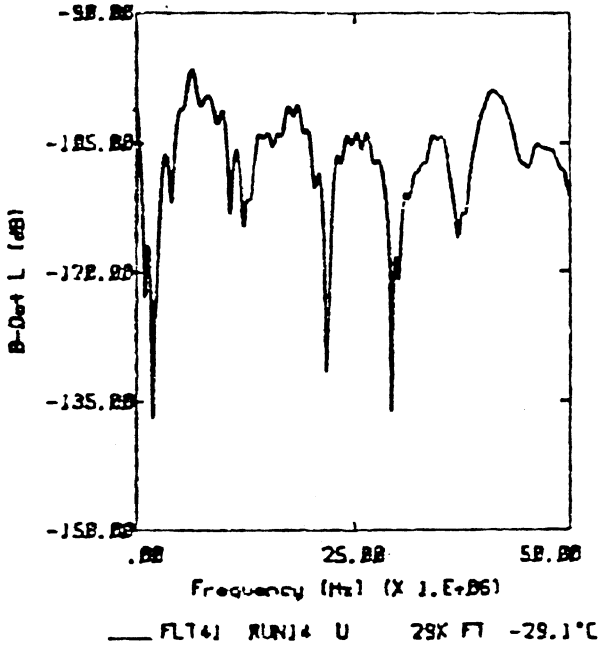
B-Dot L (dB)
Frequency (Hz) (X 1.E+06)
FLT41 RUN14 U 29K FT -29.1°C

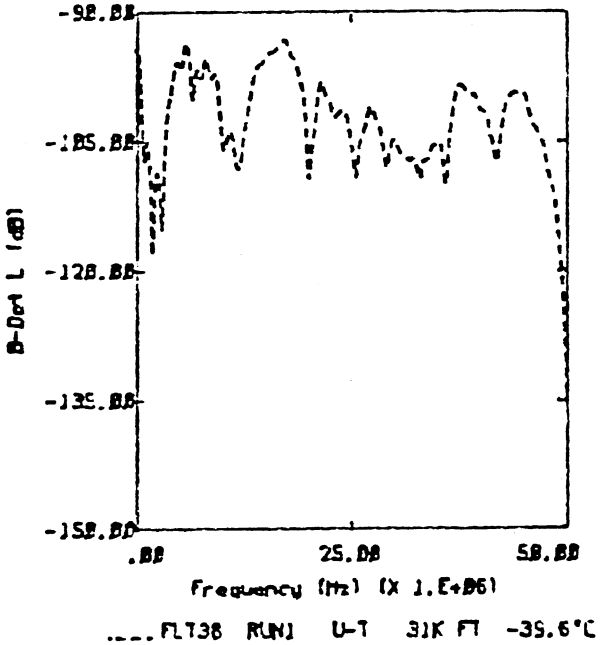
B-Dot L (dB)
Frequency (Hz) (X 1.E+06)
FLT38 RUN1 U-T 31K FT -39.6°C

Category 1

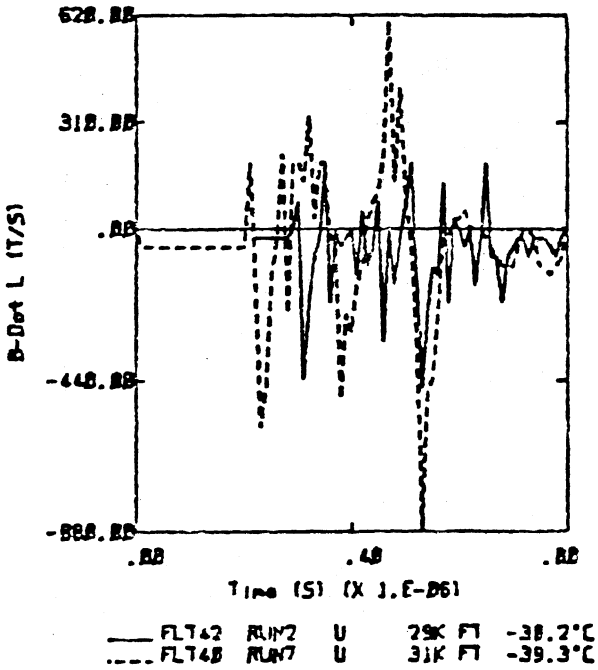
620.00
310.00
.00
-440.00
-880.00
.00
.40
.80
B-Dot L (T/S)
Time (S) (X 1.E-06)
FLT42 RUN2 U 29K FT -38.2°C
FLT48 RUN7 U 31K FT -39.3°C

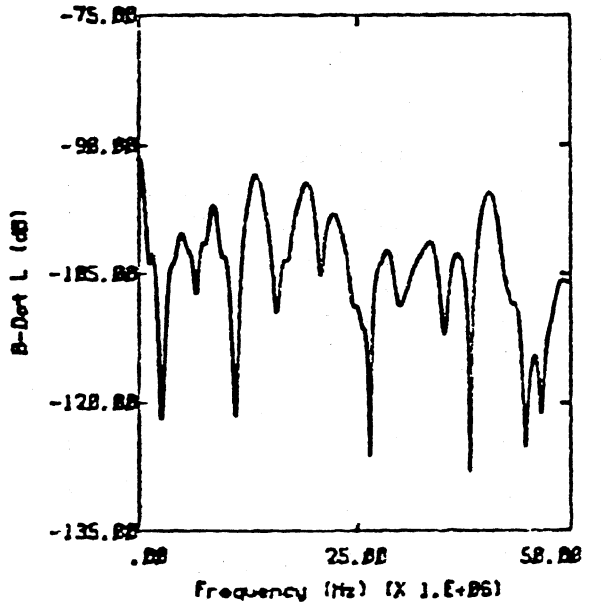
-75.00
-90.00
-105.00
-120.00
-135.00
.00
25.00
50.00
B-Dot L (dB)
Frequency (Hz) (X 1.E+06)
FLT42 RUN2 U 29K FT -38.2°C

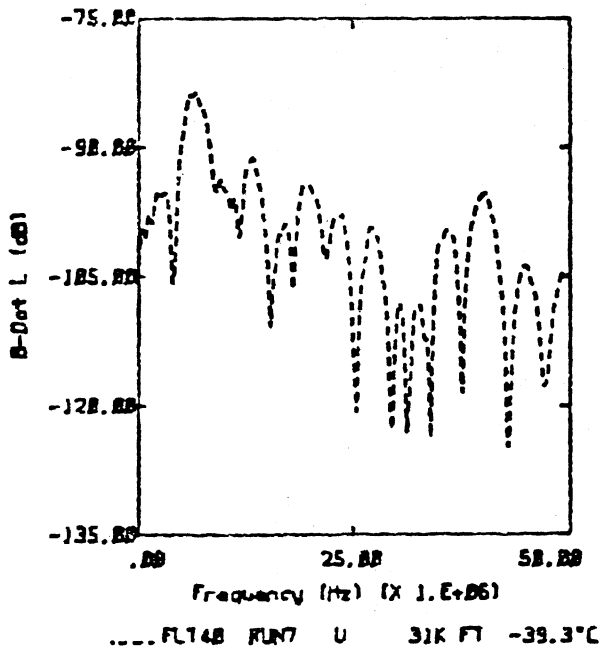
-75.00
-90.00
-105.00
-120.00
-135.00
.00
25.00
50.00
B-Dot L (dB)
Frequency (Hz) (X 1.E+06)
FLT48 RUN7 U 31K FT -39.3°C

Category 1

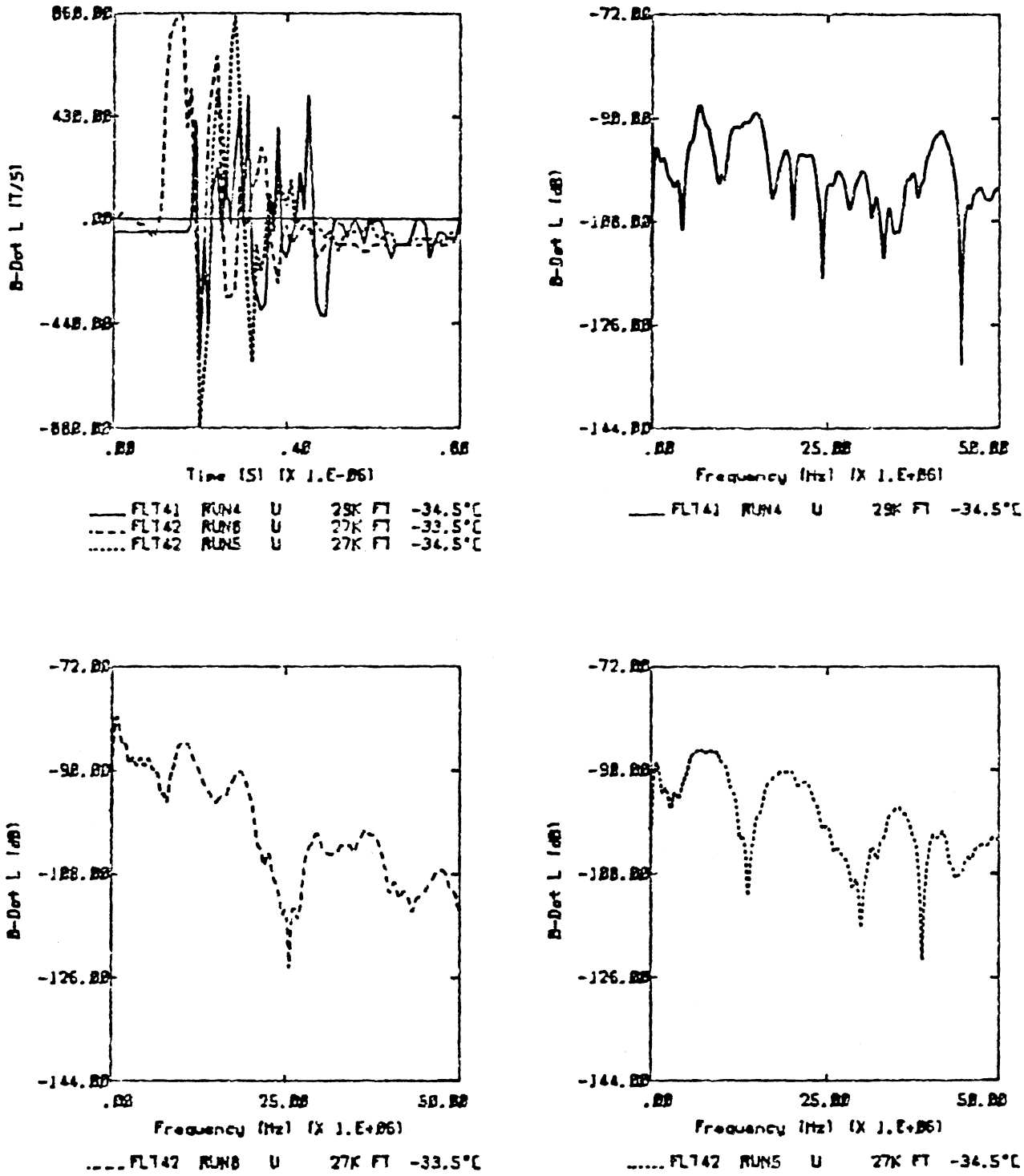
B-Dot L (T/S)
Time (S) (X 1.E-06)
FLT41 RUN4 U 29K FT -34.5°C
FLT42 RUN8 U 27K FT -33.5°C
FLT42 RUN5 U 27K FT -34.5°C
B-Dot L (dB)
Frequency (Hz) (X 1.E+06)
FLT41 RUN4 U 29K FT -34.5°C
FLT42 RUN8 U 27K FT -33.5°C
FLT42 RUN5 U 27K FT -34.5°C

Category 1

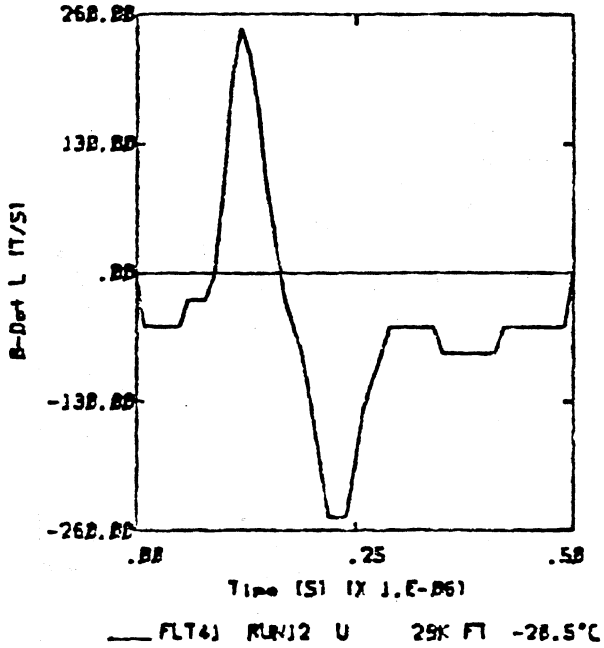
260.00
130.00
.00
-130.00
-260.00
B-Dot L (T/S)
.00
.25
.50
Time (S) (X 1.E-06)
FLT41 RUN12 U 29K FT -28.5°C

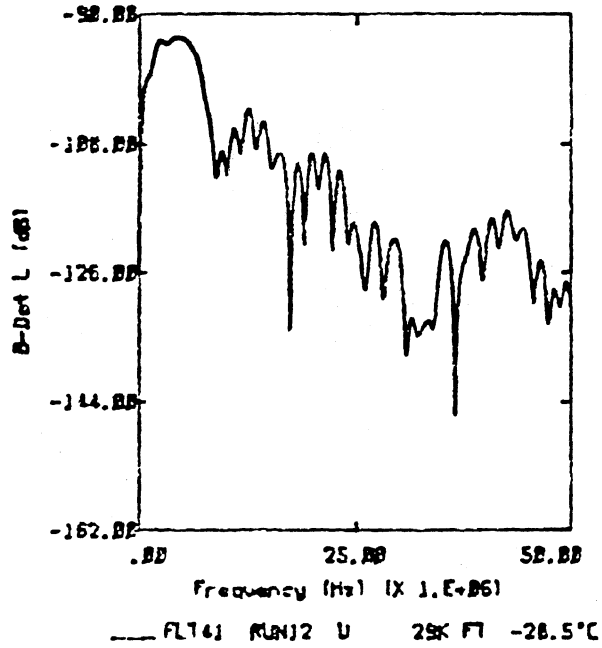
-90.00
-108.00
-126.00
-144.00
-162.00
B-Dot L (dB)
.00
25.00
50.00
Frequency (Hz) (X 1.E+06)
FLT41 RUN12 U 29K FT -28.5°C

Category 2

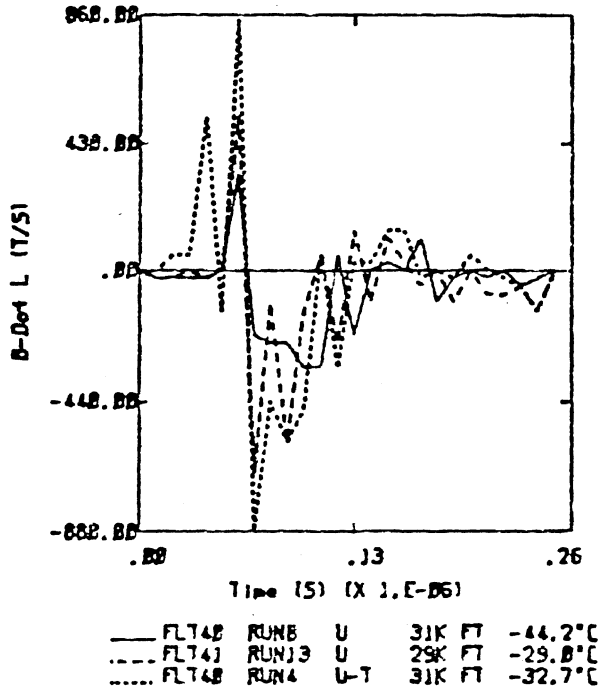
B-Dot L (T/S)
Time (S) (X 1.E-06)
FLT48 RUN8 U 31K FT -44.2°C
FLT41 RUN13 U 29K FT -29.0°C
FLT48 RUN4 U-T 31K FT -32.7°C

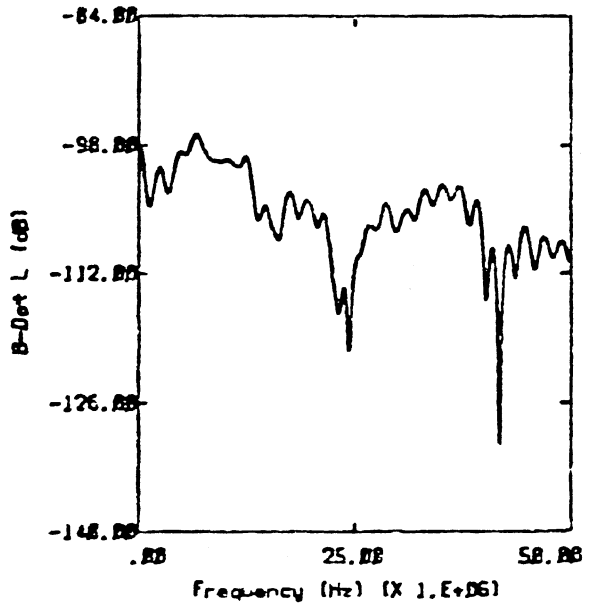
B-Dot L (dB)
Frequency (Hz) (X 1.E+06)
FLT48 RUN8 U 31K FT -44.2°C

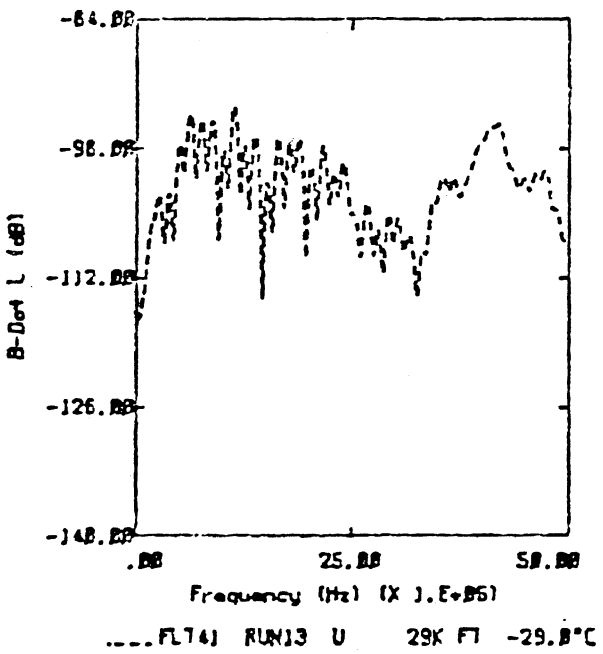
B-Dot L (dB)
Frequency (Hz) (X 1.E+06)
FLT41 RUN13 U 29K FT -29.0°C

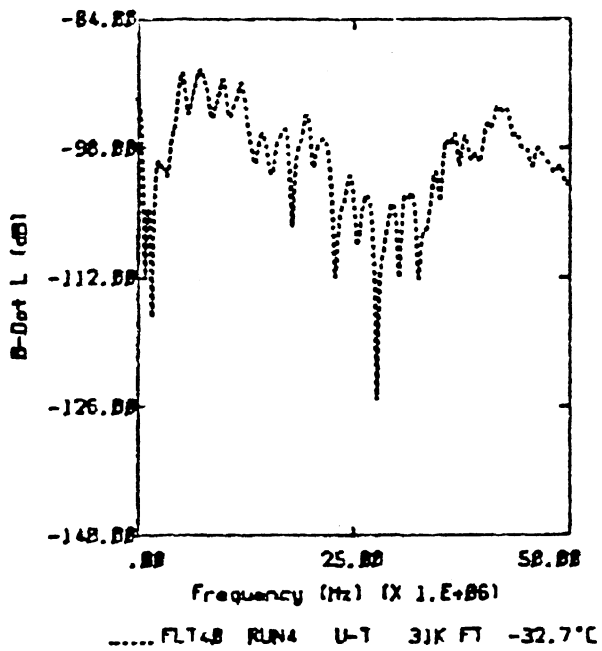
B-Dot L (dB)
Frequency (Hz) (X 1.E+06)
FLT48 RUN4 U-T 31K FT -32.7°C

Category 3

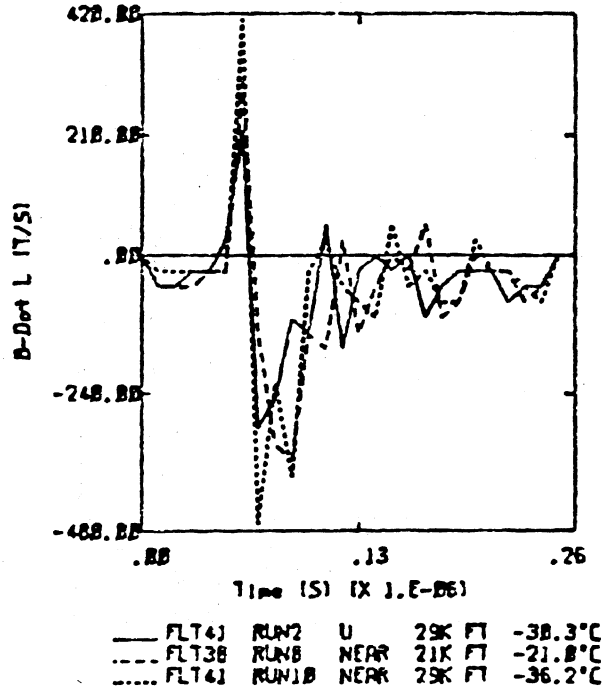
420.00
210.00
.00
-240.00
-480.00
B-Dot L (T/S)
.00
.13
.26
Time (S) (X 1.E-06)
FLT41 RUN2 U 29K FT -38.3°C
FLT38 RUN8 NEAR 21K FT -21.0°C
FLT41 RUN10 NEAR 29K FT -36.2°C

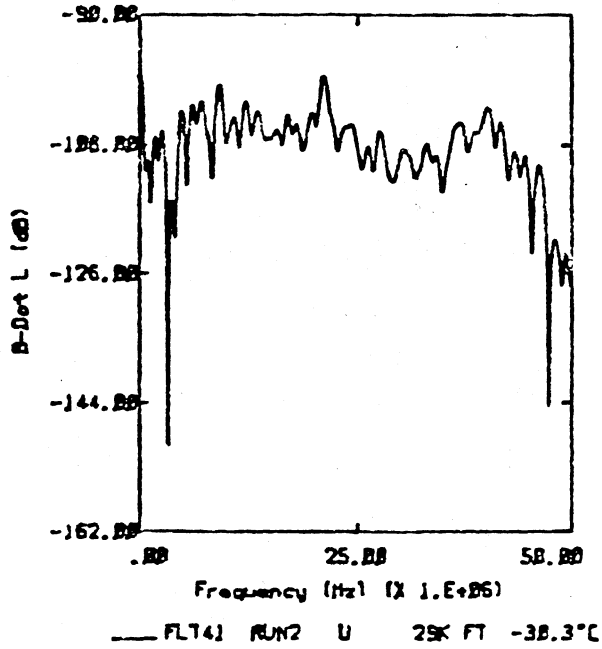
-90.00
-108.00
-126.00
-144.00
-162.00
B-Dot L (dB)
.00
25.00
50.00
Frequency (Hz) (X 1.E+06)
FLT41 RUN2 U 29K FT -38.3°C

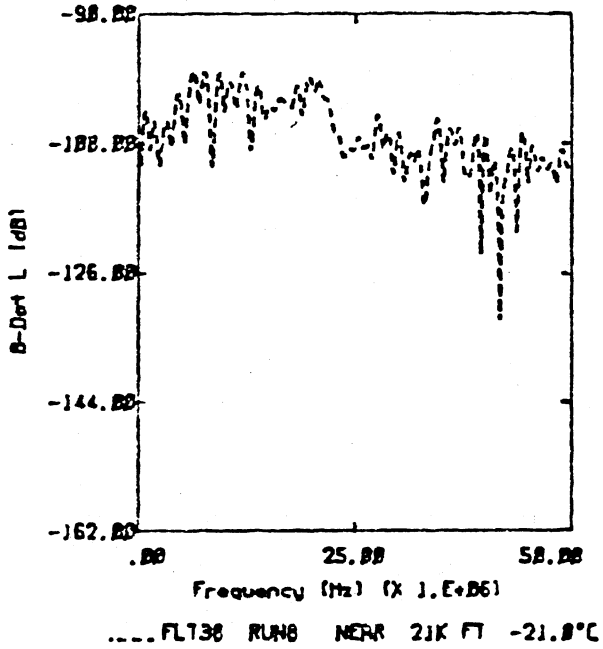
-90.00
-108.00
-126.00
-144.00
-162.00
B-Dot L (dB)
.00
25.00
50.00
Frequency (Hz) (X 1.E+06)
FLT38 RUN8 NEAR 21K FT -21.0°C

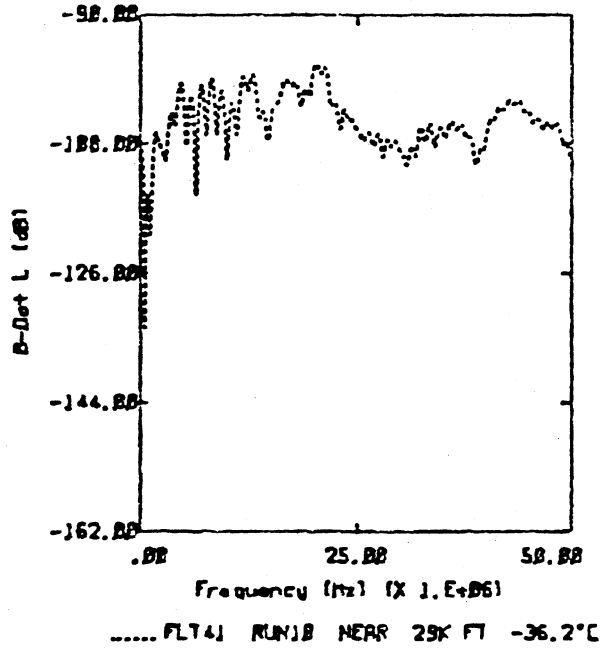
-90.00
-108.00
-126.00
-144.00
-162.00
B-Dot L (dB)
.00
25.00
50.00
Frequency (Hz) (X 1.E+06)
FLT41 RUN10 NEAR 29K FT -36.2°C

Category 3

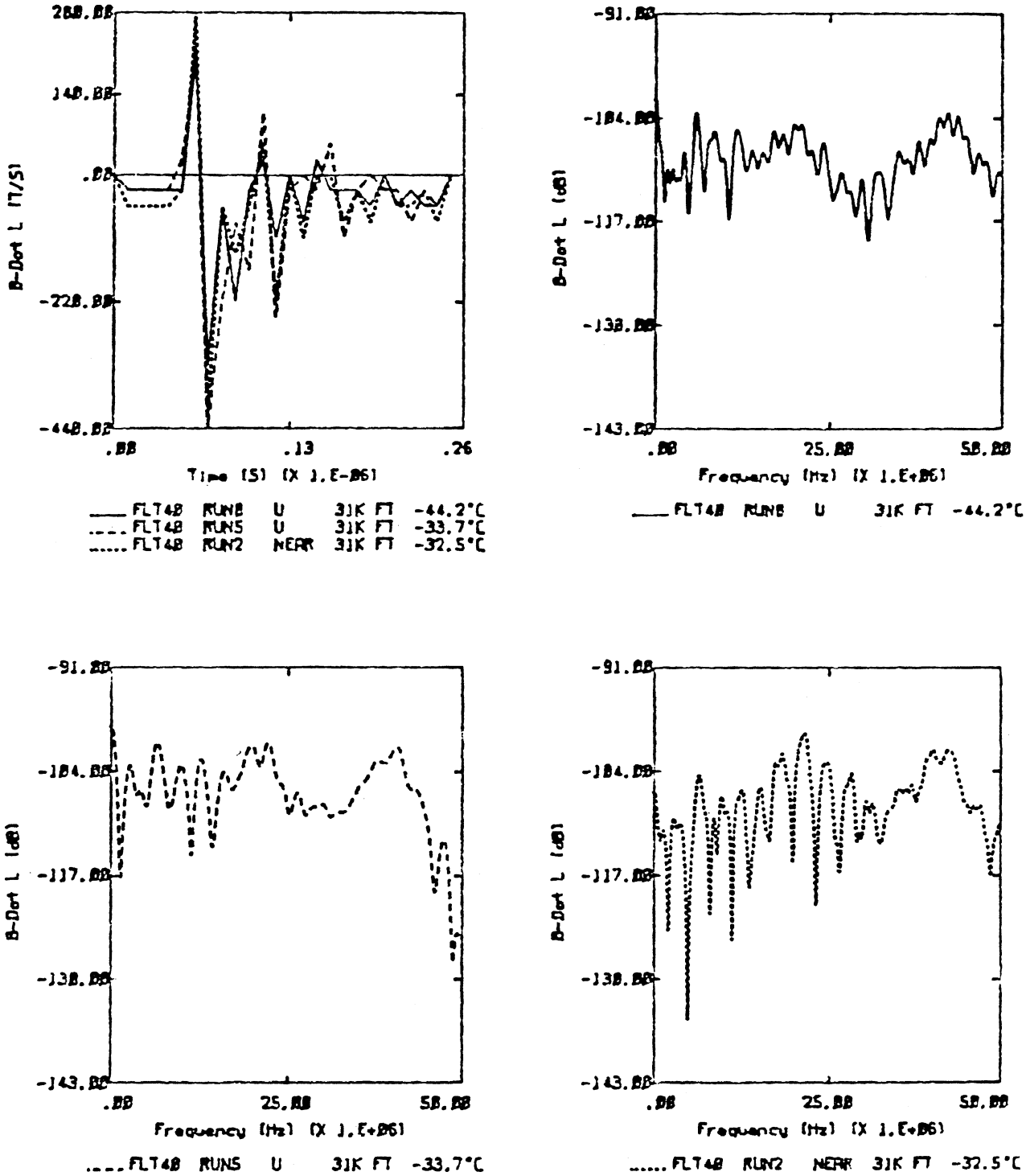
B-Dot L (T/S)
Time (S) (X 1.E-06)
FLT48 RUN8 U 31K FT -44.2°C
FLT48 RUN5 U 31K FT -33.7°C
FLT48 RUN2 NEAR 31K FT -32.5°C
B-Dot L (dB)
Frequency (Hz) (X 1.E+06)
FLT48 RUN8 U 31K FT -44.2°C
FLT48 RUN5 U 31K FT -33.7°C
FLT48 RUN2 NEAR 31K FT -32.5°C

Category 3

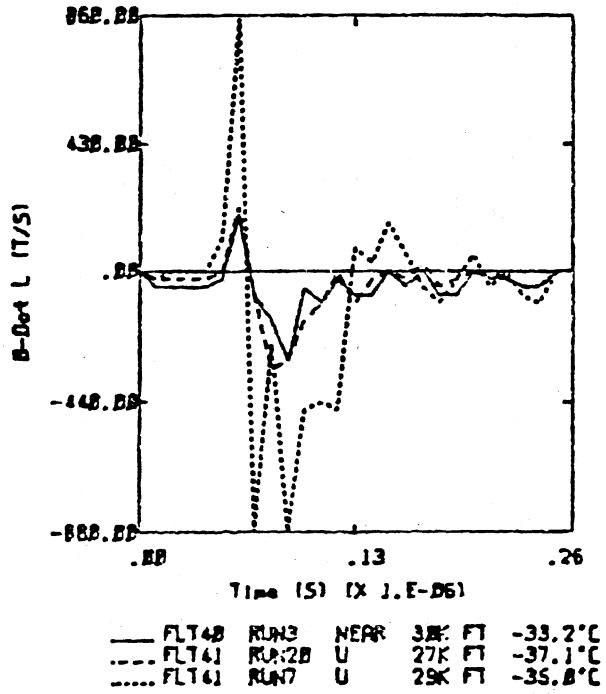
B-Dot L (T/S)
Time (S) (X 1.E-06)
FLT48 RUN3 NEAR 38K FT -33.2°C
FLT41 RUN28 U 27K FT -37.1°C
FLT41 RUN7 U 29K FT -35.8°C

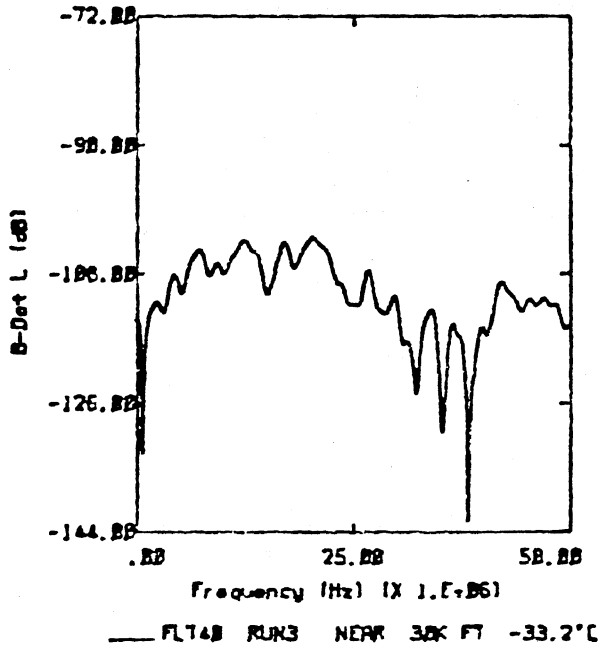
B-Dot L (dB)
Frequency (Hz) (X 1.E+06)
FLT48 RUN3 NEAR 38K FT -33.2°C

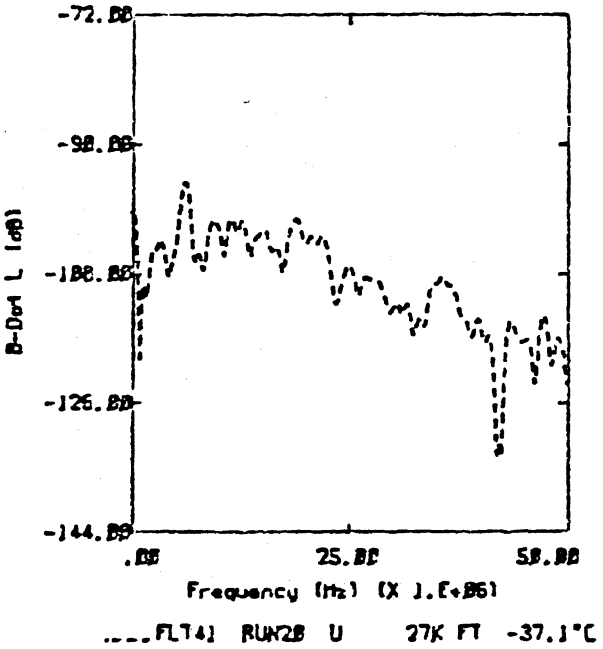
B-Dot L (dB)
Frequency (Hz) (X 1.E+06)
FLT41 RUN28 U 27K FT -37.1°C

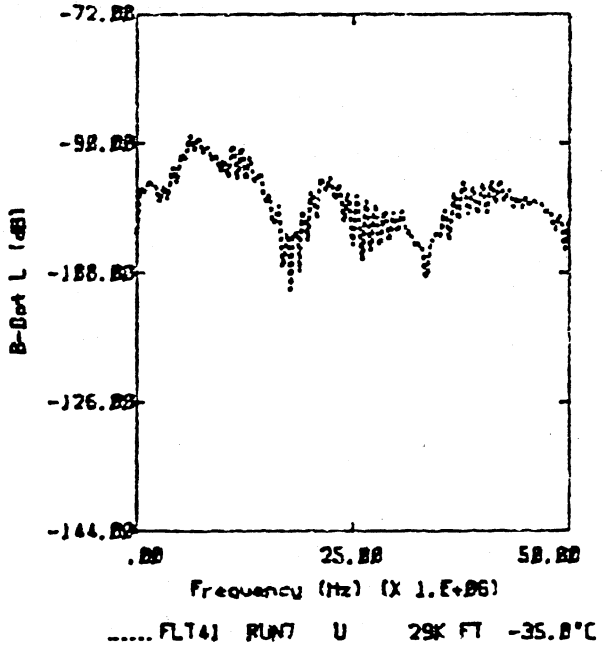
B-Dot L (dB)
Frequency (Hz) (X 1.E+06)
FLT41 RUN7 U 29K FT -35.8°C

Category 3

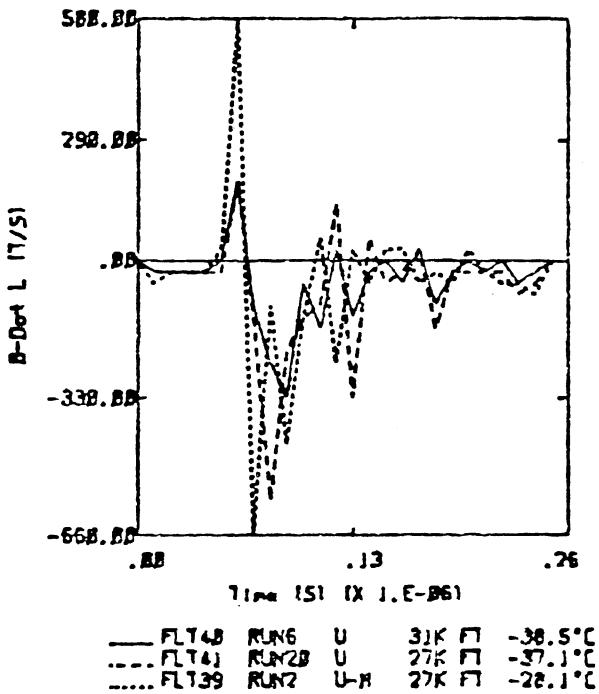
B-Dot L (T/S)
Time (S) (X 1.E-06)
FLT48 RUN6 U 31K FT -38.5°C
FLT41 RUN2B U 27K FT -37.1°C
FLT39 RUN2 U-M 27K FT -28.1°C

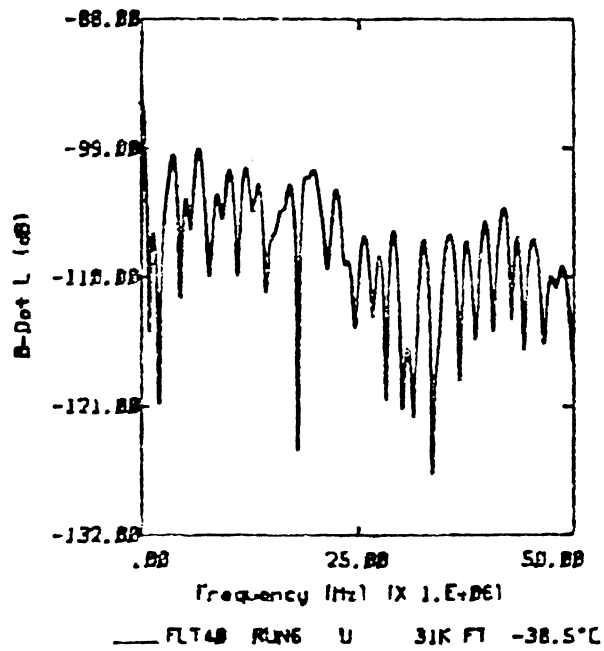
B-Dot L (dB)
Frequency (Hz) (X 1.E+06)
FLT48 RUN6 U 31K FT -38.5°C

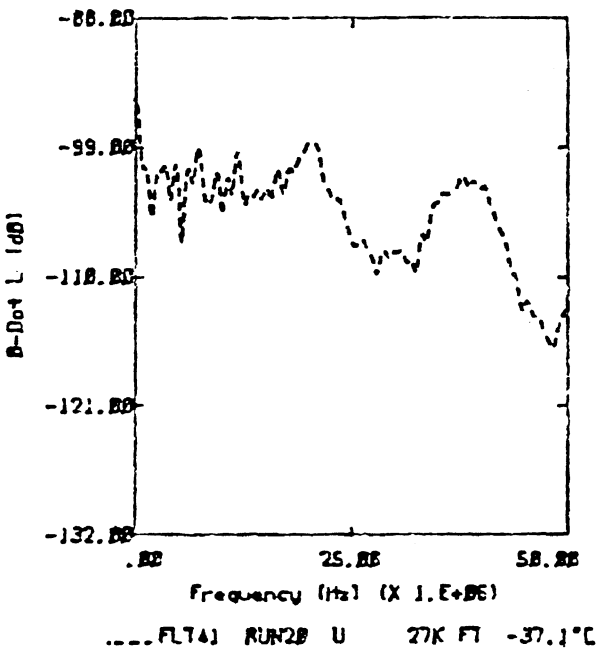
B-Dot L (dB)
Frequency (Hz) (X 1.E+06)
FLT41 RUN2B U 27K FT -37.1°C

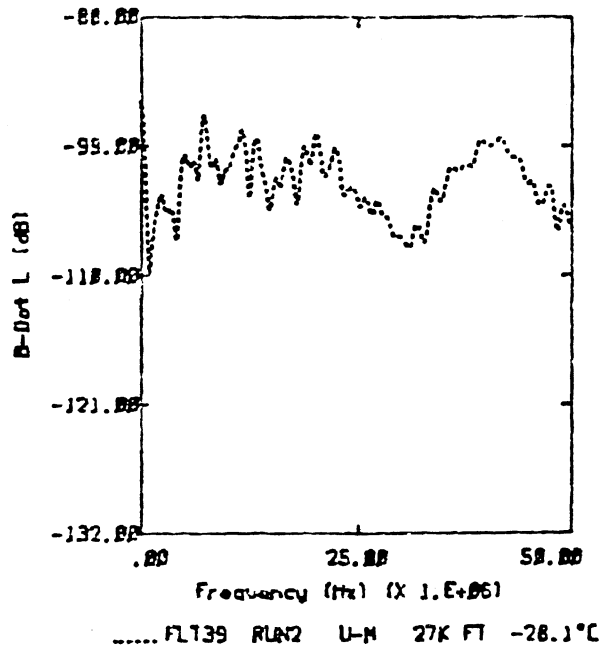
B-Dot L (dB)
Frequency (Hz) (X 1.E+06)
FLT39 RUN2 U-M 27K FT -28.1°C

Category 3

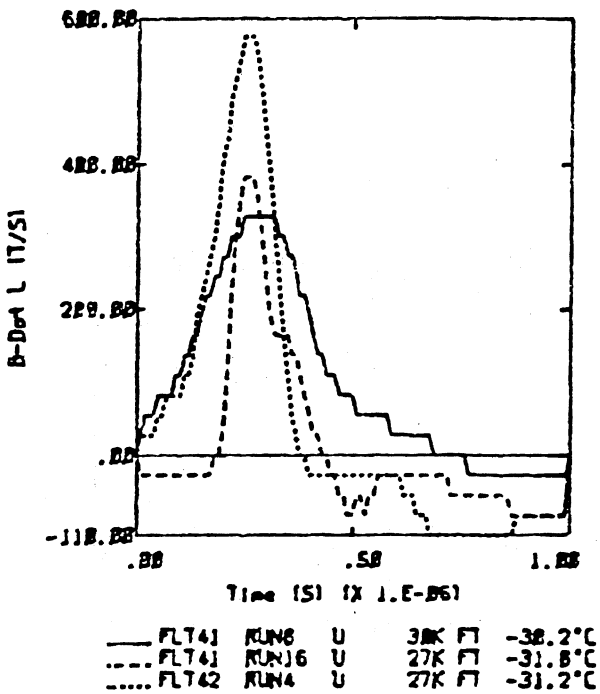
B-Dot L (T/S)
Time (S) (X 1.E-06)
FLT41 RUN8 U 30K FT -30.2°C
FLT41 RUN16 U 27K FT -31.8°C
FLT42 RUN4 U 27K FT -31.2°C

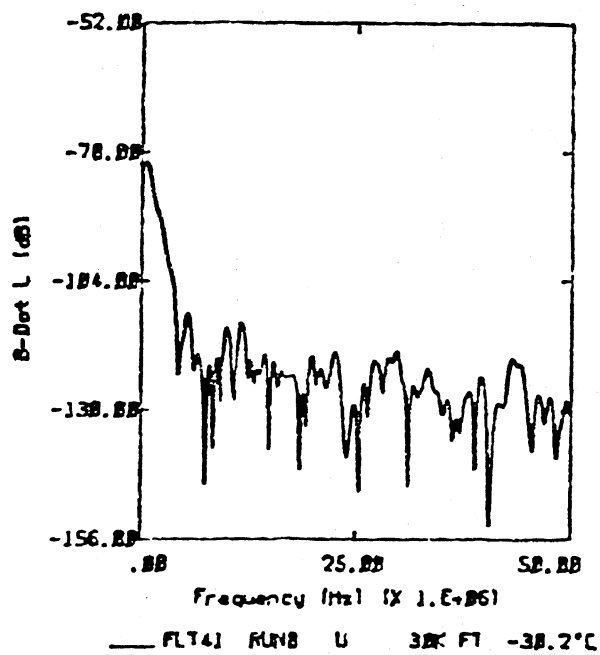
B-Dot L (dB)
Frequency (Hz) (X 1.E+06)
FLT41 RUN8 U 30K FT -30.2°C

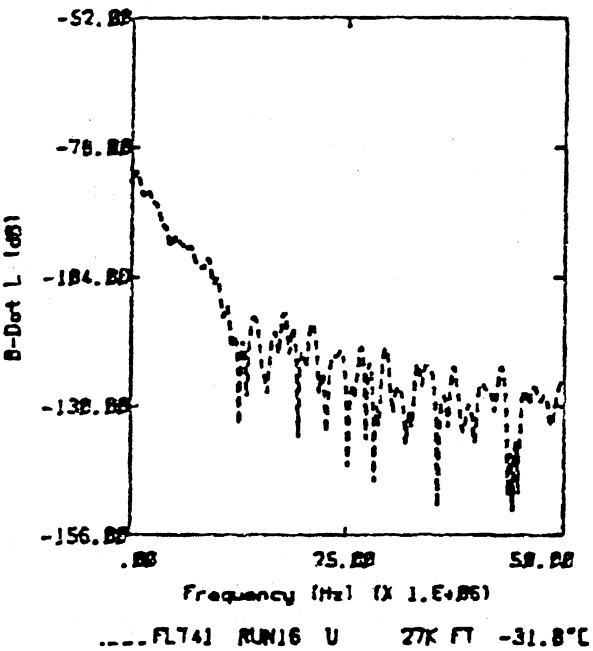
B-Dot L (dB)
Frequency (Hz) (X 1.E+06)
FLT41 RUN16 U 27K FT -31.8°C

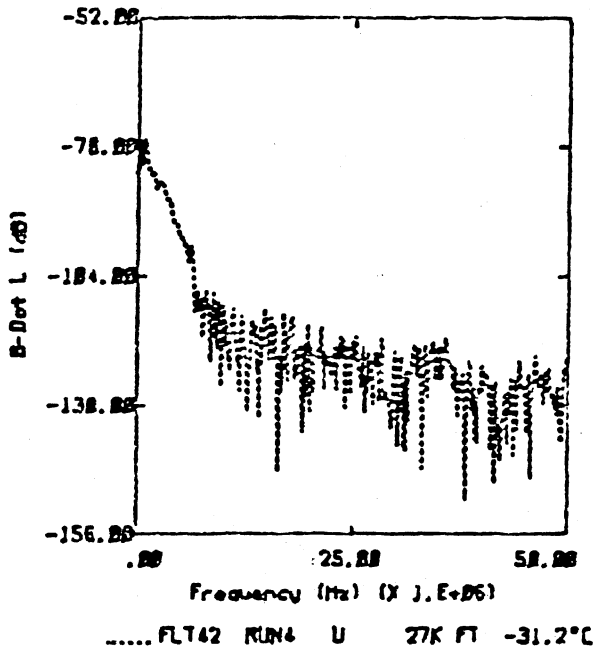
B-Dot L (dB)
Frequency (Hz) (X 1.E+06)
FLT42 RUN4 U 27K FT -31.2°C

Category 4

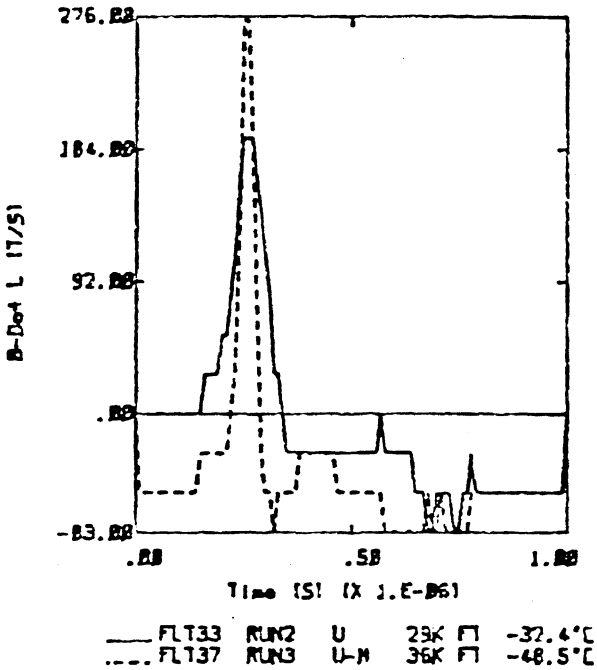
276.00
184.00
92.00
.00
-83.00
B-Dot L (T/S)
.00
.50
1.00
Time (S) (X 1.E-06)
FLT33 RUN2 U 29K FT -32.4°C
FLT37 RUN3 U-M 36K FT -48.5°C

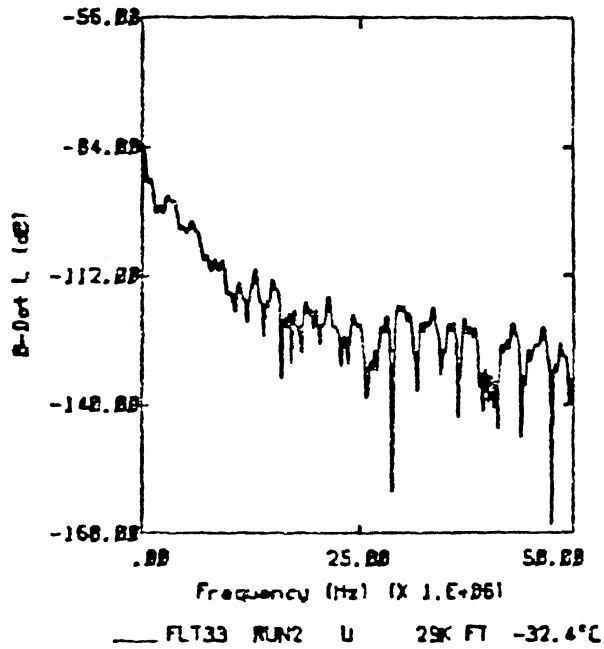
-56.00
-84.00
-112.00
-140.00
-168.00
B-Dot L (dB)
.00
25.00
50.00
Frequency (Hz) (X 1.E+06)
FLT33 RUN2 U 29K FT -32.4°C

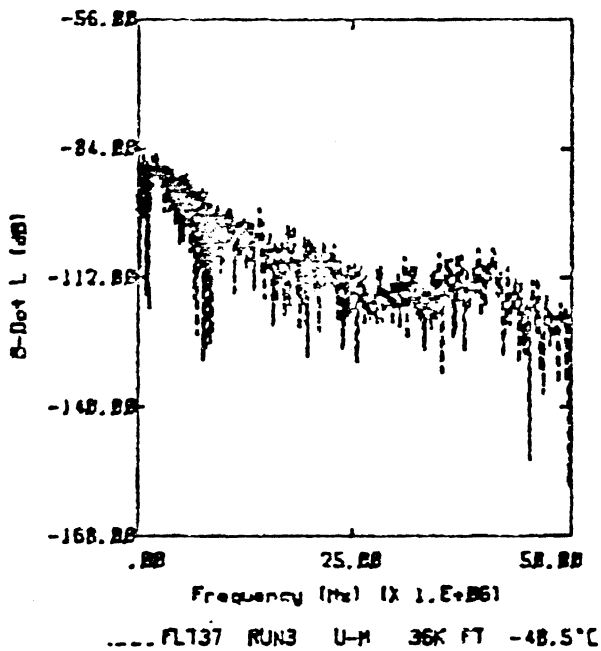
-56.00
-84.00
-112.00
-140.00
-168.00
B-Dot L (dB)
.00
25.00
50.00
Frequency (Hz) (X 1.E+06)
FLT37 RUN3 U-M 36K FT -48.5°C

Category 4

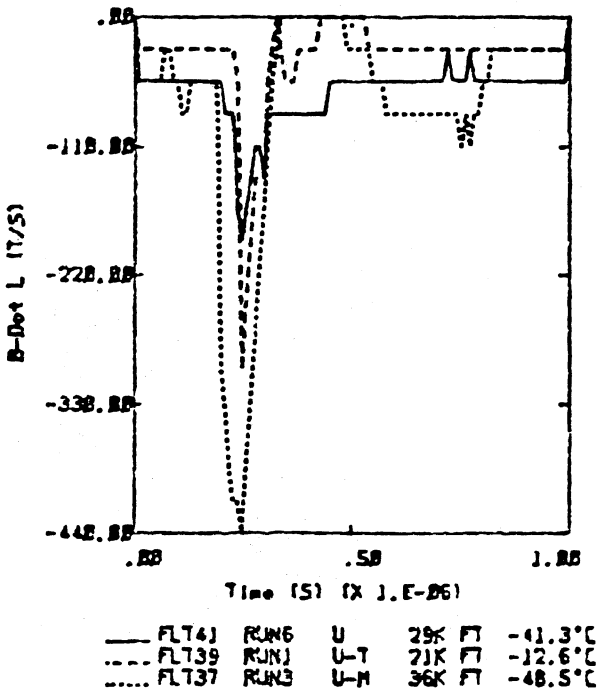
.00
-110.00
-220.00
-330.00
-440.00
B-Dot L (T/S)
.00
.50
1.00
Time (S) (X 1.E-06)
FLT41 RUN6 U 29K FT -41.3°C
FLT39 RUN1 U-T 21K FT -12.6°C
FLT37 RUN3 U-M 36K FT -48.5°C

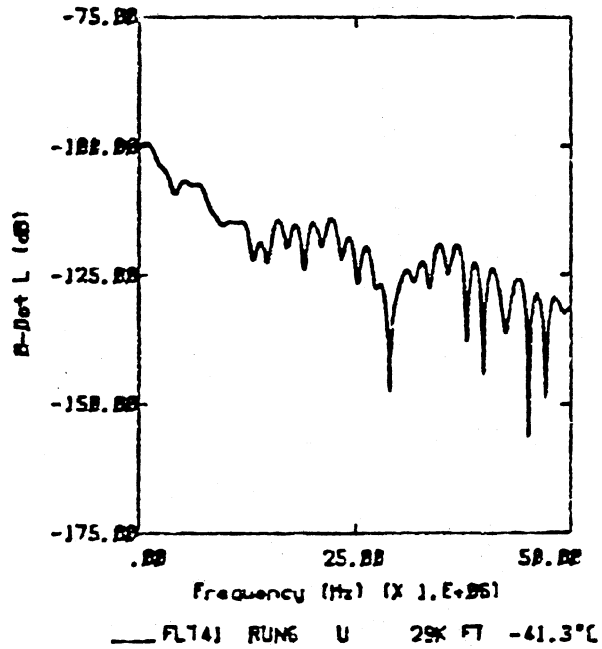
-75.00
-100.00
-125.00
-150.00
-175.00
B-Dot L (dB)
.00
25.00
50.00
Frequency (Hz) (X 1.E+06)
FLT41 RUN6 U 29K FT -41.3°C

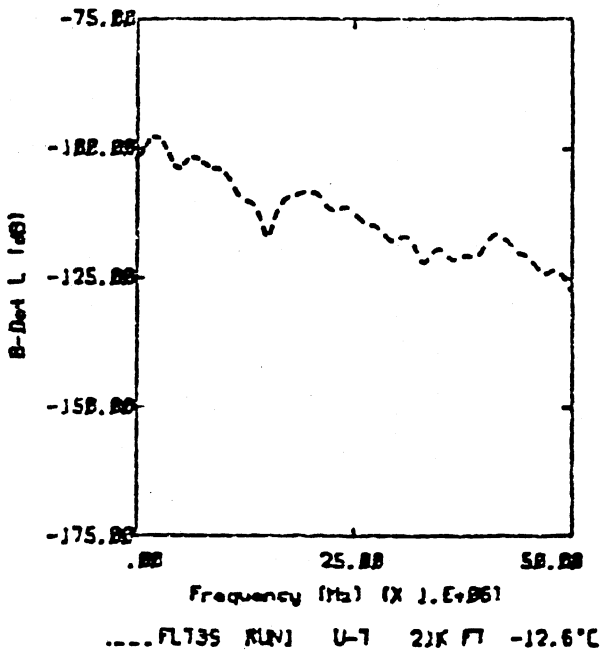
-75.00
-100.00
-125.00
-150.00
-175.00
B-Dot L (dB)
.00
25.00
50.00
Frequency (Hz) (X 1.E+06)
FLT39 RUN1 U-T 21K FT -12.6°C

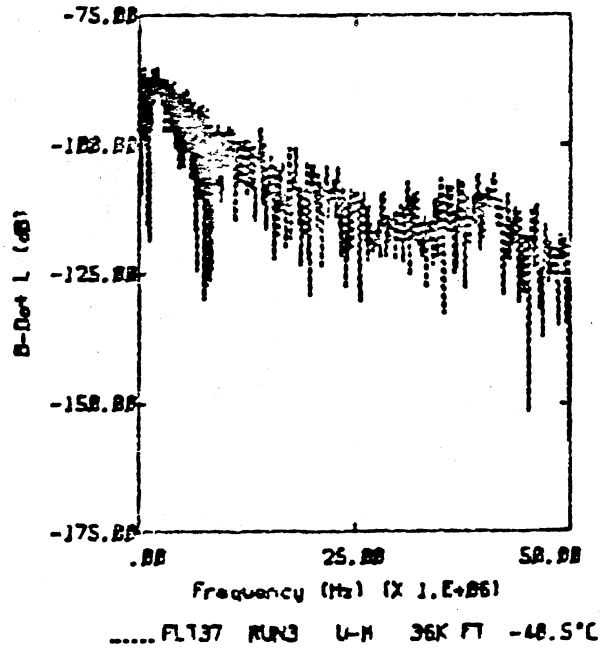
-75.00
-100.00
-125.00
-150.00
-175.00
B-Dot L (dB)
.00
25.00
50.00
Frequency (Hz) (X 1.E+06)
FLT37 RUN3 U-M 36K FT -48.5°C

Category 5

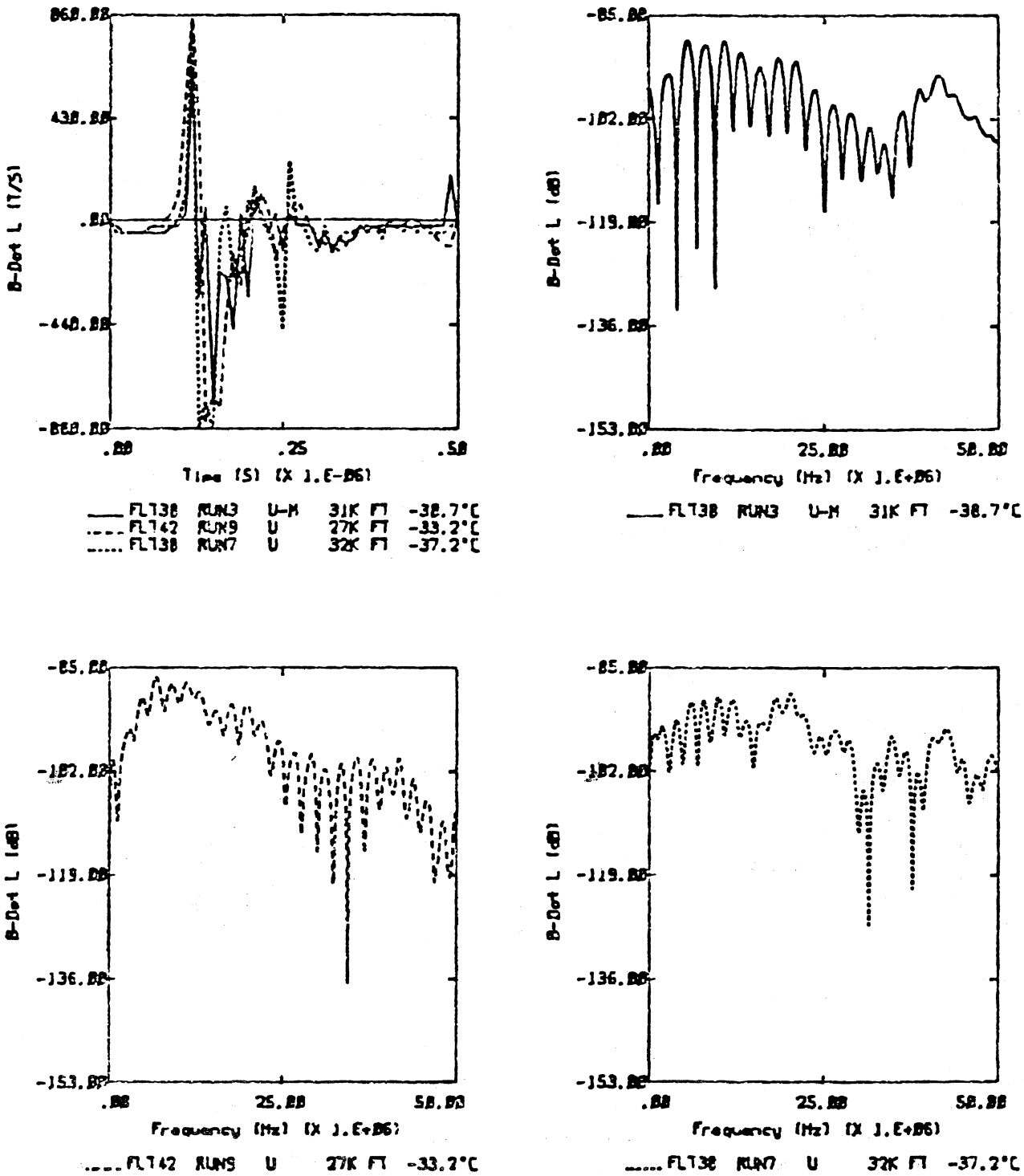
B-Dot L (T/S)
Time (S) (X 1.E-06)
FLT38 RUN3 U-M 31K FT -38.7°C
FLT42 RUN9 U 27K FT -33.2°C
FLT38 RUN7 U 32K FT -37.2°C
B-Dot L (dB)
Frequency (Hz) (X 1.E+06)
FLT38 RUN3 U-M 31K FT -38.7°C
FLT42 RUN9 U 27K FT -33.2°C
FLT38 RUN7 U 32K FT -37.2°C

Category 6

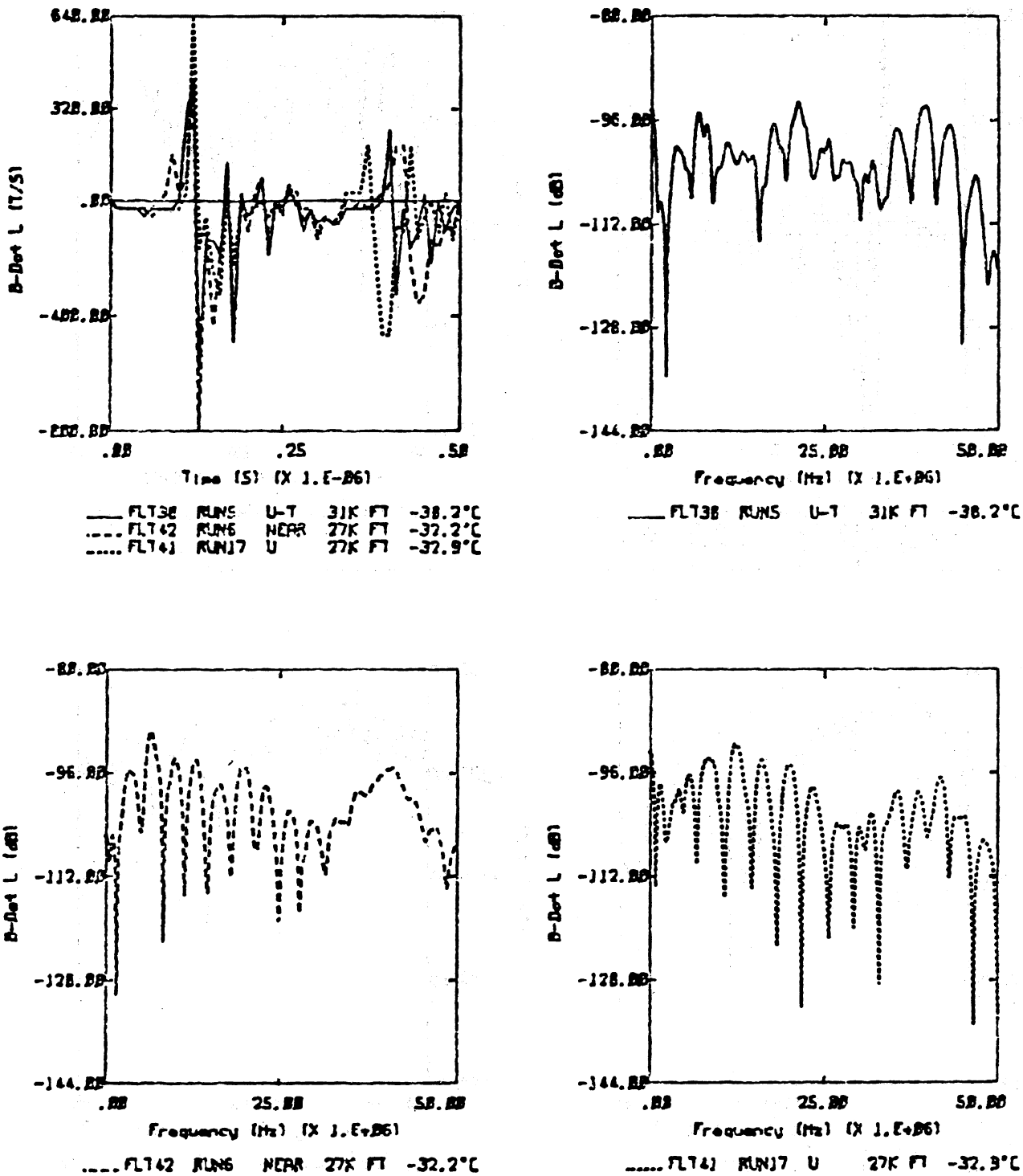
B-Dot L (T/S)
Time (S) (X 1.E-06)
FLT38 RUN5 U-T 31K FT -38.2°C
FLT42 RUN6 NEAR 27K FT -32.2°C
FLT41 RUN17 U 27K FT -32.9°C
B-Dot L (dB)
Frequency (Hz) (X 1.E+06)
FLT38 RUN5 U-T 31K FT -38.2°C
FLT42 RUN6 NEAR 27K FT -32.2°C
FLT41 RUN17 U 27K FT -32.9°C

Category 6

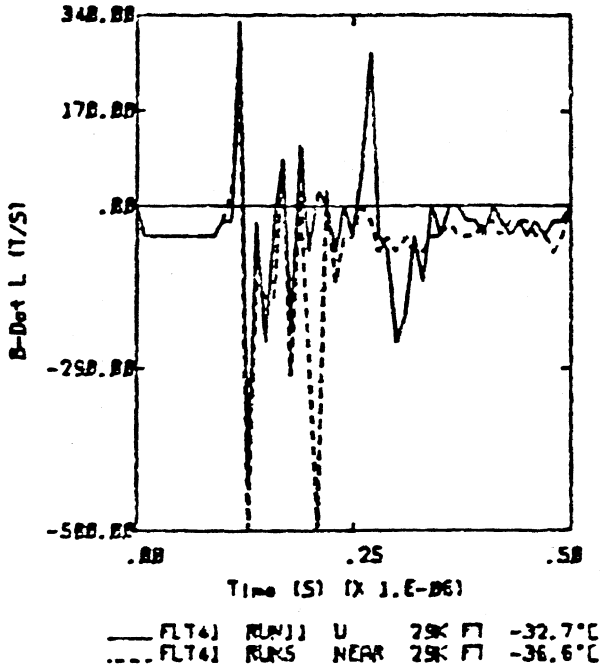
348.00
170.00
.00
-250.00
-500.00
.00
.25
.50
B-Dot L (T/S)
Time (S) (X 1.E-06)
FLT41 RUN11 U 25K FT -32.7°C
FLT41 RUN5 NEAR 25K FT -36.6°C

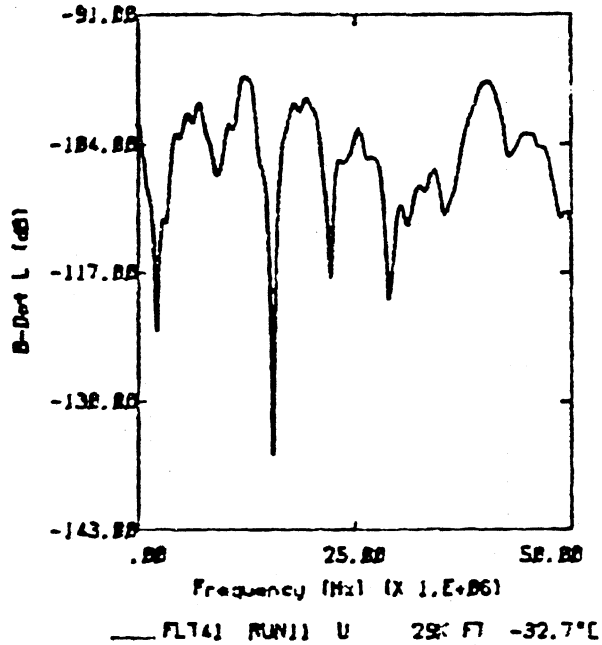
-91.00
-104.00
-117.00
-130.00
-143.00
.00
25.00
50.00
B-Dot L (dB)
Frequency (Hz) (X 1.E+06)
FLT41 RUN11 U 25K FT -32.7°C

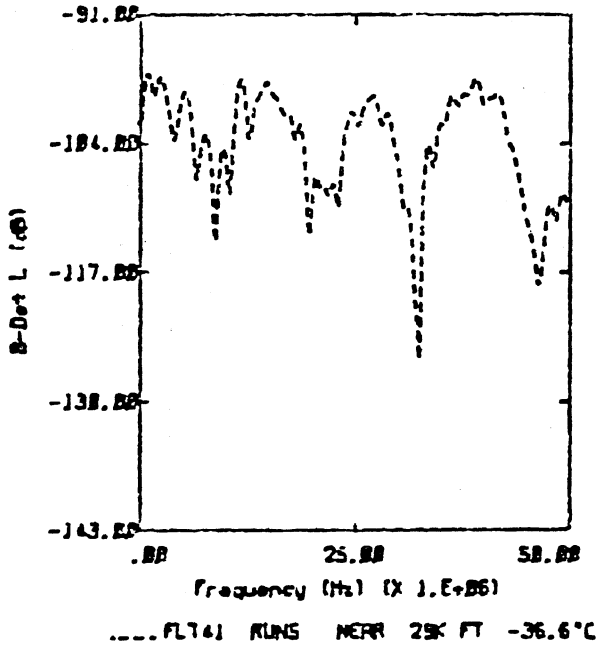
-91.00
-104.00
-117.00
-130.00
-143.00
.00
25.00
50.00
B-Dot L (dB)
Frequency (Hz) (X 1.E+06)
FLT41 RUN5 NEAR 25K FT -36.6°C

Category 6

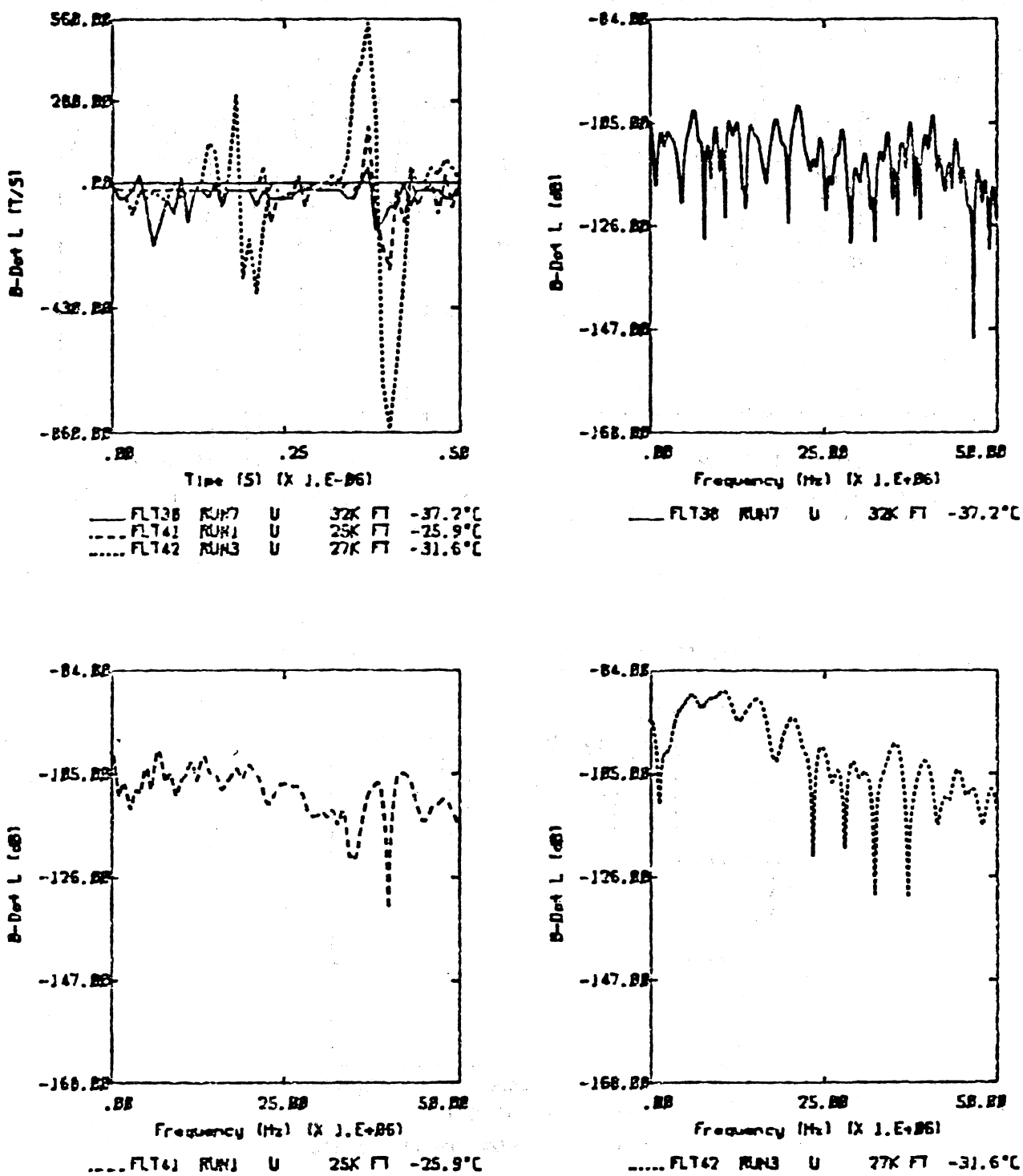
B-Dot L (T/S)
Time (S) (X 1.E-06)
FLT38 RUN7 U 32K FT -37.2°C
FLT41 RUN1 U 25K FT -25.9°C
FLT42 RUN3 U 27K FT -31.6°C
B-Dot L (dB)
Frequency (Hz) (X 1.E+06)
FLT38 RUN7 U 32K FT -37.2°C
FLT41 RUN1 U 25K FT -25.9°C
FLT42 RUN3 U 27K FT -31.6°C

Category 6

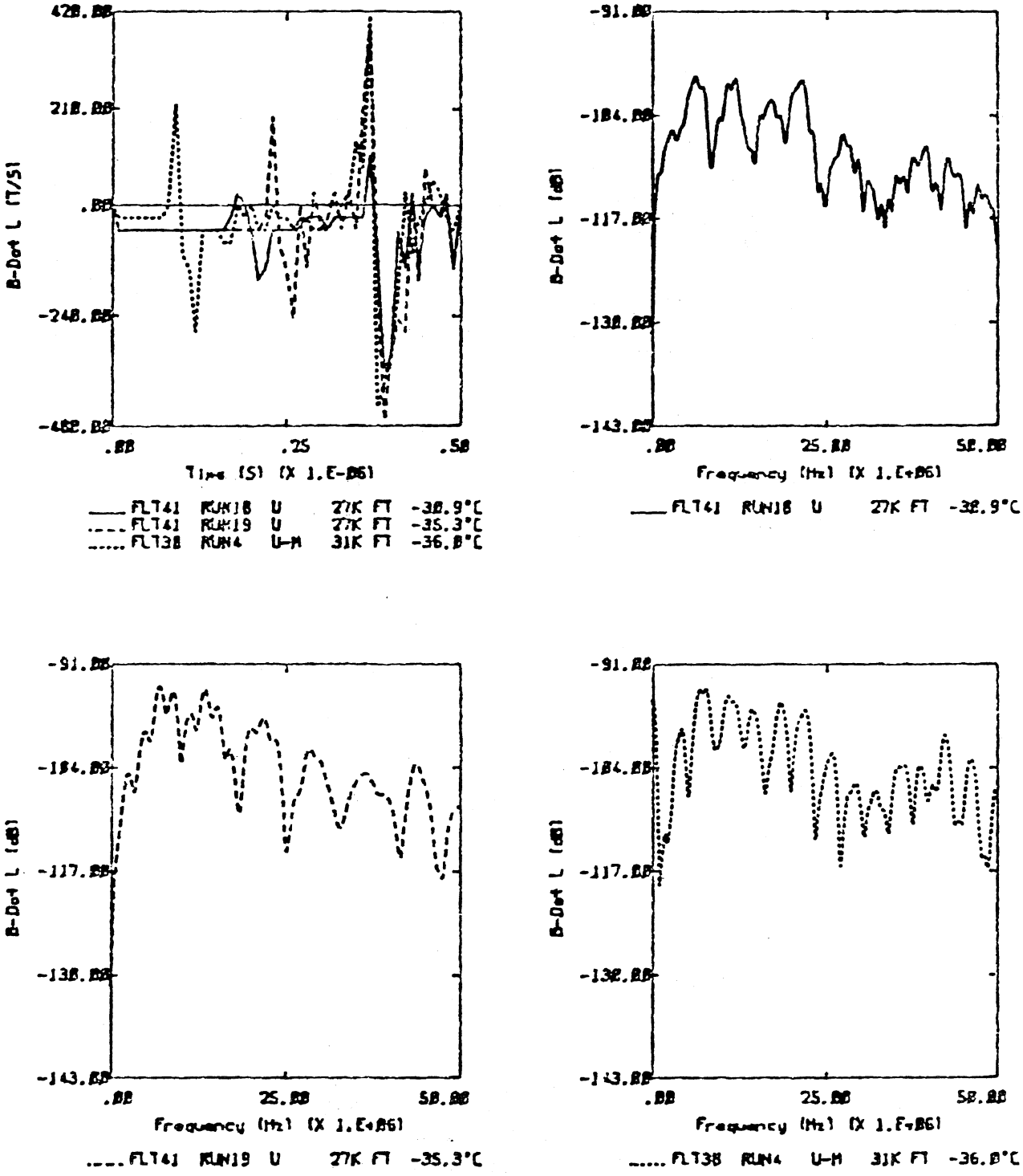
B-Dot L (T/S)
Time (S) (X 1.E-06)
FLT41 RUN18 U 27K FT -38.9°C
FLT41 RUN19 U 27K FT -35.3°C
FLT38 RUN4 U-M 31K FT -36.0°C
B-Dot L (dB)
Frequency (Hz) (X 1.E+06)
FLT41 RUN18 U 27K FT -38.9°C
FLT41 RUN19 U 27K FT -35.3°C
FLT38 RUN4 U-M 31K FT -36.0°C

Category 6

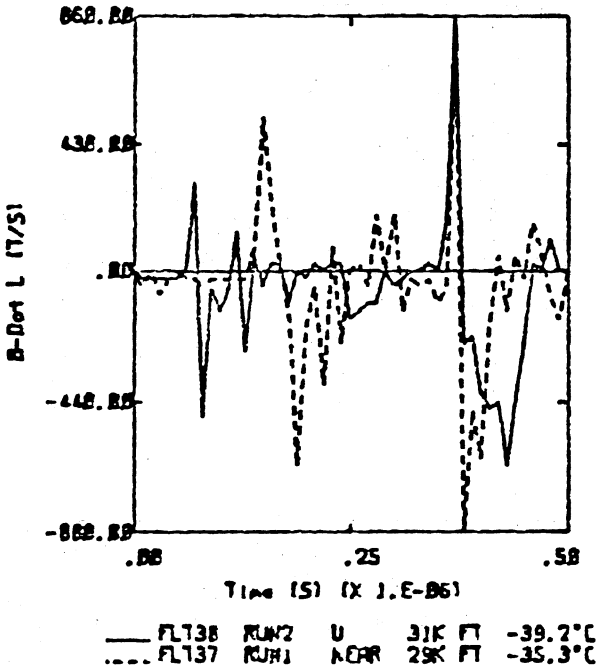
B-Dot L (T/S)
Time (S) (X 1.E-06)
FL738 RUN2 U 31K FT -39.2°C
FL737 RUN1 NEAR 29K FT -35.3°C

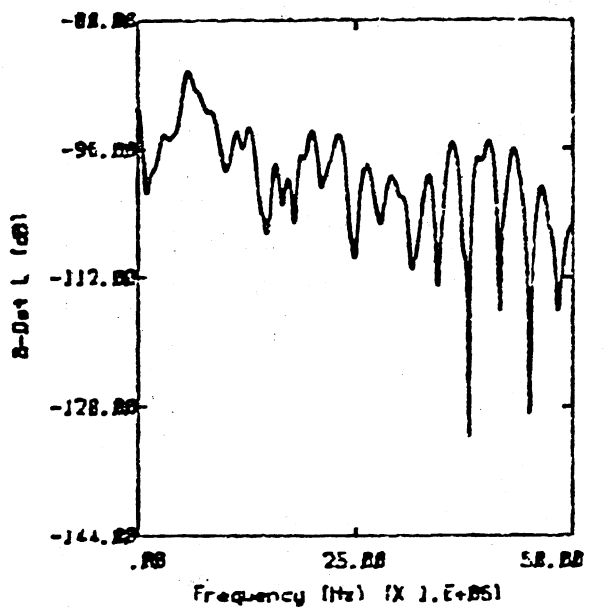
B-Dot L (dB)
Frequency (Hz) (X 1.E+06)
FL738 RUN2 U 31K FT -39.2°C

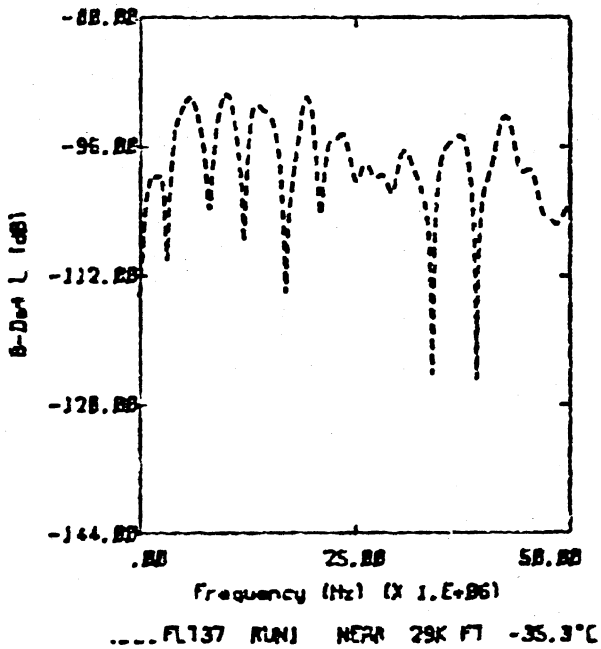
B-Dot L (dB)
Frequency (Hz) (X 1.E+06)
FL737 RUN1 NEAR 29K FT -35.3°C

Category 6

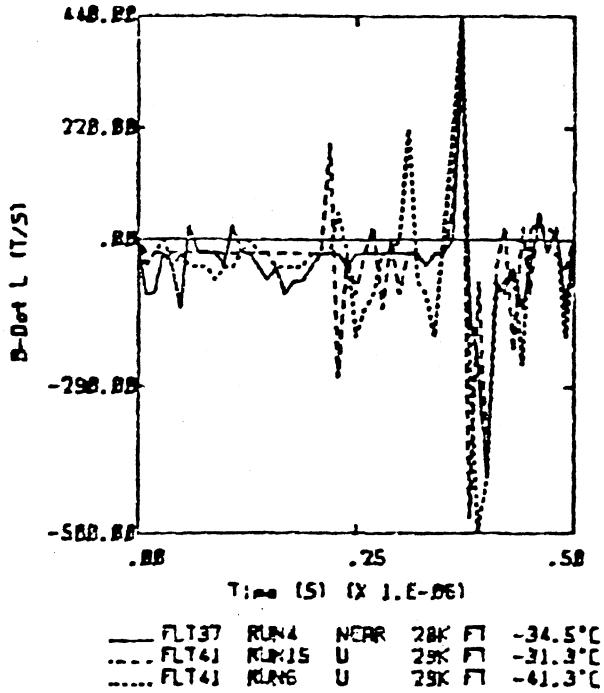
448.00
224.00
.00
-224.00
-448.00
B-Dot L (T/S)
.00
.25
.50
Time (S) (X 1.E-06)
FLT37 RUN4 NEAR 28K FT -34.5°C
FLT41 RUN15 U 29K FT -31.3°C
FLT41 RUN6 U 29K FT -41.3°C

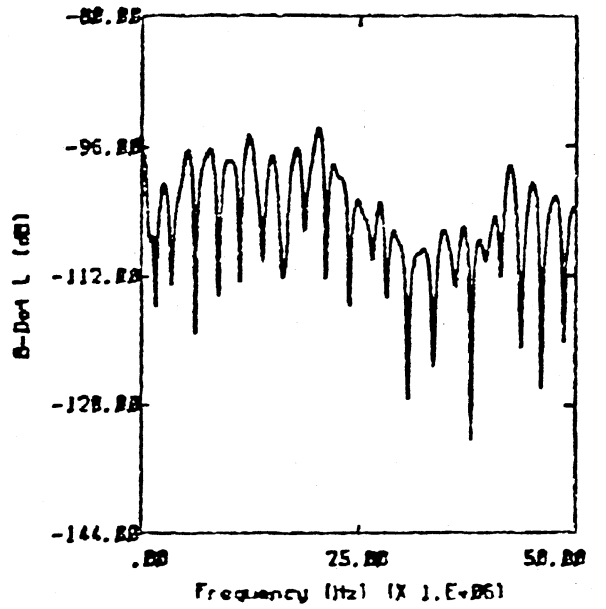
-80.00
-96.00
-112.00
-128.00
-144.00
B-Dot L (dB)
.00
25.00
50.00
Frequency (Hz) (X 1.E+06)
FLT37 RUN4 NEAR 28K FT -34.5°C

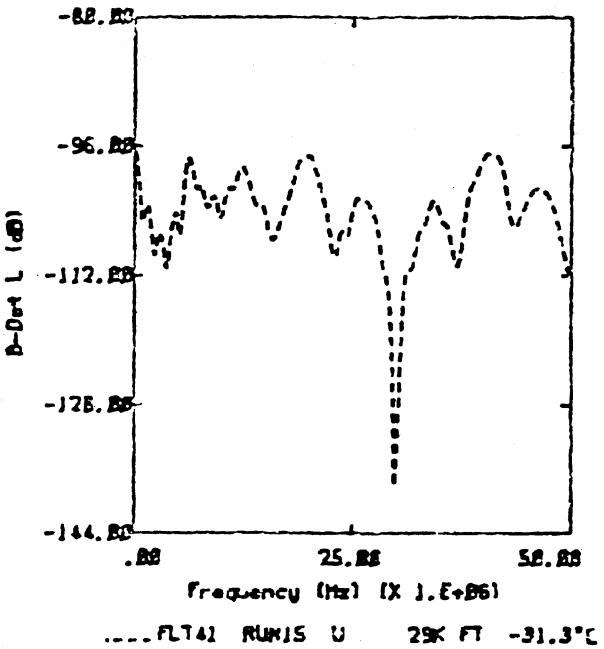
-80.00
-96.00
-112.00
-128.00
-144.00
B-Dot L (dB)
.00
25.00
50.00
Frequency (Hz) (X 1.E+06)
FLT41 RUN15 U 29K FT -31.3°C

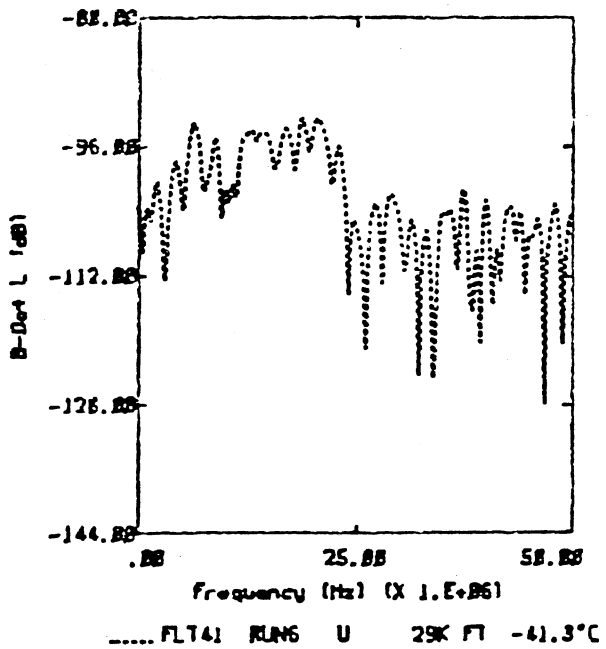
-80.00
-96.00
-112.00
-128.00
-144.00
B-Dot L (dB)
.00
25.00
50.00
Frequency (Hz) (X 1.E+06)
FLT41 RUN6 U 29K FT -41.3°C

Category 6

1. Report No.	2. Government Accession No.	3. Recipient's Catalog No.
NASA CR-3902		

4. Title and Subtitle	5. Report Date
INVESTIGATIONS INTO THE TRIGGERED LIGHTNING RESPONSE OF THE F106B THUNDERSTORM RESEARCH AIRCRAFT	June 1985
	6. Performing Organization Code
7. Author(s)	8. Performing Organization Report No.
Terence H. Rudolph, Rodney A. Perala, Paul M. McKenna, and Steven L. Parker	EMA-85-R-02
	10. Work Unit No.
9. Performing Organization Name and Address	
Electro Magnetic Applications, Inc. P.O. Box 26263 Denver, CO 80226	11. Contract or Grant No. NAS1-16984
	13. Type of Report and Period Covered
12. Sponsoring Agency Name and Address	Contractor Report
National Aeronautics and Space Administration Washington, DC 20546	14. Sponsoring Agency Code 505-34-13-34

15. Supplementary Notes

Langley Technical Monitor: Felix L. Pitts

16. Abstract

An investigation has been conducted into the lightning characteristics of the NASA F106B thunderstorm research aircraft. The investigation includes analysis of measured data from the aircraft in the time and frequency domains. Linear and nonlinear computer modelling has also been performed. In addition, new computer tools have been developed, including a new enhanced nonlinear air breakdown model, and a subgrid model useful for analyzing fine details of the aircraft's geometry. Comparison of measured and calculated electromagnetic responses of the aircraft to a triggered lightning environment are presented.

17. Key Words (Suggested by Author(s))	18. Distribution Statement
Triggered Lightning Finite Difference Analysis Air Breakdown Modelling Subgrid Modelling	Unclassified – Unlimited [redacted] Subject Category 47

19. Security Classif. (of this report)	20. Security Classif. (of this page)	21. No. of Pages	22. Price
Unclassified	Unclassified	203	

~~Available: NASA's Industrial Applications Center~~

NASA-Langley, 1985